THE CREATION OF ANIONS BY RYDBERG ELECTRON TRANSFER OR LASER VAPORIZATION AND THEIR EXAMINATION USING ANION PHOTOELECTRON SPECTROSCOPY

by

Sandra M. Ciborowski

A dissertation submitted to Johns Hopkins University in conformity with the requirements for the degree of Doctor of Philosophy.

Baltimore, Maryland

December 2019

Abstract

Negatively charged atomic, molecular, and cluster ions were studied in the gas phase by anion photoelectron spectroscopy. The photoelectron spectra map the electronic structure of these anionic species and, when combined with theoretical calculations, the geometry of the anionic and corresponding neutral species can be determined. A variety of experiments were performed using time-of-flight mass spectrometry coupled with negative ion photoelectron spectroscopy, after the negative ions were made by assorted sources. These studies focused on a wide range of electron binding strengths, i.e., from diffuse electron states to valence-bound states, and included organic molecules that exist in a few conformations, each with different multipole moments; atomic metal anions; complexes between atomic or cluster metal anions and small molecules; and superatomic anions, which have varied ligands.

After introducing the experimental methods, **Chapter III** presents these studies in detail, starting with the multiple dipole-bound anions that introduced our Rydberg Electron Transfer capabilities, the correlation-bound anion of *p*-chloroaniline, and the dipole- and/or quadrupole-bound anions of the succinonitrile, dicyanocyclohexane and silatrane molecules and divulging into the more strongly bound negative ions from interactions of metal atoms and clusters with pyridine, hydroxylamine, water, and carbon dioxide, as well as the hardness of metal borides and the effects ligands have on cobalt sulfide superatoms.

Advisor:	Dr. Kit H. Bowen
Committee:	Dr. Art Bragg
	Dr. Howard Fairbrother

Acknowledgments

Firstly, I would like to thank my research advisor, Dr. Kit H. Bowen. He was the first person at Johns Hopkins University to believe in my potential as an experimental physical chemist. He has always prioritized his graduate students and noticed their contributions to his research.

Secondly, I thank my committee members, Drs. Art E. Bragg and D. Howard Fairbrother, for being willing to sit through my oral examinations and dissertation defense, as well as being wonderful professors in the classroom. My gratitude also goes to Dr. Harris J. Silverstone for standing in as an alternate board member for my oral exams.

Next, I would like to thank Gaoxiang Liu, who was my lab partner for most of my time in the Bowen lab. Although we had our disagreements about how to accomplish various tasks, we were able to compromise and find a solution to any problem we faced.

Drs. Allyson Buytendyk and Jacob Graham immediately preceded us on the Pulsed Source Apparatus, making many of the subsequent experiments possible and giving us the unique tool of Rydberg Electron Transfer coupled with photoelectron spectroscopy. Both Allyson and Jacob were instrumental in and supportive during my first year of graduate study at Johns Hopkins, while I learned many of the processes and inner workings of the Bowen lab.

Drs. Evan Collins and Zach Hicks were available and willing to answer just about any question, ranging from basic electronics to designs that were machine-specific. Their guidance and support have made numerous studies in this thesis possible.

Nic Blando has not only been encouraging and helpful with any project proposed in lab, but he has been a supportive and invaluable friend to me. He has been extremely selfless and a great support inside and outside of the lab.

I have had the pleasure of witnessing and assisting with the growth of younger students in the lab. Linjie Wang has quickly adapted and taken to the surface machine. Mary Marshall has grown immeasurably in the last few years, becoming a lead on all things related to electrospray and the Pulsed Ionization Photoelectron Spectroscopy (PIPES) apparatus. With the help of Zhaoguo Zhu and Rachel Harris, Mary has taken Evan's design and construction of ESI coupled to the PIPES apparatus to full fruition. Zhaoguo is developing into a knowledgeable and valuable member of the ESI-PIPES team. Rachel is not only blossoming into an expert experimental chemist and knowledgeable machinist but is also an unflappable friend in and out of the lab. Already, her unfailing encouragement and understanding has supported a number of projects in her short time being part of the Bowen lab. More recent additions, Marica Dipalo, Moritz Blankenhorn and Lucas Hansen, have begun to show great promise and their excellent learning abilities to master a number of techniques used throughout the lab. There have been a number of undergraduate students, visiting students and professors, and other colleagues who have been a support system in various aspects of the lab and in my growth as an effective researcher.

I would like to thank the generous and gallant departmental facilities manager, Boris Steinberg, for all of his help, ranging from keys to machining. In addition, I thank the wonderful people who run our department and take care of the intricacies of paperwork and other items I, as a graduate student, do not have to worry about; Lauren, Jasmine, and

Meghan were always helpful and a sounding board for many students, and Indira and Cassandra were willing to help tackle any problem or assist with anything they could.

My former advisors' support and encouragement have not gone unseen over my time at Johns Hopkins. Dr. Carol Ann Miderski was my first physical chemistry professor and stimulated my interest in pursuing a higher degree in such. Dr. Emmanuel Ojadi fortified my drive toward a doctorate degree and was supportive and helpful throughout my transition to Johns Hopkins University and into the job market thereafter.

Lastly, but absolutely not least, I thank my family and friends. Without the support of my parents and siblings, none of my college and graduate career would have been possible. My parents, Bonnie and Bob, have always reinforced my ambitions and encouraged my imagination, keeping a realistic but optimistic view of my future and abilities. Also, they made sure I always had a ride to and from the airport on my trips, and my dad even joined me on one – truly a memorable experience. My sister, Laura, and brother, Danny, have also strengthened my belief in myself and comforted me when things have not seemed to go well. I am humbled by and so appreciative for the love and support that my boyfriend, Brandon, has given me the last few years. I have had a number of friends who have listened to and helped with anything that came up during my graduate career, for them I am eternally grateful.

While each graduate school experience is different and I may not remember every person who has influenced me, I am glad that I have been given the various opportunities and have grown from the hardships I faced along the way. Thank you for all of the support, laughter, patience, love, advice, encouragement, tears, and hugs!

TABLE OF CONTENTS

TABLE OF TABLES

TABLE OF FIGURES

I. Introduction

Spanning across many processes in chemistry and physics are the interactions between electrons and atoms, molecules, or clusters. These interactions result in a negative ion, a.k.a. anion, that, relative to the neutral species, has an excess electron and experiments describe the degree of perturbation this electron can have on the neutral species. When stable negative ions are formed due to such an interaction, they can exist at varying levels of stability, i.e., from correlation-bound to valence-bound anions.[1-36] As other molecules are introduced to these negative ions, complexes and other products, such as those resulting from proton transfer or activation, can be formed.

Experimental techniques can utilize electric and magnetic fields to manipulate these anions. In our instruments, we use electric grids to accelerate the ions, electrostatic lenses and deflector plates to direct the ions, and electric and magnetic fields to guide electrons resulting from the interaction of the ions with a photon beam. Our techniques are mass spectrometry and anion photoelectron spectroscopy.

Mass spectrometry is based on the principles of kinetic and potential energy of a charged particle. More specifically, that the kinetic and potential energies of the charged particle are equivalent. Thus, the relationship between the time of flight down the tube of known length and the mass of the ion is

$$t = k\sqrt{\frac{m}{q}}$$

where t is the time it takes for the particle to pass from the extraction region to the detector k is a constant, m is the mass of the particle, and q is the charge of said particle. Our mass spectrometers can detect both negative and positive ions.

Our photoelectron spectrometers study negative ions, since we are interested in information regarding the neutral molecules. Anion photoelectron spectroscopy is governed by the energy-conserving relationship:

$$h\nu = EKE + EBE$$

where the hν is the photon energy of a fixed frequency laser, EKE is the electron kinetic energy, and EBE is the electron binding energy. Since the wavelength and thus frequency of the Nd:YAG or excimer laser are known and the mass and flight time of the electrons is known, the EBE is determined.

Relative intensities within a photoelectron spectrum depend on the Franck-Condon overlap of the ground-state anion and the corresponding neutral electronic states. A pictorial representation of photoelectron spectroscopy, including arrows representing the energy of the photons, the EKEs of the photodetached electrons, and the EBEs, is displayed in Figure I.1. The adiabatic electron affinity (EA) is the energetic difference between the ground state of the anion and the ground state of the corresponding neutral state. Significant geometrical changes between the negative ion and the analogous neutral, which presents with a low Franck-Condon overlap, may lead to transitions not being observed in the photoelectron spectrum. Vertical detachment energies (VDEs) are the transitions from the ground state of the anion to other vibrational and/or excited states of the neutral molecule. If there is enough energy from the laser to probe excited states of the neutral, higher binding energy peaks, i.e., higher VDEs, will be observed. The VDEs with the greatest Franck-Condon overlap will appear as more intense peaks in the spectrum.

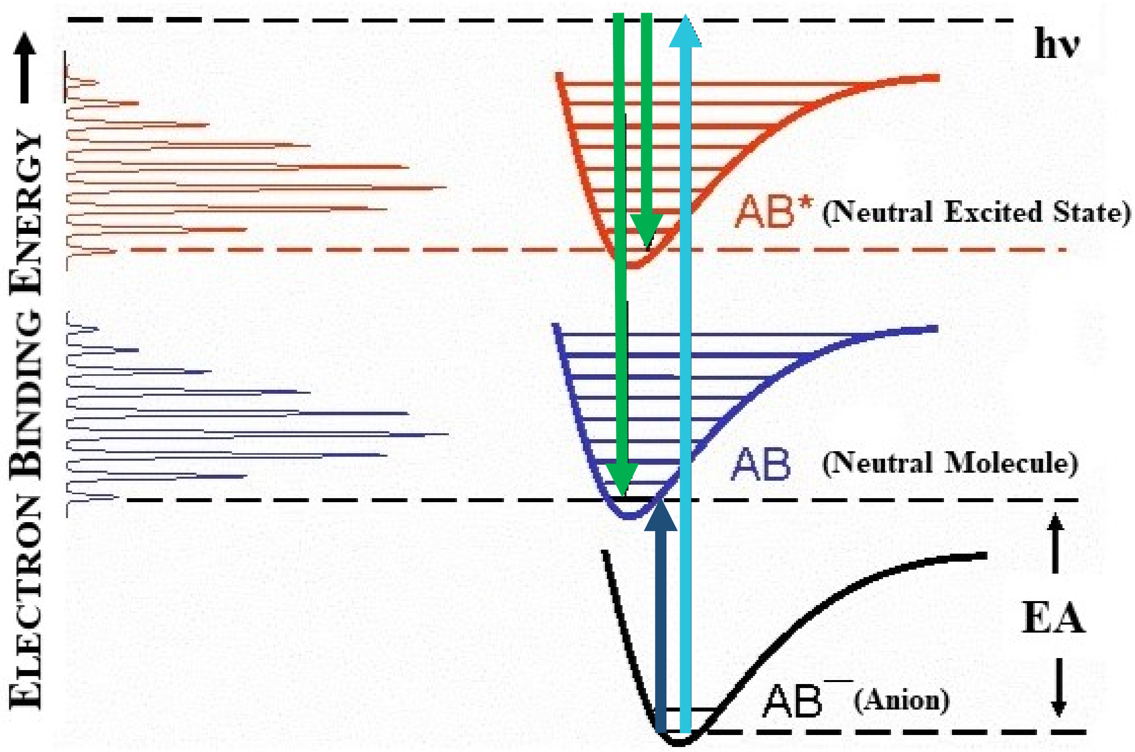

Figure I.1. Pictorial Representation of Anion Photoelectron Spectroscopy. The Light Blue Arrow Depicts the Photon Energy of the Fixed Frequency Laser; the Green Arrows Show the EKEs; the Dark Blue Arrow Illustrates One EBE, Corresponding to the EA. Adapted from D. Andrews, R. Calvi, and W. C. Lineberger, *Photoelectron Imaging Spectroscopy of Copper-Methanol Anion Complexes*, U. of Colorado, Boulder, Presentation at OSU International Symposium on Molecular Spectroscopy (2008).

This dissertation is divided into a few divisions, each focusing on a different aspect of anion photoelectron spectroscopy studies. In Chapter II, explanation of the various negative ion sources, as well as further information on the photoelectron spectrometers, is provided. Specific studies using a multitude of these sources are presented in Chapter III and are divided into two main subcategories of increasing binding strength of the electron to the neutral atom, molecule, or cluster. The Appendices supply extensive details on improvements made to different apparatuses, in addition to designed novel sources, many of which have been manufactured and implemented in experiments.

References

1. S. M. Ciborowski, R. M. Harris, G. Liu, C. J. Martinez-Martinez, P. Skurski, and K. H. Bowen, *J. Chem. Phys.* **150**, 161103 (2019).
2. J. P. Rogers, C. S. Anstöter, and J. R. R. Verlet, *J. Phys. Chem. Lett.* **9**, 2504 (2018).
3. J. P. Rogers, C. S. Anstöter, and J. R. R. Verlet, *Nature Chem.* **10**, 341 (2018).
4. J. N. Bull and J. R. R. Verlet, *Sci. Adv.* **3**, e1603106 (2017).
5. J. P. Rogers, C. S. Anstöter, J. N. Bull, B. F. E. Curchod, and J. R. R. Verlet, *J. Phys. Chem. A* **123**, 1602 (2019).
6. J. V. Coe, J. T. Snodgrass, C. B. Freidhoff, K. M. McHugh, and K. H. Bowen, *Chem. Phys. Lett.* **124**, 274 (1986).
7. P. Storoniak, H. Wang, Y. J. Ko, X. Li, S. T. Stokes, S. Eustis, K. H. Bowen, and J. Rak, in Practical Aspects of Computational Chemistry III, edited by J. Leszczynski and M. K. Shukla (Springer, Boston, MA, 2014).
8. M. Haranczyk, M. Gutowski, X. Li, and K. H. Bowen, *Proc. Natl. Acad. Sci*. **104**, 4804 (2007).
9. K. Mazurkiewicz, M. Haranczyk, M. Gutowski, J. Rak, D. Radisic, S. N. Eustis, D. Wang, and K. H. Bowen, *J. Am. Chem. Soc*. **129**, 1216 (2007).
10. D. Svozil, P. Jungwirth, and Z. Havlas, *Collect. Czech. Chem. Commun.* **69**, 1395 (2004).
11. M. R. Nimlos and G. B. Ellison, *J. Phys. Chem*. **90**, 2574 (1986).

12. O. Dolgounitcheva, V. G. Zakrzewski, and J. V. Ortiz, *Chem. Phys. Lett*. **307**, 220 (1999).

13. E. F. Belogolova, G. Liu, E. P. Doronina, S. M. Ciborowski, V. F. Sidorkin, and K. H. Bowen, *J. Phys. Chem. Lett*. **9**, 1284 (2018).

14. T. Sommerfeld, *J. Chem. Phys*. **121**, 4097 (2004).

15. J. H. Hendricks, H. L. de Clercq, S. A. Lyapustina, C. A. Fancher, T. P. Lippa, J. M. Collins, S. T. Arnold, G. H. Lee, and K. H. Bowen, in Structures and Dynamics of Clusters, Proceedings of Yamada Conference XLIII, Shimoda, Japan, 1995, edited by T. Kondow, K. Kaya, and A. Terasaki (Universal Academy Press, Tokyo, 1996), p. 321.

16. C. Desfrançois, H. Abdoul-Carime, C. Adjouri, N. Khelifa, and J. P. Schermann, *Europhys. Lett*. **26**, 25 (1994).

17. R. A. Popple, C. D. Finch, and F. B. Dunning, *Chem. Phys. Lett*. **234**, 172 (1995).

18. L. Suess, Y. Liu, R. Parthasarathy, and F. B. Dunning, *J. Chem. Phys*. **119**, 12890 (2003).

19. C. Desfrançois, *Phys. Rev. A* **51**, 3667 (1995).

20. K. D. Jordan and F. Wang, *Annu. Rev. Phys. Chem*. **54**, 367 (2003).

21. M. Gutowski, P. Skurski, K. D. Jordan, and J. Simons, *Int. J. Quantum Chem*. **64**, 183 (1997).

22. C. G. Bailey, C. E. H. Dessent, M. A. Johnson, and K. H. Bowen, *J. Chem. Phys*. **104**, 6976 (1996).

23. G. H. Lee, S. T. Arnold, J. G. Eaton, and K. H. Bowen, *Chem. Phys. Lett*. **321**, 333 (2000).

24. N. I. Hammer, K. Diri, K. D. Jordan, C. Desfrançois, and R. N. Compton, *J. Chem. Phys.* **119**, 3650 (2003).

25. J. H. Hendricks, S. A. Lyapustina, H. L. de Clercq, J. T. Snodgrass, and K. H. Bowen, *J. Chem. Phys*. **104**, 7788 (1996).

26. I. Kulakowska, M. Geller, B. Lesyng, and K. L. Wierzchowski, *Biochim. Biophys. Acta* **361**, 119 (1974).

27. C. Desfrançois, Y. Bouteiller, J. P. Schermann, D. Radisic, S. T. Stokes, K. H. Bowen, N. I. Hammer, and R. N. Compton, *Phys. Rev. Lett*. **92**, 083003 (2004).

28. H. Abdoul-Carime and C. Desfrançois, *Eur. Phys. J. D* **2**, 149 (1998).

29. M. V. N. A. Prasad, R. F. Wallis, and R. Herman, *Phys. Rev. B* **40**, 5924 (1989).

30. G. L. Gutsev, P. Jena, and R. J. Bartlett, *J. Chem. Phys*. **111**, 504 (1999).

31. J. V. Coe, G. H. Lee, J. G. Eaton, S. T. Arnold, H. W. Sarkas, and K. H. Bowen, *J. Chem. Phys*. **92**, 3980 (1990).

32. R. N. Compton, H. S. Carman, C. Desfrançois, H. Abdoul-Carmine, J. P. Schermann, J. H. Hendricks, S. A. Lyapustina, and K. H. Bowen, *J. Chem. Phys*. **105**, 3472 (1996).

33. T. Sommerfeld, *Phys. Chem. Chem. Phys*. **4**, 2511 (2002).

34. C. Desfrançois, H. Abdoul-Carime, N. Khelifa, and J. P. Schermann, *Phys. Rev. Lett*. **73**, 2436 (1994).

35. D. J. Goebbert, K. Pichugin, and A. Sanov, *J. Chem. Phys*. **131**, 164308 (2009).

36. C. Desfrançois, V. Periquet, Y. Bouteiller, and J. P. Schermann, *J. Phys. Chem. A* **102**, 1274 (1998).

II. Experimental Methods

We utilize a variety of anion sources on our gas-phase machines within our lab. They range from very gentle electron attachment, as in Rydberg electron transfer (RET), to disruptive and destructive techniques, e.g., the Pulsed Arc Current Ionization Source (PACIS). The most common of these sources tends to be varieties of the laser vaporization source. These methods will be further explained.

The Rydberg electron transfer (RET) source combines photon excitation of and intermolecular transfer of electrons. In our RET source, we thermally expand a beam of potassium, K, atoms, using the oven designed and implemented by Allyson Buytendyk with Jacob Graham. The potassium atoms are excited by two photons: the first is from a red (766.7 nm) pulse of light and the second is a blue (410-440 nm) pulse. The two pulses are generated from individual dye lasers. The red laser is a Spectra Physics PDL-1, pumped by a Continuum Surelite II-10; the blue laser is a new Sirah Cobra (sold by Spectra Physics), pumped by a Continuum Surelite II-20. Since the RET process is based on the resonant process corresponding to specific energies, the variability of the blue light over multiple wavelengths is crucial to making certain fragile anions. The Sirah Cobra offers the ability to adjust the wavelength of the blue light using the computer program. For our setup, the red laser is brought in from the top of Ch. 1 and 2 on the PSA-RET apparatus, while the blue enters through the window on the rear side of the instrument, both meeting in the extraction region of the time-of-flight mass spectrometer (TOF-MS). The red should be aligned with the entrance of the internal RET oven as well as the apertures on Ch. 2; the blue should be aligned through the window as well as the skimmer in Ch. 0, though both of these may need slight adjustments depending on the experiment and the amount of ion signal. Once the potassium has been pumped to the chosen energy level, the neutral molecules are introduced, typically using the pulse valve in Ch. 0. Two pictorial representations of these processes are presented in Figure II.1.

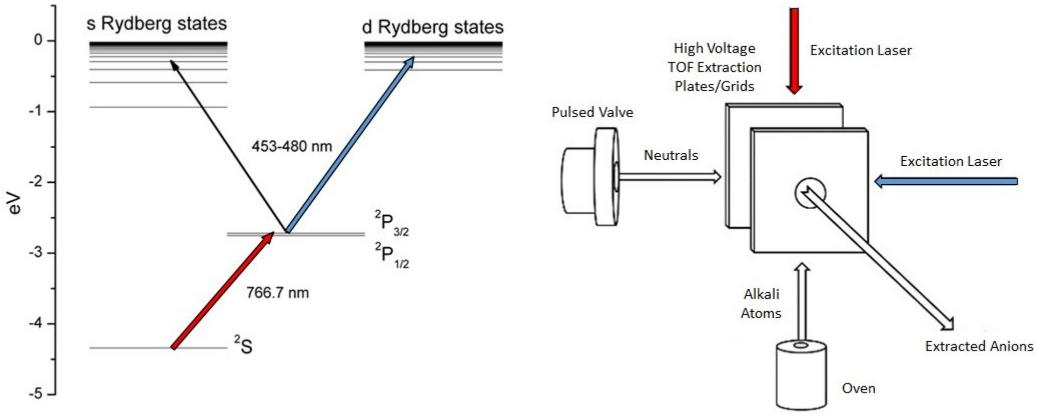

Figure II.1. (A) Pumping Scheme of the Potassium Atoms, using the Two Dye Lasers. (B) Pictorial representation of the RET Experimental Setup.

Another method that can be used to create Rydberg atoms is the Electron Bombardment Ionizer (EBI) source, mounted on the outer wall of Ch. 2 on the PSA-RET apparatus, whose schematic can be seen in Figure II.2[1] and more details can be found in Section IV.G. By flowing in a gas of choice, the filament, whose current and float voltage can be adjusted, excites electrons in the gas atoms and the source will only allow the still neutral Rydberg atoms to pass into its center by varying the voltages on the three internal, concentric grids. However, this is not the sole purpose of this source; as its name suggests, the filaments can be utilized as the source of electrons to create anions and cations of interest. Operating the filaments in this fashion also gives the possibility of tuning the energy of the electrons by manipulating the float voltage and/or current applied. This format can be relatively destructive compared to that of RET. Additionally, the source could be used as a way to introduce a reactant gas, by way of the needle valve on the gas inlet.

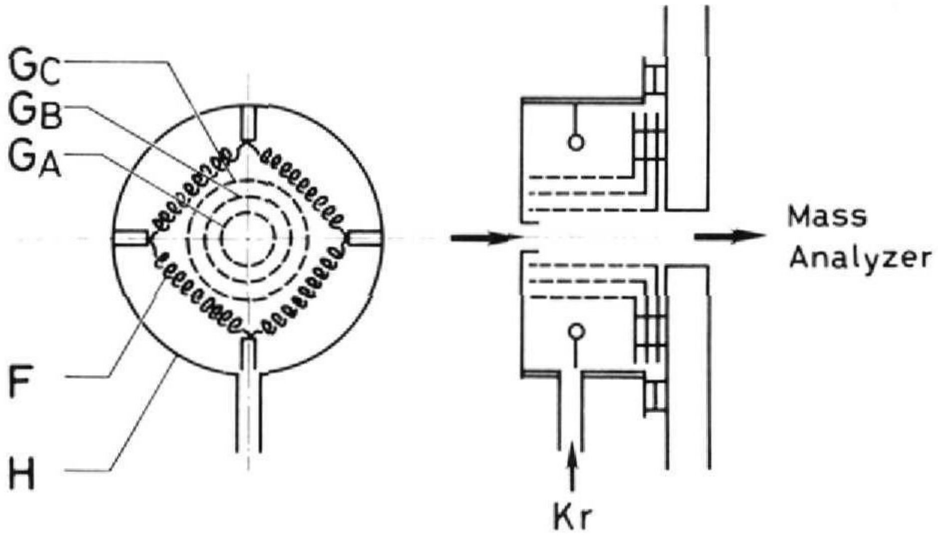

Figure II.2. SCHEMATIC OF THE ELECTRON BOMBARDMENT IONIZER, INCLUSIVE OF THE THREE GRIDS, FILAMENTS, GAS INLET, AND HOUSING. REPRODUCED WITH PERMISSION FROM *J. PHYS. CHEM.* 90, 1552 (1986). COPYRIGHT (1986) AMERICAN CHEMICAL SOCIETY.[1]

There are a few varieties of the laser vaporization source (LVS) that are available on our apparatuses, including a closed-housing rod source with the pulse valve directly behind the rod, a closed-housing rod source with the pulse valve at an angle behind the rod, an open-housing rod source (commonly referred to as the laser photoemission source), and a new disk-target source with two housing styles. The specific designs of two closed-housing and the target LVSs are included in the appendices (Section IV.C) of this thesis. In all of these designs, the anions are created in a plasma by the laser striking the rod, potentially in combination with a gas or other molecule introduced by the pulse valve. Also, many of these versions now have the option of a reaction cell that can be attached to the front of the housing and provide a means to introduce a reactant gas outside of the main laser interaction region of the source. A note about the laser vaporization techniques: many researchers claim that the dimensions and capacity of the waiting room inside the housing and nozzle make a significant difference in what species are made; we have seen this to a certain extent but have not fully explored the variations that are possible, given the multitude of nozzle designs that could be utilized in these sources.

A source that combines the photoemission source with a matrix assisted, laser desorption ionization (MALDI)-like source is the infrared (IR) desorption source, more commonly referred to as the "Biosource" in our lab. The sample is crushed onto a graphite rod, where the IR light from the Continuum Minilite II, Nd:YAG laser is used to heat the sample/graphite and vaporize the sample into the vacuum. When the pulsed valve expels helium, the sample is forced into a region where the second harmonic of the Surelite SLI-10, "source" laser is used to ablate a metal wire or small disk, usually of hafnium or yttrium, respectively. A schematic of this source is presented in Figure II.3.

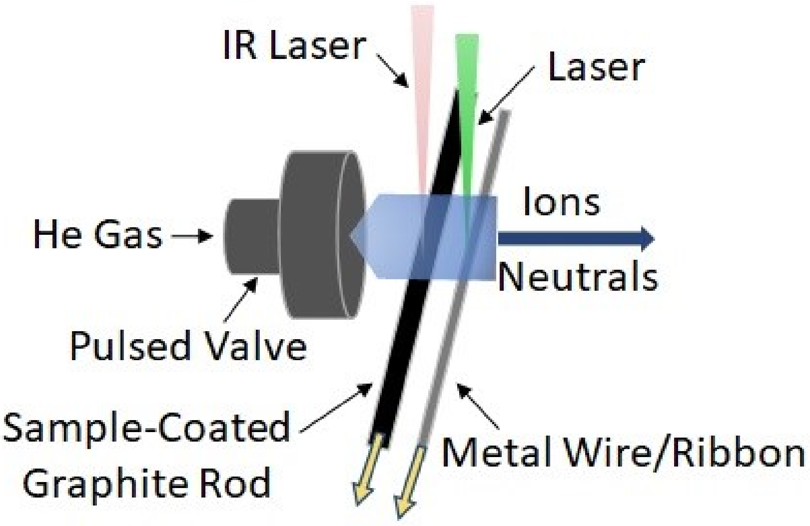

Figure II.3. Schematic of the Infrared (IR) Desorption Source, which combines a MALDI-like technique with laser photoemission.

While the Biosource is similar to RET, in the way that we are able to make parent anions of the sample, the pulsed arc cluster ionization source (PACIS) is related to the laser vaporization sources. A high voltage pulse between two electrodes, typically one is aluminum and the other copper, introduces the sample that is pressed within one of the electrodes to the TOF-MS via a pulsed valve, normally backed with either hydrogen or helium gas. The quartz cube, shown in Figure II.4, isolates the electrodes from the rest of the source and instruments. The long channel is thought to increase cluster growth, after being thrust forward by the helium or hydrogen gas. More details of the initial design can be found in *Z. Phys. D* **20**, 417 (1991) and *Science* **315**, 356 (2007).[2,3]

After the anions are formed by one or more of these sources, they are introduced into the time-of-flight mass spectrometer and mass analyzed; this portion can be done for both cations and anions, though not simultaneously. After this analysis, the anions are mass gated, effectively choosing a single mass peak to further analyze by anion

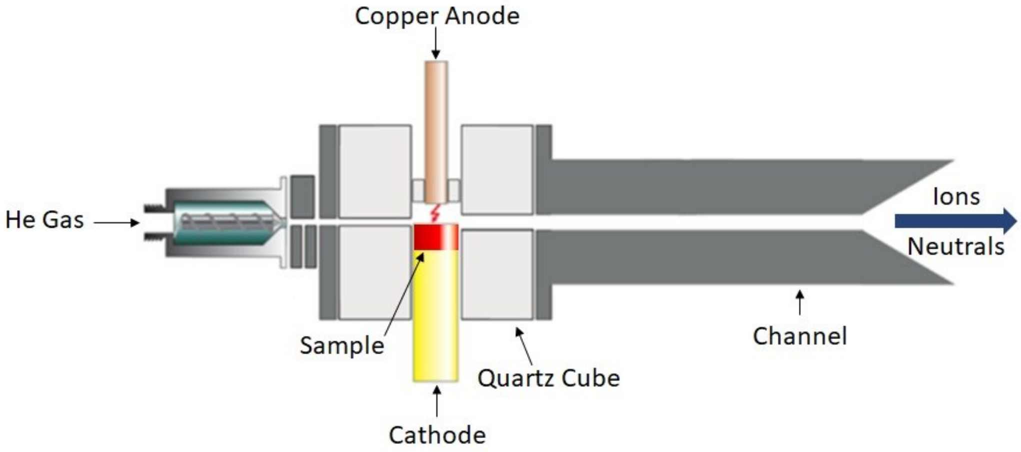

Figure II.4. Schematic of the PACIS Source, Including the Sample, Electrodes, Long Channel for Clustering, and Pulsed Valve Input. Adapted from Gerd Gantefoer's Website at Uni. Konstanz and *Science* 315, 356 (2007).[3]

photoelectron spectroscopy (PES). There are two spectrometers that we have to complete this: magnetic bottle (MB) and velocity-map imaging (VMI).

For the MB spectrometer, the mass-gated anions are decelerated to have nearly zero kinetic energy when in the interaction region. Once there, a pulsed laser, either a Nd:YAG or excimer, interacts with the ions, removing electrons. The photodetached electrons are then guided up the flight tube by the magnetic fields, as displayed in Figure II.5.[4] At the end of which is a multichannel plate, which detects the electrons. Based on the amount of time that it takes for the electrons to reach the detector, the velocity and thus energy can be extrapolated. Since this process is governed by the relationship: hν = EBE + EKE, where the hν is the energy of the laser, EBE is the electron binding energy and EKE is the electron kinetic energy, the corresponding binding energies of the electrons can be determined. To note, the third and fourth harmonics of a Nd:YAG laser and the ArF wavelength from the excimer laser are most commonly used in our MB spectrometer.

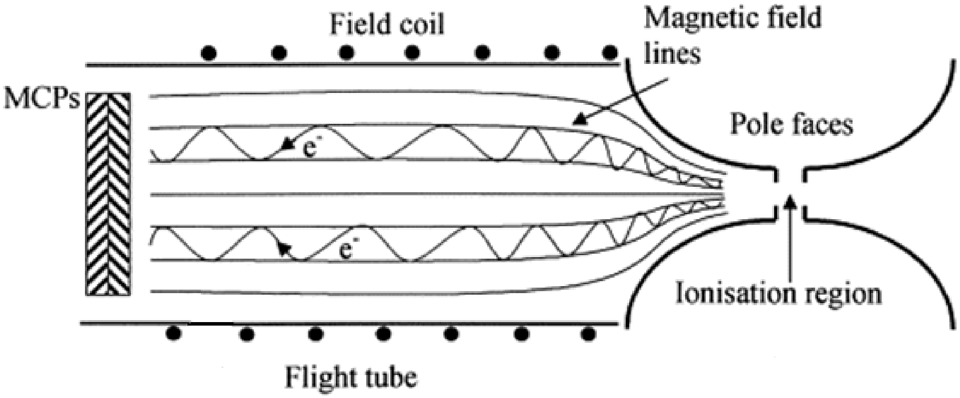

Figure II.5. SCHEMATIC OF A MAGNETIC BOTTLE PHOTOELECTRON SPECTROMETER; THE IONS AND THE LASER PULSE WOULD INTERACT IN THE "IONISATION REGION". REPRODUCED FROM *J. ELECTRON SPECTROSC.* **112**, 151 (2000), COPYRIGHT 2000, WITH PERMISSION FROM ELSEVIER.[4]

Similarly, the VMI spectrometer also ascertains the binding energies of the electrons. However, the VMI spectrometer involves electric fields, i.e., a series of plates with divided voltages, to guide the electrons after the mass-gated, un-decelerated anions reach the interaction region of the TOF-MS and are referenced to the appropriate path of travel. These photodetached electrons interact with a pulsed multichannel plate (PMCP) and a subsequent phosphor screen (Figure II.6), which is monitored by a CCD camera.[5] Using a computer program, BASEX, the center slice of the 3-D image is extrapolated and plotted. This also relates to the equation above and directly correlates to the binding energies of the electrons detached by the laser. Typically, for our VMI spectrometer, the first and second harmonics of a Nd:YAG laser are utilized. More specific information regarding the

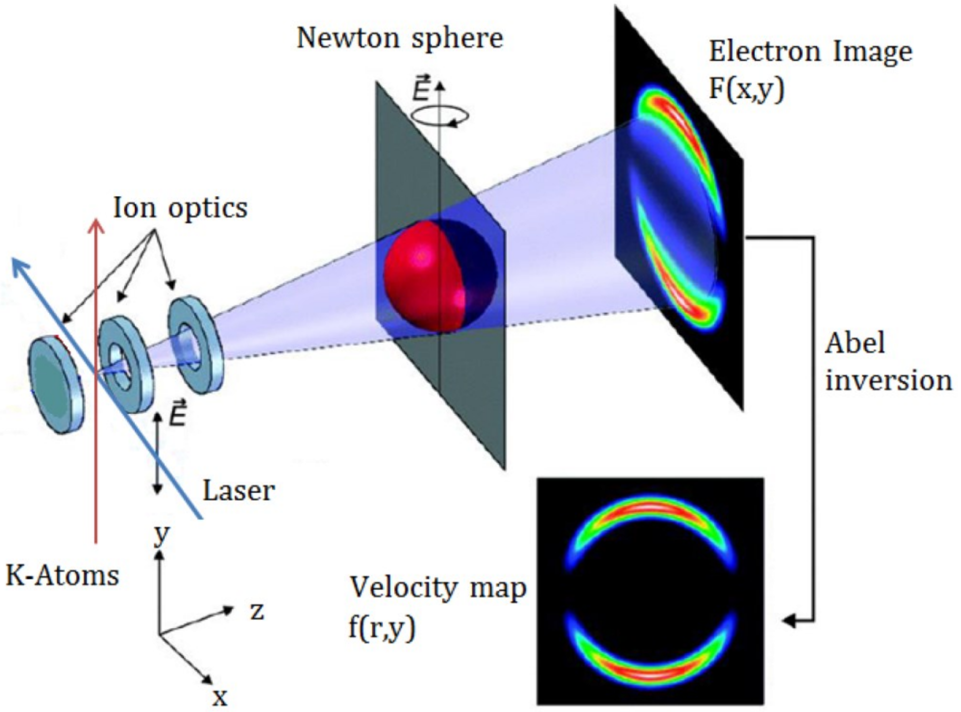

Figure II.6. Schematic of Velocity Map Imaging Spectroscopy. Reproduced from A. Wituschek, "Versuchsanleitung: Fortgeschrittenen Praktikum, Teil II", Universität Freiburg, Germany, 2016.[5]

anisotropy parameter, β, can be determined from the VMI spectra. A *β* value around 2 is consistent with an outgoing *p* wave, which means that photodetachment occurred from an *s*-orbital with nearly zero angular momentum.[6] Spatially diffuse excess electron states, i.e., those with excess electrons viewed as possessing *s*-orbital character, will present with β values equivalent to two; variations in the measured β values can result from minor distortions in electric fields and/or small stray magnetic fields.[7]

The photoelectron spectra can be compared to theoretical calculations to validate the computational methods, as well as reveal specific geometric structures.

References

1. K. Mitsuke, T. Kondow, and K. Kuchitsu, *J. Phys. Chem.* **90**, 1552 (1986).
2. H. R. Siekmann, C. Lüder, J. Faehrmann, H. O. Lutz, and K. H. Meiwes-Broer, *Z. Phys. D* **20**, 417 (1991).
3. X. Li, A. Grubisic, S. T. Stokes, J. Cordes, G. F. Ganteför, K. H. Bowen, B. Kiran, M. Willis, P. Jena, R. Burgert, and H. Schnöckel, *Science* **315**, 356 (2007).
4. A. M. Rijs, E. H. G. Backus, C. A. de Lange, N. P. C. Westwood, and M. H. M. Janssen, *J. Electron Spectrosc.* **112**, 151 (2000).
5. A. Wituschek, "Versuchanleitung: Fortgeschrittenen Praktikum, Teil II", Universität Freiburg, Germany, 2016.
6. C. L. Adams, H. Schneider, K. M. Ervin, and J. M. Weber, *J. Chem. Phys.* **130**, 074307 (2009).
7. E. C. Red, A. M. Juárez, D. Rolles, and A. Aguilar, *Rev. Mex. Ris. S* **56**, 100 (2010).

III. Anion Photoelectron Spectroscopic Studies

There are two main sections to this thesis, which are distinctive based on the strength of the binding of systems studied. In the first, the excess electron is bound very weakly to the molecule and is shown by low binding energies in the photoelectron spectra. In the latter, the electrons are bound much more tightly, causing a larger difference between the anion and neutral geometries and, thus, presenting as broader peaks at higher binding energies.

III.A. Weakly Bound Excess Electrons

As alluded to above, there is a range of interactions that a single electron can have with a neutral molecule, some of which are much weaker when compared to the others. Here, we focus on those that exhibit sharp, low binding energy peaks in the photoelectron spectra. Such peaks are characteristic of the similarities in geometry of the neutrals and their corresponding anions, coming from the strong Franck-Condon overlap.

The following studies range from correlation-bound anions to slightly stronger interactions of quadrupole and dipole binding of the excess electron. Correlation effects tend to be the weakest interactions and are often involved in all bonding to some degree. An anion bound solely from correlation effects is rare to isolate. Other studies have focused on an electron binding to the positive end or portion of a dipole or quadrupole moment of a molecule. Though there are ambiguities in the threshold for quadrupole moments, it is well known that the dipole moment must be at least 2.5 Debye to bind an electron. Frequently, whether a molecule exhibits a dipole or quadrupole moment also depends on the conformer that is present. More specific details are forthcoming.

III.A.1. Dipole-Bound Anions: Formed by Rydberg Electron Transfer (RET) and Studied by Velocity Map Imaging-Anion Photoelectron Spectroscopy (VMI-aPES)

Sandra M. Ciborowski, Gaoxiang Liu, Jacob D. Graham, Allyson M. Buytendyk, and Kit H. Bowen

Reprinted by permission from Springer Nature Customer Service Center GmbH: Springer Nature, The European Physical Journal D – Atomic, Molecular, Optical and Plasma Physics, *Eur. Phys. J. D* (2018) 72: 139. https://doi.org/10.1140/epjd/e2018-90182-y.

III.A.1.a. Abstract

Here, we demonstrate the capabilities of the unique combination of Rydberg Electron Transfer (RET) and Velocity Map Imaging-Anion Photoelectron Spectroscopy (VMI-aPES) to form dipole bound anions and to measure their photoelectron spectra. For these purposes, we have chosen the dipole bound anions of acetonitrile, ammonia-water dimer, water dimer, dimethyl sulfoxide and thymine as examples. All of these had been previously formed and/or studied but by other methodologies.

III.A.1.b. Introduction

The interactions between electrons and atoms, molecules, or clusters govern many processes in chemistry and physics. When stable negative ions are formed as a result of these interactions, they may exist either as valence anions or as diffuse electron states [1-39]. As negative ions, they can be mass-analyzed in mass spectrometers and, once mass-selected, their anion photoelectron spectra can be measured. While we can utilize a variety of ion sources to create negative ions, we focus here on the Rydberg electron transfer (RET) anion source as a means of forming them and on velocity map imaging as a technique for measuring their anion photoelectron spectra.

Rydberg electron transfer (RET) is a gentle process that transfers an electron from a highly-excited atom to a neutral molecule, forming a negative ion. In RET, a pulsed, helium-seeded beam of neutral molecules is crossed with a continuous, thermal beam of potassium atoms, which have been excited to one of their Rydberg levels by two dye laser pulses: one set at a fixed frequency to pump the potassium atoms to their $^2P_{3/2}$ state and the other tuned to the appropriate *n*d Rydberg level. Upon collision of the neutral molecule and the highly excited Rydberg atom, charge transfer occurs, forming an ion pair. Once it separates into ions, the anions produced by RET are pulsed through a time-of-flight mass spectrometer, mass-selected, photodetached by another laser pulse, and their resultant electrons energy-analyzed by anion photoelectron spectroscopy (aPES). Negative ion photoelectron spectroscopy (aPES) is a powerful tool for probing electronic structure information about neutral molecules and/or clusters. Anion PES is governed by the energy-conserving relationship, $hv = EBE + EKE$, where hv is the energy of the photon beam, EBE is the binding energy of the electron, and EKE is the kinetic energy of the electron. Our time-of-flight mass spectrometric and photoelectron spectroscopic apparatus has previously been described [11,40]. The apparatus includes both a magnetic bottle energy analyzer, which has a resolution of about 35 meV at EKE of 1 eV, as well as a velocity-map imaging (VMI) energy analyzer, with $\Delta E/E \sim 0.03$. The most common information provided by anion photoelectron spectra is the vertical detachment energy (VDE) of the anion being studied. The VDE is the photodetachment transition energy from the anion's ground state to its neutral counterpart at the structure of the anion. (Photodetachment is an ultra-fast and therefore vertical process.) The adiabatic electron affinity (EA) is the energy difference between the ground states of the anion and its neutral counterpart. Its appearance in a photoelectron spectrum is dependent on the structural similarity between the anion and its neutral, i.e., on Franck-Condon overlap. In most of the anions presented here, the structures of the anion and its neutral are almost identical, making the VDE and the EA values essentially the same values. The VDE value in a given photoelectron spectrum is the electron binding energy (EBE) corresponding to the intensity maximum of the lowest EBE peak in the spectrum. When the VDE value is small, the electron binding energy for that anion is also small and in all likelihood the geometries of the anion and its corresponding neutral molecule are quite similar. The RET technique allows us to create unusually fragile anions. Here, we demonstrate some of the capabilities of this one-of-a-kind combination of a Rydberg electron transfer anion source and velocity map imaging-anion photoelectron spectroscopy. Velocity map imaging is the electron energy analysis technique of choice for measuring the anion photoelectron spectra of low VDE anions.

III.A.1.c. Results

Below in Figure III.A.1, we present mass spectra of eight anions made with our RET ion source, whereas in Figures III.A.2-7, we present the corresponding anion photoelectron spectra of six of those same systems. Five of the six anions presented in Figure III.A.2-7 are dipole bound anions. For molecules (or small clusters) that do not form valence anions, they can often form dipole bound anions when their dipole moments are

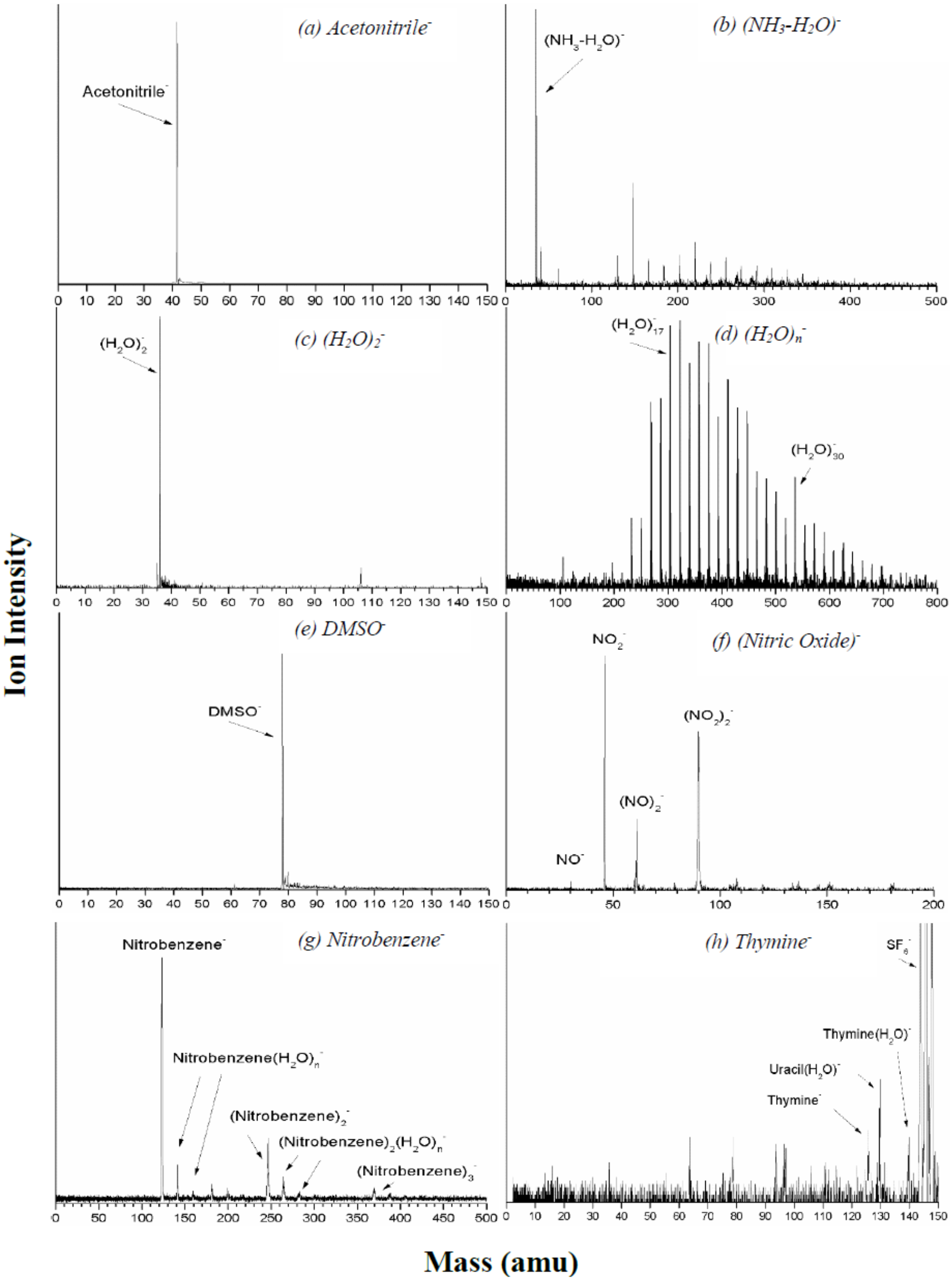

Figure III.A.1. Mass spectra of the anions: (a) acetonitrile anion, (b) ammonia-water dimer anion, $(NH_3\text{-}H_2O)^-$, (c) water dimer anion, $(H_2O)_2^-$, (d) water cluster anions, $(H_2O)_n^-$, (e) dimethyl sulfoxide anion, DMSO$^-$, (f) nitric oxide anions, NO$^-$, (g) nitrobenzene anions, and (h) thymine anions, made with the Rydberg electron transfer (RET) source and analyzed by our TOF mass spectrometer.

large enough to capture an excess electron. The critical dipole moment required is equal or greater than ~2.5 Debye. The RET and VMI-aPES combination is especially well-suited for studying dipole bound anion states.

Figures III.A.2-7 present anion photoelectron spectra of the species we formed by RET. Since RET is a resonant process, the K** Rydberg level used to make a given anion is indicated on the spectrum by *n*d, where *n* is the principle quantum number. For the five dipole bound anions discussed here, Table III.A.1 compares VDE values from previous experiments, from the present RET-aPES experiments, and from theory, along with listing the dipole moments of their neutral counterparts.

Acetonitrile was found to form a dipole bound anion in both stand-alone RET experiments [14-16], in conventional anion photoelectron experiments using a non-RET anion source [17,20,30,36], and through theoretical calculations [19,30]. Our photoelectron spectrum of the acetonitrile anion, generated and measured by the combined RET-VMI-

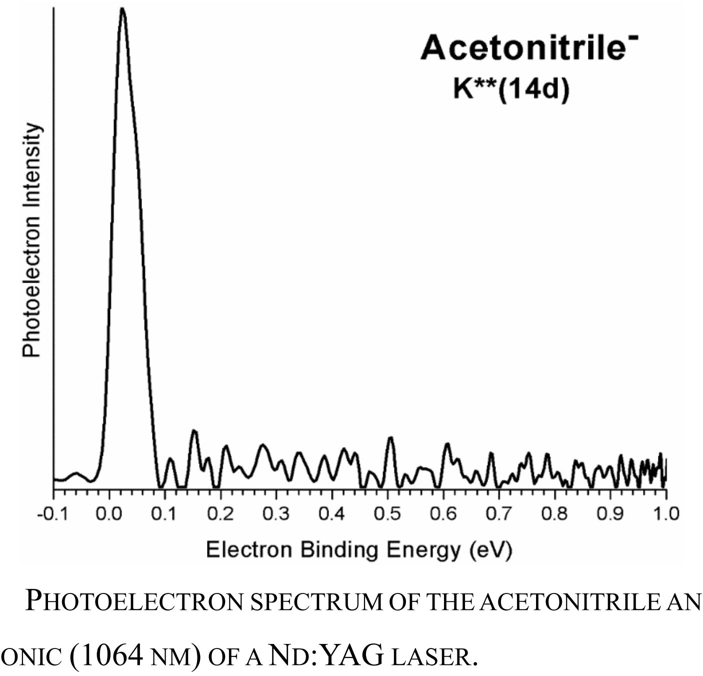

Figure III.A.2. PHOTOELECTRON SPECTRUM OF THE ACETONITRILE ANION TAKEN WITH THE FIRST HARMONIC (1064 NM) OF A ND:YAG LASER.

Table III.A.1. Comparison of the vertical detachment energy (VDE) values from this work, previous experiments, and theoretical calculations for the studied anionic species.

Anionic Species	Dipole Moment (μ, D)	VDE (meV)		
		Current Exp.	Previous Exp.	Theory
Acetonitrile	3.92[a,b]	22	3,[c] 11,[d] 12,[e] 18.0,[f] 18.2[g]	13.4,[h] 15.5[g]
$(NH_3\text{-}H_2O)$	2.9[i]	7	9[i]	13.5[j]
$(H_2O)_2$	2.6[i,k]	35	42[i,l] 45,[k,m] 48[n]	41.9[o]
DMSO	3.96[a,b]	5	7.4,[a] 13.9[b]	13.9[b]
Thymine	4.13[p]	71	69[q]	51,[r] 69[g]

[a]See ref. 16; [b]See ref. 26; [c]See ref. 20; [d]See ref. 15,16,36; [e]See ref. 14; [f]See ref. 17; [g]See ref. 30; [h]See ref. 19; [i]See ref. 21; [j]See ref. 22; [k]See ref. 23; [l]See ref. 33; [m]See ref. 13;

aPES technique, is shown in Figure III.A.2. The single, narrow peak at very low electron binding energy (EBE) is characteristic of diffuse electron states, such as dipole bound anions. The peak's narrowness is due to the structures of the anion and the neutral being nearly identical. The low EBE value of its peak center (low VDE) is due to its excess electron being weakly bound. While there is some variation in the acetonitrile anion's VDE values listed in Table III.A.1, they are also broadly consistent.

While ammonia alone has a relatively low dipole moment of ~1.4 D, its hetero-dimer with water, i.e., $(NH_3\text{-}H_2O)$, has a dipole moment of 2.9 D. This led us to predict that it would form a dipole bound dimer anion. Stand-alone RET experiments and calculations showed that it does [21,22]. Our anion photoelectron spectrum of $(NH_3\text{-}H_2O)^-$, generated and measured by the combined RET-VMI-aPES technique, is shown in Figure III.A.3. VDE comparisons in Table III.A.1 are again broadly consistent with one another.

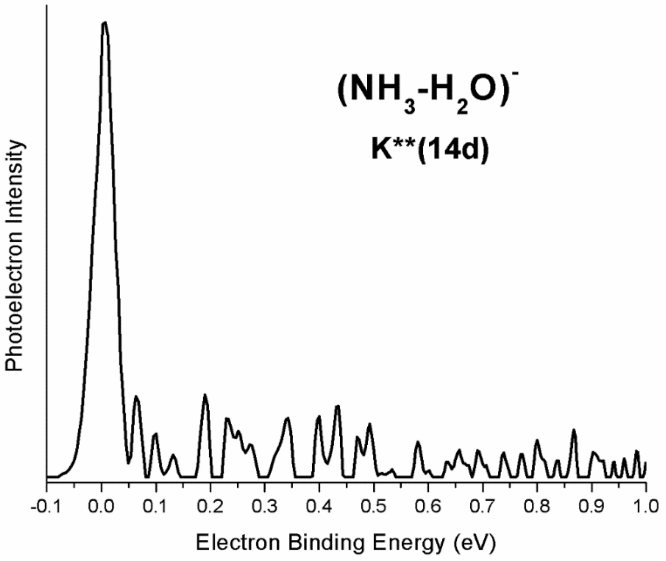

Figure III.A.3. PHOTOELECTRON SPECTRUM OF THE AMMONIA-WATER DIMER ANION TAKEN WITH THE FIRST HARMONIC (1064 NM) OF A ND:YAG LASER.

While the water molecule also has a modest dipole moment of ~1.85 D, its dimer, i.e., $(H_2O)_2$, has a dipole moment of ~2.6 D [21,23] and, since it is greater than 2.5 D, it forms a dipole bound anion. The water dimer anion, $(H_2O)_2^-$, was the first dipole bound anion to be seen by anion photoelectron spectroscopy [13,21,23,24,33]. Our anion photoelectron spectrum of $(H_2O)_2^-$, generated and measured by the combined RET-VMI-aPES technique, is shown in Figure III.A.4. VDE comparisons in Table III.A.1 are consistent with one another.

Dimethyl sulfoxide ($(CH_3)_2SO$) has a dipole moment of 3.96 D and was shown by through stand-alone RET experiments to form a dipole bound anion [16,26]. Our anion photoelectron spectrum of DMSO$^-$, generated and measured by the combined RET-VMI-

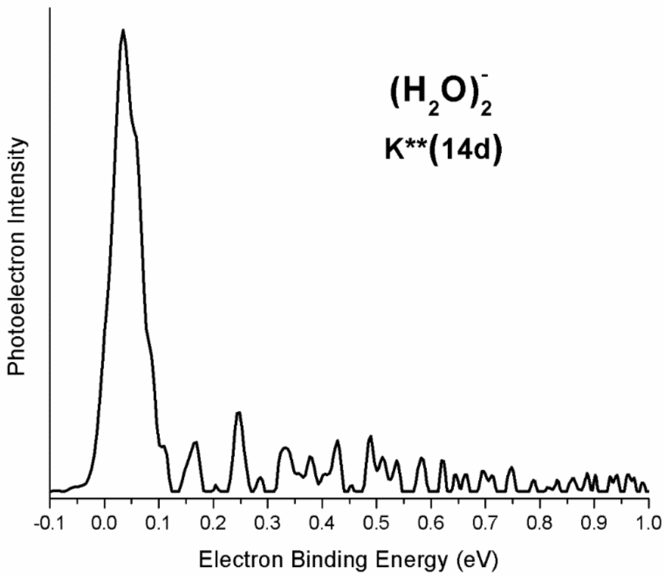

Figure III.A.4. PHOTOELECTRON SPECTRUM OF THE WATER DIMER ANION TAKEN WITH THE FIRST HARMONIC (1064 NM) OF A ND:YAG LASER.

aPES technique, is shown in Figure III.A.5, again in broad agreement with other measurements.

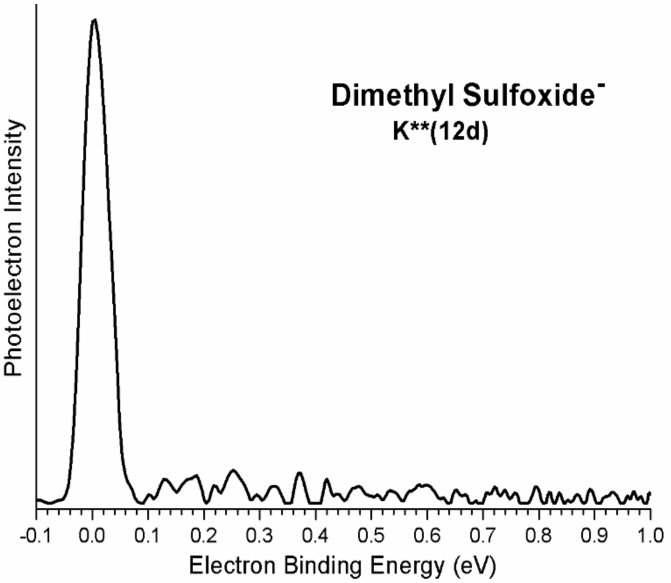

Figure III.A.5. PHOTOELECTRON SPECTRUM OF THE DIMETHYL SULFOXIDE ANION, $DMSO^-$, TAKEN WITH THE FIRST HARMONIC (1064 NM) OF A ND:YAG LASER.

Thymine has a dipole moment of 4.13 D and, thus, is also able to bind an excess electron via its dipolar field. A combination of experimental and theoretical assessments agrees [27,28,30,38]. Our anion photoelectron spectrum of the thymine dipole bound anion, generated and measured by the combined RET-VMI-aPES technique, is shown in Figure III.A.6, and is again in broad agreement with other measurements.

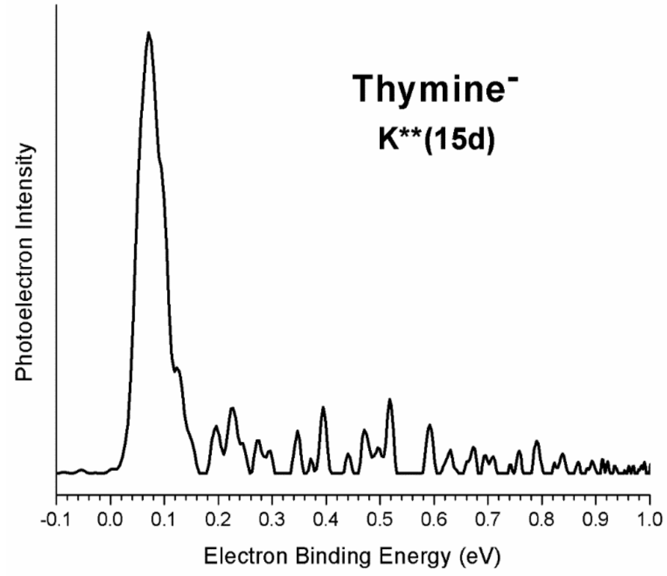

Figure III.A.6. PHOTOELECTRON SPECTRUM OF THE THYMINE ANION TAKEN WITH THE FIRST HARMONIC (1064 NM) OF A ND:YAG LASER.

The last spectrum to be presented is that of $(H_2O)_{17}^-$. While not a dipole bound anion, it is nevertheless a diffuse electron state and is usually considered to be an embryonic hydrated electron state. It was originally measured by both stand-alone RET and conventional anion photoelectron spectroscopy [24,33]. Our anion photoelectron spectrum of $(H_2O)_{17}^-$, generated and measured by the combined RET-VMI-aPES technique, is shown in Figure III.A.7 and matches previous anion photoelectron spectra of it quite well.

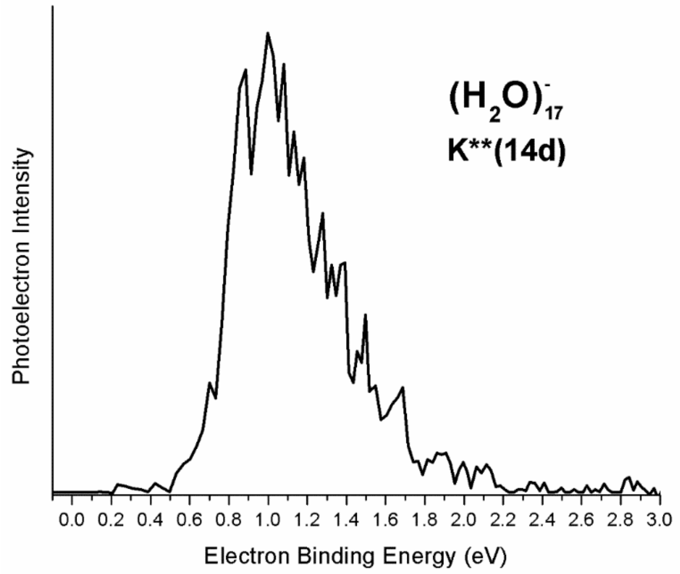

Figure III.A.7. PHOTOELECTRON SPECTRUM OF THE WATER CLUSTER ANION, $(H_2O)_{17}^-$, TAKEN WITH THE FIRST HARMONIC (1064 NM) OF A ND:YAG LASER.

III.A.1.d. Summary

Here, we have presented a collection of mostly dipole-bound, anion photoelectron spectra, generated and measured by our combined RET-VMI-aPES technique, for the purpose of demonstrating the capabilities of this unique methodology.

Acknowledgement

This material is based on work supported by the U. S. National Science Foundation under Grant No. CHE-1664182 (KHB).

Statement of Contribution

S. M. C., G. L., and K. H. B. contributed to writing this manuscript. S. M. C., G. L., J. D. G., and A. M. B. conducted the RET-VMI-aPES experiments.

References

1. G. H. Lee, S. T. Arnold, J. G. Eaton, H. W. Sarkas, K. H. Bowen, C. Ludewigt, and H. Haberland, *Z. Phys. D* **20**, 9 (1991).

2. J. G. Eaton, S. T. Arnold, and K. H. Bowen, *Int. J. Mass Spec. Ion Proc.* **102**, 303 (1990).
3. J. V. Coe, J. T. Snodgrass, C. B. Freidhoff, K. M. McHugh, and K. H. Bowen, *J. Chem. Phys.* **87**, 4302 (1987).
4. J. V. Coe, J. T. Snodgrass, C. B. Freidhoff, K. M. McHugh, and K. H. Bowen, *Chem. Phys. Lett.* **124**, 274 (1986).
5. P. Storoniak, H. Wang, Y. J. Ko, X. Li, S. T. Stokes, S. Eustis, K. H. Bowen, and J. Rak, in *Practical Aspects of Computational Chemistry III*, edited by J. Leszczynski and M. K. Shukla (Springer, Boston, MA, 2014).
6. M. Haranczyk, M. Gutowski, X. Li, and K. H. Bowen, *Proc. Natl. Acad. Sci.* **104**, 4804 (2007).
7. K. Mazurkiewicz, M. Haranczyk, M. Gutowski, J. Rak, D. Radisic, S. N. Eustis, D. Wang, and K. H. Bowen, *J. Am. Chem. Soc.* **129**, 1216 (2007).
8. D. Svozil, P. Jungwirth, and Z. Havlas, *Collect. Czech. Chem. Commun.* **69**, 1395 (2004).
9. M. R. Nimlos and G. B. Ellison, *J. Phys. Chem.* **90**, 2574 (1986).
10. O. Dolgounitcheva, V. G. Zakrzewski, and J. V. Ortiz, *Chem. Phys. Lett.* **307**, 220 (1999).
11. E. F. Belogolova, G. Liu, E. P. Doronina, S. M. Ciborowski, V. F. Sidorkin, and K. H. Bowen, *J. Phys. Chem. Lett.* **9**, 1284 (2018).
12. T. Sommerfeld, *J. Chem. Phys.* **121**, 4097 (2004).

13. J. H. Hendricks, H. L. de Clercq, S. A. Lyapustina, C. A. Fancher, T. P. Lippa, J. M. Collins, S. T. Arnold, G. H. Lee, and K. H. Bowen, in *Structures and Dynamics of Clusters*, *Proceedings of Yamada Conference XLIII, Shimoda, Japan, 1995*, edited by T. Kondow, K. Kaya, and A. Terasaki (Universal Academy Press, Tokyo, 1996), p. 321.
14. C. Desfrançois, H. Abdoul-Carime, C. Adjouri, N. Khelifa, and J. P. Schermann, *Europhys. Lett.* **26**, 25 (1994).
15. R. A. Popple, C. D. Finch, and F. B. Dunning, *Chem. Phys. Lett.* **234**, 172 (1995).
16. L. Suess, Y. Liu, R. Parthasarathy, and F. B. Dunning, *J. Chem. Phys.* **119**, 12890 (2003).
17. C. Desfrançois, *Phys. Rev. A* **51**, 3667 (1995).
18. K. D. Jordan, F. Wang, *Annu. Rev. Phys. Chem.* **54**, 367 (2003).
19. M. Gutowski, P. Skurski, K. D. Jordan, and J. Simons, *Int. J. Quantum Chem.* **64**, 183 (1997).
20. C. G. Bailey, C. E. H. Dessent, M. A. Johnson, and K. H. Bowen, *J. Chem. Phys.* **104**, 6976 (1996).
21. C. Desfrançois, B. Baillon, J. P. Schermann, S. T. Arnold, J. H. Hendricks, and K. H. Bowen, *Phys. Rev. Lett.* **72**, 48 (1994).
22. P. Skurski and M. Gutowski, *J. Chem. Phys.* **108**, 6303 (1998).
23. G. H. Lee, S. T. Arnold, J. G. Eaton, and K. H. Bowen, *Chem. Phys. Lett.* **321**, 333 (2000).
24. C. Desfrançois, N. Khelifa, A. Lisfi, J. P. Schermann, J. G. Eaton, and K. H. Bowen, *J. Chem. Phys.* **95**, 7760 (1991).

25. Y. Bouteiller, C. Desfrançois, J. P. Schermann, Z. Latajka, and B. Silvi, *J. Chem. Phys.* **108**, 7967 (1998).
26. N. I. Hammer, K. Diri, K. D. Jordan, C. Desfrançois, and R. N. Compton, *J. Chem. Phys.* **119**, 3650 (2003).
27. J. H. Hendricks, S. A. Lyapustina, H. L. de Clercq, J. T. Snodgrass, and K. H. Bowen, *J. Chem. Phys.* **104**, 7788 (1996).
28. I. Kulakowska, M. Geller, B. Lesyng, and K. L. Wierzchowski, *Biochim. Biophys. Acta* **361**, 119 (1974).
29. C. Desfrançois, Y. Bouteiller, J. P. Schermann, D. Radisic, S. T. Stokes, K. H. Bowen, N. I. Hammer, and R. N. Compton, *Phys. Rev. Lett.* **92**, 083003 (2004).
30. H. Abdoul-Carime and C. Desfrançois, *Eur. Phys. J. D* **2**, 149 (1998).
31. M. V. N. A. Prasad, R. F. Wallis, and R. Herman, *Phys. Rev. B* **40**, 5924 (1989).
32. G. L. Gutsev, P. Jena, and R. J. Bartlett, *J. Chem. Phys.* **111**, 504 (1999).
33. J. V. Coe, G. H. Lee, J. G. Eaton, S. T. Arnold, H. W. Sarkas, and K. H. Bowen, *J. Chem. Phys.* **92**, 3980 (1990).
34. R. N. Compton, H. S. Carman, C. Desfrançois, H. Abdoul-Carmine, J. P. Schermann, J. H. Hendricks, S. A. Lyapustina, and K. H. Bowen, *J. Chem. Phys.* **105**, 3472 (1996).
35. T. Sommerfeld, *Phys. Chem. Chem. Phys.* **4**, 2511 (2002).
36. C. Desfrançois, H. Abdoul-Carime, N. Khelifa, and J. P. Schermann, *Phys. Rev. Lett.* **73**, 2436 (1994).
37. D. J. Goebbert, K. Pichugin, and A. Sanov, *J. Chem. Phys.* **131**, 164308 (2009).
38. D. Svozil, T. Frigato, Z. Havlas, and P. Jungwirth, *Phys. Chem. Chem. Phys.* **7**, 840 (2005).

39. C. Desfrançois, V. Periquet, Y. Bouteiller, and J. P. Schermann, *J. Phys. Chem. A* **102**, 1274 (1998).

40. A. M. Buytendyk, J. D. Graham, K. D. Collins, K. H. Bowen, C.-H. Wu, and J. I. Wu, *Phys. Chem. Chem. Phys.* **17**, 25109 (2015).

III.A.2. The Correlation-Bound Anion of *p*-Chloroaniline

Sandra M. Ciborowski, Rachel M. Harris, Gaoxiang Liu, Chalynette J. Martinez-Martinez, Piotr Skurski and Kit H. Bowen, Jr.

Reprinted from *J. Chem. Phys.* **150** (16) (2019) 161103, DOI: 10.1063/1.5096986, with the permission of AIP Publishing.

III.A.2.a. Abstract

The *p*-chloroaniline anion was generated by Rydberg electron transfer (RET) and studied via velocity-map imaging (VMI) anion photoelectron spectroscopy. The vertical detachment energy (VDE) of the *p*-chloroaniline anion was measured to be 6.6 meV. This value is in accord with the VDE of 10 meV calculated by Skurski and coworkers. They found the binding of the excess electron in the *p*-chloroaniline anion to be dominated by correlation effects with only a small contribution from the long-range dipole potential. As such, the *p*-chloroaniline anion is the first essentially correlation-bound anion to be observed experimentally.

III.A.2.b. Introduction

Very weak attractions between electrons and neutral molecules exert subtle influences on many phenomena in chemistry. When these attractions result in the formation of bound anions, their weakly-bound excess electrons occupy extremely diffuse orbitals. In principle, there exist several types of diffuse excess electron anion states, their binding deriving from electron-correlation, electron-polarizability, electron-dipole, or electron-quadrupole interactions, or, as often is the case, from some combination thereof. Anions formed by these particular interactions may be expected to possess excess electron binding strengths that increase roughly in the order: correlation-bound, quadrupole-bound, polarizability-bound, and dipole-bound anions. In order to study these anion categories separately, it is desirable to select examples, whose excess electron binding interactions, other than the one of interest, are either absent or negligible.

Contributions to excess electron binding and anion stability due to the aforementioned excess electron binding interactions have been examined in several theoretical studies.[1-10] Among these interactions, electron correlation effects are perhaps the most elusive, in part because they contribute to excess electron binding to some degree in most weakly bound anions. Excess electron binding due to correlation has been the focus of several landmark computational investigations.[5-10]

Calculations by Skurski and coworkers[10] found the excess electron in the *p*-chloroaniline anion to be highly spatially diffuse and its binding to be overwhelmingly due to electron correlation effects. While *p*-chloroaniline has a significant dipole moment (3.28 D), leading to competition between dipole-binding and correlation, it is electron correlation that was found to dominate excess electron binding in the *p*-chloroaniline anion. Even so, it is the anion's residual dipole-bound character that is likely responsible for the excess electron density preferring to reside toward the positive end of the molecular dipole. Upon finding the structures of the anion and its neutral counterpart to be essentially identical, Skurski *et al.* chose to calculate the excess electron binding energy at the equilibrium geometry of the *p*-chloroaniline anion. Their calculated value of 10 meV is therefore the vertical detachment energy (VDE) of the *p*-chloroaniline anion. Because of the close structural similarity between the *p*-chloroaniline anion and its neutral counterpart, this anion's VDE value can be assumed to be only incrementally greater than neutral *p*-chloroaniline's electron affinity (EA) value.

We have examined excess electron binding to *p*-chloroaniline by measuring the photoelectron spectrum of its parent anion. Neutral *p*-chloroaniline is an aromatic amine, also known as 4-chloroaniline. It has many agricultural, pharmaceutical, and industrial uses and has been characterized by a wide variety of physical and chemical means.[11-42] In addition to studies of neutral *p*-chloroaniline, its positive ion has also been characterized by both mass spectrometric and spectroscopic methods. While theory predicted its parent anion to be stable, the *p*-chloroaniline anion had not been observed experimentally prior to the current study.

In this work, we present the negative ion mass spectrum of the *p*-chloroaniline anion, which was made by Rydberg electron transfer (RET), along with its anion photoelectron spectrum, which was measured via velocity-map imaging (VMI) anion photoelectron spectroscopy. Using the latter, we determine the VDE value of the *p*-chloroaniline anion and compare it to its theoretically predicted value.

III.A.2.c. Experimental Methods

Rydberg electron transfer (RET) provides a fragile-anion-friendly environment in which to form previously inaccessible diffuse and otherwise weakly-bound electron states. In RET, an electronically-excited Rydberg atom transfers its outer electron to a target neutral molecule during their collision, resulting in an ion pair which separates into atomic cation and molecular anion products.[43,44] RET is a slow electron attachment process, in which the receding positive ion plays a uniquely stabilizing role. As a result, Rydberg electron transfer provides an unusually gentle, highly quantum state-specific, laser-tunable, anion formation environment. In a typical RET experiment, atoms are optically pumped to specific Rydberg states (n*) at the point where they collide with a beam of neutral target molecules. In the present case, the target is a beam of *p*-chloroaniline molecules, these having been vaporized in a heated pulsed valve and expanded with 10 psig of helium gas. To generate high intensities of product anions, we use alkali (K) atoms and two pulsed dye lasers. One laser optically-pumps to the $^2P_{3/2}$ level of the potassium atoms, while the second laser selectively excites that population to the ns and nd Rydberg levels of interest. Beams of Rydberg-excited K atoms and neutral target molecules cross between the ion extraction grids of our time-of flight mass analyzer/selector. There, parent anions of *p*-chloroaniline are formed by RET and accelerated (after a short delay) into a flight tube, along which they are mass-selected, prior to being photodetached. See Figure III.A.8 for a schematic of our apparatus.

Anion photoelectron (photodetachment) spectroscopy is conducted by crossing a beam of negative ions with a fixed-frequency photon beam and energy-analyzing the resultant photodetached electrons. This technique is governed by the energy-conserving relationship: hν = EBE + EKE, where hν is the photon energy, EBE is the electron binding

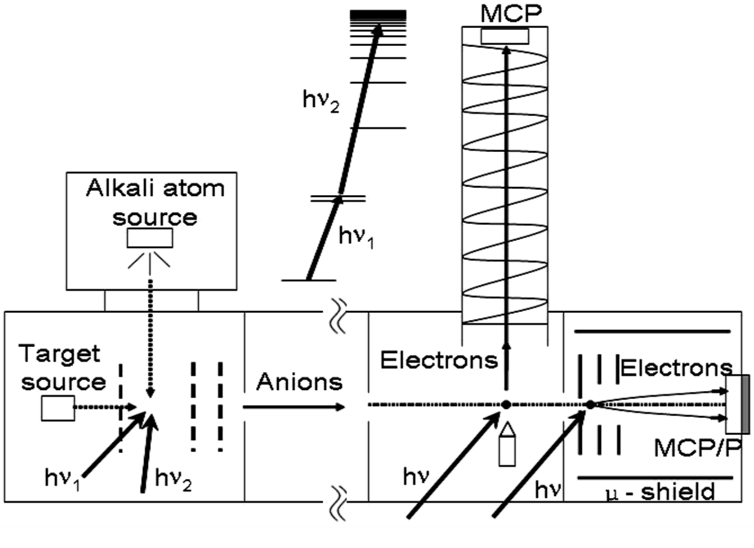

Figure III.A.8. SCHEMATIC OF OUR COMBINED RYDBERG ELECTRON TRANSFER (RET) - VELOCITY-MAP IMAGING (VMI) ANION PHOTOELECTRON SPECTROMETER.

(photodetachment transition) energy, and EKE is the electron kinetic energy. The electron energies of the photodetached electrons are measured using a velocity-map imaging (VMI) anion photoelectron spectrometer, which has been described previously.[44] There, mass-selected anions are crossed with 1064 nm, linearly polarized photons from a Nd:YAG laser. The resultant photodetached electrons are then accelerated along the axis of the ion beam toward a position-sensitive detector, which is coupled to a CCD camera. The BASEX method is used to reconstruct the two-dimensional image, formed by the sum of these electrons, into a portion of the three-dimensional distribution. Our resulting anion photoelectron spectrum is calibrated relative to the well-known photoelectron spectrum of NO^-.[45]

III.A.2.d. Results and Discussion

The mass spectrum of *p*-chloroaniline anions is presented in Figure III.A.9. All four nestled mass peaks are due to the natural abundance isotope pattern of the *p*-chloroaniline

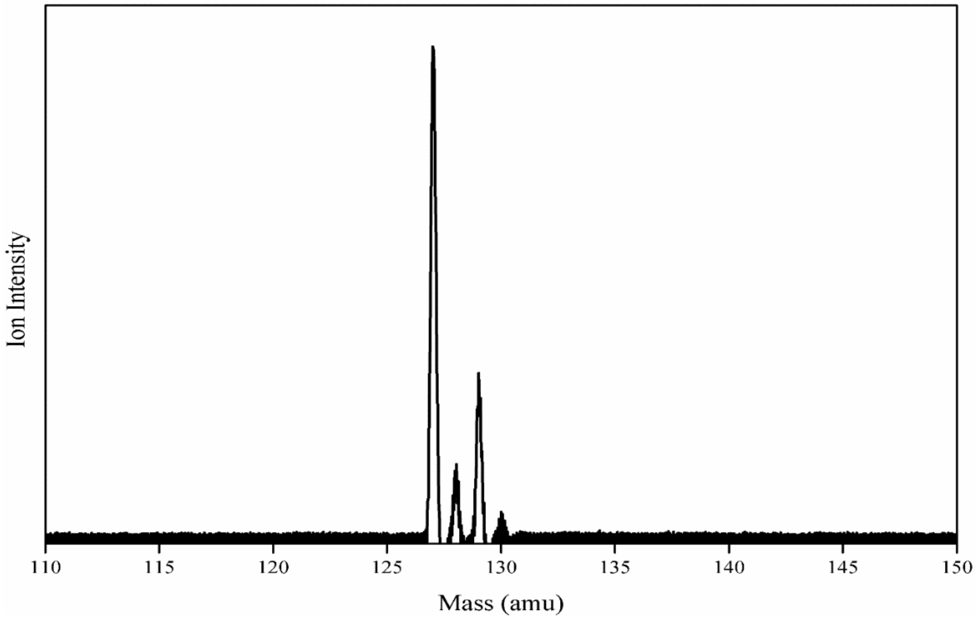

Figure III.A.9. MASS SPECTRUM OF *P*-CHLOROANILINE ANIONS MADE BY RYDBERG ELECTRON TRANSFER (N* = 14D).

parent anion. Since RET is a resonant process, we surveyed several Rydberg levels, i.e., n* = 12d to 15d, to find the most intense ion signal. It occurred at the n* = 14d Rydberg level. The photoelectron spectrum for the *p*-chloroaniline anion, is presented in Figure III.A.10. It consists of a single broad, symmetric peak located near an EBE of zero. The width of this peak is entirely due to instrumental resolution limitations. To precisely locate the EBE value of the peak's maximum, we applied a Gaussian fit, finding it to be 6.6 meV. This is the VDE value of the *p*-chloroaniline anion, and as mentioned above, this value is only slightly greater than the EA value of neutral *p*-chloroaniline. Thus, our measured VDE value is in good agreement with the predicted VDE value of 81 cm^{-1} or 10 meV, calculated by Skurski and coworkers, using *ab initio* CCSD(T)/aug-cc-pVDZ+5*s*4*p*3*d* methodology.[10] The agreement between our measurement and their computations supports

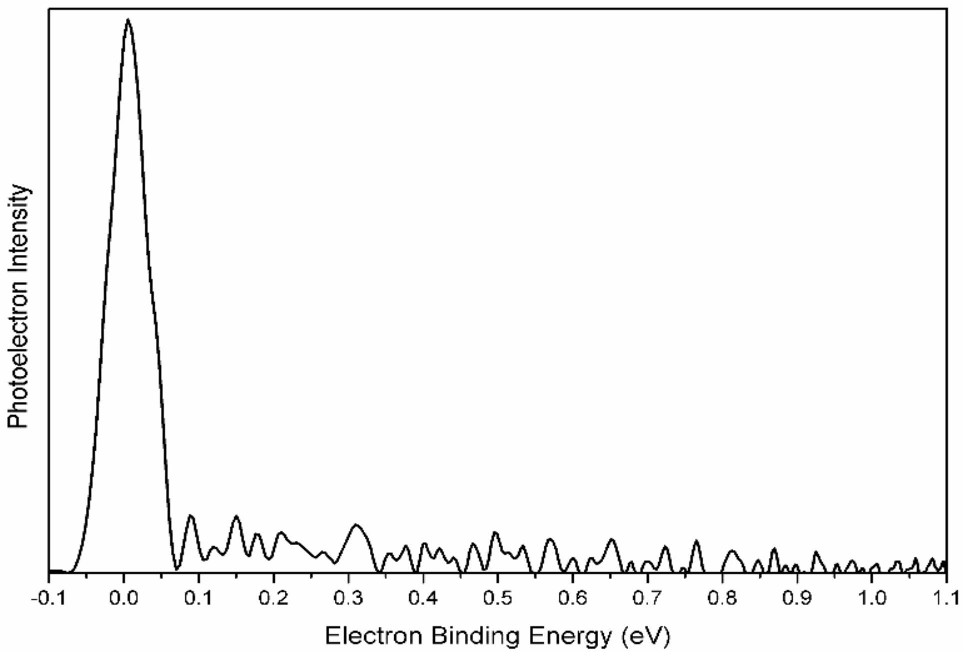

Figure III.A.10. ANION PHOTOELECTRON SPECTRUM OF *P*-CHLOROANILINE ANIONS MEASURED BY VELOCITY-MAP IMAGING (VMI) PHOTOELECTRON SPECTROSCOPY USING 1.165 EV (1064 NM) PHOTONS.

Skurski and coworkers' finding that the *p*-chloroaniline anion is primarily a correlation-bound anion with minor excess electron binding contributions from dipole binding. Thus, the *p*-chloroaniline anion, whose excess electron is incredibly weakly bound, sits near the base of a hierarchy of increasing excess electron binding interaction strengths. In addition, the *p*-chloroaniline anion is the first essentially correlation-bound anion to be observed experimentally.

Acknowledgements

This material is based on work supported by the U.S. National Science Foundation under Grant No. CHE-1664182 (KHB). We thank Dr. Vincent Ortiz for discussions.

References

1. J. Simons, *Annu. Rev. Phys. Chem.* **62**, 107 (2011).
2. P. Skurski, M. Gutowski, and J. Simons, *J. Chem. Phys.* **110**, 274 (1999).
3. J. Simons and P. Skurski, in *Theor. Prospect Negat. Ions*, edited by J. Kalcher (Research Signpost, Trivandrum, 2002), pp. 99–120.
4. M. Gutowski and P. Skurski, *Recent Res. Dev. Phys. Chem.* **3**, 245 (1999).
5. M. Gutowski, K. D. Jordan, and P. Skurski, *J. Phys. Chem. A* **102**, 2624 (1998).
6. T. Sommerfeld, B. Bhattarai, V. P. Vysotskiy, and L. S. Cederbaum, *J. Chem. Phys.* **133**, 114301 (2010).
7. V. K. Voora, A. Kairalapova, T. Sommerfeld, and K. D. Jordan, *J. Chem. Phys*. **147**, 214114 (2017).
8. M. Gutowski, P. Skurski, A. I. Boldyrev, J. Simons, and K. D. Jordan, *Phys. Rev. A* **54**, 1906 (1996).
9. V. K. Voora and K. D. Jordan, *J. Phys. Chem. A* **118**, 7201 (2014).

10. S. Smuczyńska, I. Gwarda, I. Anusiewicz, and P. Skurski, *J. Chem. Phys*. **130**, 124316 (2009).
11. United States Environ. Prot. Agency TSCA Chem. Subst. Invent. (2018).
12. A. Boehncke, J. Kielhorn, G. Konnecker, C. Pohlenz-Michel, and I. Mangelsdorf, *4-Chloroaniline* (Geneva, 2003).
13. P. Ekici, G. Leupold, and H. Parlar, *Chemosphere* **44**, 721 (2001).
14. M. Del Nogal Sánchez, C. Pérez Sappó, J. L. Pérez Pavón, and B. M. Cordero, *Anal. Bioanal. Chem.* **404**, 2007 (2012).
15. A. F. Pizon, A. R. Schwartz, L. M. Shum, J. C. Rittenberger, D. R. Lower, S. Giannoutsos, M. A. Virji, and M. D. Krasowski, *Clin. Toxicol.* **47**, 132 (2009).
16. M. Kiese and G. Renner, *Naunyn-Schmiedeberg's Arch. Für Exp. Pathol. Und Pharmakologie* **246**, 163 (1963).
17. A. Di Corcia and R. Samperi, *Anal. Chem*. **62**, 1490 (1990).
18. W. K. Gavlick, *J. Chromatogr. A* **623**, 375 (1992).
19. M. C. Hennion, P. Subra, V. Coquart, and R. Rosset, *Fresenius. J. Anal. Chem.* **339**, 488 (1991).
20. W. J. Ehlhardt and J. J. Howbert, *Drug Metab. Dispos.* **19**, 366 (1993).
21. H. G. Bray, S. P. James, and W. V. Thorpe, *Biochem. J.* **64**, 38 (1956).
22. A. Moreale and R. Van Bladel, *J. Soil Sci.* **27**, 48 (1976).
23. R. Kühn, M. Pattard, K. D. Pernak, and A. Winter, *Water Res.* **23**, 495 (1989).
24. J. Trotter, S. H. Whitlow, and T. Zobel, *J. Chem. Soc. A Inorganic, Phys. Theor.* **19**, 353 (1966).
25. J. H. Palm, *Acta Crystallogr.* **21**, 473 (1966).

26. G. Ploug-Sørenson and E. K. Andersen, *Acta Crystallogr. Sect. C Cryst. Struct. Commun.* **41**, 613 (1985).

27. A. P. Marchetti, *J. Chem. Phys.* **56**, 5101 (1972).

28. A. P. Marchetti, *J. Chem. Phys.* **57**, 5475 (1972).

29. N. Nishi and M. Kinoshita, *Bull. Chem. Soc. Jpn.* **49**, 1221 (1976).

30. R. Ambrosetti, A. Colligiani, P. Grigolini, and F. Salvetti, *J. Chem. Phys*. **60**, 459 (1974).

31. H. C. Meal, *J. Chem. Phys.* **24**, 1011 (1956).

32. J. Huang, J. L. Lin, and W. B. Tzeng, *Chem. Phys. Lett.* **422**, 271 (2006).

33. A. P. Marchetti, *Chem. Phys. Lett.* **23**, 213 (1973).

34. G. N. R. Tripathi and J. E. Katon, *J. Chem. Phys*. **70**, 1383 (1979).

35. J. L. D. Sky and E. I. Von Nagy-Felsobuki, *J. Mol. Struct.* **475**, 241 (1999).

36. V. B. Singh, R. N. Singh, and I. S. Singh, *Spectrochim. Acta* **22**, 927 (1966).

37. K. Othmen, P. Boule, B. Szczepanik, K. Rotkiewicz, and G. Grabner, *J. Phys. Chem. A* **104**, 9525 (2000).

38. P. F. Cox, R. L. Every, and O. L. Riggs, *Corrosion* **20**, 299t (1964).

39. M. A. V. Ribeiro Da Silva, J. R. B. Gomes, and A. I. M. C. L. Ferreira, *J. Phys. Chem. B* **109**, 13356 (2005).

40. M. Straka, K. Růžička, and V. Růžička, *J. Chem. Eng. Data* **52**, 1375 (2007).

41. V. Piacente, P. Scardala, D. Ferro, and R. Gigli, *J. Chem. Eng. Data* **30**, 372 (1985).

42. J. Padmanabhan, R. Parthasarathi, V. Subramanian, and P. K. Chattaraj, *J. Phys. Chem. A* **110**, 9900 (2006).

43. R. N. Compton and N. I. Hammer, in *Adv. Gas-Phase Ion Chemistry*, edited by N. G. Adams and L. M. Babcock (Elsevier Science, Amsterdam, 2001), pp. 257 -305.
44. E. F. Belogolova, G. Liu, E. P. Doronina, S. M. Ciborowski, V. F. Sidorkin, and K. H. Bowen, *J. Phys. Chem. Lett*. **9**, 1284 (2018).
45. J. H. Hendricks, H. L. De Clercq, C. B. Freidhoff, S. T. Arnold, J. G. Eaton, C. Fancher, S. A. Lyapustina, J. T. Snodgrass, and K. H. Bowen, *J. Chem. Phys.* **116**, 7926 (2002).

III.A.3. The Ground State, Quadrupole-Bound Anion of Succinonitrile Revisited

Gaoxiang Liu, Sandra M. Ciborowski, Jacob D. Graham, Allyson M. Buytendyk,
Kit H. Bowen

Reprinted from *J. Chem. Phys.* **151** (10) (2019) 101101, with the permission of AIP Publishing.

III.A.3.a. Abstract

Using a combination of Rydberg electron transfer and negative ion photoelectron spectroscopy, we revisited an earlier study which, based on several separate pieces of evidence, had concluded that *trans*- and *gauche*-succinonitrile can form quadrupole bound anions (QBA) and dipole bound anions (DBA), respectively. In the present work, succinonitrile anions were formed by Rydberg electron transfer and interrogated by negative ion photoelectron spectroscopy. The resulting anion photoelectron spectra exhibited distinctive spectral features for *both* QBA and DBA species in the *same* spectrum, thereby providing direct spectroscopic confirmation of previous indirect conclusions. Just as importantly, this work also introduces the integrated combination of Rydberg electron transfer and anion photoelectron spectroscopy as a powerful, tandem technique for studying diffuse excess electron states.

III.A.3.b. Introduction

Negative ions can be formed not only through attachment of electrons to conventional, valence orbitals but also due to electron capture by long-range, electrostatic forces and/or dispersion effects. Negative ions formed by the latter route possess excess electrons that are very weakly bound and spatially diffuse. The component electrostatic potentials associated with these forces can be expressed through the multipole expansion for a given charge distribution as monopole, dipole, quadrupole, octupole… moments, although this representation is strictly valid only at a distance. Nevertheless, in cases where there is no valence binding of the excess electron, and where all but one of the electrostatic moments are null, it is customary to credit that non-zero moment as the primary interaction responsible for any excess electron binding that is observed. The best studied case among these are dipole-bound anions, i.e., anions whose excess electrons are weakly bound due to the dipolar fields of the anions' neutral counterparts. The formation of dipole bound anions have been postulated as the first step in electron attachment to polar molecules, and for that reason they are sometimes referred to as "doorway" states.[1-16]

The next higher term in the multipole expansion is the quadrupole moment. Unlike dipole-bound anions, evidence for quadrupole-bound anions, where electrons are bound by long-range charge-quadrupole attraction, has been scarce. Quadrupole-bound anions were first predicted theoretically in 1979.[17] Early experimental searches for quadrupole-bound anions examined the negative ions of carbon disulfide,[18,19] formamide,[20] para-dinitrobenzene,[21] and small clusters of magnesium oxide.[12,22] However, due either to a lack of theoretical confirmation and/or to strong indications that they were instead valence-bound, the excess electrons in none of these exhibited the weakly bound and/or spatially diffuse properties expected of quadrupole bound anions.

The first convincing evidence for the existence of quadrupole bound anions was presented by Schermann, Desfrancois, Bowen, and Compton in 2004.[23] Their conclusion, that the *trans*-succinonitrile anion is a quadrupole bound anion, was based on two different types of experimental measurements and on their theoretical calculations. **1.** Rydberg electron transfer (RET) experiments were performed by crossing a beam of succinonitrile molecules with a beam of laser-excited Rydberg atoms and monitoring the formation of parent succinonitrile anions mass spectrometrically as a function of Rydberg principle quantum number, n. The succinonitrile beam contained both *trans*- and *gauche*-conformers, with the former possessing a large quadrupole moment but a null dipole moment and with the latter exhibiting a large dipole moment.[24] These experiments were conducted at both the University of Paris Nord using xenon Rydberg atoms and at the University of Tennessee using rubidium Rydberg atoms. Both RET experiments gave fully consistent results, with each exhibiting a sharply-peaked, anion intensity versus n feature at and around n = 12. Application of the semi-empirical formula, $EA = 23\ eV/n^{2.8}$, implied an electron affinity (EA) of 22 meV for the molecules that formed anions at n = 12.[25] This was interpreted as the EA value of neutral *trans*-succinonitrile and as evidence for it having formed a ground state, quadrupole bound anion. Surprisingly, however, neither of the Rydberg electron transfer experiments showed discernible evidence for a sharply-peaked feature, corresponding to the expected dipole bound anion of *gauche*-succinonitrile, even though such peaks are characteristic of dipole bound anions formed in RET experiments.

2. The other type of experimental measurement performed on succinonitrile anions utilized negative ion photoelectron spectroscopy and was conducted at Johns Hopkins University. There, a beam of succinonitrile anions was formed by a nozzle-ion source, mass-selected, and photodetached, after which its photoelectrons were energy analyzed.[26] The resulting anion photoelectron spectrum exhibited a sharp peak at an electron binding energy (EBE) of 108 meV and with two weaker molecular vibrational features at higher electron binding energies. Its spectral profile was typical of dipole bound anion photoelectron spectra.[3] Because of this distinctive signature and the EBE value of its principle peak, it was interpreted as being due to the dipole bound, *gauche*-succinonitrile anion with an EA value of 108 meV for neutral *gauche*-succinonitrile. Interestingly, however, there was no evidence for a photoelectron peak with an EBE value in the vicinity of 22 meV and thus no indication of a quadrupole bound anion. On the other hand, such weakly-bound excess electrons could have easily been field-detached by the gauntlet of electric fields from multiple lenses along the ion path in that particular apparatus, if in fact quadrupole bound anions had been formed by the nozzle-ion source.

Thus, while the Rydberg electron transfer experiment gave evidence for a quadrupole bound, *trans*-succinonitrile anion but not for a dipole bound, *gauche*-succinonitrile anion, the anion photoelectron spectroscopic experiment gave evidence for a dipole bound, *gauche*-succinonitrile anion but not for a quadrupole bound, *trans*-succinonitrile anion. Nevertheless, DFT/B3LYP calculations conducted as part of that work found the anions of *trans*- and *gauche*-succinonitrile to be quadrupole bound and dipole bound, respectively. Thus, the conclusion that the *trans*-succinonitrile anion is a ground state, quadrupole bound anion was based on several separate pieces of evidence.

Subsequent high-level calculations on succinonitrile anions by Sommerfeld concluded that while the dipole moment of *gauche*-succinonitrile is sufficient to explain excess electron binding in its anion, excess electron binding in the *trans*-succinonitrile anion is more complex and is due both to the quadrupole moment of *trans*-succinionitrile and to electron correlation effects, with the latter playing the larger role.[24] Dispersion is an electron correlation effect. In diffuse excess electron states, such as dipole bound and quadrupole bound anions, London dispersion forces, acting between the diffuse excess electron cloud and its home (neutral) molecule, can have attractive interactions that are comparable to or even exceed those of electron-multipole interactions.[10,27] Dispersion appears to have made an important contribution to excess electron binding in the *trans*-succinonitrile anion and possibly in the *gauche*-succinonitrile anion as well. In anion photoelectron spectra, sharp peaks at low electron binding energies are characteristic of all types of *diffuse-electron anion states*, e.g., correlation-bound,[9,28,29] polarizability-bound, dipole-bound,[2-4] quadrupole-bound,[23] and double Rydberg anions.[30] This is because the weak interaction between the excess electron and its home molecule leads not only to low excess electron binding energies for the resulting anion, but it also leaves the anion and its corresponding neutral in nearly identical structures, leading to high Franck-Condon overlap and narrow peaks.

In the years since 2004, interest in quadrupole bound anions has continued to grow with the development of several new computational models,[31-34] the theoretical prediction of specific quadrupole-bound anions,[24,35] and the observation of excited, quadrupole-bound states in a valence-bound, ground state anion.[36]

In the present work, we revisit succinonitrile anions, using the unique combination of Rydberg electron transfer to efficiently prepare their ground state, diffuse-electron anion states and negative ion photoelectron spectroscopy to directly and spectroscopically measure their electron binding energies. This approach allows us to comprehensively tackle unfinished business from the earlier work and to present a more complete story.

III.A.3.c. Experimental Method

Figure III.A.11 presents a schematic of our combined Rydberg electron transfer - anion photoelectron (photodetachment) spectroscopic apparatus. The RET region, where target molecules and optically-prepared Rydberg atoms collide to form anions, is on the left, while the photoelectron region, where the resultant mass-selected anions are photodetached and their electrons energy-analyzed, is on the right. A beam of neutral succinonitrile molecules was generated by expanding succinonitrile vapor in helium (10 psig) through the nozzle of a pulsed valve into vacuum. This beam was then crossed with an effusive beam of potassium atoms, which had been excited to *nd* Rydberg states in two steps using two dye lasers. One dye laser pumped the potassium atoms to the $^2P_{3/2}$ state using 766.7 nm photons, while the other was tuned to reach specific Rydberg levels. Upon collisions between Rydberg excited potassium atoms and succinonitrile molecules inside

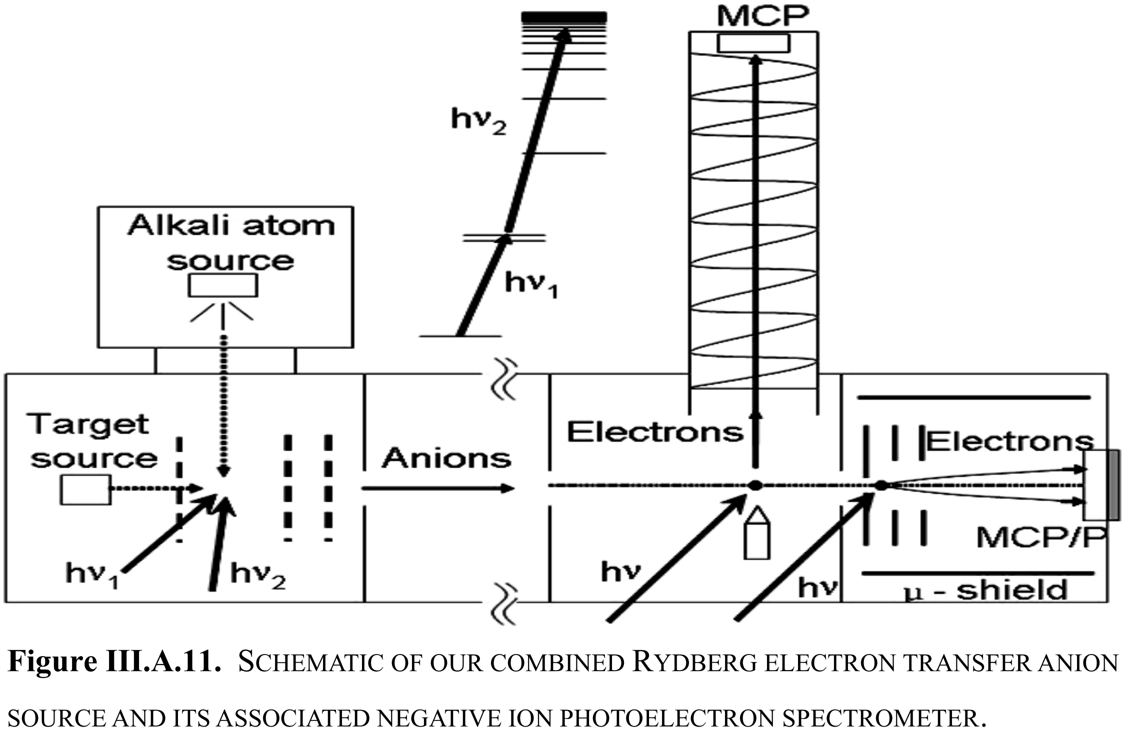

Figure III.A.11. SCHEMATIC OF OUR COMBINED RYDBERG ELECTRON TRANSFER ANION SOURCE AND ITS ASSOCIATED NEGATIVE ION PHOTOELECTRON SPECTROMETER.

the ion extraction region of the apparatus, charge transfer occurred, producing potassium cations and parent succinonitrile anions, which momentarily formed ion pairs before dissociating into their component ions. The nascent anions were then pulsed into the negative ion photoelectron spectrometer portion of the apparatus, where they were mass-selected using time-of-flight mass spectrometry before their electrons were photodetached using 1064 nm linearly-polarized light from a Nd:YAG laser. The kinetic energies of these photoelectrons were then measured using a velocity-map imaging (VMI) spectrometer. (An available "magnetic bottle" type electron energy analyzer on this apparatus was not used in this work.) VMI analysis was achieved by accelerating the electrons along the axis of the ion beam toward a position-sensitive detector coupled to a CCD camera. The resulting two-dimensional image was then reconstructed via the BASEX method,[37] yielding the corresponding anion photoelectron spectrum. Since the photoelectron technique is governed by the energy-conserving relationship, hv = EKE + EBE, where hv, EKE, and EBE are the photon energy, the electron kinetic energy, and the electron binding (transition) energy, respectively, knowing hv and measuring EKE values, provides corresponding EBE values. Photoelectron spectra in this work were calibrated against the well-known spectrum of NO^-.[26]

III.A.3.d. Results and Discussions

The study in 2004 was interpreted in terms of the *trans*-succinonitrile anion being a quadrupole bound anion, whose neutral counterpart had an electron affinity of 22 meV, and in terms of the *gauche*-succinonitrile anion being a dipole-bound anion state, whose corresponding neutral had an electron affinity of 108 meV. That work provides a reference point for the present combination RET - photoelectron study of succinonitrile anions.

Figure III.A.12 presents the photoelectron spectra of succinonitrile anions made by charge transfer with Rydberg potassium atoms, K**(*11d*), presented alongside its corresponding velocity mapping image. In the anion photoelectron spectrum at the left, two sharp peaks at low electron binding energies are in evidence. For the reasons described above, both of these peaks are symptomatic of photoelectron spectroscopic signatures of diffuse excess electron states. The lower EBE peak is centered at 18 meV with a full width at half-maximum (fwhm) ~40 meV, while the higher EBE peak is centered at 135 meV

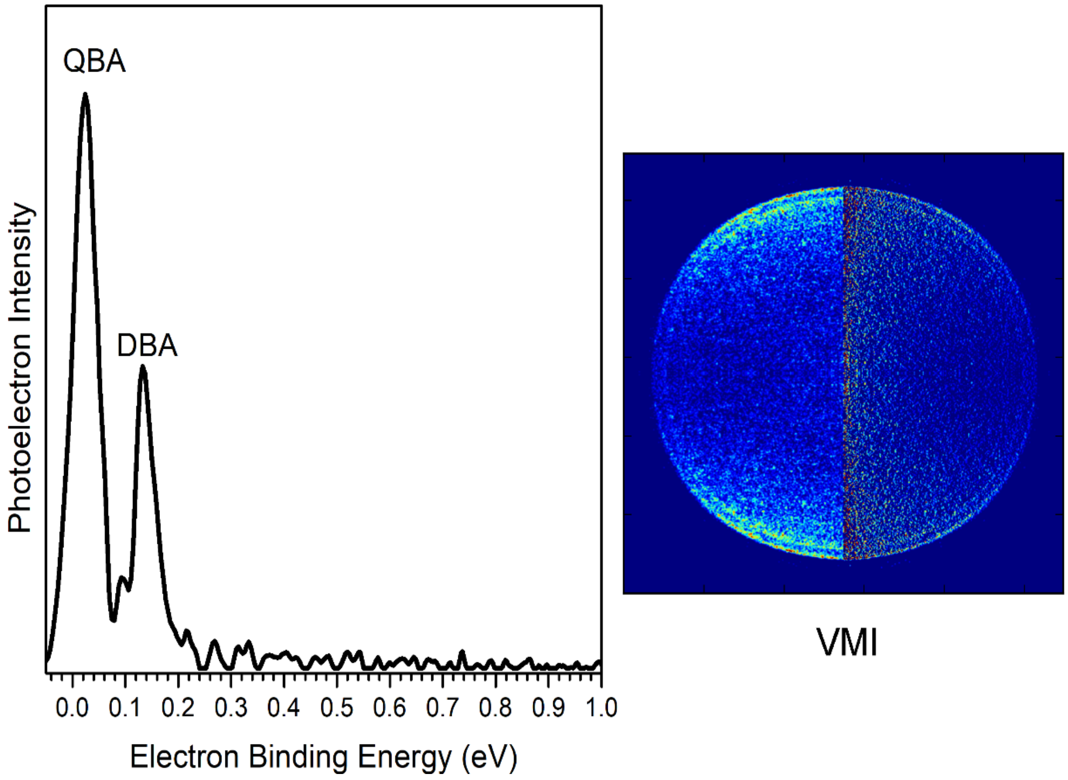

Figure III.A.12. At left: Anion photoelectron spectrum showing both quadrupole- and dipole-bound succinonitrile anions made by collisions of succinonitrile molecules with Rydberg potassium atoms, K**(*11d*). At right: The corresponding velocity mapping image (VMI), taken with linearly-polarized light that was aligned perpendicular to the direction of the anion beam. The left side shows its raw image, while the right side shows its processed image. Note the two rings at the outer edge of the image.

with a fwhm of ~33 meV, where the peak widths are a consequence of the resolution of the instrument. These peak centers are vertical detachment energies (VDE), i.e., the transition energy from the anion to its corresponding neutral at the geometry of the anion. Since the structures of diffuse excess electron states (anions) and their corresponding neutrals are essentially identical, their measured VDE values are also the adiabatic electron affinity (EA) values of their corresponding neutrals. Thus, the EA value of 22 meV estimated through RET in the earlier work and the EBE value of 11 meV calculated at about the same time[24] both compare reasonably well with the EA = VDE value of 18 meV determined in the present photoelectron work. Furthermore, the EA = VDE value of 108 meV determined by photoelectron spectroscopy in the earlier work compares well with the EA = VDE value of 135 meV in the present combined RET-photoelectron work. It is clear that the VDE and EA values determined in the present work are in satisfactory accord with corresponding EA and VDE values measured in the earlier work, albeit under different experimental circumstances. As a result, we interpret the lower EBE peak in Figure III.A.12 as arising from the ground state, quadrupole bound anion (QBA) of *trans*-succinonitrile and the slightly higher EBE peak there as arising from the ground state, dipole-bound anion (DBA) of *gauche*-succinonitrile. Figure III.A.12 thus presents strong evidence for *both* QBA and DBA species in the *same* spectrum, i.e., measured by the same technique. Our sightings of both QBA and DBA species over our RET n-region of n = 11d - 15d also raises the question of whether the sharp feature centered at n = 12 over the relatively narrow RET n-region of n = 10 - 15 in the earlier (2004) experiments might have also included both QBA and DBA species.

In addition to the foregoing, affirmation that the two peaks in Figure III.A.12 originate from different types of succinonitrile anions is also supported by the fact that we see slight, yet definitive variations in their intensity ratios as a function of nearby n principal quantum numbers. This is because electron attachment to diffuse electron anion states in RET is a resonant process, and maximal electron transfer efficiency can occur at different Rydberg n numbers, when electrons are attached via different multipole interactions.

The photoelectron VMI image in Figure III.A.12 reveals significant anisotropy in both the dipole- and quadrupole-bound states of the succinonitrile anion. The anisotropy parameters, β, for the photodetached quadrupole- and dipole- bound electrons were each calculated to be between 1.8-2.0, which is close to the theoretical upper limit. A large β value is consistent with an outgoing *p* wave, which means that photodetachment occurred from an *s*-orbital with nearly zero angular momentum.[38] Since both dipole- and quadrupole-bound succinonitrile anions are spatially diffuse excess electron states, their excess electrons can be viewed as possessing *s*-orbital character, consistent with the observed anisotropy.

Acknowledgements

This material is based on work supported by the (U.S.) National Science Foundation (NSF) under grant number, CHE-1664182 (K.H.B.). This work is dedicated to R. N. Compton, C. Desfrancois, and the late J.-P. Schermann, our former collaborators, who are among the seminal contributors to this field.

References

1. R. A. Bachorz, W. Klopper, M. Gutowski, X. Li, and K. H. Bowen, *J. Chem. Phys.* **129**, 054309 (2008).
2. A.M. Buytendyk, A.M. Buonaugurio, S.J. Xu, J.M. Nilles, K.H. Bowen, N. Kirnosov, and L. Adamowicz, *J. Chem. Phys.* **145**, 024301 (2016).
3. E. F. Belogolova, G. Liu, E. P. Doronina, S. Ciborowski, V. F. Sidorkin, and K. H. Bowen, *J. Phys. Chem. Lett.* **9**, 1284 (2018).
4. S. M. Ciborowski, G. Liu, J. D. Graham, A. M. Buytendyk, and K. H. Bowen, *Eur. Phys. J. D* **72**, 139 (2018).
5. J. V. Coe, G. H. Lee, J. G. Eaton, S. T. Arnold, H. W. Sarkas, C. Ludewigt, H. Haberland, D. R. Worsnop, and K. H. Bowen, *J. Chem. Phys*. **92**, 3980 (1990).
6. C. Desfrancois, B. Baillon, J. P. Schermann, S. T. Arnold, J. H. Hendricks, and K. H. Bowen, *Phys. Rev. Lett*. **72**, 48 (1994).
7. R. N. Compton, H. S. Carman, Jr., C. Desfrancois, H. Abdoul-Carime, J. P. Schermann, J. H. Hendricks, S. A. Lyapustina, and K. H. Bowen, *J. Chem. Phys*. **105**, 3472 (1996).
8. N. I. Hammer, R. J. Hinde, R. N. Compton, K. Diri, K. D. Jordan, D. Radisic, S. T. Stokes, and K. H. Bowen, *J. Chem. Phys.* **120**, 685 (2004).
9. S. M. Ciborowski, R. H. Harris, G. Liu, C. J. Martinez-Martinez, P. Skurski, and K. H. Bowen, *J. Chem. Phys.* **150**, 161103 (2019).
10. G. Gutowski, P. Skurski, A. I. Boldyrev, J. Simons, and K. D. Jordan, *Phys. Rev. A: At., Mol., Opt. Phys.* **54** 1906 (1996).
11. J. Simons and K. D. Jordan, *Chem. Rev.* **87**, 535 (1987).
12. J. Simons, *J. Phys. Chem. A* **112**, 6401 (2008).

13. D. L. Huang, C. G. Ning, H. T. Liu, and L. S. Wang, *J. Phys. Chem. Lett*. **6**, 2153 (2015).
14. V. K. Voora and K. D. Jordan, *J. Phys. Chem. A* **118**, 7201 (2014).
15. T. Sommerfeld, *J. Phys. Chem. A* **108**, 9150 (2004).
16. T. Sommerfeld, *J. Chem. Phys*. **126**, 124301 (2007).
17. K. D. Jordan and J. F. Liebman, *Chem. Phys. Lett*. **62**, 143 (1979).
18. C. Desfrancois, N. Khelifa, J. P. Schermann, T. Kraft, M. W. Ruf, and H. Hotop, *Z. Phys. D* **27**, 365 (1993).
19. R. N. Compton, F. B. Dunning, and P. Nordlander, *Chem. Phys. Lett*. **253**, 8 (1996).
20. C. Desfrancois, V. Periquet, S. Carles, J. P. Schermann, and L. Adamowicz, *Chem. Phys.* **239**, 475 (1998).
21. C. Desfrancois, V. Periquet, S. A. Lyapustina, T. P. Lippa, D. W. Robinson, K. H. Bowen, H. Nonaka, and R. N. Compton, *J. Chem. Phys*. **111**, 4569 (1999).
22. M. Gutowski, P. Skurski, X. Li, and L. S. Wang, *Phys. Rev. Lett*. **85**, 3145 (2000).
23. C. Desfrancois, Y. Bouteiller, J.P. Schermann, D. Radisic, S. T. Stokes, K. H. Bowen, N. I. Hammer, and R. N. Compton, *Phys. Rev. Lett.* **92**, 083003 (2004).
24. T. Sommerfeld, *J. Chem. Phys.* **121**, 4097 (2004).
25. C. Desfrancois, *Phys. Rev. A.* **51**, 3667 (1995).
26. J. Hendricks, H. de Clercq, C. B. Freidhoff, S. T. Arnold, J. G. Eaton, C. Fancher, S. A. Lyapustina, J. T. Snodgrass, and K. H. Bowen, *J. Chem. Phys*. **116**, 7926 (2002).
27. R. A. Bachorz, W. Klopper, M. Gutowski, X. Li, K. H. Bowen, *J. Chem. Phys.* **129** 054309 (2008).
28. J. N. Bull and J. R. R. Verlet, *Sci. Adv.* **3**, e1603106 (2017).

29. J. P. Rogers, C. S. Anstöter, and J. R. R. Verlet, *Nat. Chem*. **10**, 341 (2018).

30. S. J. Xu, J. M. Nilles, J. H. Hendricks, S. A. Lyapustina, and K. H. Bowen, *J. Chem. Phys.* **117**, 5742 (2002).

31. W. R. Garrett, *J. Chem. Phys*. **136**, 054116 (2012).

32. T. Sommerfeld, *J. Chem. Theory Comput*. **9**, 4866 (2013).

33. K. Fossez, X. Mao, W. Nazarewicz, N. Michel, W. R. Garrett, and M. Płoszajczak, *Phys. Rev. A* **94**, 032511 (2016).

34. X. Mao, K. Fossez, and W. Nazarewicz, *Phys. Rev. A* **98**, 062515 (2018).

35. T. Sommerfeld, K. M. Dreux, and R. Joshi, *J. Phys. Chem. A* **118**, 7320 (2014).

36. G. Z. Zhu, Y. Liu, and L. S. Wang, *Phys. Rev. Lett*. **119**, 023002 (2017).

37. V. Dribinski, A. Ossadtchi, V. A. Mandelshtam, and H. Reisler, *Rev. Sci. Instrum.* **73**, 2634 (2002).

38. C. L. Adams, H. Schneider, K. M. Ervin, and J. M. Weber, *J. Chem. Phys.* **130**, 074307 (2009).

III.A.4. Observation of the Dipole- and Quadrupole-Bound Anions of 1,4-Dicyanocyclohexane

Gaoxiang Liu, Sandra M. Ciborowski, Cody Ross Pitts, Jacob D. Graham, Allyson M. Buytendyk, Thomas Lectka, and Kit H. Bowen

Phys. Chem. Chem. Phys., 2019, **21**, 18310, **DOI:** 10.1039/C9CP04010B - Reproduced by permission of the PCCP Owner Societies.

III.A.4.a. Abstract

Quadrupole-bound anions are negative ions in which their excess electrons are loosely bound by long-range electron-quadrupole attractions. Experimental evidence for quadrupole-bound anions has been scarce; until now, only *trans*-succinonitrile had been experimentally confirmed to form a quadrupole-bound anion. In this study, we present experimental evidence for a new quadrupole-bound anion. Our combined Rydberg electron transfer/anion photoelectron spectroscopy study demonstrates that the *ee* conformer of 1,4-dicyanocyclohexane (DCCH) supports a quadrupole-bound anion state, and that the *cis*-DCCH conformer forms a dipole-bound anion state. The electron binding energies of the quadrupole- and dipole-bound anions are measured as 18 and 115 meV, respectively, both of which are in excellent agreement with theoretical calculations by Sommerfeld.

III.A.4.b. Introduction

Negative ions can be formed due to electron capture by long-range, electrostatic forces, in which the excess electrons reside in diffuse non-valence orbitals. The component potentials associated with these electrostatic forces can be expressed through the multipole expansion for a given charge distribution, e.g., dipole, quadrupole, and octupole moments. Whereas this representation is strictly valid only at a distance, in cases where there is no valence electron binding, and where all but one of the electrostatic moments are null, it is customary to attribute that non-zero moment as the primary attractive interaction responsible for the binding of the excess electron. The formation of such weakly-bound states is thought to be the initial step in certain electron attachment processes, thus these are also referred as "doorway" states.[1-11] The best studied category of weakly-bound anions are dipole-bound anions, i.e., anions whose excess electrons are weakly tethered by the dipolar fields of the anions' neutral counterparts.[12-24]

The next higher term in the multipole expansion is the quadrupole moment. Unlike dipole-bound anions, the evidence for quadrupole-bound anions, where their excess electrons are bound by the long-range charge-quadrupole attraction, has been scarce. Quadrupole-bound anions were first predicted theoretically in 1979.[25] Early experimental studies on quadrupole-bound anions were conflicting: the anions of carbon disulfide, formamide, and para-dinitrobenzene were investigated by Rydberg electron transfer and suggested to be quadrupole-bound anions, but the lack of theoretical support rendered them less convincing;[26-29] the small cluster anions of magnesium oxide were investigated by photoelectron spectroscopy and interpreted as quadrupole-bound anions, but their high electron binding energies and rather localized orbitals made them more characteristic of conventional valence-bound anions.[30] It was not until 2004 that Schermann, Bowen, and Compton presented the first convincing evidence of quadrupole-bound anions by combining results from two different, but complimentary experimental techniques: the dipole-bound anion state of the *gauche*-succinonitrile conformer was revealed by anion photoelectron spectroscopy, and the quadrupole-bound anion state of the *trans*-succinonitrile conformer was revealed by Rydberg electron transfer.[31] While each of these techniques revealed one type of a multipole-bound anion, they were each unable to discern the other type. This led us to revisit this earlier study using the unique combination of Rydberg electron transfer and negative ion photoelectron spectroscopy. In that study, the anion photoelectron spectra of succinonitrile anions, which were formed via Rydberg electron transfer, exhibited distinctive features for both dipole- and quadrupole-bound anions in the same photoelectron spectrum, providing direct spectroscopic confirmation for the presence of both multipole-bound states in the same molecule and in a single experiment.[32]

Additional progress in the study of quadrupole-bound anions has included the development of computational models,[33-36] theoretical prediction of several stable quadrupole-bound anions,[37] and the discovery of excited-state, quadrupole-bound states in a valence-bound anion.[38] Despite these advances, however, the *trans*-succinonitrile anion remained the only experimentally-confirmed example of a ground-state, quadrupole-bound anion. The search for quadrupole-bound anions is intrinsically challenging because (*i*) their weakly-bound nature requires specialized experimental techniques for making and analyzing them; (*ii*) unlike dipole-bound anions, whose electron binding energies are proportionally correlated to the magnitude of the neutrals' dipole moments, there is no clear correlation between the magnitude of the molecular quadrupole moment and the electron binding energy of the quadrupole-bound anion;[37] thus, the prediction of stable quadrupole-bound anions relies heavily on high-level *ab initio* calculations; (*iii*) if the molecule can sustain both quadrupole-bound and valence-bound states, the nascent quadrupole-bound state may quickly decay into the more stable valence-bound state, hiding the incipient quadrupole-bound anion state from view.[38]

Recently, several neutral molecules have been theoretically predicted by Sommerfeld to form quadrupole-bound anions.[37] Among these, the 1,4-dicyanocyclohexane (DCCH) molecule was seen as a promising candidate for the experimental interrogation for two reasons. While its conformers were predicted to support both dipole- and quadrupole-bound anionic states, it was not predicted to form a valence state. In addition, its laboratory synthesis was deemed to be more tractable than other candidates. In the present work, the parent anions of DCCH were formed by Rydberg electron transfer and interrogated by velocity mapping imaging, anion photoelectron spectroscopy. The resulting anion photoelectron spectra exhibited distinctive spectral features for both dipole- and quadrupole-bound anions, whose electron binding energies were measured as 115 meV and 18 meV, respectively. These values are in excellent agreement with theoretical calculations. Thermodynamic analysis rationalized the relative quantity of the two types of anions.

III.A.4.c. Experimental Methods

III.A.4.c.i. Synthesis of 1,4-Dicyanocyclohexane

This compound can be prepared according to a known literature procedure.[39,40] It was obtained as a mixture of *cis*- and *trans*- conformations, which appeared as an off-white solid; m.p. 54-55 °C. Characterization data: 1H NMR (400 MHz, $CDCl_3$) δ 2.77-2.72 (2H, m), 2.10-1.97 (4H, m), 1.89-1.75 (4H, m); 13C NMR (400 MHz, $CDCl_3$) δ 120.9, 120.8, 26.3, 26.2, 26.1, 26.0; ν_{max}/cm^{-1} 2238 (CN, strong).

III.A.4.c.ii. Anion Photoelectron Spectroscopy

Our Rydberg electron transfer/anion photoelectron spectroscopy apparatus has been described previously.[23.24.32,41] Anion photoelectron spectroscopy is conducted by crossing a mass-selected beam of negative ions with a fixed-frequency photon beam and energy-analyzing the resultant photodetached electrons. This technique is governed by the energy-conserving relationship, $h\nu = \mathrm{EKE} + \mathrm{EBE}$, where $h\nu$, EKE, and EBE are the photon energy, the electron kinetic energy, and the electron binding (transition) energy, respectively. Electron kinetic energies were measured using a velocity-map imaging (VMI) spectrometer. Mass-selected anions were crossed with 1064 nm, linearly polarized photons in an electric field. The resultant photodetached electrons were accelerated along the axis of the ion beam toward a position-sensitive detector coupled to a CCD camera. The two-dimensional image formed from the sum of the electrons was reconstructed into a portion of the three-dimensional distribution via the BASEX method.[42] Photoelectron spectra are calibrated against the well-known spectrum of NO^-.[43]

DCCH anions were generated by our Rydberg electron transfer (RET) source. Neutral DCCH molecules were vaporized in a pulsed valve, which was heated to 140 °C, and then supersonically expanded with 10 psi of helium gas. DCCH anions, $DCCH^-$, were formed when neutral DCCH molecules collided with a thermally-expanded beam of potassium atoms, which had been excited to specific Rydberg states in two steps using two dye lasers. One dye laser pumped the potassium atoms to the $^2P_{3/2}$ state with 766.7 nm light, while the other was tuned to reach specific *nd* Rydberg levels, where *n* is the principal quantum number. In this study, Rydberg levels from $n = 13d$ to $18d$ were selected. Upon electron transfer and subsequent ion-pair separation, the resulting anions, $DCCH^-$, were extracted into a time-of-flight mass spectrometer. There, they were mass-selected before having their excess electrons photodetached and energy-analyzed by velocity-map imaging spectroscopy.

III.A.4.c.iii. Calculations

The electron affinities of DCCH had been accurately calculated by Sommerfeld in an earlier contribution.[37] The calculations conducted during the present work serve to explain the relative amounts of dipole- versus quadrupole-bound DCCH anions that were formed. The second-order Møller-Plesset perturbation theory calculations were performed with the ORCA computational chemistry software package.[44] All calculations were carried out with the resolution of identify (RI) and the RIJCOSX approximation.[45] The cc-pVTZ basis set[46] was used throughout our calculations in conjugation with the auxiliary basis sets def2/J[47] and cc-pVTZ/C[48]. Frequency calculations were performed to verify the optimized structures and transition states.

III.A.4.d. Results and Discussions

Figure III.A.13.a shows the structures of the three DCCH conformers. In *cis*-DCCH, one CN group is at the equatorial(*e*) site, and the other one is at the axial(*a*) position. The *trans*-DCCH can have two conformers, which are labeled as *aa*-DCCH and *ee*-DCCH, depending on the positions of the CN groups. Since the sample was synthesized as a mixture of *trans*- and *cis*-conformations, all three conformers were present. Also provided in Figure III.A.13.a are calculated dipole and quadrupole moments of these conformers as well as their vertical electron affinity (VEA) values.[37] Calculations show that the *aa*-DCCH molecule is unable to form a weakly-bound anion; the *ee*-DCCH, which has a vanishing dipole moment but a significant quadrupole moment, can form a quadrupole-bound anion with a VEA of 19 meV; the *cis*-DCCH, which has a large dipole moment, can form a dipole-bound anion with a VEA of 108 meV.

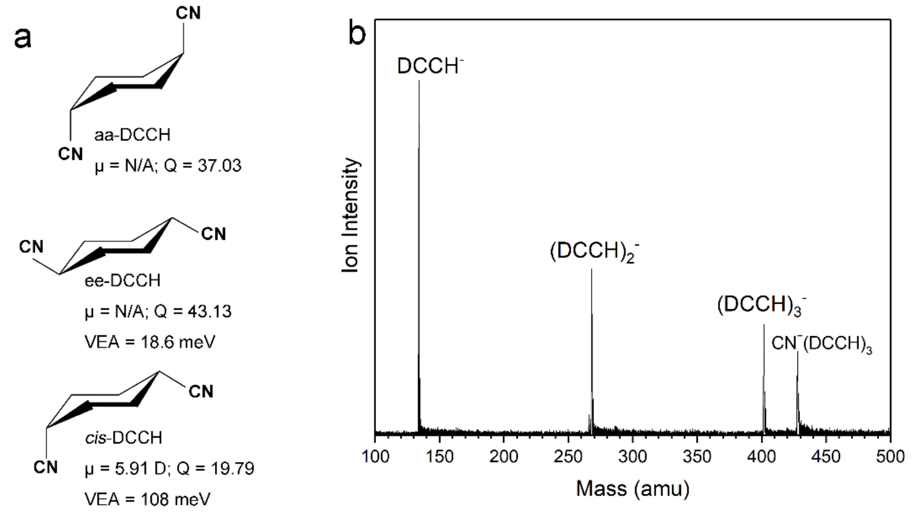

Figure III.A.13. (a) Structures of the *trans*- and *cis*- isomers of 1,4-dicyanocyclohexane (DCCH), along with their electronic properties. The unit of the quadrupole moment, Q, is the atomic unit ea_0^2. (b) Mass spectrum of molecular and cluster anions of DCCH made by Rydberg electron transfer.

Figure III.A.13.b presents a representative mass spectrum of molecular and cluster anions of DCCH made via Rydberg electron transfer (RET). Cluster anions of the dimer and trimer of DCCH are observed, demonstrating the capability of RET to make not only molecular, but also cluster anions. A mass peak corresponding to CN^- physisorbed (solvated) by three DCCH molecules is also observed. The CN^- anion results from the dissociative electron attachment to DCCH clusters. While it would be interesting to investigate the nature of electron binding to DCCH clusters, i.e., quadrupole-binding, dipole-binding or a synergy of quadrupole- and dipole-binding, the focus of the present study is on identifying the weakly-bound states of the DCCH parent molecular anion, $DCCH^-$.

Figure III.A.14 presents the anion photoelectron spectra of DCCH anions made at different Rydberg *n* levels. Spectra collected at *n* = *13d*, *14d*, and *18d* Rydberg levels are

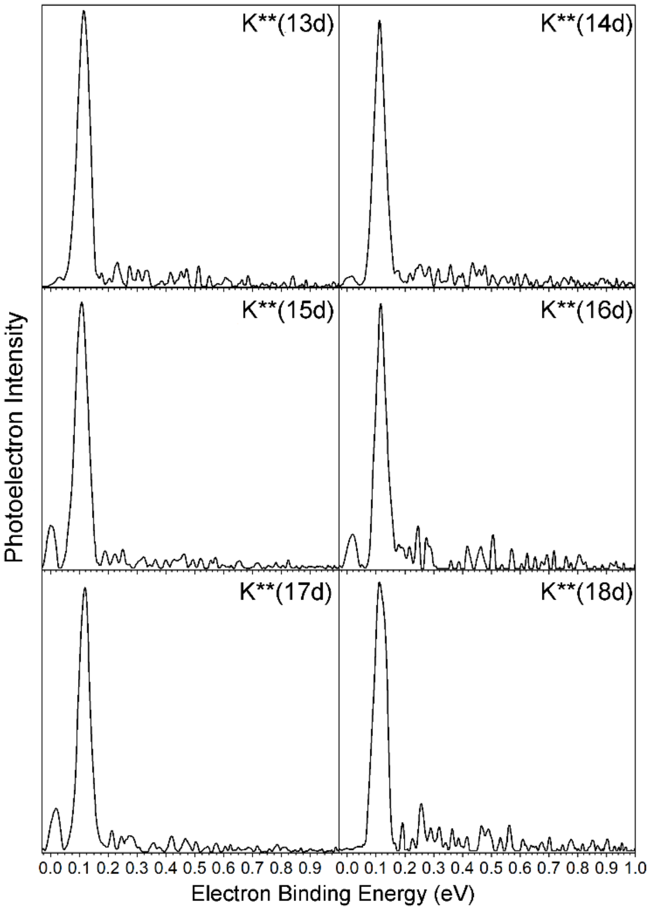

Figure III.A.14. ANION PHOTOELECTRON SPECTRA OF DIPOLE- AND QUADRUPOLE-BOUND DCCH ANIONS, DCCH$^-$, MADE AT DIFFERENT RYDBERG LEVELS (*N* = *13D*-*18D*).

dominated by a single sharp peak at a low electron binding energy (EBE). For spectra obtained at *n* = *15d*, *16d* and *17d*, an additional sharp, yet weaker peak appears on the lower EBE side of the principal peak. These sharp peaks at low EBE in photoelectron spectra are the signature of weakly-bound anions. In RET, the electron attachment to diffuse electron states occurs via resonance charge transfer, and thus maximal electron transfer efficiency occurs at different Rydberg levels, when electrons are attached to different multipole environments. Therefore, the appearance of the lower EBE feature at only *n* = *15d*-*17d* suggests that it is associated with a different multipole field environment than is the higher

EBE feature. The lower EBE peak is centered at 18 meV, with a full width at half-maximum (fwhm) of ~37 meV. The higher EBE peak is centered at 115 meV, with a fwhm of ~35 meV. These peaks are due to the photodetachment transitions between the anions and their corresponding neutral molecules. Therefore, the vertical detachment energy (VDE) values of these two peaks are 18 and 115 meV, respectively. When anion photoelectron spectra are dominated by single sharp peaks, it strongly suggests a close similarity between the structures of the anion and its neutral counterpart. In such cases of structural similarity, the anion's VDE value will be almost identical to that of its corresponding neutral's adiabatic electron affinity (EA) and to its VEA value. By comparing our experimentally-determined VDE values with VEA values from previous calculations,[37] we assigned the feature at 18 meV to be the signature of the quadrupole-bound anion of *ee*-DCCH, and the feature at 115 meV to be the signature of the dipole-bound anion of *cis*-DCCH.

Figure III.A.15 presents a representative photoelectron image of dipole- and quadrupole-bound DCCH anions, which were formed at the *n = 17d* Rydberg level. The inner brighter ring corresponds to the dipole-bound anion state, while the outer weaker intensity ring corresponds to the quadrupole-bound anion state. Both dipole- and quadrupole-bound anion states show significant anisotropy. The anisotropy parameters, β, of the photodetached dipole-bound electrons are calculated to be between 1.8-2.0. For the photodetached quadrupole-bound electrons their β values are calculated to be 1.4-1.6. Since both the dipole- and quadrupole-bound states can be viewed as spatially diffuse *s*-character orbitals, the matter wave of photodetached electrons should have *p* character and a sizeable β value close to 2.[49] The experimental β value associated with the photodetached

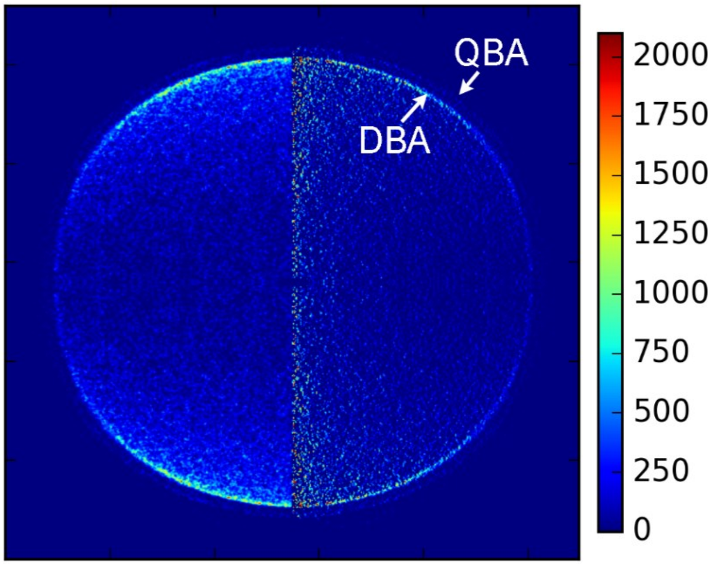

Figure III.A.15. PHOTOELECTRON IMAGE OF DCCH ANIONS COLLECTED AT THE $n = 17d$ RYDBERG LEVEL.

dipole-bound electrons is consistent with this number. While the β value associated with the photodetached quadrupole-bound electrons is less than expected, it may only be because the intensity of photodetached quadrupole-bound electrons was too low to yield an accurate evaluation of β.

The feature from quadrupole-bound anions is only weakly seen in the photoelectron spectrum and the velocity map image of DCCH anions (Figure III.A.15), suggesting that only a small portion of the DCCH anions are quadrupole-bound. We explain this with a quantum mechanical and thermodynamic analysis, the results of which are summarized in Table III.A.2 and Figure III.A.16. Calculations at the RI-MP2/cc-pvtz level of theory reveal that the *aa*-DCCH, which is unable to bind an excess electron, is the most stable conformer. The *cis*-DCCH, which forms dipole-bound anions, is 5.1 kJ/mol higher in energy, while *ee*-DCCH, which forms quadrupole-bound anions, is the least stable conformer, at 9.3 kJ/mol above *aa*-DCCH. As shown in Figure III.A.16, quantum calculations show barriers

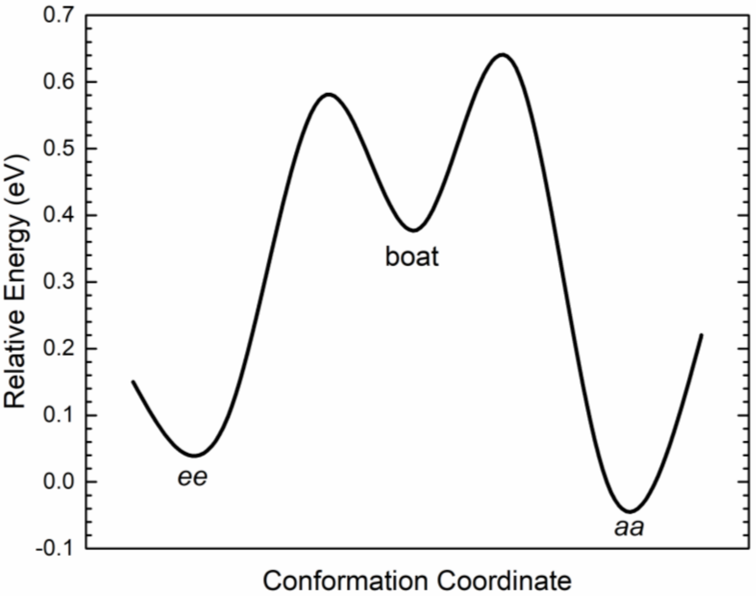

Figure III.A.16. POTENTIAL ENERGY SURFACE FOR NEUTRAL *TRANS*-DCCH ALONG THE CONFORMATION COORDINATE CONNECTING THE *EE*- AND THE *AA*-CONFORMERS.

of 0.56 and 0.63 eV for the interconversion from *ee* to *aa* and from *aa* to *ee*, respectively. Such interconversions constantly occur at room temperature when DCCH is in the solid state. In the molecular beam, however, due to the low temperature achieved by supersonic expansion and the lack of external energy input, these barriers are high enough to quench interconversion. Therefore, we estimate the composition of DCCH conformers in the molecular beam to be similar to that in the DCCH vapor before expansion, i.e., in the heated pulse valve. A thermodynamic analysis shows that at an elevated pulse valve temperature

TABLE III.A.2. RELATIVE ENERGIES, E_{REL}, OF THE THREE DCCH CONFORMERS AND THEIR RELATIVE PERCENTAGES, P, AT ROOM AND EXPERIMENTAL TEMPERATURES.

	E_{rel} (kJ/mol)	$P_{25°C}$ (%)	$P_{140°C}$ (%)	Anion Type
aa-DCCH	0	85.1	77.6	Electron not bound
cis-DCCH	5.1	10.9	17.3	Dipole-bound
ee-DCCH	9.3	2.0	5.1	Quadrupole-bound

(140°C), nearly 80% of the DCCH exists as the *aa* conformer. Therefore, most of the DCCH in the molecular beam will not form anions. The neutral candidate for the dipole-bound anion, *cis*-DCCH, makes up 17.3% of the DCCH in the beam, while the neutral candidate for the quadrupole-bound anion, *ee*-DCCH, makes up only 5.1%. Therefore, only a small portion of DCCH neutral molecules in the beam can form quadrupole-bound anions. This is the main reason for the weak intensity of the quadrupole-bound feature compared to the dipole-bound feature in the photoelectron spectra. While increasing the pulse valve temperature favors the conversion to *ee*-DCCH, temperatures higher than 140°C were found to cause the sample to decompose.

III.A.4.e. Summary

In this contribution, we present experimental evidence for a new, ground state, quadrupole-bound anion obtained in a combined Rydberg electron transfer-anion photoelectron spectroscopic study. The sharp peaks in the photoelectron spectra and the highly anisotropic rings in photoelectron imaging reveal the dipole- and quadrupole-bound anion states of $DCCH^-$. The quadrupole- and dipole-bound electron affinities are measured as 18 and 115 meV, respectively, these being in excellent agreement with previous theoretical calculations.[37] The discovery of this new quadrupole-bound anion extends the knowledge base about quadrupole-bound anions and provides an experimental benchmark for additional theoretical modelling.

Acknowledgements

This material is based upon work supported by the (U.S.) National Science Foundation (NSF) under Grant No. CHE-1664182 (KHB). This material is also based on work supported by the (U.S.) National Science Foundation (NSF) under Grant No. CHE-90079165 (TL).

References

1. I. Dabkowska, J. Rak, M. Gutowski, J. M. Nilles, S. T. Stokes, D. Radisic, and K. H. Bowen, *Phys. Chem. Chem. Phys*. **6**, 4351 (2004).
2. L. Chomicz, M. Zdrowowicz, F. Kasprzykowski, J. Rak, A. Buonaugurio, Y. Wang, and K. H. Bowen, *J. Phys. Chem. Lett*. **4**, 2853 (2013).
3. R. A. Bachorz, W. Klopper, M. Gutowski, X. Li, and K. H. Bowen, *J. Chem. Phys*. **129**, 054309 (2008).
4. S. J. Xu, J. M. Nilles, and K. H. Bowen, *J. Chem. Phys.* **119**, 10696 (2003).
5. T. Sommerfeld, *J. Phys. Chem. A* **108**, 9150 (2004).
6. S. N. Eustis, D. Radisic, K. H. Bowen, R. A. Bachorz, M. Haranczyk, G. Schenter, and M. Gutowski, *Science* **319**, 936 (2008).
7. T. Sommerfeld, *J. Chem. Phys*. **126**, 124301 (2007).
8. J. Kelly, S. Xu, J. Graham, M. Nilles, D. Radisic, A. Buonaugurio, K. H. Bowen, N. Hammer, and G. Tschumper, *J. Phys. Chem. A* **118**, 11901 (2014).
9. J. N. Bull and J. R. R. Verlet, *Sci. Adv*. **3**, e1603106 (2017).
10. J. P. Rogers, C. S. Anstöter, and J. R. R. Verlet, *Nat. Chem.* **10**, 341 (2018).
11. V. K. Voora and K. D. Jordan, *J. Phys. Chem. A.* **118**, 7201 (2014).
12. K. D. Jordan, *Acc. Chem. Res.* **12**, 36 (1979).
13. J. Simons and K. D. Jordan, *Chem. Rev.* **87**, 535 (1987).
14. G. Gutowski, P. Skurski, A. I. Boldyrev, J. Simons, and K. D. Jordan, *Phys. Rev. A: At., Mol., Opt. Phys.* **54**,1906 (1996).

15. J. Simons, *J. Phys. Chem. A*. **112**, 6401 (2008).
16. J. V. Coe, G. H. Lee, J. G. Eaton, S. T. Arnold, H. W. Sarkas, C. Ludewigt, H. Haberland, D. R. Worsnop, and K. H. Bowen, *J. Chem. Phys.* **92**, 3980 (1990).
17. C. Desfrancois, B. Baillon, J. P. Schermann, S. T. Arnold, J. H. Hendricks, and K. H. Bowen, *Phys. Rev. Lett.* **72**, 48 (1994).
18. J. H. Hendricks, S.A. Lyapustina, H. L. de Clercq, J. T. Snodgrass, and K. H. Bowen, *J. Chem. Phys.* **104**, 7788 (1996).
19. R. N. Compton, H. S. Carman, Jr., C. Desfrancois, H. Abdoul-Carime, J. P. Schermann, J. H. Hendricks, S. A. Lyapustina, and K. H. Bowen, *J. Chem. Phys*. **105**, 3472 (1996).
20. N. I. Hammer, R. J. Hinde, R. N. Compton, K. Diri, K. D. Jordan, D. Radisic, S. T. Stokes and K. H. Bowen, *J. Chem. Phys.* **120**, 685 (2004).
21. D. L. Huang, C. G. Ning, H. T. Liu, and L. S. Wang. *Phys. Chem. Lett.* **6**, 2153 (2015).
22. A. M. Buytendyk, A. M. Buonaugurio, S.-J. Xu, J. M. Nilles, K. H. Bowen, N. Kirnosov, and L. Adamowicz, *J. Chem. Phys.* **145**, 024301 (2016).
23. E. F. Belogolova, G. Liu, E. P. Doronina, S. Ciborowski, V. F. Sidorkin, and K. H. Bowen, *J. Phys. Chem. Lett.* **9**, 1284 (2018).
24. S. M. Ciborowski, G. Liu, J. D. Graham, A. M. Buytendyk, and K. H. Bowen, *Eur. Phys. J. D* **72**, 139 (2018).
25. K.D. Jordan and J.F. Liebman, *Chem. Phys. Lett.* **62**, 143 (1979).
26. C. Desfrancois, N. Khelifa, J.P. Schermann, T. Kraft, M. W. Ruf, and H. Hotop, *Z. Phys. D* **27**, 365 (1993).
27. R. N. Compton, F. B. Dunning, and P. Nordlander, *Chem. Phys. Lett.* **253**, 8 (1996).

28. C. Desfrancois, V. Periquet, S. Carles, J. P. Schermann, and L. Adamowicz, *Chem. Phys.* **239**, 475 (1998).
29. C. Desfrancois, V. Periquet, S. A. Lyapustina, T. P. Lippa, D. W. Robinson, K. H. Bowen, H. Nonaka, and R. N. Compton, *J. Chem. Phys*. **111**, 4569 (1999).
30. M. Gutowski, P. Skurski, X. Li, and L. S. Wang, *Phys. Rev. Lett.* **85**, 3145 (2000).
31. C. Desfrancois, Y. Bouteiller, J. P. Schermann, D. Radisic, S. T. Stokes, K. H. Bowen, N. I. Hammer, and R. N. Compton, *Phys. Rev. Lett.* **92**, 083003 (2004).
32. G. Liu, S. M. Ciborowski, J. D. Graham, A. M. Buytendyk, and K. H. Bowen, *J. Chem. Phys.*, accepted.
33. W.R. Garrett, *J. Chem. Phys.* **136**, 054116 (2012).
34. T. Sommerfeld, *J. Chem. Theory Comput.* **9,** 4866 (2013).
35. K. Fossez, X. Mao, W. Nazarewicz, N. Michel, W. R. Garrett, and M. Płoszajczak, *Phys. Rev. A* **94**, 032511 (2016).
36. X. Mao, K. Fossez, and W. Nazarewicz, *Phys. Rev. A* **98**, 062515 (2018).
37. T. Sommerfeld, K. M. Dreux, and R. Joshi, *J. Phys. Chem. A*. **118**, 7320 (2014).
38. G. Z. Zhu, Y. Liu, and L. S. Wang, *Phys. Rev. Lett.* **119**, 023002 (2017).
39. R. Malachowski, J. J. Wasowska, and S. Jóźkiewicz, *Chem. Ber.* **71**, 759 (1938).
40. C. Bengtsson, S. Blaho, D. B. Saitton, K. Brickmann, J. Broddefalk, Ö. Davidsson, T. Drmota, R. Folmer, K. Hallberg, S. Hallén, R. Hovland, E. Isin, P. Johannesson, B. Kull, L. O. Larsson, L. Löfgren, K. E. Nilsson, T. Noeske, N. Oakes, A. T. Plowright, V. Schnecke, P. Ståhlberg, P. Sörme, H. Wan, E. Wellner and L. Öster, *Bioorg. Med. Chem.* **19**, 3039 (2011).

41. S. M. Ciborowski, R. M. Harris, G. Liu, C. J. Martinez-Martinez, P. Skurski, and K. H. Bowen, *J. Chem. Phys.* **150**, 161103 (2019).
42. V. Dribinski, A. Ossadtchi, V. A. Mandelshtam, and H. Reisler, *Rev. Sci. Instrum.* **73**, 2634 (2002).
43. J. Hendricks, H. de Clercq, C. B. Freidhoff, S. T. Arnold, J. G. Eaton, C. Fancher, S. A. Lyapustina, J. T. Snodgrass, and K. H. Bowen, *J. Chem. Phys.* **116**, 7926 (2002).
44. F. Neese, *WIREs Comput. Mol. Sci*. **2**, 73 (2012).
45. F. Neese, A. Wennmohs, U. Hansen, and U. Becker, *Chem. Phys.* **356**, 98 (2008).
46. T. H. Dunning, Jr., *J. Chem. Phys*. **90**, 1007 (1989).
47. F. Weigend, *Phys. Chem. Chem. Phys.* **8**, 1057 (2006).
48. F. Weigend, A. Kohn and C. Hattig, *J. Chem. Phys.* **116**, 3175 (2012).
49. C. L. Adams, H. Schneider, K. M. Ervin, and J. M. Weber, *J. Chem. Phys.* **130**, 074307 (2009).

III.A.5. Dipole-Bound Anions of Intramolecular Complexes

Elena F. Belogolova, Gaoxiang Liu, Evgeniya P. Doronina, Sandra M. Ciborowski, Valery F. Sidorkin, Kit H. Bowen

Reprinted with permission from *J. Phys. Chem. Lett.* 2018, 9, 6, 1284-1289, Copyright 2018 American Chemical Society.

III.A.5.a. Abstract

Dipole-bound molecular anions are often envisioned as unperturbed neutral, polar molecules with single excess electrons. Here, we report the observation of intramolecular structural distortions within silatrane molecules due to the formation of their dipole-bound anions. The combination of Rydberg electron transfer-anion photoelectron spectroscopy (RET-PES) and ab-initio computational methodologies (CCSD and MP2) was used to study 1-hydro- (**HS**) and 1-fluoro- (**FS**) silatranes and their dipole bound anions, **HS**$^-$ and **FS**$^-$. The vertical detachment energies (VDE) of **HS**$^-$ and **FS**$^-$ were measured to be 48 and 93 meV, respectively. Ab initio calculations accurately reproduced these VDE values as well as their photoelectron spectral profiles. This work revealed significant shortening (by ~0.1 Å) of dative Si←N bond lengths when **HS** and **FS** formed dipole-bound anions, **HS**$^-$ and **FS**$^-$. Detailed computational (Franck-Condon) analyses explained the absence of vibrational features in the photoelectron spectra of **HS**$^-$ and **FS**$^-$.

III.A.5.b. Main Text

Dipole-bound anions can be formed by the interaction of electrons with highly polar neutral molecules or small clusters.[1-6] The formation of dipole-bound states is thought to be the initial step in the attachment of electrons to many polar molecules. Thus, dipole bound anions that play this role are sometimes referred to as “doorway” or “stepping stone” states.[7-16] A combination of experimental findings and theoretical predictions imply that molecules with dipole moments greater than 2.5 Debye can form dipole-bound anions.[17-18] The excess electron in a dipole-bound molecular anion can be envisioned as a highly delocalized cloud, tethered at the positive end of the molecular dipole and extending over a relatively large volume. Since it interacts only weakly with the larger molecule, the excess electron's binding energy is very small, and there is little distortion of the molecule's nuclear framework. For these reasons, dipole bound anions exhibit a distinctive anion photoelectron spectroscopic signature, consisting of a single narrow peak at very low electron binding energy.[19-20] The narrow peak derives from the fact that the structures of dipole-bonded molecular anions are essentially the same as their corresponding neutral molecules, which in turn leads to near perfect Franck-Condon overlap and thus to a single narrow peak. In cases where significant structural distortion does occur, however, additional peaks can appear in the anion photoelectron spectra. These are often seen in the dipole bound anions of hydrogen-bond, dimers and trimers, such as $(HF)_2$,[21,22] and Indole$(H_2O)_{1,2}$[16], where inter-molecular structural changes have occurred. Such peaks are due to combination bands of molecular and inter-molecular (weak) vibrations. The dipole bound anions of *lone molecules* do not show clear evidence of structural distortion, i.e., they tend to exhibit single narrow peaks in their anion photoelectron spectra without evidence of additional Franck-Condon combination bands.

Silatranes, $XSi(OCH_2CH_2)_3N$ (see Figure III.A.17) are highly polar (~6-9 D) molecular cages with labile, internal Si←N dative bonds. These bonds are strongly sensitive to the nature of their axial substituents, X, and to external factors.[23-27] An attractive interaction Si←N in silatranes predetermines the peculiarity of their structure, unusual spectral characteristics, and reactivity, as well as a wide spectrum of biological activity.[23,24]

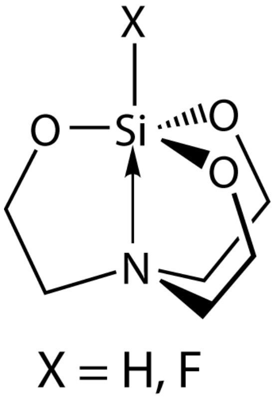

Figure III.A.17. STRUCTURE OF 1-HYDRO- (HS) AND 1-FLUORO- (FS) SILATRANE.

Here, we present results from our combined experimental-theoretical study of 1-hydro-silatrane (**HS**) and 1-fluoro-silatrane (**FS**) and their anions. These two were initially selected because they do not have low-lying vacant orbitals (primarily of π-type)[25-28] and therefore are candidates for forming dipole-bound anions, **HS**$^-$ and **FS**$^-$. It is also important to note that **HS** and **FS** differ in their Si←N bond strengths,[23,25] and that their geometries are known from electron diffraction studies.[29,30]

The formation of the anions, **HS**$^-$ and **FS**$^-$ benefited from our use of specialized experimental methods. Rydberg electron transfer (RET) is the ideal technique for forming dipole-bound anions. Schermann, Compton, Hammer, and ourselves have used RET extensively to prepare dipole-bound anions and analyze their electron binding energies (EBE) using a semi-empirical formula.[17,18,31-33] The recently developed combination of RET and anion photoelectron spectroscopy (PES), however, provides a somewhat more comprehensive picture of dipole bound anion energetics and structural aspects. In this work, we used our one-of-a-kind, RET-PES apparatus and state-of-the-art *ab initio* computational methods to study the dipole-bound anions of 1-hydro- (**HS**) and 1-fluoro- (**FS**) silatrane, i.e., **HS**$^-$ and **FS**$^-$.

Silatrane anions, **HS**$^-$ and **FS**$^-$, were generated by a Rydberg electron transfer (RET) source. Neutral silatrane molecules, **HS** and **FS**, were vaporized in a heated pulsed valve and expanded with 10 psig of helium gas. Their anions, **HS**$^-$ and **FS**$^-$, were formed when the neutral **HS** and **FS** molecules collided with a thermally-expanded beam of potassium atoms, which had been excited to *n*d Rydberg states, where *n* is the principal quantum number,) in two steps using two dye lasers. The anion signals were found to optimize at the 14d Rydberg state for **HS**$^-$ and 13d Rydberg state for **FS**$^-$. The anions were then extracted into a time-of-flight mass spectrometer and mass-selected, after which their excess electrons were photodetached with another laser and energy-analyzed using velocity-map imaging spectroscopy. Details of the experiments are presented in the Supporting Information.

Figure III.A.18 presents the anion photoelectron spectra of **HS**$^-$ and **FS**$^-$. The comb-like spikes along the baseline are due to noise and are of no consequence. Each spectrum consists of a major, sharp peak at rather low electron binding energy (EBE), strongly implying that **HS**$^-$ and **FS**$^-$ are dipole-bound anions. For **HS**$^-$, the EBE peak is centered at 48 meV with a full-width-half-maximum (FWHM) of about 35 meV (Figure III.A.18A). The EBE peak of **FS**$^-$ is centered at 93 meV also with a FWHM of about 35 meV (Figure III.A.18B), 35 meV being only slightly greater than the experimental resolution. We assign these two peaks as the origins of the transitions between the dipole-bound anions and their corresponding neutral molecules. Therefore, the VDE values for **HS**$^-$ and **FS**$^-$ anions are 48 meV and 93 meV, respectively. Note that the EBE value of **FS**$^-$ is higher than that of **HS**$^-$,

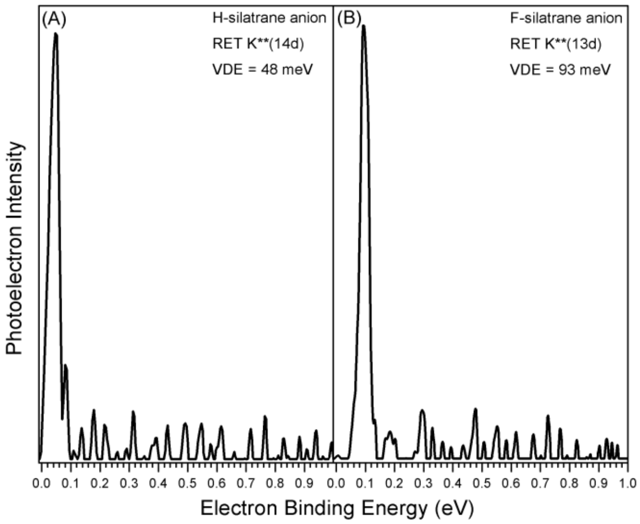

Figure III.A.18. Anion photoelectron spectra of the dipole-bound anions of (A) 1-hydro- and (B) 1-fluoro-silatrane measured with the first harmonic of a Nd:YAG laser (1064 nm, 1.165 eV).

which is to be expected due to the higher dipole moment of **FS** as compared with **HS** (Table S1). In photoelectron spectra such as these, which are dominated by single sharp peaks due to the close similarity between the structures of the anion and its neutral counterpart, the anion's VDE value is only slightly greater than the value of its corresponding neutral's electron affinity (EA).

The computed C_3 symmetry structures of **HS**, **FS**, and their dipole-bound anions, **HS**$^-$ and **FS**$^-$, optimized at MP2/B2(s) and CCSD/6-31++G(d,p) levels of theory are presented in Figure III.A.19. Both the $^2A_1$ dipole-bound anions and their corresponding neutral molecules were all found to exhibit single minima on their potential energy surfaces. For neutral molecules, the CCSD/6-31++G(d,p) method accurately reproduces the Si←N bond lengths, $d_{Si\leftarrow N}$, as determined from electron diffraction data[29,30] to within about 0.03 Å, while with the MP2/B2(s) method, the discrepancy is about. 0.05 Å. More importantly, regardless of the method used for geometry optimization, a significant

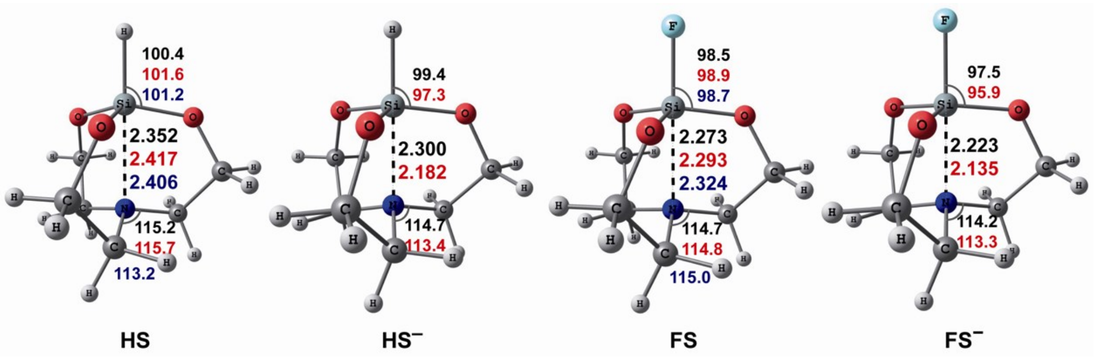

Figure III.A.19. MP2/B2(s) (in black) and CCSD/6-31++G(d,p) (in red) optimized geometries of silatranes, HS and FS, and their dipole-bound anions, HS$^-$ and FS$^-$. Electron diffraction structural parameters for HS and FS are shown in blue. The bond lengths are in Å and the bond angles in degrees. B2(s) is the 6-311++G(d,p) triple-zeta basis set augmented with an additional diffuse s function on each H atom and a set of diffuse s and p functions on the other atoms (see further description in the Supporting Information).

deformation of the coordination center around the silicon atom, $XSiO_3N$, is observed upon the addition of an excess electron. This is also accompanied by an increase in η_e, i.e., the pentacoordinate character or trigonal bipyramidal structure of the silicon atom (Figure III.A.19, Table S2). Such structural deformation is mainly manifested by a decrease in $d_{Si\leftarrow N}$ in the anion compared to that of its corresponding neutral. So, as a measure of the silatrane geometry response to the extra electron addition, we have chosen the $\Delta d_{Si\leftarrow N}$ value, that is defined as the difference between the experimental Si←N bond lengths for neutral molecules and the calculated bond lengths for their dipole-bound anions. For **HS$^-$**, $\Delta d_{Si\leftarrow N}$ is predicted to be 0.106 Å when calculated by the MP2/B2(s) method and 0.224 Å when computed by the CCSD/6-31++G(d,p) method. For **FS$^-$**, $\Delta d_{Si\leftarrow N}$ is computed to be 0.101 Å by MP2/B2(s) and 0.189 Å by CCSD/6-31++G(d,p) (see Figure S1, its legend and corresponding comments).

It is pertinent to note that, upon formation of *valence-bound* silatrane anions, calculations show their dative Si←N bonds elongating rather than shortening.[34]

Figure III.A.20 shows that the spin density in **HS**$^-$ and **FS**$^-$ is localized outside the nuclear frame on the positive dipole end, confirming them as dipole-bound anions (see also the Figure S2). Therewith, in accordance with the dipole moment values in **HS** and **FS**, the electron cloud density for **FS**$^-$ is higher than for **HS**$^-$ (see, for example, ref. 35).

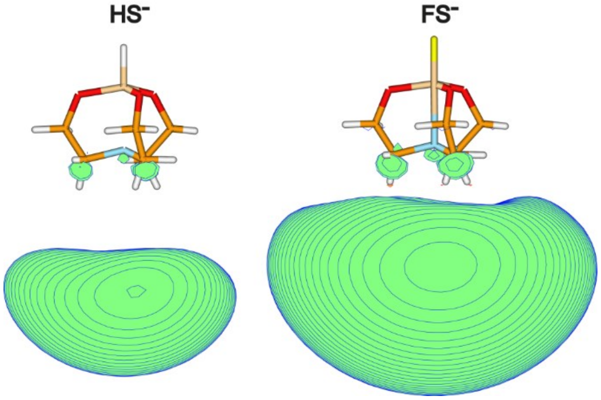

Figure III.A.20. SPIN DENSITY DISTRIBUTIONS OF HS$^-$ AND FS$^-$ OBTAINED AT THE MP2/B2(S) LEVEL (PLOTTED WITH 0.00003 E·BOHR^{-3} CONTOUR SPACING.).

The experimental and calculated VDE values for the dipole-bound anions, **HS**$^-$ and **FS**$^-$, are presented in Table III.A.3. The MP2/aug-cc-pVDZ+5s5p4d(N) and MP2/aug-cc-pVDZ+5s5p(H_3) methods predict negative VDE values, incorrectly estimating the stability of the dipole-bound anions. Only methods that invoke basis sets with a large number of diffuse functions and/or account for more electron correlation give qualitatively correct predictions on electron attachment to these molecules. Exceptional agreement with experimental VDE values is observed when using the CCSD/6-31++G(d,p) geometries with MP2/aug-cc-pVDZ+5s5p4d(H_3N) and MP2/B2(s) methods. On the other hand, for MP2/B2(s) geometries, the best quality VDE calculations are demonstrated by using CCSD

Table III.A.3. Experimental and calculated values of the vertical detachment energies (VDE, in eV) for the dipole-bound anions, **HS**$^-$ and **FS**$^-$. The red boxes encapsulate the combinations of theoretical methods for geometry and energies that best match experiment.

Geometry	CCSD/6-31++G(d,p)		MP2/B2(s)	
Energy	**HS**$^-$	**FS**$^-$	**HS**$^-$	**FS**$^-$
Exp.	**0.048**	**0.093**	**0.048**	**0.093**
MP2/aug-cc-pVDZ+5s5p4d(N)	-0.003	0.001	-0.005	-0.001
MP2/aug-cc-pVDZ+5s5p(H_3)	-0.004	-0.004	-0.005	-0.004
MP2/aug-cc-pVDZ+5s5p4d(H_3N)	0.050	0.094	0.031	0.072[a]
MP2/B2(s)	0.047	0.089	0.031	0.068
MP2/B2	0.052	0.099	0.033	0.075
CCSD/B2(s)	0.063	0.111	0.042	0.086
CCSD(T)/B2(s)	0.066	0.115	0.045	0.089
CCSD/B2	0.068	0.120	0.045	0.094
CCSD(T)/B2	0.071	0.123	0.048	0.097

[a] The same VDE value was obtained using the MP2/aug-cc-pVDZ+7s7p8d(N) method.

and CCSD(T) methods with the B2(s) and B2 basis sets. Noticeably, the electron affinities (EA) of **HS** and **FS** are calculated at the CCSD(T)/B2 level to be 39 and 90 meV, respectively, these being slightly lower than their VDE values, as expected. Since the VDE and EA values virtually coincide when there is near perfect Franck-Condon overlap as is the case for dipole bound anions, the EA values of **HS** and **FS** were not separately determinable by the experiment. The $\Delta d_{Si\leftarrow N}$ values predicted by CCSD/6-31++G(d,p) are considerably larger than those predicted by MP2/B2(s), specifically by 0.108 Å for **HS**$^-$ and 0.088 Å for **FS**$^-$ (see Figure III.A.19). Since excellent agreement between the experimental and calculated VDE values is found for both MP2 and CCSD optimized geometries, it is difficult to determine which geometry is more accurate based only on the quality of the VDE calculations.

The choice between the geometry optimization methods for silatranes and their anions can also be done using the Franck-Condon simulation of the photoelectron spectra of **HS**$^-$ and **FS**$^-$ (Figure III.A.21). An excellent match between experimental and theoretical photoelectron spectra is achieved when using the MP2 optimized geometries for **HS**$^-$ and **FS**$^-$ (Figure III.A.21.A and III.A.21.B). The estimated FWHM values for the dominant peak in the theoretical photoelectron spectra of **HS**$^-$ and **FS**$^-$ (0.036 and 0.035 eV, respectively) agree with the experimental widths. The simulated photoelectron spectra of **HS**$^-$ and **FS**$^-$ using the CCSD geometries have complex vibrational profiles, which are fundamentally different from the observed experimental photoelectron spectra (Figures III.A.21.C and D). As a result, we conclude that the CCSD/6-31++G(d,p) method overestimates the change of the Si←N bond length and also other structural parameters when an excess electron is attached to **HS** or **FS**. The MP2/B2(s) level of theory predicts more accurate anionic geometries and reasonable $\Delta d_{Si\leftarrow N}$ values of 0.106 Å for **HS**$^-$ and 0.101 Å for **FS**$^-$. Such a large deformation of bond contacts is unprecedented for dipole-bound molecular anions.

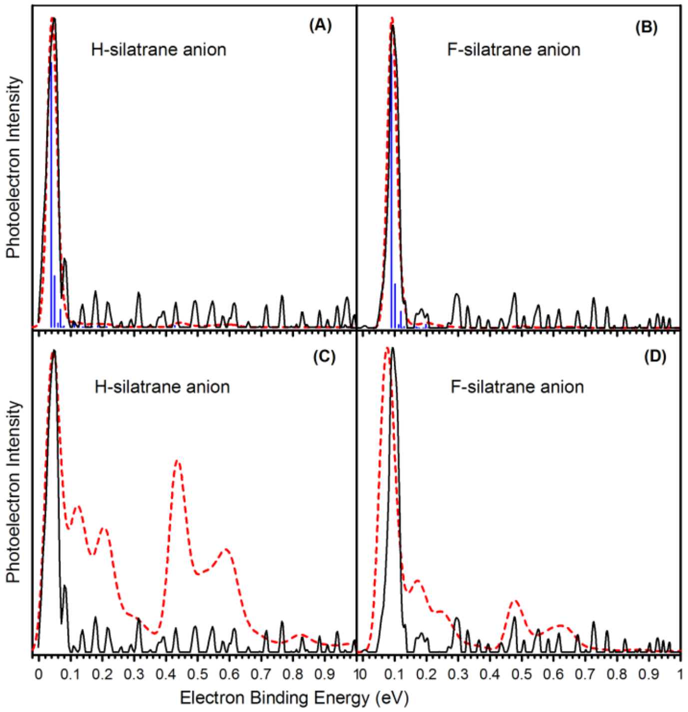

Figure III.A.21. Overlaid experimental (black solid line) and Franck–Condon (red dashed line) photoelectron spectra of HS$^-$ and FS$^-$. Vibrational progressions are given by a blue line spectrum. (A-B) MP2/B2(s) geometry optimizations and normal vibrational modes, in determining the position of the 0-0 transition we used the CCSD(T)/B2 AEA value (0.039 eV) for HS$^-$ and the CCSD/B2 AEA value (0.090 eV) for FS$^-$; (C-D) CCSD/6-31++G(d,p) optimized geometries and MP2/B2(s) normal vibrational modes.

Franck-Condon factors are listed in Table S3. We show that the main peaks in the simulated photoelectron spectra of **HS**$^-$ and **FS**$^-$ are formed by the superposition of the 0_0^0, 1_0^1, 4_0^1 and 0_0^0, 1_0^1, 6_0^1 transitions, respectively. These transitions are spaced apart from one another by less than 0.03 eV, which is comparable to the instrumental resolution. This situation can explain the observed asymmetry and broadening at the bottom of the **HS**$^-$ and **FS**$^-$ peaks on their high electron binding energy sides. The geometric relaxation upon the attachment of an electron occurs mainly along the first and fourth normal vibrational modes in **HS** and along the first and sixth modes in **FS**. They correspond to the Si←N dative bond stretching and torsional motion of the SiO_3 and $N(CH_2)_3$ fragments around the C_3 symmetry axis in the silatrane molecule. The corresponding harmonic vibrations have very low frequencies (ω): for **HS**, $\omega_1 = 85$ cm^{-1} and $\omega_4 = 235$ cm^{-1} with increases of 2 and 10 cm^{-1}, respectively, upon transition to the anionic state; for **FS**, $\omega_1 = 91$ cm^{-1} and $\omega_6 = 237$ cm^{-1} with increases by 0 and 14 cm^{-1}, respectively, in the anionic state. The reason for this is the high lability of the Si←N dative bond in **HS**, **FS,** and their dipole-bound anions, where less than 0.017 eV of energy is needed to change the Si←N distance by 0.1 Å (see Figure S1 and refs. 36-38). Consequently, the vibrational transitions (0_0^0, 1_0^1, 4_0^1) and (0_0^0 ,1_0^1 6_0^1), which are associated with the donor-acceptor moiety $XSiO_3 \leftarrow N(CH_2)_3$, are very energetically close and form a separate, narrow main peak (typical of dipole bound anions) in the photoelectron spectra of **HS**$^-$ and **FS**$^-$.

In addition to the above, the vibrational transitions 13_0^1 at 0.11 eV and 33_0^1 at 0.19 eV for **HS**$^-$ and 22_0^1 at ~0.20 eV for **FS**$^-$ were observed in their theoretical spectra (Table S3). However, despite the significant structural changes in the coordination center $XSiO_3N$ of **HS** and **FS** upon the extra electron attachment, the intensity of these additional peaks in the photoelectron spectra of **HS**$^-$ and **FS**$^-$ does not exceed the noise level in the experimental spectrum. Indeed, judging from the Franck-Condon factors values (Table S3), the relatively rigid modes 13 (HSiO bending) and 33 (CO bond stretching) in **HS** and mode 22 (SiF bond stretching) in **FS** are practically not populated upon the electron photodetachment from **HS**$^-$ and **FS**$^-$.

To summarize, we report the observation of an unusual structural change when a *lone molecule* (intramolecular complex) forms dipole-bound anions. This provides new insight into our current understanding about dipole-bound anions, where excess electrons are weakly bound to the neutral molecular framework. The novel combination of Rydberg electron transfer and photoelectron spectroscopy is promising for investigating anions which were not easily attained previously.

Supporting Information

Detailed experimental and theoretical methods. Raw velocity map images; Table S1 with the dipole moments of silatranes; Table S2 with experimental and calculated (at different theory levels) structural parameters of silatranes and their anions; Table S3 with FC factors, intensities and transition energies in the PES of silatrane anions; Figure S1 with CCSD(T)/B2(s)//MP2/B2(s) energies of H- and F-silatranes and their anions as functions of the Si···N distance; Figure S2 with SOMO of HS^- and FS^-; Cartesian coordinates of the molecules depicted in Figure III.A.19.

Acknowledgments

We are grateful to Dr. O. Trofimova and Dr. Y. Bolgolva for providing samples of 1-hydro- and 1-fluoro-silatranes. The experimental part of this material is based on work supported by the (US) National Science Foundation (NSF) under Grant No. CHE-1664182 (KHB).

References

1. K. D. Jordan, *Acc. Chem. Res.* **12**, 36 (1979).
2. J. Simons and K. D. Jordan, *Chem. Rev.* **87***,* 535 (1987).
3. G. Gutowski, P. Skurski, A. I. Boldyrev, J. Simons, and K. D. Jordan, *Phys. Rev. A* **54**, 1906 (1996).
4. J. Simons, *J. Phys. Chem. A* **112***,* 6401 (2008).

5. H. T. Liu, C. G. Ning, D. L. Huang, P. D. Dau, and L. S. Wang, *Angew. Chem. Int. Ed.* **52**, 8976 (2013).
6. D. Huang, H. Liu, C. Ning, G. Zhu, and L. Wang, *Chem. Sci.* **6**, 3129 (2015).
7. I. Dabkowska, J. Rak, M. Gutowski, J. M. Nilles, S. T. Stokes, D. Radisic, and K. H. Bowen, *Phys. Chem. Chem. Phys.* **6**, 4351 (2004).
8. L. Chomicz, M. Zdrowowicz, F. Kasprzykowski, J. Rak, A. Buonaugurio, Y. Wang, and K. H. Bowen, *J. Phys. Chem. Lett*. **4**, 2853 (2013).
9. R. A. Bachorz, W. Klopper, M. Gutowski, X. Li, and K. H. Bowen, *J. Chem. Phys*. **129**, 054309 (2008).
10. S. J. Xu, J. M. Nilles, and K. H. Bowen, *J. Chem. Phys.* **119**, 10696 (2003).
11. T. Sommerfeld, *J. Phys. Chem. A* **108**, 9150 (2004).
12. S. N. Eustis, D. Radisic, K. H. Bowen, R. A. Bachorz, M. Haranczyk, G. Schenter, and M. Gutowski, *Science* **319**, 936 (2008).
13. T. Sommerfeld, *J. Chem. Phys.* **126**, 124301 (2007).
14. C. Desfrancois, B. Baillon, J. P. Schermann, S. T. Arnold, J. H. Hendricks, and K. H. Bowen, *Phys. Rev. Lett.* **72**, 48 (1994).
15. J. Kelly, S. Xu, J. Graham, M. Nilles, D. Radisic, A. Buonaugurio, K. Bowen, N. Hammer, and G. Tschumper, *J. Phys. Chem. A* **118**, 11901 (2014).
16. A. M. Buytendyk, A. M. Buonaugurio, S. J. Xu, J. M. Nilles, K. H. Bowen, N. Kirnosov, and L. Adamowicz, *J. Chem. Phys.* **145**, 024301 (2016).
17. R. N. Compton and N. I. Hammer, *Adv. Gas Phase Ion Chem.*; JAI Press: Stamford, CT, U.S.A.; 2001.

18. C. Desfrancois, N. Khelifa, A. Lisfi, J. P. Schermann, J. G. Eaton, and K. H. Bowen, *J. Chem. Phys.* **95**, 7760 (1991).
19. K. D. Jordan and W. Luken, *J. Chem. Phys.* **64**, 2760 (1976).
20. A. W. Castleman and K. H. Bowen, *J. Phys. Chem.* **100**, 12911 (1996).
21. J. H. Hendricks, H. L. de Clercq, S. A. Lyapustina, and K. H. Bowen, *J. Chem. Phys.* **107**, 2962 (1997).
22. M. Gutowski and P. Skurski, *J. Chem. Phys.* **107**, 2968 (1997).
23. V. Pestunovich, S. Kirpichenko, and M. Voronkov, *The Chemistry of Organic Silicon Compounds*; Wiley: Chichester, U.K.; 1998.
24. J. K. Puri, R. Singh, and V. K. Chahal, *Chem. Soc. Rev.* **40**, 1791 (2011).
25. E. F. Belogolova, and V. F. Sidorkin, *J. Phys. Chem. A.* **117**, 5365 (2013).
26. V. F. Sidorkin, E. F. Belogolova, and E. P. Doronina, *Phys. Chem. Chem. Phys.* **17**, 26225 (2015).
27. V. F. Sidorkin, E. F. Belogolova, Y. Wang, V. Jouikov, and E. P. Doronina, *Chem. Eur. J.* **23**, 1910 (2017).
28. A. B. Trofimov, V. G. Zakrzewski, O. Dolgounitcheva, J. V. Ortiz, V. F. Sidorkin, E. F. Belogolova, M. Belogolov, and V. A. Pestunovich, *J. Am. Chem. Soc.* **127**, 986 (2005).
29. I. F. Shishkov, L. V. Khristenko, F. M. Rudakov, A. V. Golubinskii, L. V. Vilkov, S. S. Karlov, G. S. Zaitseva, and S. Samdal, *Struct. Chem.* **15**, 11 (2004).
30. G. Forgács, M. Kolonits, I. Hargittai, *Struct. Chem*. **1**, 245 (1990).
31. N. Hammer, K. Diri, K. Jordan, C. Desfrancois, and R. Compton, *J. Chem. Phys.* **119**, 3650 (2003).

32. N. Hammer, R. N. Compton, L. Adamowicz, and S. Stepanian, *Phys. Rev. Lett.* **94**, 153004 (2005).

33. N. Hammer, R. Hinde, R. Compton, K. Diri, K. Jordan, D. Radisic, S. T. Stokes, and K. Bowen, *J. Chem. Phys.* **120**, 685 (2004).

34. E. F. Belogolova, T. I. Vakul'skaya, and V. F. Sidorkin, *Phys. Chem. Chem. Phys.* **17**, 12735 (2015).

35. D. M. A. Smith, A. F. Jalbout, L. Smets, L. Adamowicz, L. *Chem. Phys.* **260**, 45 (2000).

36. V. F. Sidorkin and E. P. Doronina, *Organometallics* 2009, *28*, 5305–5315.

37. G. I. Csonka and P. Hencsei, *J. Comput. Chem.* **15**, 385 (1994).

38. M. W. Schmidt, T. L. Windus, and M. S. Gordon, *J. Am. Chem. Soc.* **117**, 7480 (1995).

III.B. More Strongly Bound Anions

Typically, the excess electron and the neutral molecule have strong interactions in valence bound anions. Thus, these anions tend to have the greatest variations in geometry when compared to the corresponding neutral and typically poor Franck-Condon overlap. Unlike the weakly bound systems where the peaks are sharp and at low binding energies, the photoelectron spectra exhibit broad features at higher energies.

As the complexity of the binding interaction between an atom or cluster with a small molecule changes, various features appear in photoelectron spectra. For instance, if an atomic metal anion is simply solvated by a water molecule, then the complex's photoelectron spectrum will display peaks like that of the atomic anion but shifted to higher binding energies. However, if the atomic metal anion has a water molecule chemisorbed, i.e., has activated a water molecule, then new features at a variety of binding energies corresponding to this new complex appear; theory helps discern what structures are consistent with the new peaks.

In the following studies, atomic and cluster metal anions, their complexes with small molecules, and large metal-based clusters with various ligands are described through combinations of anion photoelectron spectroscopic experiments and theoretical calculations.

III.B.1. Photoelectron Spectroscopic and Computational Study of Pyridine-Ligated Gold Cluster Anions

Gaoxiang Liu, Sandra M. Ciborowski, and Kit H. Bowen

Reprinted with permission from *J. Phys. Chem. A* 2017, **121**, 31, 5817-5822.

III.B.1.a. Abstract

Pyridine-ligated gold cluster anions were studied through a combination of negative ion photoelectron spectroscopy and density functional theory calculations. Small gold cluster anions ligated by pyridine, $Au_n(py)^-$ were generated with a ligation cell coupled to a laser vaporization source (LVS). We showed that pyridine is weakly bound (physisorbed) to the Au_2^- moiety of $Au_2(py)^-$ by interactions between its gold atoms and either the hydrogen atoms or the π-ring of pyridine. We also found that pyridine's lone electron pair strongly binds (chemisorbs) to both $Au_3(py)^-$ and $Au_4(py)^-$ through single gold atoms on each of these clusters. Bonding analysis of two isomers of $Au_4(py)^-$ supported the presence of two different ligand binding motifs, these differing in terms of the gold atom to which pyridine binds.

III.B.1.b. Introduction

The synthesis of sub-nanometer gold clusters with a precise number of metal atoms and organic ligands has been the subject of intensive research.[1] The size-dependent physical and chemical properties of these nanoclusters have made them promising materials for a broad range of applications including catalysis[2-5], chemical sensing[6,7], optical imaging[8,9] and biomedicine[10-12]. Particular compositions are often achieved by solution-phase reduction syntheses, including size-focusing methodologies[13] or ligand-exchange-induced size/structure transformation processes[14]. Organic ligands such as thiols[15], phosphines[16] and alkynes[17] are used to control the growth of gold clusters to specific sizes and to stabilize the prepared nanoclusters[13]. The bonding and interaction between specific organic ligands and gold cluster cores play a critical role in determining the structure, stability and functionality of gold nanoclusters.[18] Metal-ligand interactions are also relevant to metal-protein recognition at a molecular level, with these guiding the synthesis of metalloproteins having desirable properties.[19]

Extensive theoretical work has investigated the effect of ligation on the structures and energetics of various size gold cluster cores.[20-22] Examining how certain ligands can stabilize gold clusters of specific size has provided insight into the growth mechanism of atomically precise ligated gold clusters.[20-22] For example, density functional theory (DFT) calculations were performed on the absorption of methylthiol onto various gold cores Au_n^Z (n = 1-8, 12, 13, 20; Z = 0, -1, +1).[21] In another study, DFT was employed to analyze the binding energies of small Au_n clusters (n = 1-7, 11) with various lone-pair ligands (L = SH_2, NH_3, PCl_3, PMe_3, etc.).[23] For even-sized gold clusters, it was found that covalent Au_n-L bonds were formed when the ligands' (L) lone pairs interacted with the Au_n moiety's lowest unoccupied molecular orbital (LUMO). For odd-sized gold clusters, the bonding was found to be dominated by the interaction between the ligands' lone pairs and the Au_n core's singly-occupied molecular orbital (SOMO).[23] While many theoretical studies have been conducted on the nature of the bonding interactions between gold cluster cores and their ligands, direct experimental measurements pertaining to those interactions have been limited. Ligated gold clusters are commonly characterized by electrospray ionization mass spectrometry (ESI-MS)[24], X-ray diffraction (XRD)[25] and UV-Vis spectroscopy[26], which yield information on the clusters' sizes, crystal structures, and optical properties, respectively. These, however, provide little insight into the nature of binding between ligands and gold clusters.

Recently, gas-phase experiments which couple ESI-MS with techniques, such as collision induced dissociation (CID) and surface induced dissociation (SID), have been used to characterize the ligand-core interactions and binding energies of ligated gold clusters.[27] Johnson, Laskin, and co-workers investigated fragmentation patterns and binding energies of mass-selected triphenylphosphine (TPP) ligated gold cluster cations using ESI-MS-SID and found that the $Au_8(TPP)_6^+$ ion is remarkably stable towards dissociation, likely due to its large ligand binding energy.[28] Their strategy, however, required that ligated gold clusters first be synthesized in solution and then introduced into the gas phase using ESI. The choices of ligated gold clusters that could be studied in the gas phase by this approach were limited to those that could be synthesized in solution.[29-31] Since most of the ligands used in solution synthesis are thiols and phosphines, only a limited number of interaction motifs between ligands and gold cores have been explored using these methods.[1,27] Thus, an experimental approach which affords an opportunity to investigate interactions between a wider variety of ligands and different size gold clusters may help to sample a broader range of interactions.

In this work, a novel cluster beam source was developed and used to prepare pyridine-ligated gold cluster anions, $Au_n(\text{pyridine})^-$. This source comprises a laser vaporization source (LVS) and a ligation cell. Pyridine (py) was chosen as a ligand for these experiments because of its simplicity and its binding flexibility; it can interact via its lone pair or its π-ring. Moreover, pyridine-ligated gold clusters are not easily synthesized in solution. The $Au_n(py)^-$ cluster anions formed by this source were identified and mass-selected by mass spectrometry (MS), their excess electrons were photodetached and energy-analyzed by anion photoelectron spectroscopy (PES), and the resulting spectra were analyzed and interpreted through density functional theory (DFT) calculations. This combination of experiment and theory led to insight into the nature of the interactions between the gold cluster cores and their pyridine ligand.

III.B.1.c. Experimental and Computational Methods

Anion photoelectron spectroscopy is conducted by crossing a beam of mass-selected negative ions with a fixed-frequency photon beam and energy-analyzing the resultant photodetached electrons. The photodetachment process is governed by the energy-conserving relationship: hν = EBE + EKE, where hν is the photon energy, EBE is the electron binding energy, and EKE is the electron kinetic energy. Our apparatus consists of a laser vaporization cluster anion source with an attached ligation cell, a time-of-flight mass spectrometer, a Nd:YAG photodetachment laser, and a magnetic bottle electron energy analyzer[32]. The photoelectron spectrometer resolution is ~35 meV at 1 eV EKE. The third (355 nm) and fourth (266 nm) harmonic outputs of a Nd:YAG laser were used to photodetach electrons from mass-selected Au_n^- and $Au_n(py)^-$ clusters. Photoelectron spectra were calibrated against the well-known atomic transitions of atomic Cu^-.[33]

A schematic of our LVS-coupled ligation cell source is shown in Figure III.B.1. Gold cluster anions were generated by laser vaporization of a pure gold foil wrapped around an aluminum rod. The resultant plasma was cooled with helium gas delivered by a pulsed valve (PV1) having a backing pressure of a 100 psig. The resulting gold cluster anions then traveled through a ligation cell (4-mm diameter), where they were mixed with pyridine vapor. The pyridine vapor was introduced into the ligation cell by a second pulsed valve (PV2). The resulting $Au_n(py)^-$ anionic clusters were mass-analyzed by the time-of-flight mass spectrometer and their photoelectron spectra were recorded.

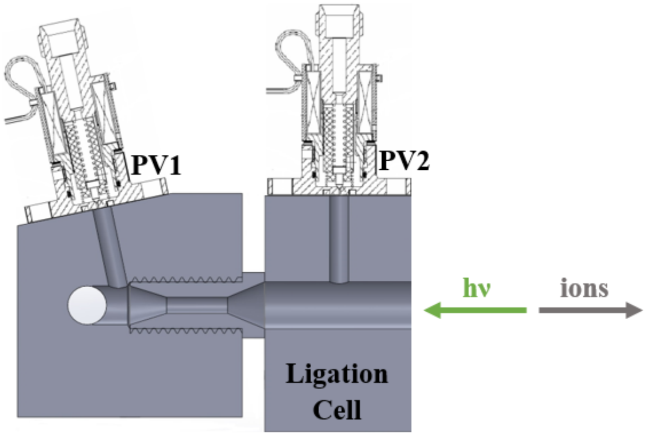

Figure III.B.1. SCHEMATIC OF THE LASER VAPORIZATION HOUSING COUPLED WITH A LIGATION CELL.

Density functional theory calculations were performed with the ORCA computational chemistry software package.[34] All calculations were carried out with the Becke Perdew (BP86) functional[35] with the D3 dispersion correction[36] and the RIJCOSX approximation[37]. The Ahlrichs Def2 basis sets were used throughout our calculations.[38] For geometry optimization, Def2-SVP and auxiliary Def2-SVP/J basis sets were chosen for hydrogen, nitrogen, and carbon atoms; the Stuttgart effective core potential SDD[39] and ECP basis set Def2-TZVP|Def2-TZVP/J were used for gold atoms. Single-point calculations were then improved with larger basis sets: Def2-TZVP|Def2-TZVP/J for hydrogen, nitrogen, and carbon atoms, and SDD|Def2-QZVPP|Def2-QZVPP/J for gold atoms. Vertical detachment energies (VDE) were computed from the energetic difference between the relaxed anionic complex and its corresponding neutral species at the geometry of the relaxed anion. Electron affinities (EA) were calculated from the energy differences between the relaxed anionic complex and its relaxed neutral counterpart. Frequency calculations were performed to verify that no imaginary frequencies existed and all optimized structures were minima.

III.B.1.d. Results

III.B.1.d.i. Experimental

The mass spectra, with and without pyridine (py) pulsed into the ligation cell, are shown in Figure III.B.2. This work focuses on relatively small gold-pyridine clusters. With no pyridine in the ligation cell, Au_n^- cluster anions (n = 2-5) are observed in the mass spectrum; when pyridine is added to the cell, a new series of $Au_n(py)^-$ complexes appears. While $Au_n(py)^-$ and Au_n^- show comparable ion intensities for n = 2-5, $Au(py)^-$ has a very low ion intensity despite the abundance of Au^-. The mass spectra clearly show that pyridine binds to gold cluster anions.

Photoelectron spectra of Au_n^- and $Au_n(py)^-$ were recorded for n = 2-4, and these are displayed in Figure III.B.3. The photoelectron spectra for Au_n^- agree well with those measured in previous studies.[40] For $Au_2(py)^-$, its lowest EBE spectral band covers EBE = 1.7 to 2.5 eV, and it exhibits two distinct features. These comprise a relatively broad peak centered at EBE = 2.11 eV and a sharp peak centered at EBE = 2.34 eV. These spectral features suggest the coexistence of two $Au_2(py)^-$ isomers, in which their pyridine molecules are weakly bound (physisorbed) to their Au_2^- moieties in both cases. There, the gold dimer anion moieties act as the chromophores for photodetachment, and for that reason the resulting spectra look like Au_2^- spectra, just shifted to slightly higher EBE values by their ion-molecule interaction energies.[41] The electron affinities (EA) for the neutral counterparts of these two isomers, obtained by extrapolating the lower EBE edges of their

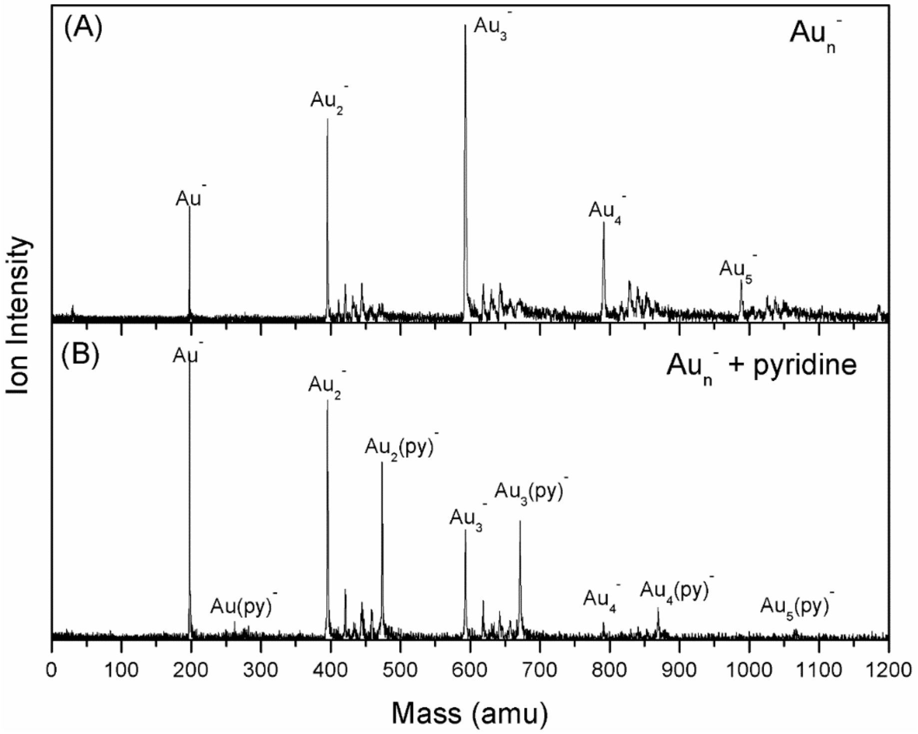

Figure III.B.2. THE MASS SPECTRA OF (A) GOLD CLUSTER ANIONS, AU_N^-, AND (B) PYRIDINE-LIGATED GOLD CLUSTER ANIONS, $AU_N(PY)^-$.

peaks to baseline, are estimated to be 1.7 eV and 2.3 eV. (The band at EBE ~ 3 eV may be due to excited electronic states or to a chemisorbed isomer, but that feature was not pursued in this study.)

For $Au_3(py)^-$ and $Au_4(py)^-$, broad spectral features appear at lower EBE values than those of the relatively narrow peaks of Au_3^- and Au_4^-. This means that they are not weakly bound (physisorbed) anion-molecule complexes. In fact, it implies that the energetics of the molecular orbitals (MO) of the Au_3^- and Au_4^- cores are substantially modified by interaction with pyridine, indicating strong, chemisorbed interactions in these anionic complexes. For $Au_3(py)^-$, transitions with maximum spectral intensities at 2.93 and 3.43 eV are identified, with corresponding EA values of 2.5 and 3.2 eV. For $Au_4(py)^-$, the EBE peaks with maxima at 2.03 and 2.36 eV are likely due to different isomers, and the EA

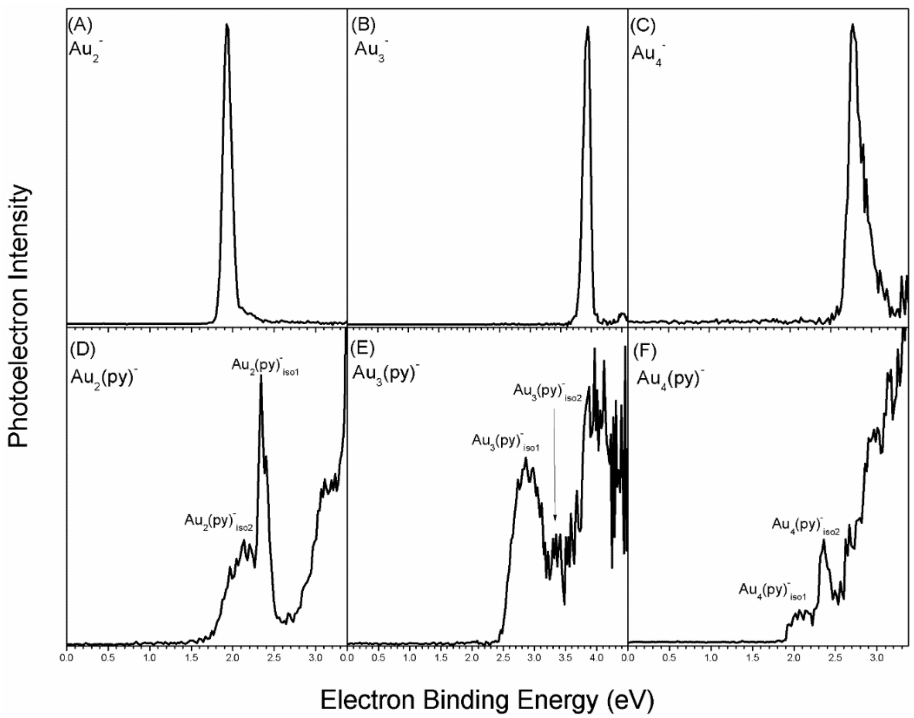

Figure III.B.3. PHOTOELECTRON SPECTRA OF (A-C) AU_N^- AND (D-F) $AU_N(PY)^-$ ($N = 2$-4).

values of their neutral counterparts are determined as 1.9 and 2.2 eV. (The higher EBE features in both of these cases may again be due to excited electronic states or to a chemisorbed isomer, but we did not pursue them in this study.)

III.B.1.d.ii. Computational

DFT calculations were performed to account for the multiple features observed in the photoelectron spectra of $Au_n(py)^-$. The optimized structures, relative energies, experimental/theoretical VDE values of $Au_n(py)^-$ and experimental/theoretical EA values of their neutral molecule counterparts, $Au_n(py)$, are presented in Table III.B.1. The lowest energy structure for $Au_2(py)^-$ is a complex, where the anionic Au_2^- moiety weakly interacts with the hydrogen atoms of pyridine (see $Au_2(py)^-_{iso1}$ in Table III.B.1). The distances between Au and H are around 2.7 Å which is typical for hydrogen-bond like interaction, i.e., solvation effect. In $Au_2(py)^-_{iso2}$, the Au_2^- moiety is predicted to interact strongly with pyridine, i.e., a pyridine-ligated Au_2^-, and to exhibit a VDE value of 1.16 eV. There is, however, no feature there in our spectrum. For $Au_2(py)^-_{iso3}$, however, the prediction of a weakly bound complex (VDE = 1.96 eV) is in agreement with the observed feature at VDE = 2.11 eV (see $Au_2(py)^-_{iso3}$ in Table III.B.1). For $Au_3(py)^-$, two stable products were identified. For both isomers, the gold trimer moieties adopted linear geometries. Pyridine ligated the Au_3^- moieties either through the end gold atom (see $Au_3(py)^-_{iso1}$ in Table III.B.1) or through the middle gold atom (see $Au_3(py)^-_{iso2}$). Two of the three calculated $Au_4(py)^-$ cluster anion isomers exhibit corresponding features in the $Au_4(py)^-$ spectrum, and both of these are chemisorbed systems, i.e., pyridine-ligated gold clusters. The Au_4 moieties in $Au_4(py)^-_{iso1}$ and in $Au_4(py)^-_{iso2}$ exhibit Y-shaped structures. There is no evidence for $Au_4(py)^-_{iso3}$ in the photoelectron spectrum; its Au_4 moiety is predicted to have a diamond-shape.

III.B.1.e. Discussion

Table III.B.1 presents comparisons between experimentally-determined and theoretically-calculated VDE and EA values. Experimental VDE values are generally more reliable measurements than experimental EA values, since the former are simply peak locations, while the latter involve extrapolations. Due to differences in the structures of anions and their neutral counterparts, the EA-determining origin transition may not always correspond to the extrapolated lowest EBE side of the spectral band. Table III.B.1 shows excellent agreement between experimental and theoretical VDE values, although for the reasons stated the agreement between experimental and theoretical EA values is not as good.

To understand why the Au(py)$^-$ ion intensity in the mass spectrum is so weak, we calculated the potential energy between a gold anion, Au$^-$, and a pyridine molecule. As shown in Figure S2, the interaction is largely repulsive. As described above, both the broad peak at EBE = 2.11 eV and the sharp peak at EBE = 2.34 eV in the Au_2(py)$^-$ spectrum are due to weakly bound complexes, where pyridine is physisorbed to the Au_2^- moiety. These VDE values agree relatively well with the calculated VDE values. Moreover, the calculated structures for these isomers are consistent with this interpretation. Since no spectral feature was seen in the vicinity of EBE = 1.16 eV in the photoelectron spectrum, the predicted strongly ligated (chemisorbed) isomer, $Au_2(py)^-_{iso2}$, was not present in the experiment. Its absence may be explained by examining the relaxed potential energy scan shown in Figure S3. There, one sees a 0.62 eV high barrier between $Au_2(py)^-_{iso2}$ and the "weakly-ligated" $Au_2(py)^-_{iso3}$. This barrier may keep $Au_2(py)^-_{iso3}$ from converting to $Au_2(py)^-_{iso2}$, even though the latter is lower in energy. Physically, the barrier is understandable in terms of electrostatic repulsion, i.e., the interaction between pyridine's lone pair and the negatively-charged Au_2^- moiety.

The two isomers of the Au_3(py)$^-$ cluster are due to pyridine being chemisorbed (strongly bound) to its gold trimer moiety. The two EBE peaks exhibited in the photoelectron spectrum of Au_3(py)$^-$ correspond to the calculated VDE values of EBE = 2.84 eV and EBE = 3.50 eV. The gold tetramer moieties in $Au_4(py)^-_{iso1}$ and $Au_4(py)^-_{iso2}$ are Y-shaped, and both isomers are chemisorbed (ligated) clusters. The two EBE peaks exhibited in the photoelectron spectrum of Au_4(py)$^-$ correspond to the calculated VDE values of EBE = 1.92 eV and EBE = 2.22 eV. Since no spectral feature was seen in the vicinity of EBE = 1.70 eV in the photoelectron spectrum of Au_4(py)$^-$, the predicted chemisorbed isomer, $Au_4(py)^-_{iso3}$, with its diamond-shaped gold tetramer moiety was not present in the experiment.

The differing bonding motifs in $Au_{1,2}(py)^-$ versus $Au_{3,4}(py)^-$ may be due to different negative charge densities on $Au_{1,2}^-$ versus $Au_{3,4}^-$. While the excess negative charge is highly localized in the cases of $Au_{1,2}^-$, it is likely to be somewhat delocalized in the cases of $Au_{3,4}^-$. Diffuse electron distributions may have the effect of reducing electrostatic repulsion between $Au_{3,4}^-$ and pyridine and with it the type of barrier seen in Figure S3, making it easier to form chemisorbed (ligated) cluster anions.

To gain more insight into the interaction between pyridine and gold cluster anions, the two isomers of $Au_4(py)^-$ observed in the experiment were selected as candidates for molecular orbital (MO) and charge analyses. The frontier orbitals of $Au_4(py)^-_{iso1}$, $Au_4(py)^-_{iso2}$ and pyridine are presented in Chart 1. The Au_4 moieties in $Au_4(py)^-_{iso1}$ and $Au_4(py)^-_{iso2}$ have net charges of -0.87e and -1.07e, respectively. Orbital analysis indicates that the bonding motif differs depending on which gold atom interacts with pyridine. For $Au_4(py)^-_{iso1}$, while its SOMO-1 and SOMO-2 are mostly the MOs of Au_4, its SOMO shows a strong participation of the LUMO of pyridine. The SOMO likely includes strong electron back-bonding from the Au_4 metal core to pyridine. The back-bonding is also manifested by a decrease of the negative charge on the Au_4 moiety from -1e to -0.87e. Such back-bonding effects strengthen the interactions between pyridine and the gold cluster, resulting in a shorter, 2.13 Å Au-N bond, compared to the 2.26 Å bond in $Au_4(py)^-_{iso2}$ (Figure S1). The back-bonding also helps to stabilize the anionic complex, making $Au_4(py)^-_{iso1}$ 0.18 eV lower in energy than $Au_4(py)^-_{iso2}$ (Table III.B.1). For $Au_4(py)^-_{iso2}$, its SOMO is mainly the combination of gold atomic orbitals; thus, electron detachment from this orbital should resemble electron detachment from Au$_4^-$. This is consistent with the sharp transition in the photoelectron spectrum [Figure III.B.3F]. The SOMO-1 for Au$_4$(py)$^-_{\text{iso2}}$ shows that the ligand-metal interaction is primarily between the metal core and the lone-pair of pyridine.

To summarize this work, a new source which couples LVS and a ligation cell was developed to make pyridine-ligated gold cluster anions, Au$_n$(py)$^-$. A combined anion photoelectron spectroscopic and DFT study confirmed the structures of stable Au$_n$(py)$^-$ (n = 2-4) and explored the nature of their bonding interactions. The excess electrons on the gold cores had significant effects on the structures of the ligated gold cluster anions and thus on their binding motifs.

Chart III.B.1. FRONTIER MOLECULAR ORBITALS OF PYRIDINE AND AU$_4$(PY)$^-$ CLUSTER ANIONS OBSERVED IN EXPERIMENTS

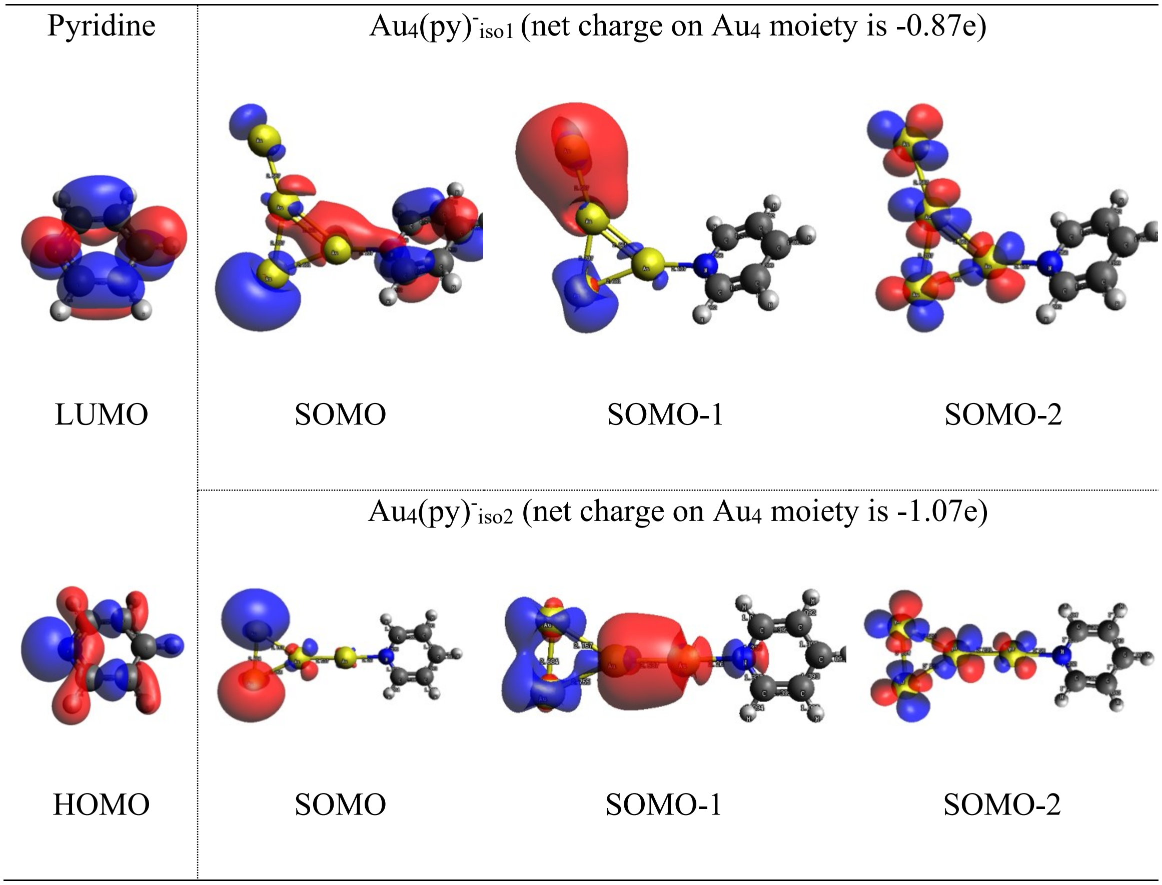

Table III.B.1. OPTIMIZED STRUCTURES, RELATIVE ENERGIES, EXPERIMENTAL/THEORETICAL EA VALUES OF NEUTRAL $\mathrm{Au}_N(\mathrm{py})$, AND EXPERIMENTAL/THEORETICAL VDE VALUES OF $\mathrm{Au}_N(\mathrm{py})^-$

Anion	Optimized Structure	ΔE	Expt. EA	Theo. EA	Expt. VDE	Theo. VDE
$\mathrm{Au_2(py)^-_{iso1}}$	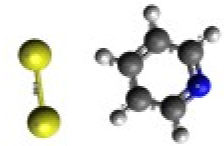	0	2.3	2.36	2.34	2.47
$\mathrm{Au_2(py)^-_{iso2}}$	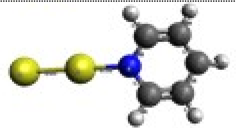	0.06	N/A	0.94	N/A	1.16
$\mathrm{Au_2(py)^-_{iso3}}$	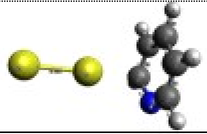	0.15	1.7	1.40	2.11	1.96
$\mathrm{Au_3(py)^-_{iso1}}$	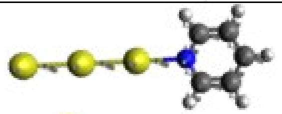	0	2.5	2.68	2.93	2.84
$\mathrm{Au_3(py)^-_{iso2}}$	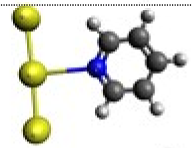	0.19	3.2	2.20	3.43	3.50
$\mathrm{Au_4(py)^-_{iso1}}$	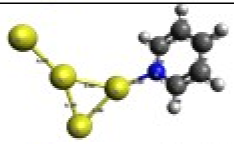	0	1.9	1.41	2.03	1.92
$\mathrm{Au_4(py)^-_{iso2}}$	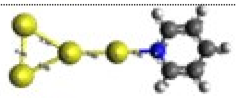	0.18	2.2	2.13	2.36	2.22
$\mathrm{Au_4(py)^-_{iso3}}$	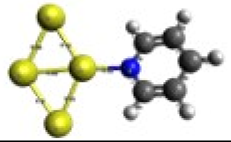	0.21	N/A	1.50	N/A	1.70

The unit of energy is eV. N/A indicates the corresponding isomer was not observed in the experiment.

Acknowledgments

This material is based on work supported by the Office of Naval Research (ONR), Multidisciplinary University Research Initiative (MURI) under Grant No. N00014-15-1-2681.

References

1. R. Jin, C. Zeng, M. Zhou, and Y. Chen, *Chem. Rev.* **116**, 10346 (2016).
2. Y. Zhu, H. Qian, M. Zhu, and R. Jin, *Adv. Mat.* **22**, 1915 (2010).
3. S. Gaur, H. Wu, G. G. Stanley, K. More, C. S. S. R. Kumar, and J. J. Spivey, *Catalysis Today* **208**, 72 (2013).
4. W. Chen and S. Chen, *Angew. Chem.* **48**, 4386 (2009).
5. C. Yu, G. Li, S. Kumar, H. Kawasaki, and R. Jin, *J. Phys. Chem. Lett.* **4**, 2847 (2013); J. Oliver-Meseguer, J. R. Cabrero-Antonino, I. Domínguez, A. Leyva-Pérez, and A. Corma, *Science* **338**, 1452 (2012).
6. M. A. H. Muhammed, P. K. Verma, S. K. Pal, R. C. A. Kumar, S. Paul, R. V. Omkumar, and T. Pradeep, *Chem. Eur. J.* **15**, 10110 (2009).
7. Z. Wu, M. Wang, J. Yang, X. Zheng, W. Cai, G. Meng, H. Qian, H. Wang, and R. Jin, *Small* **8**, 2027 (2012).
8. G. Ramakrishna, O. Varnavski, J. Kim, D. Lee, and T. Goodson, *J. Am. Chem. Soc.* **130**, 5032 (2008).
9. R. Philip, P. Chantharasupawong, H. Qian, R. Jin, and J. Thomas, *Nano Lett.* **12** 4661 (2012).
10. A. George, E. S. Shibu, S. M. Maliyekkal, M. S. Bootharaju, and T. Pradeep, *ACS Appl. Mater. Interfaces* **4**, 639 (2012).

11. T. Xiaohong, and J. Rongchao, J. *WIREs Nanomed. Nanobiotechnol.* **5**, 569 (2013).
12. O. A. Wong, R. J. Hansen, T. W. Ni, C. L. Heinecke, W. S. Compel, D. L. Gustafson, and C. J. Ackerson, *Nanoscale* **5**, 10525 (2013).
13. R. Jin, H. Qian, Z. Wu, Y. Zhu, M. Zhu, A. Mohanty, and N. Garg, *J. Phys. Chem. Lett.* **1**, 2903 (2010).
14. C. Zeng, Y. Chen, A. Das, and R. Jin, *J. Phys. Chem. Lett.* **6**, 2976 (2015).
15. Y. Negishi, K. Nobusada, and T. Tsukuda, *J. Am. Chem. Soc.* **127**, 5261 (2005).
16. X.-K. Wan, Z.-W. Lin, and Q.-M. Wang, *J. Am. Chem. Soc.* **134**, 14750 (2012).
17. P. Maity, H. Tsunoyama, M. Yamauchi, S. Xie, and T. Tsukuda, *J. Am. Chem. Soc.* **133**, 20123 (2011).
18. M. Walter, J. Akola, O. Lopez-Acevedo, P. D. Jadzinsky, G. Calero, C. J. Ackerson, R. L. Whetten, H. Grönbeck, and A. Häkkinen. *PNAS* **105**, 9157 (2008).
19. T. Dudev, and C. Lim, *Annu. Rev. Biophys.* **37**, 97 (2008).
20. G. Shafai, S. Hong, M. Bertino, and T. S. Rahman, *J. Phys. Chem. C* **113**, 12072 (2009).
21. B. M. Barngrover and C. M. Aikens, *J. Phys. Chem. A* **117**, 5377 (2013).
22. D. Jiang, *Nanoscale* **5**, 7149 (2013).
23. T. Rajský and M. Urban, *J. Phys. Chem. A* **120**, 3938 (2016).
24. D. M. Black, N. Bhattarai, R. L. Whetten, and S. B. H. Bach, *J. Phys. Chem. A* **118**, 10679 (2014).
25. D. Crasto, S. Malola, G. Brosofsky, A. Dass, and H. Häkkinen, *J. Am. Chem. Soc.* **136**, 5000 (2014).
26. C. Zeng, C. Liu, Y. Pei, and R. Jin, *ACS Nano* **7**, 6138 (2013).
27. G. E. Johnson and J. Laskin, *Analyst* **141**, 3573 (2016).

28. G. E. Johnson, T. Priest, and J. Laskin, *Chem. Sci.* **5**, 3275 (2014).

29. G. E. Johnson, A. Olivares, D. Hill, and J. Laskin, *Phys. Chem. Chem. Phys.* **17**, 14636 (2015).

30. G. E. Johnson, T. Priest, and J. Laskin, *ChemPlusChem* **78**, 1033 (2013).

31. P. Chakraborty, A. Baksi, E. Khatun, A. Nag, A. Ghosh, and T. Pradeep, *J. Phys. Chem. C* **121**, 10971 (2017).

32. X. Zhang, G. Liu, G. Ganteför, K. H. Bowen, and A. N. Alexandrova, *J. Phys. Chem. Lett.* **5**, 1596 (2014).

33. J. Ho, K. M. Ervin, and W. C. Lineberger, *J. Chem. Phys.* **93**, 6987 (1990).

34. F. Neese, *WIREs Comput. Mol. Sci.* **2**, 73 (2012).

35. A. D. Becke, *Phys. Rev. A* **38**, 3098 (1988); J. P. Perdew, *Phys. Rev. B* **33**, 8822 (1986).

36. S. Grimme, J. Antony, S. Ehrlich, and H. Krieg, *J. Chem. Phys.* **132** (2010) DOI: 10.1063/1.3382344.

37. F. Neese, F. Wennmohs, A. Hansen, and U. Becker, *Chem. Phys.* **356**, 98 (2008).

38. F. Weigend and R. Ahlrichs, *Phys. Chem. Chem. Phys.* **7**, 3297 (2005), DOI: 10.1039/B508541A; F. Weigend, *Phys. Chem. Chem. Phys.* **8**, 1057 (2006).

39. D. Andrae, U. Häußermann, M. Dolg, H. Stoll, and H. Preuß. *Theor. Chim. Acta* **77**, 123 (1990).

40. H. Häkkinen, B. Yoon, U. Landman, X. Li, H.-J. Zhai, and L.-S. Wang, *J. Phys. Chem. A* **107**, 6168 (2003).

41. X. Zhang, E. Lim, S. K. Kim, and K. H. Bowen, *J. Chem. Phys.* **143**, 174305 (2015).

III.B.2. Activation of Hydroxylamine by Single Gold Atomic Anions

Gaoxiang Liu, Sandra M. Ciborowski, Zhaoguo Zhu, and Kit H. Bowen

Reprinted with permission from *Int. J. Mass Spectrom.* 435 (2019) 114-117.

III.B.2.a. Abstract

Hydroxylamine (HA) is a potential component in next-generation monopropellants. In this work, we present a combined anion photoelectron spectroscopic and density functional theory study of the reaction between a single HA molecule and a single gold atomic anion, Au^-. This study shows that an Au^- anion can activate a HA molecule by inserting into its N-O bond. Our calculations show this reaction to be facilitated by the presence of two minimum energy crossing points (MECP's), i.e., spin flips, along the reaction pathway.

III.B.2.b. Introduction

Replacing hydrazine with less toxic ionic liquids as monopropellants in spacecraft thrusters is appealing from both a safety and an environmental perspective. Hydroxylammonium nitrate (HAN) is one such ionic liquid being considered. In fact, HAN is a component in the monopropellant used in NASA's Green Propellant Infusion Mission.[1,2] Studies of both the thermal and catalytic decomposition mechanisms of HAN have informed the further development of HAN-based monopropellants and thus of thrusters.[3-18] Hydroxylamine (H_2NOH, HA) is a major thermal decomposition product of HAN. As such, HA can further decompose on heated iridium catalysts, creating ignition conditions in HAN-based propellants.[17,19]

Single metal atoms are sometimes seen as models for mimicking active sites in heterogenous catalysts.[20-25] Studying molecular activation and catalysis using gas-phase, metal atomic ions can help to better understand bond activation, dissociation, and new bond formation at the molecular level and thus to aid the design of new catalysts.[26-29] In the present work, we focused on studying the activation of HA by single gold atomic anions. Molecular activation by gold ions has received considerable attention in gas-phase studies. While the gold atomic cation has been found to activate various molecules,[30-34] the gold atomic anion tends to be inert in activating small molecules.[35-42] An exception, however, is the activation of CO_2 by Au^-, a process that involves only charge transfer and not bond breaking.[43-44] Here, we utilize a combination of anion photoelectron spectroscopy and density functional theory (DFT) to provide strong evidence that Au^- can break the N-O bond in HA, thus activating it. As shown below, Au^- spin states play critical roles in activating HA.

III.B.2.c. Experimental and Computational Methods

Anion photoelectron spectroscopy is conducted by crossing a beam of mass-selected negative ions with a fixed-frequency photon beam and energy-analyzing the resultant photodetached electrons. The photodetachment process is governed by the energy-conserving relationship: hν = EBE + EKE, where hν is the photon energy, EBE is the electron binding energy, and EKE is the electron kinetic energy. Our apparatus consists of a laser vaporization cluster anion source with an attached ligation cell, a time-of-flight mass spectrometer, a Nd:YAG photodetachment laser (operating at 355 nm), and a magnetic bottle electron energy analyzer with a resolution is ~35 meV at 1 eV EKE.[45] Photoelectron spectra were calibrated against the well-known atomic transitions of atomic Cu^-.[46]

The interaction between Au^- and HA was studied using a laser vaporization-reaction cell arrangement.[47] Atomic gold anions were generated by laser vaporization of a pure gold foil wrapped around an aluminum rod. The resultant plasma was cooled with helium gas delivered by a pulsed valve, having a backing pressure of 100 psig. The resulting gold anions then traveled through a ligation cell (4-mm diameter, 5-cm length), where it encountered HA/H_2O mixed vapor. The HA/H_2O mixed vapor was introduced into the ligation cell by a second pulsed valve, within which resided a drop of hydroxylamine water solution (since HA in its pure form is hazardous, it is sold dissolved in water, 50 wt%). The second pulse valve is backed by 15 psig ultra high purity helium. The resulting $[Au(HA)]^-$ anionic clusters were then mass-analyzed and mass-selected by the time-of-flight mass spectrometer and their photoelectron spectra measured.

Density functional theory calculations were performed with the ORCA computational chemistry software package.[48] All calculations were carried out with the PBE0 functional[49,50] with the D3 dispersion correction[51] and the RIJCOSX approximation[52]. The Ahlrichs Def2 basis sets, Def2-TZVP were used throughout our calculations[53]. The Stuttgart effective core potential, SDD[54] and the ECP basis set, Def2-TZVP|Def2-TZVP/J were used for the gold atoms. Vertical detachment energies (VDE) were computed from the energetic difference between the relaxed anionic complex and its corresponding neutral species at the geometry of the relaxed anion. Frequency calculations were performed to verify that no imaginary frequencies existed and all optimized structures were minima. The minimum-energy crossing points (MECPs) for the intersection of the electronic states of different spin multiplicities were searched for and located by using the method developed by Harvey et al.[55]

III.B.2.d. Results and Discussions

The mass spectra with or without the addition of the HA/H_2O mixed vapor into the reaction cell are shown in Figure III.B.4. With no HA/H_2O mixed vapor, only Au^- was observed in the mass spectrum. After adding HA/H_2O vapor to the reaction cell, peaks due to both $[Au(H_2O)]^-$ and $[Au(HA)]^-$ complexes appeared in the mass spectrum, these resulting from the interaction of Au^- with HA or H_2O, respectively. $[Au(H_2O)]^-$ has been studied in our previous work and is not the focus of the current study.[41] $[Au(HA)]^-$, on the other hand, could exist either as $Au^-(HA)$, where HA is physisorbed onto Au^- or as a $[Au(HA)]^-$ complex, where one or more bonds in HA (N-H, O-H or N-O bond) have been broken. This latter case would correspond to the activation of HA.

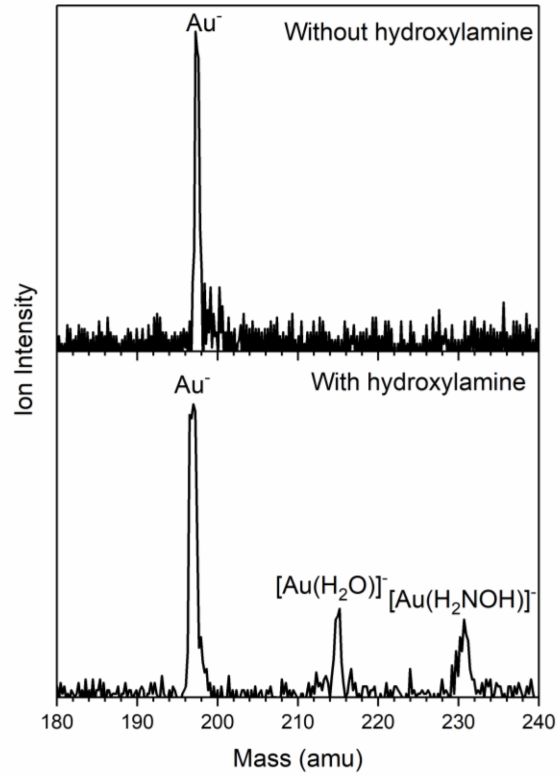

Figure III.B.4. THE MASS SPECTRA OF AU^- ANIONS WITHOUT AND WITH THE ADDITION OF HA/H_2O MIXED VAPOR.

To distinguish between these isomers, the anion photoelectron spectrum of $[Au(HA)]^-$ was measured. Typically, when an atomic metal anion is physisorbed by another molecule, the photoelectron spectrum of the resulting weakly-attached cluster anion closely resembles that of the atomic anion alone, since that anion acts as the chromophore. Thus, except for being shifted to higher electron binding energy (EBE) and its features slightly broadened, the resulting photoelectron spectrum looks like that of the atomic anion. Figure III.B.5 presents the anion photoelectron spectrum of $[Au(HA)]^-$. The evident feature in this spectrum reaches its maximal intensity at EBE = 3.00 eV. Thus, 3.00 eV is determined as the vertical detachment energy (VDE) value, i.e., the transition energy at which the Franck-Condon overlap between the anion's wavefunction and that of its neutral counterpart is at its maximum. Vibrational progressions spaced by 0.12 eV are also observed. The EBE of Au^- alone would have been at 2.3 eV, i.e., its electron affinity. Since the observed difference between the VDE values of Au^- and $[Au(HA)]^-$ is, at ~0.7 eV,

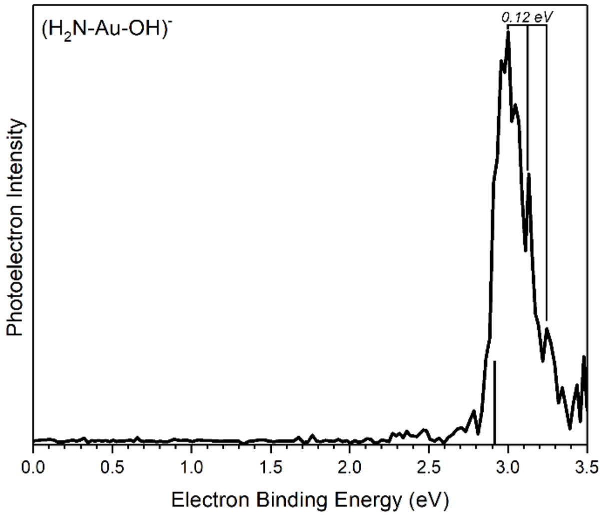

Figure III.B.5. THE PHOTOELECTRON SPECTRUM OF $[Au(HA)]^-$ TAKEN BY 3RD HARMONIC OUTPUT OF A ND:YAG LASER (3.496 EV). THE STICK SPECTRUM REPRESENTS THE CALCULATED VDE VALUE.

relatively large for an ion-molecule interaction energy, and since there is evident vibrational excitation in the spectrum, it is clear that this is not the spectrum of the anion-molecule physisorbed complex, Au$^-$(HA). The observed spectrum implies that a strong chemical interaction has occurred between Au$^-$ and HA, indicating hydroxylamine has been activated by its interaction with Au$^-$.

Figure III.B.6 presents the DFT optimized structures of different [Au(HA)]$^-$ isomers. The global minimum of [Au(HA)]$^-$ has structure in which the Au$^-$ inserts into the N-O bond of HA, that is, H_2N-Au-OH$^-$. The other isomers, H_2NO-Au-H$^-$, H-Au-NHOH$^-$ and Au$^-$(H_2NOH) are essentially iso-energetic, although all of them are ~1.8-1.9 eV higher than the global minimum. The VDE of the global minimum H_2N-Au-OH$^-$ is calculated to be 2.91 eV, which agrees well with the experimental VDE of 3.00 eV. Because H_2N-Au-OH$^-$ is the most stable calculated isomer and since its calculated VDE agrees with the experimental value, we are confident that Au$^-$ has inserted into the N-O bond of HA. The vibrational progression spaced at 0.12 eV is due to the bending modes of both N-H and O-H bonds. The Franck-Condon simulation was attempted to explain the vibrational

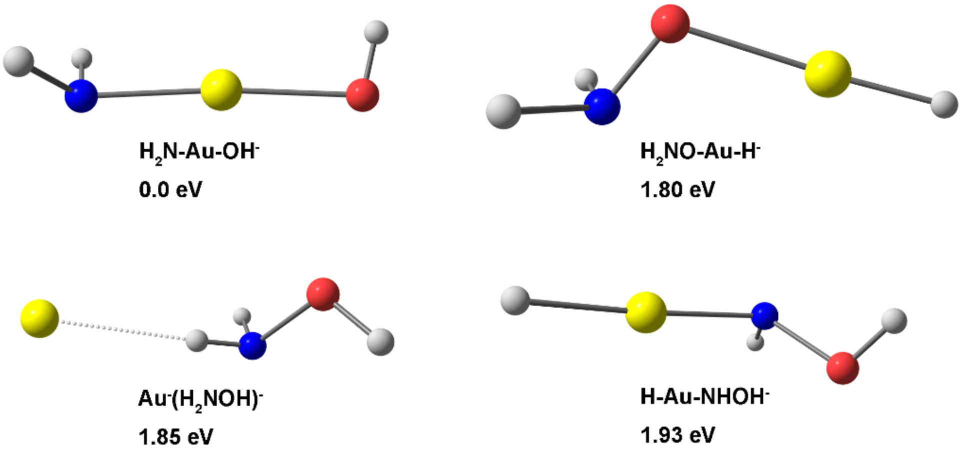

Figure III.B.6. OPTIMIZED STRUCTURES FOR [AU(HA)]$^-$ AND THEIR RELATIVE ENERGIES.

progression but failed due to the large geometry difference between the anion and neutral ground state structures.

The mechanism of HA activation by Au$^-$ was investigated by DFT calculations. The resulting reaction pathway is presented in Figure III.B.7. The most salient feature of this pathway is the role of spin states. There, the singlet reactant, Au$^-$ is converted to a triplet transition state before being converted back to the singlet product. Initially, Au$^-$ and HA are both in their singlet ground states. After having formed the singlet adduct, Au$^-$(HA), in which HA is physisorbed to Au$^-$, the insertion of Au$^-$ into the N-O bond begins to take place. Because of the rather high activation barrier (1.95 eV), however, the continuation of the reaction coordinate along the singlet surface is significantly hampered. Instead, the reaction can proceed more easily along the triplet transition state, which is only 0.73 eV above the entrance channel and much lower than the singlet transition state. The first minimal energy crossing point (MECP) is located between the physisorbed adduct and the

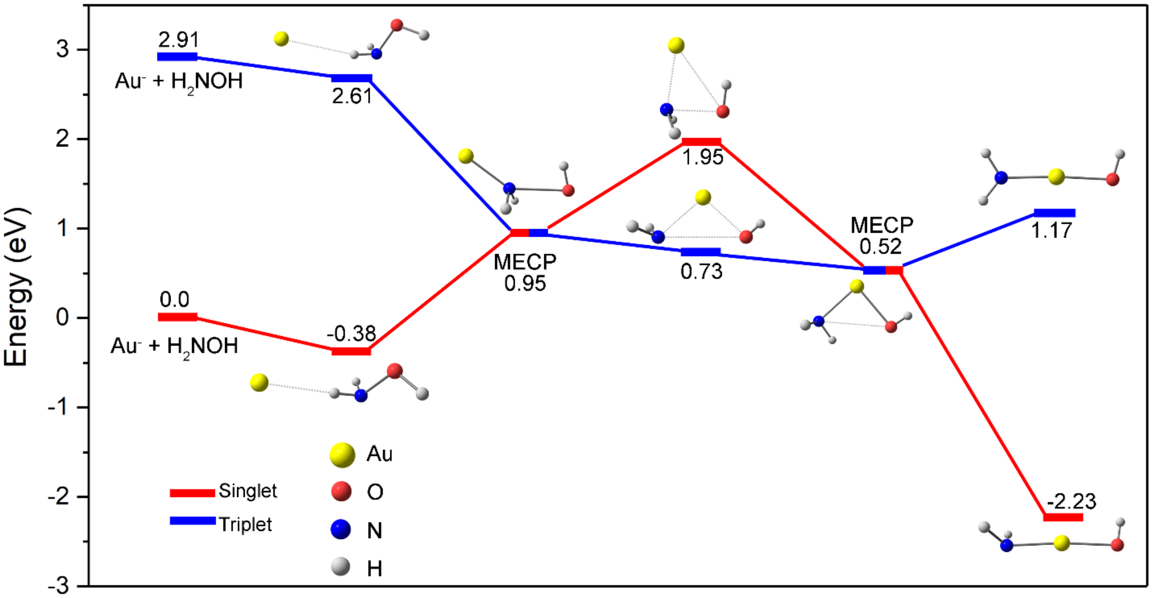

Figure III.B.7. Calculated reaction pathway for HA activation by Au$^-$. The numbers denote the relative energies of different structures.

transition states, where a crossover from the singlet to triplet surfaces occurs. This MECP is 0.95 eV higher than the entrance channel and 0.22 eV higher than the triplet transition state. Therefore, the highest barrier the reactants need to overcome is the first MECP rather than the triplet transition state. Once the first spin flip has occurred, the insertion of Au^- into the N-O bond is essentially barrier-free. After passing through the triplet transition state, where the N-O bond is significantly lengthened, the activation complex encounters a second MECP, which converts it back to singlet state and to the final H_2N-Au-OH^- product.

Usually gold anions are inert to the activation of molecules. Such inertness can be explained by its $d^{10}s^2$ ground state electron configuration: when a σ-bond is to be activated, the activating agent needs to have unpaired electrons, so that it can accept electrons from the bond to be activated. However, due to the lack of unpaired electrons in ground state Au^-, such electron transfer from the σ-bond to Au^- is prohibited. An atomic orbital hybridization, which usually includes electron promotion to the 6p orbital, is thus required. According to our TDDFT calculations, the energy needed for such promotion is around 2.9 eV, which is too high to surmount. In the present case, however, the interaction of Au^- with HA can reduce this promotion energy from 2.9 eV to 0.95 eV. As shown in Figure III.B.7, at the first MECP the $[Au(HA)]^-$ complex converts from its singlet state to its triplet state, suggesting the creation of two unpaired electrons and empty orbitals on Au moiety which can then accept the two σ electrons of the N-O bond.

The transition state is located 0.95 eV above the entrance channel, with a total activation energy of 1.33 eV (from the $Au^-(HA)$ complex). Under the thermal multi-collision conditions in the reaction cell, additional energy can be provided by collisions with the fastest He atoms in the Maxwell–Boltzmann distribution, thus making it likely to overcome such an energy barrier[56, 57].

In summary, we have demonstrated that a single gold atomic anion can activate a hydroxylamine molecule by breaking its N-O bond, inserting there, and forming the $H_2N-Au-OH^-$ complex. DFT calculations show that the spin crossover between singlet and triplet surfaces is critical for this activation to occur, as it creates the unpaired electrons and empty orbitals needed to accept the σ electron pair from the N-O bond.

Acknowledgements

This material is based on work supported by the Air Force Office of Scientific Research (AFOSR) and the National Science Foundation (NSF) under grant numbers, FA9550-15-1-0259 and CHE-1664182, respectively. We are also grateful for valuable discussions with Dr. Stefan Schneider, Dr. Steve Chambreau, Dr. Jerry Boatz, and Dr. Ghanshyam Vaghjian at Edwards Air Force Base, CA.

References

1. R. Amrousse, T. Katsumi, N. Azuma, and K. Hori, *Combust. Flame* **176**, 334 (2017).
2. NASA GPIM. https://www.nasa.gov/mission_pages/tdm/ green/overview.html (accessed January 12, 2017).
3. J. T. Cronin and T. B. Brill, *J. Phys. Chem*. **90**, 178 (1986).
4. T. B. Brill and T. P. Russell, *Proc. SPIE* 40 (1988).
5. J. T. Cronin and T. B. Brill, *Combust. Flame* **74**, 81 (1988).
6. T. B. Brill, P. D. Spohn, and J. T. Cronin, *J. Energ. Mater.* **8**, 75 (1990).
7. J. W. Schoppelrei and T. B. Brill, *J. Phys. Chem. A* **101**, 8593 (1997).
8. Y. J. Lee and T. A. Litzinger, *Combust. Sci. Technol.* **141**, 19 (1999).

9. H. Lee and T. A. Litzinger, *Combust. Flame* **127**, 2205 (2001).
10. H. Lee and T. A. Litzinger, *Combust. Flame* **135**, 151 (2003).
11. C. Kappenstein, L. Courtheoux, R. Eloirdi, S. Rossignol, D. Duprez, and N. Pillet, Catalytic Decomposition of HAN−Water Binary Mixtures, 38th AIAA/ASME/SAE/ASEE Joint Propulsion Conference & Exhibit, Joint Propulsion Conferences, American Institute of Aeronautics and Astronautics: Reston, VA, 2002.
12. L. Courtheoux, D. Amariei, S. Rossignol, and C. Kappenstein, *Appl. Catal. B* **62**, 217 (2006).
13. D. Amariei, L. Courtheoux, S. Rossignol, and C. Kappenstein, *Chem. Eng. Process.* **46**, 165 (2007).
14. S. Banerjee, S. A. Shetty, M. N. Gowrav, C. Oommen, and A. Bhattacharya, *Surf. Sci.* **653**, 1 (2016).
15. C. Oommen, S. Rajaraman, R. A. Chandru, and R. Rajeev, *IPCBEE* **10**, 205 (2011).
16. R. Amrousse, K. Hori, W. Fetimi, and K. Farhat, *Appl. Catal., B* **127**, 121 (2012).
17. R. Amrousse, T. Katsumi, N. Itouyama, N. Azuma, H. Kagawa, K. Hatai, H. Ikeda, and K. Hori, *Combust. Flame* **162**, 2686 (2015).
18. R. Amrousse, T. Katsumi, Y. Niboshi, N. Azuma, A. Bachar, and K. Hori, *Appl. Catal. A* **452**, 64 (2013).
19. S. D. Chambreau, D. M. Popolan-Vaida, G. L. Vaghjiani, and S. R. Leone, *J. Phys. Chem. Lett*. **8**, 2126 (2017).
20. H. Schwarz, P. Gonzalez-Navarrete, J. Li, M. Schlangen, X. Sun, T. Weiske, and S. Zhou, *Organometallics* **36**, 8 (2017).

21. S. M. Lang, T. M. Bernhardt, V. Chernyy, J. M. Bakker, R. N. Barnett, and U. Landman, *Angew. Chem. Int. Ed*. **56**, 13406 (2017).
22. X. L. Ding, X.N. Wu, Y. X. Zhao, and S. G. He, *Acc. Chem. Res.* **45**, 382 (2012).
23. H. Schwarz, *Isr. J. Chem.* **54**, 1413 (2014).
24. Z. Luo, A. W. Castleman Jr., and S. N. Khanna, *Chem. Rev.* **116**, 14456 (2016).
25. D. K. Bohme and H. Schwarz, *Angew. Chem. Int. Ed.* **44**, 2336 (2005).
26. H. Schwarz, S. Shaik, and J. Li, *J. Am. Chem. Soc.* **139**, 17201 (2017).
27. X. N. Li, X. P. Zou, and S. G. He, *Chinese Journal of Catalysis* **38**, 1515 (2017).
28. S. Zhou, J. Li, M. Schlangen, and H. Schwarz, *Acc. Chem. Res.* **49**, 494 (2016).
29. J. Roithova and D. Schröder, *Chem. Rev.* **110**, 1170 (2010).
30. T. M. Bernhardt, *Int. J. Mass Spec.* **243**, 1 (2005).
31. J. M. Weber, Gas Phase Chemistry of Gold Organogold Compounds, PATAI'S Chemistry of Functional Groups, 2014.
32. S. Zhou, J. Li, X. N. Wu, M. Schlangen, and H. Schwarz, *Angew. Chem. Int. Ed*. **55**, 441 (2016).
33. C. Geng, J. Li, T. Weiske, M. Schlangen, S. Shaik, and H. Schwarz, *J. Am. Chem. Soc*. **139**, 1684 (2017).
34. J. Li, S. Zhou, M. Schlangen, T. Weiske, and H. Schwarz, *Chem. Select* **3**, 444 (2016).
35. A. P. Woodham, G. Meijer, and A. Fielick, *Angew. Chem. Int. Ed.* **51**, 4444 (2012).
36. R. Pal, L. M. Wang, Y. Pei, L. S. Wang, and X. C. Zeng, *J. Am. Chem. Soc.* **134**, 9438 (2012).
37. R. F. Hockendorf, Y. Cao, and M. K. Beyer, *Organometallics* **29**, 3001 (2010).
38. W. Huang, H. J. Zhai, and L. S. Wang, *J. Am. Chem. Soc.* **132**, 4344 (2010).

39. Y. Gao, W. Huang, J. Woodford, L. S. Wang, and X. C. Zeng, *J. Am. Chem. Soc*. **131**, 9484 (2009).

40. H. J. Zhai, C. Burgel, V. Bonacic-Koutecky, and L. S. Wang, *J. Am. Chem. Soc*. **130**, 9156 (2008).

41. W. Zheng, X. Li, S. Eustis, A. Grubisic, O. Thomas, H. de Clercq, and K. Bowen, *Chem. Phys. Lett*. **444**, 232 (2007).

42. Y. Gao and X. C. Zeng, *ACS Catal.* **2**, 2614 (2012).

43. X. Zhang, E. Lim, S. K. Kim and K. H. Bowen, *J. Chem. Phys.* **143**, 174305 (2015).

44. B. J. Knurr and J. M. Weber, *J. Am. Chem. Soc*. **134**, 18804 (2012).

45. X. Zhang, G. Liu, G. Ganteför, K. H. Bowen, and A. N. Alexandrova, *J. Phys. Chem. Lett*. **5**, 1596 (2014).

46. J. Ho, K. M. Ervin, and W. C Lineberger, *J. Chem. Phys*. **93**, 6987 (1990).

47. G. Liu, S. Ciborowski, and K. Bowen, *J. Phys. Chem. A* **121**, 5817 (2017).

48. F. Neese, *WIREs Comput. Mol. Sci*. **2**, 73 (2012).

49. J. P. Perdew, M. Ernzerhof, and K. Burke, *J. Chem. Phys.* **105**, 9982 (1996).

50. J. P. Perdew, K. Burke, and M. Ernzerhof, *Phys. Rev. Lett.* **77**, 3865 (1996).

51. S. Grimme, J. Antony, S. Ehrlich, and H. Krieg, *J. Chem. Phys.* **132** (2010) DOI: 10.1063/1.3382344.

52. F. Neese, F. Wennmohs, A. Hansen, and U. Becker, *Chem. Phys.* **356**, 98 (2008).

53. F. Weigend and R. Ahlrichs, *Phys. Chem. Chem. Phys.* **7**, 3297 (2005).

54. D. Andrae, U. Häußermann, M. Dolg, H. Stoll, and H. Preuß, *Theor. Chim. Acta* **77**, 123 (1990).

55. J. N. Harvey, M. Aschi, H. Schwarz, and W. Koch, *Theo. Chem. Acc*. **99**, 95 (1998).

56. X. Zhang, G. Liu, K. Meiwes-Broer, G. Ganteför, and K. Bowen, *Angew. Chem. Int. Ed. Engl.* **55**, 9644 (2016).

57. S. M. Lang, T. M. Bernhardt, V. Chernyy, J. M. Bakker, R. N. Barnett, and U. Landman, *Angew. Chem. Int. Ed*. **56**, 13406 (2017).

III.B.3. Water Activation and Splitting by Single Metal-Atom Anions

Gaoxiang Liu, Evangelos Miliordos, Sandra M. Ciborowski, Martin Tschurl, Ulrich Boesl, Ulrich Heiz, Xinxing Zhang, Sotiris Xantheas, and Kit Bowen

Reprinted from *J. Chem. Phys.* 149, 221101 (2018); DOI: 10.1063/1.5050913, with the permission of AIP Publishing.

III.B.3.a. Abstract

We report experimental and computational results pertaining to the activation and splitting of single water molecules by single atomic platinum anions. The anion photoelectron spectra of $[Pt(H_2O)]^-$, formed under different conditions, exhibit spectral features that are due to the anion-molecule complex, $Pt^-(H_2O)$, and to the reaction intermediates, $HPtOH^-$ and H_2PtO^-, in which one and two O-H bonds have been broken, respectively. Additionally, the observations of PtO^- and H_2^+ in mass spectra strongly imply that water splitting via the reaction $Pt^- + H_2O \rightarrow PtO^- + H_2$ has occurred. Extending these studies to nickel and palladium shows that they too are able to activate single water molecules, as evidenced by the formation of the reaction intermediates, $HNiOH^-$ and $HPdOH^-$. Computations at the CCSD(T) level of theory provide structures and vertical detachment energies (VDE) for both $HMOH^-$ and H_2MO^- intermediates. The calculated and measured VDE values are in good agreement and thus support their identification.

III.B.3.b. Introduction

Water splitting holds great promise as a source of clean, abundant fuel[1-5]. While electrolysis is effective, its cost is exceedingly high. Likewise, the direct cleavage of water's O-H bond is energetically prohibitive (497.1 kJ/mol)[6]. The solution to this problem is generally thought to lie in catalytic water splitting, a process which depends critically on the activation of water molecules. A variety of molecular and cluster catalysts are known to be effective in aqueous media[7,8], on surfaces[9,10], and in gas phase environments[11,12]. Single-atom catalysts provide yet another approach. While single-atom catalysts have been found to facilitate water splitting on surfaces[13-16], water activation and splitting by single atoms in the gas phase has gone virtually unexplored. Here, we investigate this topic, addressing both water activation and water splitting by single metal atomic anions.

We had originally been inspired by experiments in which sub-nano-size platinum clusters deposited onto semiconductor nano-rods and submerged in water were found to be effective water splitting photocatalysts[17-19]. There, the overall catalytic process was $H_2O + Pt_n^- = \frac{1}{2} H_2 + Pt_n + OH^-$. Rather than studying water activation by platinum *cluster* anions, however, we chose to focus on the simplest set of relevant reactants, i.e., a *single* water molecule, a *single* metal atom (M), and a *single* excess electron (e^-), all interacting together within the sub-nano crucible of gas phase $[M(H_2O)]^-$ cluster anions. By extending these studies beyond platinum to include nickel and palladium, as well as several other transition metal atoms, we explored the activation and splitting of single water molecules by single, atomic metal anions. Our joint experimental and theoretical effort has resulted in strong evidence for both water activation and water splitting by single atomic platinum anions and for water activation (but without splitting) by single nickel and palladium anions.

III.B.3.c. Results and Discussions

Experimental studies of $[Pt(H_2O)]^-$ were conducted using a laser vaporization ion source, time-of-flight (TOF) mass spectrometry, and anion photoelectron spectroscopy[20]. Source details are presented in the supplementary materials (SM). The left panels in Figure III.B.8 present the mass spectra of the $[Pt(H_2O)]^-$ mass region along with the expected isotopic mass distribution pattern of $[Pt(H_2O)]^-$ in its top panel. Mass spectra, **A**, **B**, and **C**, show the effect of increasing the vaporization laser power in three steps (6, 8 and 11 mJ). Note that mass peaks due to PtO^- appeared and became stronger with increasing power. Control experiments without water, but under the same vaporization laser power conditions, did not result in the formation of PtO^- (Figure S1), suggesting that PtO^- had formed as a result of the reaction between Pt^- and H_2O. The identities of the two putative PtO^- mass peaks (m = 210 and 211) were confirmed by measuring their anion photoelectron spectra (see Figure S2) and comparing them to a previous report[21]. The fact that the anion photoelectron spectra at these two masses were identical also indicates that no $PtOH^-$ was present in the beam, since it would have appeared at m = 211.

The top panel on the right side of Figure III.B.8 presents the photoelectron spectrum of the platinum atomic anion, Pt^-. This spectrum is presented for reference and agrees with previous reports[22]. The lower three panels on the right side of Figure III.B.8 exhibit anion photoelectron spectra of $[Pt(H_2O)]^-$, i.e., **a**, **b**, and **c**, where in each case the subject $[Pt(H_2O)]^-$ species had been generated under the same laser vaporization (source) power conditions that had been used to measure their corresponding mass spectra, **A**, **B**, and **C**, respectively. All $[Pt(H_2O)]^-$ spectra were taken at mass = 216 to ensure that the photoelectron signals were solely from $[Pt(H_2O)]^-$. These three photoelectron spectra of $[Pt(H_2O)]^-$ clearly differ substantially from one another, strongly suggesting the presence of $[Pt(H_2O)]^-$ isomers, whose generation depended on laser vaporization (source) power. As will be explained below, the anion photoelectron spectra: **a**, **b**, and **c**, have been labeled with the identities of their $[Pt(H_2O)]^-$ isomers.

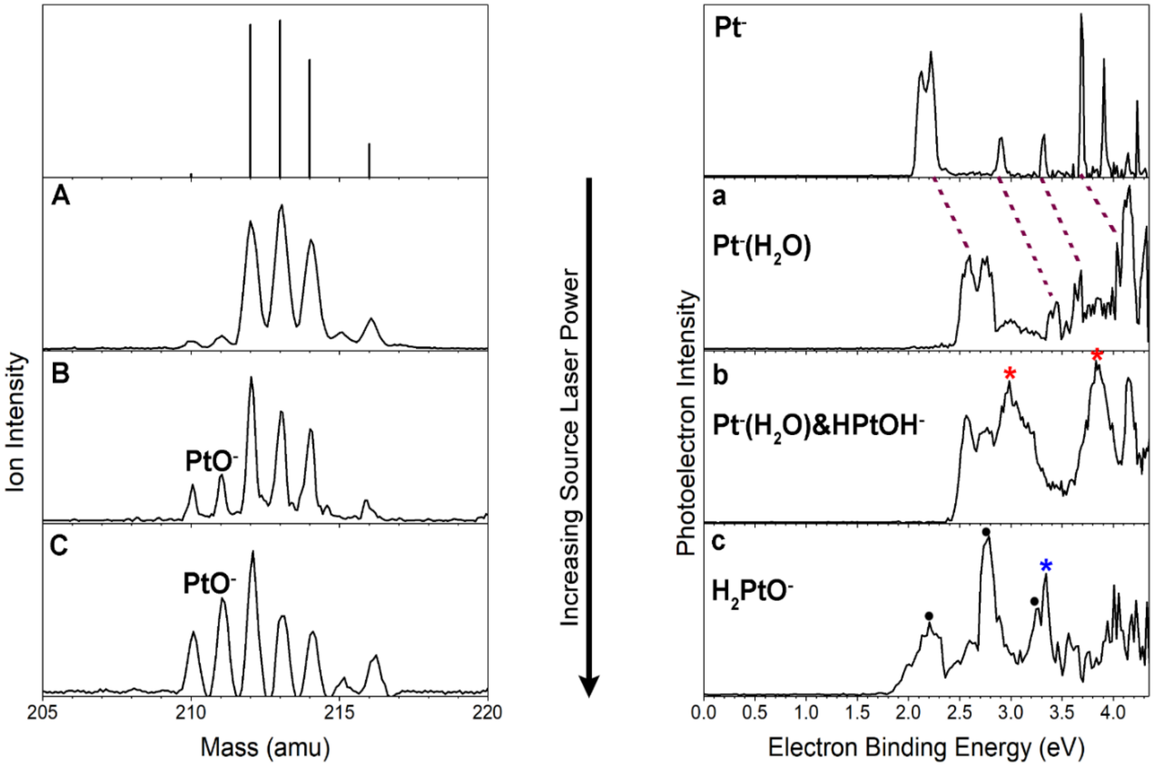

Figure III.B.8. THE TOP LEFT PANEL PRESENTS A STICK MASS SPECTRUM SHOWING THE SIMULATED ISOTOPIC MASS DISTRIBUTION OF $[Pt(H_2O)]^-$. THE PANELS BELOW IT SHOW THE MASS SPECTRA OF $[Pt(H_2O)]^-$ SPECIES FORMED UNDER THREE DIFFERENT LASER VAPORIZATION POWER SOURCE CONDITIONS; MASS SPECTRUM A WAS RECORDED UNDER LOW VAPORIZATION LASER POWER, B UNDER MODERATE VAPORIZATION LASER POWER, AND C UNDER HIGH VAPORIZATION LASER POWER. IN ALL CASES, LASER VAPORIZATION WAS CARRIED OUT USING THE SECOND HARMONIC (2.33 EV/PHOTON) OF A ND:YAG LASER. THE TOP RIGHT PANEL PRESENTS THE ANION PHOTOELECTRON SPECTRUM OF THE Pt^- ATOMIC ANION. THE PANELS BELOW IT SHOW THE ANION PHOTOELECTRON SPECTRA OF $[Pt(H_2O)]^-$ SPECIES: A, B, AND C, WHERE IN EACH CASE THE $[Pt(H_2O)]^-$ ANIONS HAD BEEN GENERATED UNDER THE SAME LASER VAPORIZATION POWER CONDITIONS USED TO RECORD THEIR CORRESPONDING MASS SPECTRA, A, B, AND C, RESPECTIVELY. IN ALL CASES, THE ANION PHOTOELECTRON SPECTRA WERE MEASURED USING THE FOURTH HARMONIC (4.66 EV/PHOTON) OF A ND:YAG LASER.

Potentially, the anionic metal-water complex, $[M(H_2O)]^-$, could exist in three different structures: (*i*) one in which M^- is "solvated" by a physisorbed water molecule, resulting in $M^-(H_2O)$, (*ii*) a structure where one of the O-H bonds in H_2O has been broken, resulting in $HMOH^-$, and (*iii*) a structure in which both O-H bonds in H_2O have been broken, resulting in H_2MO^-. As we will show, all three of these structural isomers were found to exist in the ion beam. The anionic complexes that result from one or both O-H bonds having been broken and the detached atom(s) having been reattached are water activation products. These activated species are *intermediates* along the reaction pathway that leads to H_2 formation, i.e., water splitting.

We utilized anion photoelectron spectroscopy to distinguish between these isomers.[23] Typically, when weak physisorption ("solvation") interactions occur between an anion and a water molecule, i.e., in anion-molecule complexes, the photoelectron spectral pattern of the resulting hydrated anion closely resembles that of the anion alone, except for it having been shifted to slightly higher electron binding energy (EBE) values and its features broadened. This is because M^- remains the chromophore for photodetachment; no truly chemical interactions have occurred. Photoelectron spectrum, **a**, on the right side of Figure III.B.8 is an example of such an interaction. Its spectrum displays the same spectral pattern as the photoelectron spectrum of Pt^-, which sits above it in Figure III.B.8, except for its peaks being slightly blue-shifted and broadened. The $[Pt(H_2O)]^-$ isomer in photoelectron spectrum, **a**, is thus seen to be the platinum atomic anion-water "solvation" complex, $Pt^-(H_2O)$.

At higher laser vaporization (source) power, PtO^- begins to appear in mass spectrum, **B** of Figure III.B.8. Photoelectron spectrum, **b**, exhibits both the hydrated anion spectral peaks of spectrum, **a**, as well as new features, the most prominent of which are marked with red stars at EBE values of 2.98 eV and 3.83 eV. This new feature is due to another (a second) isomer.

At still higher laser vaporization (source) power, mass peaks due to PtO^- in mass spectrum **C** have become even stronger. In its corresponding anion photoelectron spectrum, i.e., **c**, the peaks due to the solvated anion, $Pt^-(H_2O)$, have completely disappeared, and four new peaks have appeared. One of them, marked with a blue star at EBE = 3.34 eV, is due to yet another, i.e., a third, isomer of $[Pt(H_2O)]^-$, while the other three peaks, marked with black dots, exhibit EBE values that are identical to those in the photoelectron spectrum of PtO^- [see Figure S2 and Ref. 21]. There are two possible explanations for the appearance of the PtO^- photoelectron spectrum within photoelectron spectrum, **c**. (1) These peaks may have arisen due to two-photon processes, in which the first photon dissociated the newly-formed, third $[Pt(H_2O)]^-$ isomer, producing PtO^-, while a second photon photodetached an electron from PtO^-. (2) Due to the relatively high source-laser power being used in this case, another possibility is that metastable $[Pt(H_2O)]^-$ was formed in the source, and that it dissociated along the time-of-flight drift path, resulting in PtO^-, which continued to travel at the velocity of the TOF-extracted $[Pt(H_2O)]^-$ anions into the photodetachment region.[24] Since photoelectron spectrum, **c**, was taken at the unambiguous mass of $[Pt(H_2O)]^-$, this evidence alone implies that the newly-formed (third) isomer in photoelectron spectrum, **c,** must have been H_2PtO^-, and that the other fragment must have been H_2. Together, anion photoelectron spectra: **a**, **b**, and **c**, thus revealed the presence of three structural isomers of $[Pt(H_2O)]^-$, the hydrated Pt^- anion complex and two others, both of which involved O-H bond breaking.

Normally, the neutral products of a gas-phase reaction can only be indirectly deduced by counting the atom difference between reactants and charged products. Here, however, to search for the presence of H_2, which had been implied by our observations, we utilized an electron bombardment ionizer located along the beam path between the source and the TOF ion extractor. There, we changed appropriate voltages and polarities in order to record positive ion mass spectra, so that neutral H_2 could be ionized to H_2^+ and observed by our mass spectrometer. Nevertheless, when the laser vaporization (source) power was low, no H_2^+ was seen. The only cations that we observed were He^+, O^+, OH^+ and H_2O^+ as seen in Figure III.B.9 (i); all of which had formed due to ionization of H_2O/He backing gases from the source. However, when the laser power was increased to the level used to record mass spectrum, **C**, H_2^+ was detected as shown in Figure III.B.9 (ii). This observation provided direct evidence that a single platinum atomic anion reacting with a single water molecule had produced H_2.

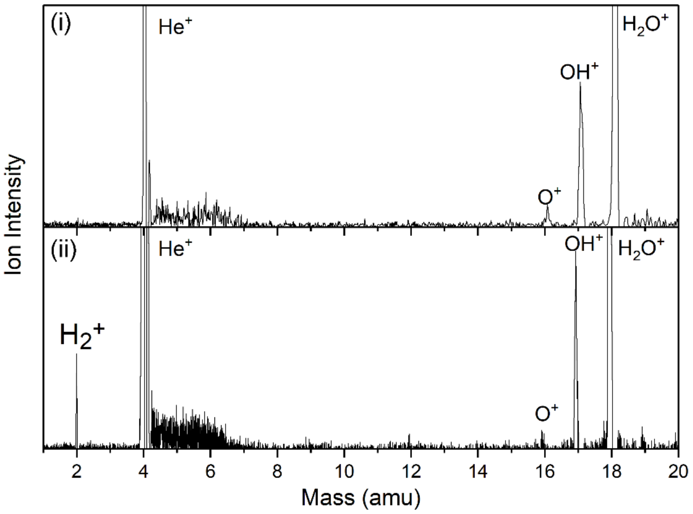

Figure III.B.9. POSITIVE ION, ELECTRON BOMBARDMENT IONIZATION MASS SPECTRA OF THE SPECIES MADE UNDER LOW VAPORIZATION LASER POWER, (I), AND HIGH VAPORIZATION LASER POWER, (II).

The photoelectron spectra of $[Pt(H_2O)_2]^-$ and $[Pt(H_2O)_3]^-$ are presented in Figure S3. The absence of new features in these spectra suggests that when Pt^- reacts with either a water dimer or trimer, it only interacts with a single water molecule, while the other water molecule(s) just solvate the $[Pt(H_2O)^-]$.

Parallel experimental studies were also conducted on $[Ni(H_2O)]^-$ and $[Pd(H_2O)]^-$. Their experimental mass spectra are presented in Figure S4, along with their expected isotopic mass distributions. Unlike in the case of $[Pt(H_2O)]^-$, neither NiO^- nor PdO^- was observed even at elevated source laser powers. Additionally, no H_2^+ was observed in either of these cases, indicating that H_2 was not formed. Figure III.B.10 presents the anion photoelectron spectra of $[Ni(H_2O)]^-$ and $[Pd(H_2O)]^-$, along with those of their corresponding atomic anions, Ni^- and Pd^-. As in anion photoelectron spectrum, **b**, in the

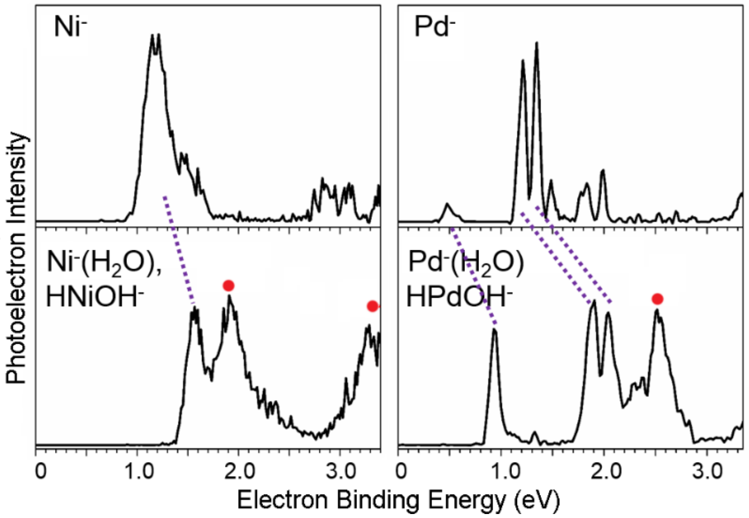

Figure III.B.10. PHOTOELECTRON SPECTRA OF THE ATOMIC METAL ANIONS, M^-, (IN THE UPPER PANELS) AND THEIR CORRESPONDING $[M(H_2O)]^-$ ANIONS (IN THE LOWER PANELS), WHERE M = NI AND PD. ALL OF THESE ANION PHOTOELECTRON SPECTRA WERE MEASURED USING THE THIRD HARMONIC (3.49 EV/PHOTON) OF A ND:YAG LASER. DOTTED TIE-LINES LINK M^- PEAKS TO THE CORRESPONDING BLUE-SHIFTED PEAKS IN THEIR $M^-(H_2O)$ ANION-MOLECULE COMPLEXES. ADDITIONAL STRUCTURAL ISOMERS ARE MARKED BY RED DOTS.

case of $[Pt(H_2O)]^-$, the photoelectron spectra of $[Ni(H_2O)]^-$ and $[Pd(H_2O)]^-$ exhibit spectral features that are due both to the solvated anion complexes, $Ni^-(H_2O)$ and $Pd^-(H_2O)$, and to additional structural isomers, these being marked by red dots in Figure III.B.10. As will be explained below, the anion photoelectron spectra of $[Ni(H_2O)]^-$ and $[Pd(H_2O)]^-$ have been labeled with the identities of their isomers.

In addition to measuring the anion photoelectron spectra of $[M(H_2O)]^-$, where M = Pt, Ni, and Pd, we also measured the photoelectron spectra of $[M(H_2O)]^-$, where M = Cu, Ag, Au, Fe, Co, and V. These latter $[M(H_2O)]^-$ species were formed utilizing the same source laser power protocol used to make $[Ni(H_2O)]^-$ and $[Pd(H_2O)]^-$ and photoelectron spectrum, **b**, in the case of $[Pt(H_2O)]^-$. The anion photoelectron spectra of $[M(H_2O)]^-$, where M = Cu, Ag, Au, Fe, Co, and V, are displayed along with their atomic anion photoelectron spectra in Figure S5. All of them are simple anion-molecule (physisorbed) complexes, i.e., $M^-(H_2O)$. It is important to note that none of them showed any photoelectron spectral features beyond those expected for an anion-molecule complex.

The details of our computational methods are presented in the SM section. Briefly, to assess the potential multi-reference nature of $[M(H_2O)]^-$ and its neutral counterparts, we initially relied on the internally-contracted Multi-Reference Configuration Interaction (icMRCI) level of theory. The resultant mainly single reference character implied by those icMRCI calculations allowed us to employ the size-extensive, Coupled Cluster Singles and Doubles with perturbatively connected Triples [CCSD(T)] approach to calculate vertical detachment energies (VDE), where VDE is the vertical energy difference between an anion's ground state and its neutral counterpart at the structure of the anion.

The EBE values of the peak maxima in the photoelectron spectra are their VDE values. We have calculated VDE values for both $HMOH^-$ and H_2MO^- isomers (M = Pt, Ni, Pd) and compared them with the measured VDE values of the new spectral features. These are presented in Table III.B.2. For the $HMOH^-$ isomer, good agreement was obtained between experimental and calculated VDE values, indicating that the water-activated isomers: $HPtOH^-$, $HNiOH^-$, and $HPdOH^-$, were all present in their respective ion beams.

As for the H_2MO^- isomer, there is strong evidence for the presence of H_2PtO^- in photoelectron spectra of $[Pt(H_2O)]^-$. The peak at EBE = 3.34 eV in anion photoelectron spectrum, **c**, is in good agreement with the theoretically-calculated EBE values of 3.40 eV and 3.45 eV. The high intensity of PtO^- in its corresponding mass spectrum, i.e., **C**, the appearance of the photoelectron spectrum of PtO^- within the mass-selected photoelectron spectrum of $[Pt(H_2O)]^-$, and the observation of H_2^+, all under relatively high source laser powers, are consistent with the presence of H_2PtO^- and with its decay into PtO^- and H_2. However, the case for the presence of H_2PtO^- at moderate source laser powers is less clear.

While mass spectrum, **B**, exhibits PtO^-, although at relatively lower intensities than does mass spectrum, **C**, and while traces of H_2^+ are detected under moderate source laser power conditions, the theoretically-predicted telltale H_2PtO^- peak at EBE ~ 3.4 eV, easily seen in photoelectron spectrum **c**, was not evident in photoelectron spectrum, **b**. Instead, the EBE ~ 3.4 eV region in photoelectron spectrum, **b**, is an intensity valley, although its floor does exhibit considerable intensity. Also, the PtO^- peaks seen in photoelectron spectrum, **c**, are absent in photoelectron spectrum, **b**. We conclude that if H_2PtO^- is formed under moderate source laser power conditions, there must be much less of it made than under higher laser power conditions. Additionally, Table III.B.2 and Figure III.B.10

provide no significant evidence for the presence of H_2NiO^- and H_2PdO^- isomers in the beam. Also, since neither NiO^-, PdO^-, nor H_2^+ were observed in $[Ni(H_2O)]^-$ and $[Pd(H_2O)]^-$ experiments, even at high source laser powers, the implication is that they were not formed.

TABLE III.B.2. EXPERIMENTALLY-DETERMINED VDE VALUES FOR $[Pt(H_2O)]^-$, $[Ni(H_2O)]^-$, AND $[Pd(H_2O)]^-$ COMPARED WITH THE COMPUTED CCSD(T)/AUG-CC-PVTZ VDE VALUES. IN THE CASE OF $[Pt(H_2O)]^-$, EXPERIMENTALLY-MEASURED VDE VALUES FOR THE ISOMER FEATURES FOUND IN PHOTOELECTRON SPECTRUM, **B**, ARE LABELED SEPARATELY FROM THAT OF THE ISOMER FEATURE FOUND IN PHOTOELECTRON SPECTRUM, **C**. EXPERIMENTALLY-DETERMINED VDE VALUES FOR THE HYDRATED-ANION COMPLEXES (ISOMERS), $Pt^-(H_2O)$, $Ni^-(H_2O)$, AND $Pd^-(H_2O)$, ARE NOT INCLUDED IN THIS TABLE.

	Theoretical VDE (eV)					Expt. VDE (eV)
$HPtOH^-$	$^2A \rightarrow {}^3A$	3.02	H_2PtO^-	$^2B_1 \rightarrow {}^3B_1$	3.45	2.98 ***b***
	$^2A \rightarrow {}^1A$	3.01		$^2B_1 \rightarrow {}^1A_1$	3.40	3.34 ***c***
	$^2A \rightarrow 2^3A$	3.70				3.83 ***b***
$HNiOH^-$	$^2A \rightarrow {}^3A$	1.81	H_2NiO^-	$^2B_1 \rightarrow {}^3B_1$	2.75	1.91
	$^2A \rightarrow {}^1A$	3.04		$^2B_1 \rightarrow {}^1A_1$	2.43	3.24
$HPdOH^-$	$^2A \rightarrow {}^3A$	2.64	H_2PdO^-	$^2B_1 \rightarrow {}^3B_1$	2.49	2.50
	$^2A \rightarrow {}^1A$	2.37		$^2B_1 \rightarrow {}^1A_1$	3.20	

High level electronic structure calculations provide insight into the reaction mechanisms and detailed rationalizations of the similarities and differences between the different metal anions. Figure III.B.11 shows the calculated potential energy pathways and key structures involved in the reactions of Ni^-, Pd^-, and Pt^- atomic anions with a single water molecule. The coordinates and energies of these structures are provided in the SM section. For example, Figure III.B.11 provides a possible explanation for why only H_2PtO^-

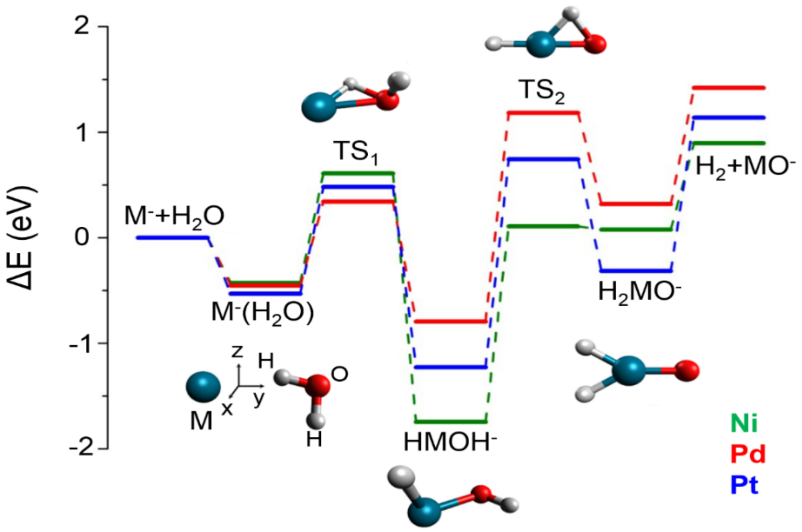

Figure III.B.11. The calculated potential energy pathways and stationary points involved in the reactions of Ni^-, Pd^-, and Pt^- with a single water molecule, H_2O. Zero-point vibrational and spin-orbit corrections are also included.

was formed among the three Group 10 systems we studied. Figure III.B.11 shows that only H_2PtO^- is definitively exothermic relative to $M^- + H_2O$.

Unlike the conversion of $M^+(H_2O)$ cationic complexes to $HMOH^+$ (M = Pd, Pt), which according to theory is endothermic[25], the transformation from $M^-(H_2O)$ anionic complexes to $HMOH^-$ is exothermic in all three (M = Ni, Pd, Pt) cases shown in Figure III.B.11. The transition state, TS_1, however, is higher in energy than the energies of both $M^- + H_2O$ and $M^-(H_2O)$ in all three cases. The barrier to be overcome is ~0.5 eV, i.e., the energy of TS_1 minus the energy of the reactants, $M^- + H_2O$ or ~1.0 eV, the energy of TS_1 minus the energy of $M^-(H_2O)$. These computed barriers include zero-point vibrational and spin-orbit corrections. Many reactions are known to proceed with barrier heights that are similar to these values.[26-29]

Let's further consider our results when the highest source-laser power was utilized, i.e., see panels **C** and **c** in Figure III.B.8. Under those circumstances, excess energy was available to the system, and in the case of H_2PtO^-, the excess energy was used both to make it and to drive the reaction to the final products, PtO^- and H_2. The excess energy is also likely responsible for the formation of metastable H_2PtO^- complexes, these having been discussed above. While the origin of the excess energy that became available under these high source-laser power conditions is not fully resolved, the options are thermal, electronic excitation, or both.

III.B.3.d. Conclusion

To summarize, we have investigated water activation and splitting by various single atomic anions, which were not previously explored in the gas phase. We demonstrated that platinum is special among all investigated metals, and that a single platinum atomic anion can both activate and split a single water molecule, while single palladium and nickel atomic anions only activate water molecules.

In the electrolysis of water, bubbles of H_2 gas form at the cathode, which is typically platinum, while bubbles of O_2 form at the anode. It is interesting to contemplate the relationship between the microscopic interaction between a single platinum atom, a single electron, and a single water molecule and the more complicated, macroscopic interaction between a platinum cathode and liquid water during electrolysis. Respectively, both processes involve surmountable energy barriers and low over-potentials, characteristically exceptional properties of platinum.

Supporting Information

Detailed experimental and theoretical methods. Supporting experimental and theoretical results inlcluding Table S1-S11 and Figures S1-S11.

Acknowledgements

The experimental part of this material is based on work supported by the (US) National Science Foundation (NSF) under grant number, CHE-1664182 (KHB) and by the Air Force Office of Scientific Research (AFOSR) under grant number, FA9550-15-1-0259 (KHB). The computational part of this work (EM & SSX) was supported by the US Department of Energy, Office of Science, Office of Basic Energy Sciences, Division of Chemical Sciences, Geosciences and Biosciences. Pacific Northwest National Laboratory (PNNL) is a multi-program national laboratory operated for DOE by Battelle. This research also used resources of the National Energy Research Scientific Computing Center, which is supported by the Office of Science of the U.S. Department of Energy under Contract No. DE-AC02-05CH11231.

References

1. D. G. Nocera, *Acc. Chem. Res*. **45**, 767 (2012).
2. K. Liu, Y. Liu, N. Liu, Y. Han, S. Lee, X. Zhang, J. Zhong, H. Huang, and Z. Kang, *Science* **347**, 970 (2015).
3. B. Rausch, M. D. Symes, G. Chisholm, and L. Cronin, *Science* **345**, 1326 (2014).
4. R. J. Roach, W. H. Woodward, A. W. Castleman Jr., A. C. Reber, and S. N. Khanna, *Science* **323**, 492 (2009).
5. M. D. Kärkäs, O. Verho, E. V. Johnston, and B. Åkermark, *Chem. Rev.* **114**, 11863 (2014).

6. J. A. Kerr, *Chem. Rev.* **66**, 465 (1966).
7. D. V. Gutsulyak, W. E. Piers, J. Borau-Garcia, and M. Parvez, *J. Am. Chem. Soc.* **135**, 11776 (2013).
8. J. Li and K. Yoshizawa, *Angew. Chem. Int. Ed.* **50**, 11972 (2011).
9. R. Subbaraman, D. Tripkovic, D. Strmcnik, K. C. Chang, M. Uchimura, A. P. Paulikas, V. Stamenkovic, and N. M. Markovic, *Science* **334**, 1256 (2011).
10. F. Jiao and H. Frei, *Angew. Chem. Int. Ed*. **48**, 1841 (2009).
11. J. Li, X. Wu, S. Zhou, S. Tang, M. Schlangen, and H. Schwarz, *Angew. Chem. Int. Ed.* **54**, 12298 (2015).
12. S. M. Lang, T. M. Bernhardt, M. Krstic, and V. M. Koutecky, *Phys. Chem. Chem. Phys.* **16**, 26578 (2014).
13. X. Yang, A. Wang, B. Qiao, J. Li, J. Liu, and T. Zhang, *Acc. Chem. Res*. **46**, 1740 (2013).
14. N. Cheng, S. Stambula, D. Wang, M. N. Banis, J. Liu, A. Riese, B. Xiao, R. Li, T. K. Shm, L. M. Liu, *et al* *Nature Comm.* **7**, 13638 (2016).
15. C. Ling, L. Shi, Y. Ouyang, X. C. Zeng, and J. Wang, *Nano Lett.* **17**, 5133 (2017).
16. J. Deng, H. Li, J. Xiao, Y. Tu, D. Deng, H. Yang, H. Tian, J. Li, P. Ren, and X. Bao, *Energy Environ. Sci.* **8**, 1594 (2015).
17. M. J. Berr, F. F. Schweinberger, M. Döblinger, K. E. Sanwald, C. Wolff, J. Breimeier, A. S. Crampton, C. J. Ridge, M. Tschurl, U. Heiz, U. *et al Nano Lett.* **12**, 5903 (2012).
18. K. Wu, H. Zhu, Z. Liu, W. Rodríguez-Córdoba, and T. Lian, *J. Am. Chem. Soc.* **134**, 10337 (2012).
19. L. Amirav, and A. P. Alivisatos, *J. Phys. Chem. Lett.* **1**, 1051 (2010).

20. X. Zhang, G. Liu, G. Ganteför, K. H. Bowen, and A. N. Alexandrova, *J. Phys. Chem. Lett.* **5**, 1596 (2014).
21. T. M. Ramond, G. E. Davico, F. Hellberg, F. Svedberg, P. Salén, P. Söderqvist, and W. C. Lineberger, *J. Mol. Spectrosc.* **216**, 1 (2002).
22. J. Thogersen, L. D. Steele, M. Scheer, C. A. Brodie, R. C. Bilodean, and K. Haugen, *J. Phys. B* **29**, 1323 (1996).
23. S. E. Eustis, D. Radisic, K. H. Bowen, R. A. Bachorz, M. Haranczyk, G. K. Schenter, and M. Gutowski, *Science* **319**, 936 (2008).
24. The fact that our mass spectra showed both PtO^- and H_2^+ as having been formed between the source and the TOF ion extractor under high source-laser power conditions also implies the formation of metastable H_2PtO^- species in the source region.
25. O. Lakuntza, J. M. Matxain, F. Ruipérez, J. N. Ugalde, and P. B. Armentrout, *Chem. Eur. J.* **19**, 8832 (2013).
26. A. Sanchez, S. Abbet, U. Heiz, W. D. Schneider, H. Hakkinen, R. N. Barnett, and U. Landman, *J. Phys. Chem. A* **103**, 9573 (1999).
27. H. Schwarz, *Angew. Chem. Int. Ed.* **54**, 10090 (2015).
28. S. M. Lang, T. Bernhardt, V. Chernyy, J. M. Hakker, R. N. Barnett, and U. Landman, *Angew. Chem. Int. Ed.* **56**, 13406 (2017).
29. X. Zhang, G. Liu, K. H. Meiwes-Broer, G. Gantefoer, and K. H. Bowen, *Angew. Chem. Int. Ed.* **55**, 9644 (2016).

III.B.4. The Metallo–Formate Anions, $M(CO_2)^-$, M = Ni, Pd, Pt, formed by Electron–Induced CO_2 Activation

Gaoxiang Liu, Sandra M. Ciborowski, Zhaoguo Zhu, Yinlin Chen, Xinxing Zhang, and Kit H. Bowen

Reproduced from *Phys. Chem. Chem. Phys.* 2019, 21, 10955; DOI: 10.1039/C9CP01915D, with permission from the PCCP Owner Societies.

III.B.4.a. Abstract

The metallo–formate anions, $M(CO_2)^-$, M = Ni, Pd, and Pt, were formed by electron–induced CO_2 activation. They were generated by laser vaporization and characterized by a combination of mass spectrometry, anion photoelectron spectroscopy, and theoretical calculations. While neutral transition metal atoms are normally unable to activate CO_2, the addition of an excess electron to these systems led to the formation of chemisorbed anionic complexes. These are covalently bound, formate–like anions, in which their CO_2 moieties are significantly reduced. In addition, we also found evidence for an unexpectedly attractive interaction between neutral Pd atoms and CO_2.

III.B.4.b. Introduction

The activation of carbon dioxide underpins its chemistry. Since the carbon atom in CO_2 is in its highest oxidation state, the activation of CO_2 inevitably involves reducing it, and that implies CO_2 accepting some degree of negative charge. Accomplishing this, however, requires at least a partial bending of CO_2. The CO_2^- anion that results from CO_2 having accepted a full negative charge is metastable; the electron affinity of CO_2 is –0.6 eV. While some studies have dealt with free carbon dioxide anions, most have focused on anionic complexes consisting of CO_2 and various other atoms and molecules.[1–43] Anion photoelectron studies of N–heterocycle–CO_2 heterogeneous anionic dimers by Kim *et al* showed significant covalent character in their intermolecular bond.[6,7] Subsequent work by Johnson *et al*[8] and by ourselves[9] added additional dimensions to this topic. In all cases, however, the CO_2 moieties were found to be partially negatively–charged and bent. Infrared photodissociation studies of transition metal–CO_2 anionic complexes by Weber *et al* further explored this topic.[10–23] Both electrostatically–bound, metal atom–multiple CO_2 anionic complexes (physisorption) and covalently–bound, metal atom–multiple CO_2 anionic complexes (chemisorption) were found. In the latter cases, the CO_2 moieties were partially bent and had accepted some significant portion of the negative charge, while in the former cases, the CO_2 were only very slightly bent, suggesting insignificant CO_2 activation. Calculations implied that the metal atoms were far away from the CO_2 moieties in the neutral complexes, and that their CO_2 moieties were structurally identical to isolated CO_2 molecules. Subsequent work in our laboratory measured the anion photoelectron spectra of copper–, silver–, and gold–CO_2 anionic dimers, finding only physisorption in the case of silver, i.e, $Ag^-(CO_2)$, only chemisorption in the case of copper, i.e., $Cu(CO_2)^-$, and both physisorbed and chemisorbed isomers for gold, i.e., $Au^-(CO_2)$ and $Au(CO_2)^-$, respectively.[24]

Here, we present our study of the Group 10 transition metal–CO_2 anionic complexes: $[Ni(CO_2)]^-$, $[Pd(CO_2)]^-$, and $[Pt(CO_2)]^-$, using anion photoelectron spectroscopy and theoretical calculations. In contrast to our previous work with the Group 11 coinage (s^1) metals, the Group 10 metals adopt richer outer electron shell configurations (d^8s^2 for Ni, d^{10} for Pd, and d^9s^1 for Pt) with significantly greater prospects for complex chemical bonding. Indeed, strong evidence for chemisorption was found in all three of the

Group 10 metal–CO_2 anionic complexes studied here, implying that Ni^-, Pd^- and Pt^- all activated CO_2 to form $Ni(CO_2)^-$, $Pd(CO_2)^-$, and $Pt(CO_2)^-$, respectively. Thus, all three of these Group 10 metal anions were seen to be able to both reduce and activate CO_2.

III.B.4.c. Methods

III.B.4.c.i. Experimental

Anion photoelectron spectroscopy is conducted by crossing a beam of mass–selected negative ions with a fixed–frequency photon beam and energy–analyzing the resultant photodetached electrons. The photodetachment process is governed by the energy–conserving relationship: $h\nu = \text{EBE} + \text{EKE}$, where $h\nu$ is the photon energy, EBE is the electron binding (photodetachment transition) energy, and EKE is the electron kinetic energy. Our apparatus consists of a laser vaporization cluster anion source, a time–of–flight mass spectrometer, a Nd:YAG photodetachment laser, and a magnetic bottle electron energy analyzer[44]. The photoelectron spectrometer resolution is ~35 meV at EKE = 1 eV. The third harmonic output of a Nd:YAG laser (355 nm) was used to photodetach electrons from mass–selected M^- and $[M(CO_2)]^-$ anions, where M = Ni, Pd, Pt. Photoelectron spectra were calibrated against the well–known atomic transitions of atomic Cu^-.[45] The $[M(CO_2)]^-$ (M = Ni, Pd, Pt) anion complexes were generated in a laser vaporization ion source. It consisted of rotating, translating nickel, palladium, or platinum rods, which were ablated with second harmonic (532 nm) photon pulses from a Nd:YAG laser, while 10%/90% He/CO_2 gas mixtures at 60 psi were expanded from a pulsed valve over the rods.

III.B.4.c.ii. Theoretical

Density functional theory calculations were performed with the ORCA computational chemistry software package.[46] All calculations were carried out with the

B3LYP functional[47] with the D3 dispersion correction[48] and the RIJCOSX approximation[49]. The Ahlrichs Def2 basis sets were used throughout our calculations[50]. For geometry optimization, Def2–TZVP and auxiliary Def2–TZVP/J basis sets[51] were chosen for carbon, oxygen and nickel atoms; the Stuttgart effective core potential SDD[52] and ECP basis set Def2–TZVP|Def2–TZVP/J were used for palladium and platinum atoms. The potential energy surfaces of neutral Ni, Pt-CO_2 along the M–C coordinate were computed by scanning the M–C bond length with a step width of 0.1 Å, while relaxing the rest of the cluster. Single–point calculations were then improved with Def2–QZVPP|Def2–QZVPP/J basis sets and all–electron relativistic calculations (ZORA). The structure of neutral $PdCO_2$ was also checked using the PBE0 and M06-L functionals.[53] The vertical detachment energy (VDE) is the energy difference between the ground state anion and its corresponding neutral at the geometry of the anion, i.e., these are vertical photodetachment transitions. The adiabatic detachment energy (ADE) is the energy difference between the lowest energy, relaxed geometry of the anion and the relaxed geometry of a structurally similar isomer (nearest minimum) of its neutral counterpart. The adiabatic electron affinity (EA) is the energy difference between the lowest energy, relaxed geometry of the anion and the relaxed geometry of the lowest energy isomer (the global minimum) of its neutral counterpart. When the nearest local minimum and the global minimum are one and the same, ADE = EA. In this work, we calculated ADE values. In the systems studied here, there is only one credible minimum for the neutral species, and it is therefore the global minimum. For that reason, we report ADE values as EA values here. Also, note that since the Franck–Condon principle governs which spectral features are seen within its anion–to–neutral wavefunction overlap window, there is often a correspondence between the lowest

EBE transition observed experimentally and the properly calculated ADE value. Franck-Condon simulation was performed for the $PdCO_2^-$ spectrum. This simulation, however, was not practical for $NiCO_2^-$ and $PtCO_2^-$ due to the large structural changes between anions and neutrals. Frequency calculations were performed to verify that no imaginary frequencies existed for any of the optimized structures.

III.B.4.d. Results and Discussion

The photoelectron spectra of $[M(CO_2)]^-$ (M = Ni, Pd, Pt) are presented in Figure III.B.12. For comparison, the atomic anion photoelectron spectra of Ni^-, Pd^-, and Pt^- are also presented above each $[M(CO_2)]^-$ spectrum there. In the anionic complexes, $[M(CO_2)]^-$, the CO_2 moiety can be either physisorbed or chemisorbed to M^-. For physisorbed complexes, the interaction between M^- and CO_2 is weak; they can be considered to be M^- anions "solvated" by CO_2 molecules, i.e., $M^-(CO_2)$. In physisorbed anion–molecule complexes such as these, their M^- anion moieties act as chromophores for photodetachment, with the resulting photoelectron spectra closely resembling the photoelectron spectral patterns of M^-, just shifted to higher electron binding energies (EBE) with their spectral features slightly broadened.[54,55] These shifts are typically a few tenths of an eV, corresponding approximately to ion–solvation stabilization energies. This spectral behavior provides a distinctive spectroscopic signature for physisorbed (solvated) anion complexes. The photoelectron spectra of $[Ni(CO_2)]^-$, $[Pd(CO_2)]^-$, and $[Pt(CO_2)]^-$, however, do not exhibit this behavior in relation to their atomic anion photoelectron spectra, i.e., Ni^-, Pd^-,and Pt^-. They are not physisorbed species. Moreover, their spectral shifts are far too large to be due to weak, solvation–like interactions. The spectral shifts between the lowest EBE features of the atomic anions and those of their corresponding

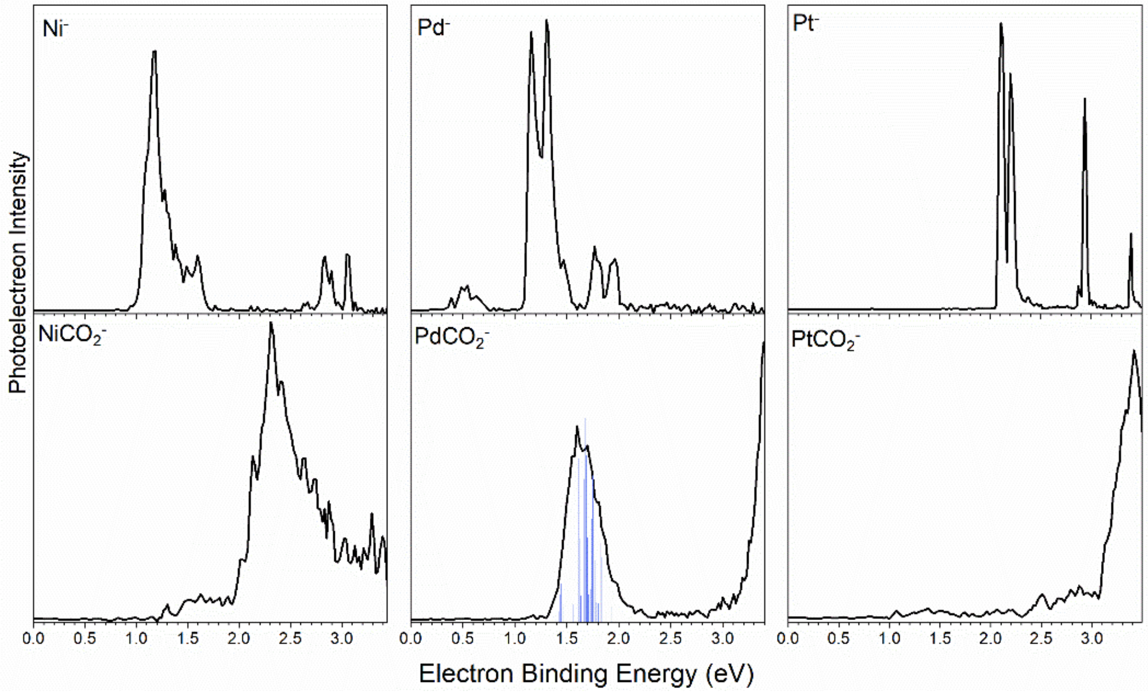

Figure III.B.12. Anion photoelectron spectra of Ni^- and $NiCO_2^-$, Pd^- and $PdCO_2^-$, and Pt^- and $PtCO_2^-$. The vertical lines in the $PdCO_2^-$ spectrum represent Franck-Condon simulated vibrational progression.

anionic complexes are about an electron volt. The anionic complexes studied here, i.e., $[Ni(CO_2)]^-$, $[Pd(CO_2)]^-$, and $[Pt(CO_2)]^-$, are chemisorbed complexes, i.e., $NiCO_2^-$, $PdCO_2^-$, and $PtCO_2^-$. Significant chemical interactions have occurred, resulting in bonds between the metal atoms and their CO_2 moieties.

Energetic parameters can also be determined from the spectra. When there is sufficient Franck–Condon overlap between the ground state of the anion and the ground state of the neutral, and when vibrational hot bands are absent, the threshold EBE (E_T) is the value of the electron affinity (EA). The E_T in $PdCO_2^-$ spectrum can be determined definitively. For $NiCO_2^-$ and $PdCO_2^-$, however, the relatively weak, shelf–like features on the low EBE side of the major peaks are likely hot bands. Thus, the E_T values for those two systems were determined by extrapolating the low EBE sides of their major peaks to baseline. In all three anionic complexes, the EBE values of the intensity maxima in their major peaks are their vertical detachment energy (VDE) values, corresponding to the transitions that have maximum Franck–Condon overlap between the ground electronic states of the anionic complexes and their neutral counterparts. The onset of the higher EBE feature in $PdCO_2^-$ spectrum is due to the vertical photodetachment transition from the ground state anion to its neutral counterpart in its first excited electronic state. The EA and VDE values of $NiCO_2^{0/-}$, $PdCO_2^{0/-}$, and $PtCO_2^{0/-}$ are listed in Table III.B.3.

TABLE III.B.3. EXPERIMENTAL AND THEORETICAL EA AND VDE VALUES FOR MCO_2 AND MCO_2^-, M = NI, PD, PT, RESPECTIVELY. ALL VALUES ARE IN EV.

	EA (Expt./Theo.)	VDE (Expt./Theo.)
$NiCO_2^{0/-}$	1.9/1.86	2.33/2.31
$PdCO_2^{0/-}$	1.3/1.10	1.60/1.57
$PtCO_2^{0/-}$	3.0/2.81	3.43/3.37

A synergy between theoretical calculations and anion photoelectron spectroscopy can provide insights into the structures, energetics and the nature of chemical bond of the investigated clusters.[55-61] The calculated structures of the anionic complexes and their corresponding neutrals are presented in Figure III.B.13. The first row shows the geomtries of the anionic complexes along with their respective HOMOs, while the second row provides the geometries of their neutral counterparts. The M–C bond length (Å), the C–O bond length (Å), and the O–C–O bond angle (in degrees) are shown for each case. For the chemisorption species, $NiCO_2^-$, $PdCO_2^-$, and $PtCO_2^-$, the M–C bond lengths are 2.01 Å, 2.03 Å, and 2.02 Å, respectively, suggesting the formation of single bonds between M and

C in all cases. The CO_2 moiety is significantly bent in all three anionic complexes, with an O–C–O bond angle of 138.26° for $NiCO_2^-$, 140.62° for $PdCO_2^-$ and 136.34° for $PtCO_2^-$, respectively. A natural population analysis shows that the CO_2 moieties in $NiCO_2^-$, $PdCO_2^-$, and $PtCO_2^-$ have negative charges of –0.75 *e*, –0.59 *e*, and –0.67 *e*, respectively. Thus, the CO_2 moiety has been significantly reduced in all of these anionic complexes. The O–C–O bond angles in all three systems are similar one another, as are the negative charges on their CO_2 moieties. The fact that they are not completely synchronized is likely due to the natural population analysis (NPA) being less reliable than the structural calculations. For the three anionic complexes, the C–O bond lengths are all between 1.22–1.23 Å, which is longer than the 1.16 Å C–O bond length in isolated CO_2 (1.16 Å). This implies that when negative charge is transferred to the CO_2 moiety, the C–O bond is elongated and weakened. Thus, $NiCO_2^-$, $PdCO_2^-$, and $PtCO_2^-$ all share a metallo–formate geometry. Furthermore, they are structurally quite similar in terms of M–C bond length, C–O bond length and O–C–O bond angle. Note that based on the calculated structures and charge distributions, Pd^- seems to have the weakest interaction with CO_2 of all three metal anions, although Pd has the lowest electron affinity which is expected to facilitate the charge transfer to the CO_2 moiety. One possible reason for Pd^- being the outlier is its electron configuration, $d_{10}s$, which is different to that of Ni^- and Pt^-, d_9s_2. The calculated EA and VDE values are listed in Table III.B.3 along with their corresponding experimental values. Excellent agreement between experimental and theoretical values, is seen for all three anionic complexes, validating the geometry optimizations shown in Figure III.B.13.

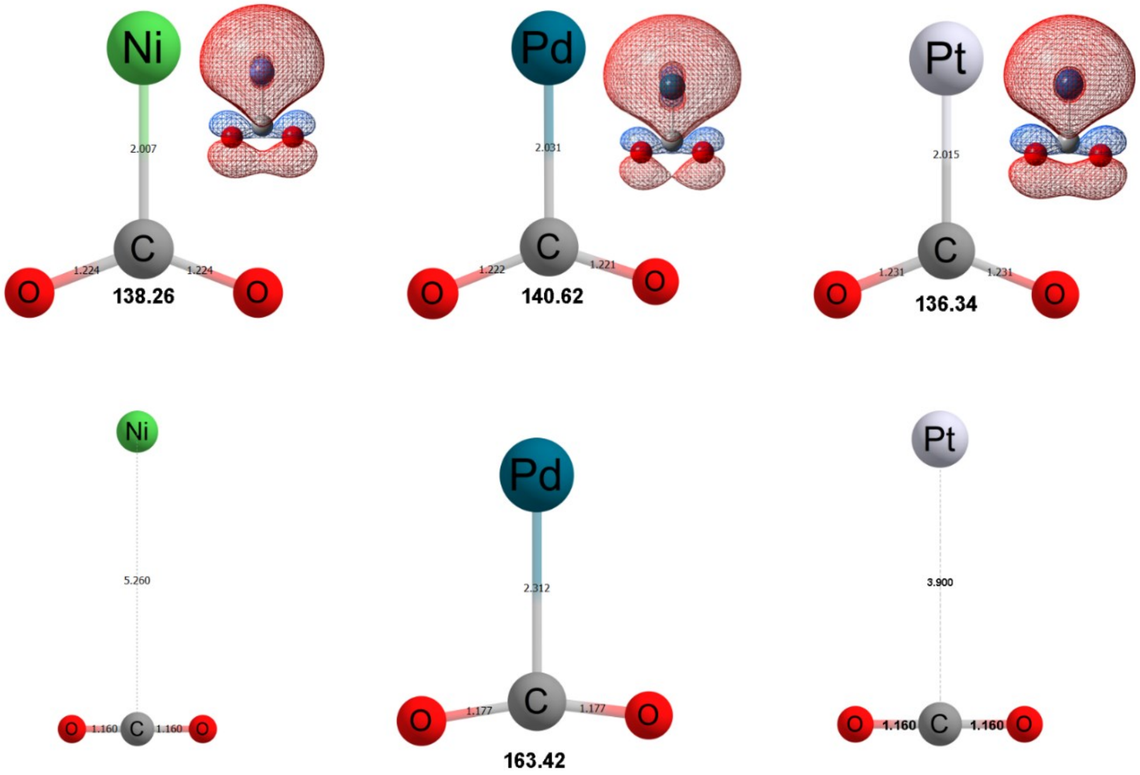

Figure III.B.13. Calculated structures of $NiCO_2^-$, $PdCO_2^-$, $PtCO_2^-$ (first row) and $NiCO_2$, $PdCO_2$, $PtCO_2$ (second row). The HOMOs of the anionic complexes are also presented.

In neutral $NiCO_2$ and $PtCO_2$, the metal atom is far away from CO_2. Also, their CO_2 moieties are structurally identical to an isolated CO_2 molecule. Therefore, large structural changes and post-detachment dissociation can occur when anionic $NiCO_2^-$ and $PtCO_2^-$ are photodetached, causing the peaks in their photoelectron spectra to widen. The potential energy surfaces of neutral $NiCO_2$ and $PtCO_2$ seem to show a shallow energy well at a M-C bond length of around 2.0 Å, but the energies of these local minima are higher than when CO_2 is far away (Figure III.B.14). The repulsive part of the neutral surfaces occurs at a M-C bond length less than 1.9 Å. Since $NiCO_2^-$ and $PtCO_2^-$ have a M-C bond length of 2.01 and 2.02 Å, respectively, the repulsive part of each neutral surface is not accessed during the vertical photodetachment process. These structural parameters show that there is little interaction between the neutral atoms of Ni and Pt and CO_2, which is as expected based on our previous research.[24] Surprisingly, however, the optimized neutral $PdCO_2$ structure shows incipient chemisorption character, that while much weaker than in its $PdCO_2^-$ anionic counterpart, is significantly stronger than the physisorption interactions seen in neutral $NiCO_2$ and $PtCO_2$. In neutral $PdCO_2$, the Pd–C bond length is 2.31 Å, which is characteristic of a metal–carbon bond. The CO_2 moiety is noticeably bent, with the O–C–O bond angle being 163.42°. The NPA analysis shows the CO_2 moiety as possessing a negative charge of –0.16 e, indicating a degree of charge transfer between neutral Pd and CO_2. The neutral $PdCO_2$ structure was also verified using the PBE0 and M06-L functionals.

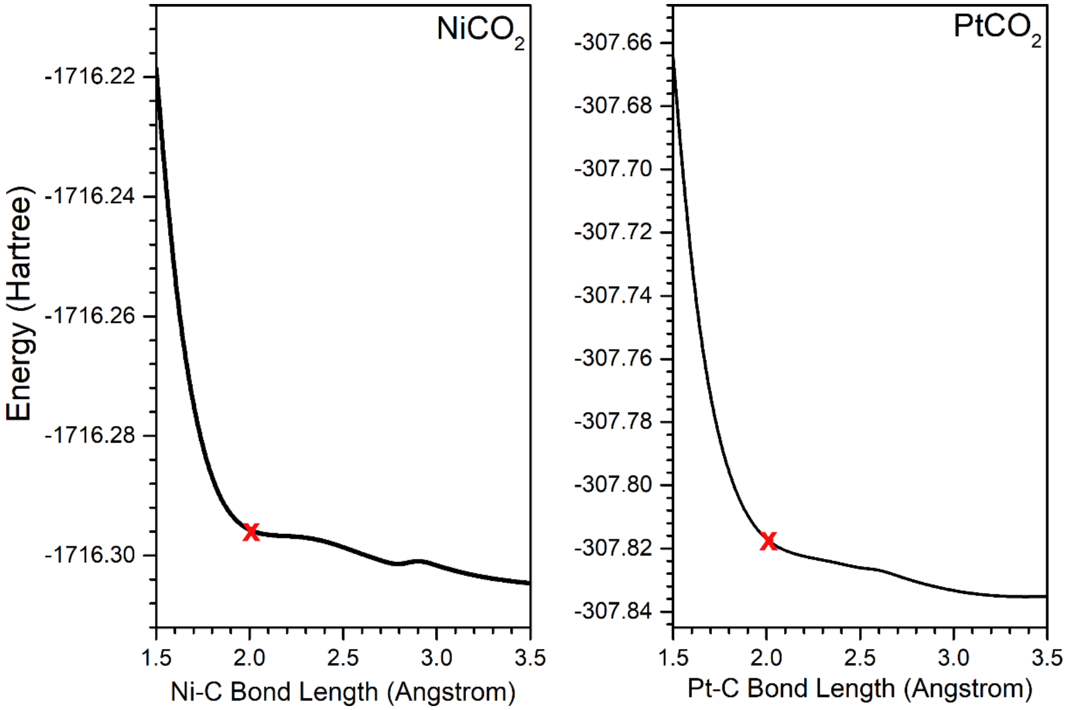

Figure III.B.14. THE POTENTIAL ENERGY SURFACES OF NEUTRAL $NiCO_2$ AND $PtCO_2$ WITH RESPECT TO THE M-C BOND LENGTH. THE RED CROSSES REPRESENT THE M-C BOND LENGTH OF OPTIMIZED ANIONIC $NiCO_2^-$ AND $PtCO_2^-$.

Both functionals yielded the same $PdCO_2$ structure as the B3LYP one. In addition, the Franck-Condon simulated spectrum of $PdCO_2^-$ reproduces the experimental one (Figure III.B.12), offering a further validation of the neutral $PdCO_2$ structure. Taken together, these features suggest that CO_2 can be activated by a single neutral Pd atom.

In order to provide further insight into the nature of the bonding in neutral $PdCO_2$, we analyzed its molecular orbitals. In most cases, the molecular orbitals of neutral $M(CO_2)$ species are composed of atomic orbitals of M and molecular orbitals of CO_2, which are essentially independent of one another. The molecular orbitals of neutral $PtCO_2$ (HOMO to HOMO–8) are presented on the left side of Figure III.B.15, and they provide typical examples of the molecular orbitals in neutral MCO_2 species. The absence of wavefunction overlap between the M and CO_2 moieties is consistent with a lack of interaction between neutral M atoms and CO_2 moieties. In the case of neutral $PdCO_2$, most of its molecular orbitals can also be viewed as independent atomic orbitals of Pd and molecular orbitals of CO_2. However, this is not the case for all orbital interactions between Pd and CO_2. The HOMO–4 and HOMO–6 orbitals, seen on the right side of Figure III.B.14, clearly result from the combination of Pd atomic orbitals and CO_2 molecular orbitals. There, one observes significant interaction, i.e., overlap, between some of the orbitals of Pd and CO_2. For HOMO–4, the interaction is mainly between the Pd d_{z^2} orbital and the B_1 orbital of bent CO_2. For HOMO–6, the interaction is through the overlap between Pd d_{xy} orbital and the B_2 orbital of bent CO_2. The wavefunction overlap between these Pd atomic and CO_2 molecular orbitals is likely the reason for the weak binding interaction and the partial charge transfer between neutral Pd atom and CO_2. Although we are unaware of corroborating experimental evidence for their weak binding, our calculations imply a

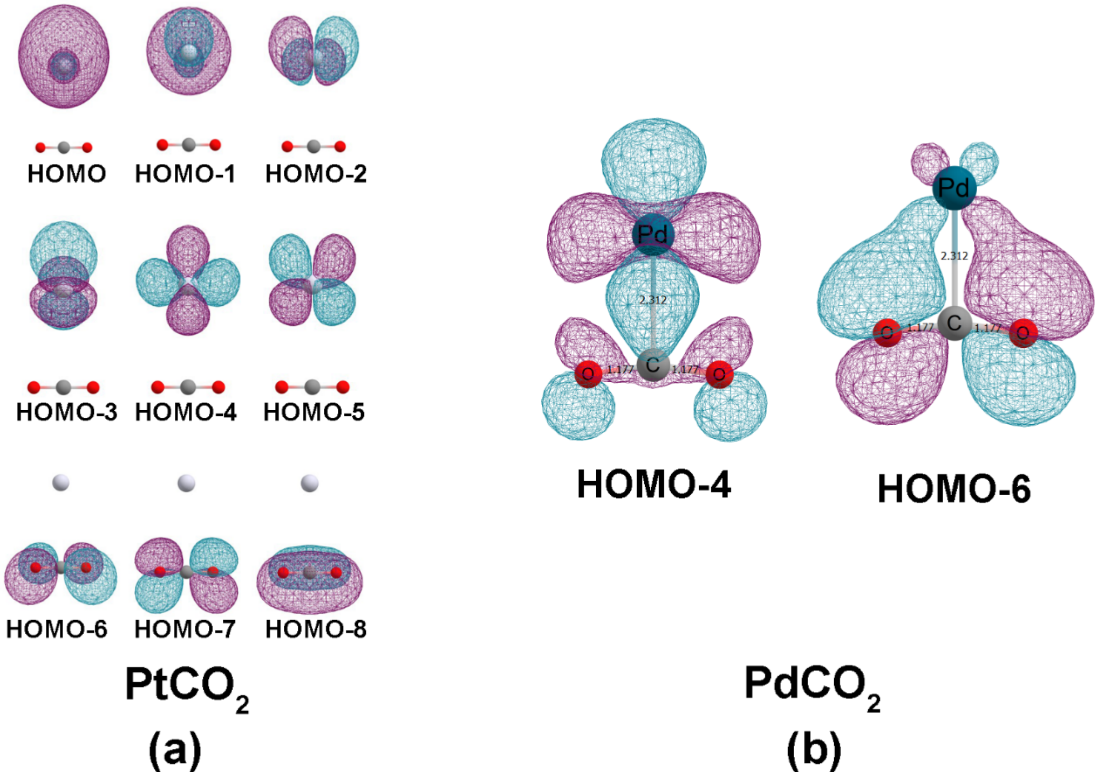

PtCO$_2$
(a)

PdCO$_2$
(b)

Figure III.B.15. Selected molecular orbitals of neutral (a) PtCO$_2$ and (b) PdCO$_2$. The overlap between the metal atomic orbitals and the CO$_2$ molecular orbitals is barely present in neutral PtCO$_2$, but is significant in neutral PdCO$_2$.

neutral PdCO$_2$ bond dissociation energy of 0.85 eV. For comparison, the bond dissociation energy of the PdCO$_2^-$ anionic complex is predicted to be 1.78 eV.

III.B.4.e. Conclusion

This combined anion photoelectron spectroscopic and computational study characterized the metallo–formate anions, M(CO$_2$)$^-$, where M = Ni, Pd, and Pt, and demonstrated that the addition of an excess electron led to significant CO$_2$ reduction in these systems. While neutral transition metals are normally incapable of reducing CO$_2$, we found evidence of an unusual attractive interaction between neutral Pd and CO$_2$.

Acknowledgement

This material is based on work supported by the U.S. National Science Foundation under Grant No. CHE–1664182 (KHB).

References

1. R. N. Compton, P. W. Reinhardt, and C. D. Cooper, *J. Chem. Phys.* **63**, 3821 (1975).
2. M. Knapp, O. Echt, D. Kreisle, T. D. Mark, and E. Recknagel, *Chem. Phys. Lett.* **126**, 225 (1986).
3. S. T. Arnold, J. V. Coe, J. G. Eaton, C. B. Freidhoff, L. H. Kidder, G. H. Lee, M. R. Manaa, K. M. McHugh, D. Patel–Misra, H. W. Sarkas, J. T. Snodgrass, and K. H. Bowen, in Proceedings of the Enrico Fermi International School of Physics, CVII Course, Varenna, edited by G. Scoles (North–Holland, Amsterdam, 1989), pp. 467–490.
4. C. E. Klots, *J. Chem. Phys*. **71**, 4172 (1979).
5. T. Tsukuda and T. Nagata, *J. Phys. Chem. A* **107**, 8476 (2003).
6. S. Y. Han, I. Chu, J. H. Kim, J. K. Song, and S. K. Kim, *J. Chem. Phys.* **113**, 596 (2000).
7. S. H. Lee, N. Kim, D. G. Ha, and S. K. Kim, *J. Am. Chem. Soc*. **130**, 16241 (2008).
8. M. Z. Kamrath, R. A. Relph, and M. A. Johnson, *J. Am. Chem. Soc*. **132**, 15508 (2010).
9. J. D. Graham, A. M. Buytendyk, Y. Wang, S. K. Kim, and K. H. Bowen, *J. Chem. Phys*. **142**, 234307 (2015).
10. J. M. Weber, *Int. Rev. Phys. Chem*. **33**, 489 (2014).
11. H. Schneider, A. D. Boese, and J. M. Weber, *J. Chem. Phys.* **123**, 074316 (2005).
12. A. D. Boese, H. Schneider, A. N. Glöß, and J. M. Weber*, J. Chem. Phys*. **122**, 154301 (2005).

13. B. J. Knurr and J. M. Weber, *J. Am. Chem. Soc*. **134**, 18804 (2012).

14. B. J. Knurr and J. M. Weber, *J. Phys. Chem. A* **117**, 10764 (2013).

15. B. J. Knurr and J. M. Weber, *J. Phys. Chem. A* **118**, 4056 (2014).

16. B. J. Knurr and J. M. Weber, *J. Phys. Chem. A* **118**, 10246 (2014).

17. B. J. Knurr and J. M. Weber, *J. Phys. Chem. A* **118**, 8753 (2014).

18. M. C. Thompson, J. Ramsay, and J. M. Weber, *J. Phys. Chem. A* **121**, 7537 (2017).

19. M. C. Thompson, L. G. Dodson, and J. M. Weber*, J. Phys. Chem. A* **121**, 4132 (2017).

20. M. C. Thompson, J. Ramsay, and J. M. Weber, *Angew. Chem. Int. Ed*. **55**, 15171 (2016).

21. L. G. Dodson, M. C. Thompson, and J. M. Weber, *J. Phys. Chem. A* **122**, 2983 (2018).

22. M. C. Thompson and J. M. Weber, *J. Phys. Chem. A* **122**, 3772 (2018).

23. L. G. Dodson, M. C. Thompson, and J. M. Weber, *Annu. Rev. Phys. Chem*. **69**, 231 (2018).

24. X. Zhang, E. Lim, S. K. Kim, and K. H. Bowen, *J. Chem. Phys*. **143**, 174305 (2015).

25. N. Kim, *Bull. Korean Chem. Soc*. **34**, 2247 (2015).

26. M. J. DeLuca, B. Niu, and M. A. Johnson, *J. Chem. Phys*. **88**, 5857 (1988).

27. S. H. Fleischman and K. D. Jordan, *J. Phys. Chem*. **91**, 1300 (1987).

28. T. Tsukuda, M. A. Johnson, and T. Nagata, *Chem. Phys. Lett.* **268**, 429 (1977).

29. J. W. Shin, N. I. Hammer, M. A. Johnson, H. Schneider, A. Glöß, and J. M. Weber, *J. Phys. Chem. A* **109**, 3146 (2015).

30. D. W. Arnold, S. E. Bradforth, E. H. Kim, and D. M. Neumark, *J. Chem. Phys*. **102**, 3493 (1995).

31. G. Markovich, R. Giniger, M. Levin, and O. Cheshnovsky, *Z. Phys. D: At., Mol. Clusters* **20**, 69 (1991).

32. D. W. Arnold, S. E. Bradforth, E. H. Kim, and D. M. Neumark, *J. Chem. Phys*. **97**, 9468 (1992).

33. D. W. Arnold, S. E. Bradforth, E. H. Kim, and D. M. Neumark, *J. Chem. Phys*. **102**, 3510 (1995).

34. A. Muraoka, Y. Inokuchi, N. I. Hammer, J. W. Shin, M. A. Johnson, and T. Nagata, *J. Phys. Chem. A* **113**, 8942 (2009).

35. K. Hiraoka and S. Yamabe, *J. Chem. Phys.* **97**, 643 (1992).

36. K. Sudoh, Y. Matsuyama, A. Muraoka, R. Nakanishi, and T. Nagata, *Chem. Phys. Lett*. **433**, 10 (2006).

37. T. Sanford, S. Y. Han, M. A. Thompson, R. Parson, and W. C. Lineberger, *J. Chem. Phys.* **122**, 054307 (2005).

38. R. F. Höckendorf, K. Fischmann, Q. Hao, C. v. d. Linde, O. P. Balaj, C. K. Siu and M. K. Beyer, *Int. J. Mass Spectrom.* **354**, 175 (2013).

39. A. Akhgarnusch, R. F. Hoeckebdorf, Q. Hao, K. P. Jaeger, C. K. Siu, and M. K. Beyer, *Angew. Chem. Int. Ed.* **53**, 9327 (2013).

40. A. Akhgarnusch and M. K. Beyer, *Int. J. Mass Spectrom*. **365**, 295 (2014).

41. R. Oh, E. Lim, X. Zhang, J. Heo, K. H. Bowen, and S. K. Kim, *J. Chem. Phys*. **146**, 134304 (2017).

42. X. Zhang, G. Liu, K. Meiwes–Broer, G. Gantefçr, and Kit Bowen, *Angew. Chem. Int. Ed.* **55**, 9644 (2016).

43. J. D. Graham, A. M. Buytendyk, X. Zhang, S. K. Kim, and K. H. Bowen, *J. Chem. Phys.* **143**, 184315 (2015).

44. G. Liu, S. M. Ciborowski, and K. H. Bowen, *J. Phys. Chem. A* **121**, 5817 (2017).

45. J. Ho, K. M. Ervin, and W. C. Lineberger, *J. Chem. Phys.* **93**, 6987 (1990).

46. F. Neese. *WIREs Comput. Mol. Sci.* **2**, 73 (2012).

47. (a) A. D. Becke, *Phys. Rev. A* **38**, 3098 (1988); (b) A. D. Becke, *J. Chem. Phys.* **98**, 5648 (1993).

48. (a) C. Lee, W. Yang, and R. G. Parr, *Phys. Rev. B* **37**, 785 (1988); (b) R. Krishnan, J. S. Binkley, R. Seeger, and J. A. Pople, *J. Chem. Phys.* **72**, 65 (1980).

49. S. Grimme, J. Antony, S. Ehrlich, and H. A. Krieg, *J. Chem. Phys.* **132**, 154104 (2010).

50. F. Neese, F. Wennmohs, A. Hansen, and U. Becker, *Chem. Phys.* **356**, 98 (2008).

51. (a) F. Weigend and R. Ahlrichs, *Phys. Chem. Chem. Phys.* **7**, 3297 (2005); (b) F. Weigend, *Phys. Chem. Chem. Phys.* **8**, 1057 (2006).

52. D. Andrae, U. Häußermann, M. Dolg, H. Stoll, and H. Preuß, *Theor. Chim. Acta* **77**, 123 (1990).

53. (a) C. Adamo and V. Barone, *J. Chem. Phys.* **110**, 6158 (1994); (b) J. P. Perdew, K. Burke, and M. Ernzerhof, *Phys. Rev. Lett.* **77**, 3865 (1997); (c) Y. Zhao and D. G. Truhlar, *J. Phys. Chem. A* **110**, 13126 (2006); (d) Y. Zhao and D. G. Truhlar, *Theo. Chem. Acc.* **120**, 215 (2007).

54. G. Liu, E. Miliordos, S. M. Ciborowski, M. Tschurl, U. Boesl, U. Heiz, X. Zhang, S. S. Xantheas, and K. H. Bowen. *J. Chem. Phys.* **149**, 22110 (2018).

55. G. Liu, Z. Zhu, S. M. Ciborowski, I. R. Ariyarathna, E. Miliordos, and K. H. Bowen, *Angew. Chem. Int. Ed.* (2019) DOI: 10.1002/anie.201903252.

56. X. Zhang, G. Liu, S. Ciborowski, and K. Bowen, *Angew. Chem. Int. Ed.* **56**, 9897 (2017).

57. K. A. Lundell, X. Zhang, A. I. Boldyrev and K. H. Bowen, *Angew. Chem. Int. Ed.* **56**, 16593 (2017).

58. P. J. Robinson, G. Liu, S. Ciborowski, C. Martinez–Martinez, J. R. Chamorro, X. Zhang, T. M. McQueen, K. H. Bowen, and A. N. Alexandrova, *Chem. Mater.* **29**, 9892 (2017).

59. X. Zhang, G. Liu, S. Ciborowski, and K. H. Bowen, *Angew. Chem. Int. Ed*. **56**, 9897 (2017).

60. E. F. Belogolova, G. Liu, E. P. Doronina, S. Ciborowski, V. F. Sidorkin, and K. H. Bowen, *J. Phys. Chem. Lett.* **9**, 1284 (2018).

61. X. Zhang, I. A. Popov, K. A. Lundell, H. Wang, C. Mu, W. Wang, H. Schnöckel, A. I. Boldyrev, and K. H. Bowen. *Angew. Chem. Int. Ed.* **130**, 14256 (2018).

III.B.5. Mystery of Three Borides: Promiscuous Metal-Boron Bonding Governing Superhard Structures

Paul J. Robinson, Gaoxiang Liu, Sandra M. Ciborowski, Chalynette J. Martinez-Martinez, Juan Chamorro, Tyrel M. McQueen, Kit H. Bowen, and Anastassia N. Alexandrova

Reprinted with permission from *Chem. Mater.* 2017, 29, 9892-9896. Copyright 2017 American Chemical Society.

III.B.5.a. Abstract

Some transition metal borides are ultra-hard. While not harder than diamond, they are easier to process, which sparks intense interest. However, we cannot predict which particular borides should be ultra-hard. A striking example is the three structurally similar diborides of Ti, Re, and Os, among which only ReB_2 is ultra-hard. For this trio, using a combination of theory and experiment done on both the small cluster models and solids, we show that the nature of the metal-boron bonds, in equilibrium and under applied mechanical stress, is the key to the hardness of these diborides. TiB_2 is purely ionic and yields to shear stress like graphite. ReB_2 is partially ionic and forms a backbond with the boron, which strengthens the B-B bonds. OsB_2 is most covalent and forms both bonding and antibonding backbonds with the boron. This weakens the boron network and the material as a whole. We thus challenge the old model for boride hardness that ignored metal-boron interactions. A general strategy for ultra-hard boride design is proposed.

III.B.5.b. Main Text

Ultrahard materials have been of interest to human kind since prehistoric times. Borides of certain transition metals form a new class of hard materials.[1-4] Being metals, these borides are easily cut with electric discharge machining and thus appear as an attractive alternative to diamond. The governing principles for the design of ultrahard borides have been proposed to be the combination of high electron density at the Fermi level (E_F) coming from the metal, making borides incompressible, and a rigid covalent boron skeleton resisting the shear stress.[5-10] The metal and boron sublattices in this model are seen independently. Here, we challenge these old principles and show that only with the inclusion of specific metal–boron bonding can we explain and design for the structure and hardness of borides.

We zoom in to a set of three diborides, which are stoichiometrically identical and structurally related yet distinct: TiB_2, ReB_2, and OsB_2 (Figure III.B.16). Among these three, only ReB_2 is ultrahard.[11-13] In all three cases, the boron sublattice is a sheet: planar in TiB_2 and corrugates as a "chair" in ReB_2 and as a "boat" in OsB_2, by analogy with the conformations of cyclohexane. These diborides demonstrate how boron, a metalloid, is

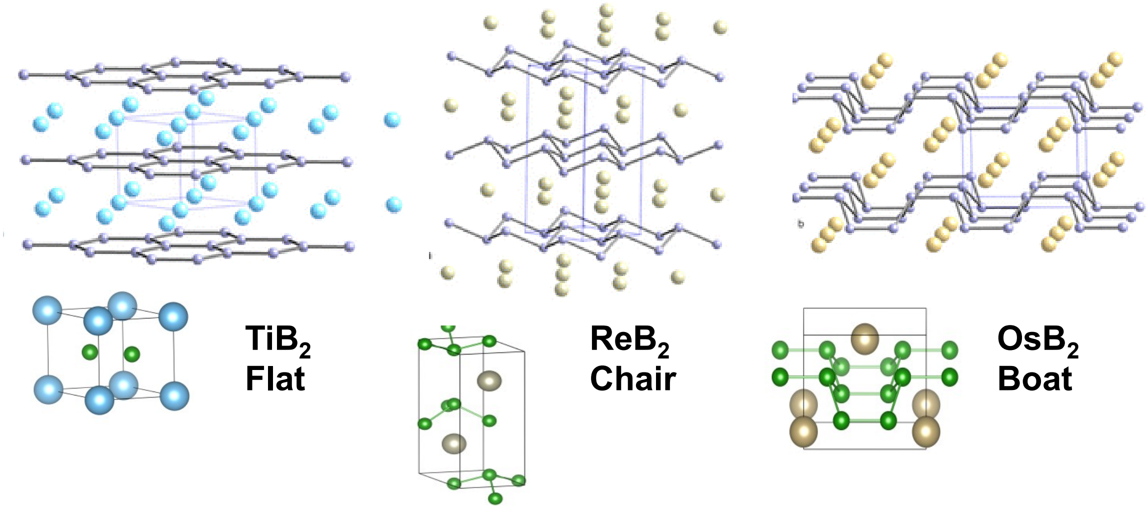

Figure III.B.16. The structures of the three borides: TiB_2 featuring a flat B-sheet, and ReB_2 and OsB_2 where the B-sheet is bent in a chair and a boat conformation, respectively.

capable of many different kinds of bonds to metals, and this promiscuity strongly dictates hardness.

Our approach links the chemical bonding in materials to that in relevant small cluster fragments, which can be studied in great detail using state-of-the-art theory and experiment. The identified critical elements in the electronic structure of the cluster are mapped back onto the solid for property rationalization and design.[14,15]

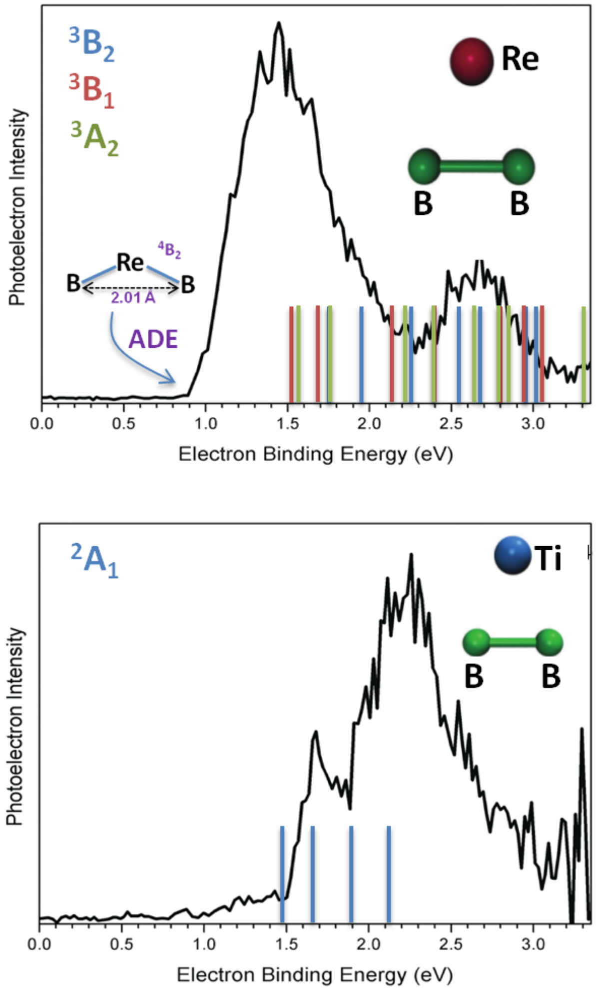

Figure III.B.17. The experimental photoelectron spectra of ReB$_2^-$ (top) and TiB$_2$ $^-$(bottom), and the theoretical assignment of spectral features.

TABLE III.B.4. THE EXPERIMENTAL AND CALCULATED PHOTOELECTRON SPECTRA OF TiB_2^- AND ReB_2^- (IN EV).

Feature	Exptl Energy	Transition	Calcd Energy
ReB_2^-			
ADE	0.9 ± 0.1	$^3A_1 \rightarrow {}^4B_1$	1.21
X	1.45 ± 0.1	$^3B_1 \rightarrow {}^4B_1$	1.51
A	1.52 ±0.1	$^3A_2 \rightarrow {}^4B_1$	1.58
B	1.65 ± 0.1	$^2A_1 \rightarrow {}^1A_1$	1.70
C	1.76 ± 0.1	$^2A_1 \rightarrow {}^3A_1$	1.76
TiB_2^-			
ADE	1.4 ± 0.1	$^2A_1 \rightarrow {}^1A_1$	1.09
X	1.68 ± 0.1	$^2A_1 \rightarrow {}^1A_1$	1.49
A	1.80 ± 0.1	$^2A_1 \rightarrow {}^3A_1$	1.53
B	1.96 ± 0.1	$^2A_1 \rightarrow {}^1A_1$	1.86
C	2.07 ± 0.1	$^2A_1 \rightarrow {}^3A_1$	2.02???

The most elementary motif that can be observed in the solids is MB_2, and thus, we begin from the $MB_2^{0/-}$ clusters (ions being included for experimental characterization with anion photoelectron spectroscopy). All clusters have C_{2v} symmetry, with the metal coordinating to the center of the B–B bond. However, they have markedly different B–B and M–B distances (see Supporting Information), indicating that metals affect the B–B bonding in different ways. TiB_2^- ($^2A_1$) has a short R(B–B) of 1.56 Å; ReB_2^- has three competing configurations: $^3B_2$, R(B–B) = 1.75 Å; $^3B_1$, R(B–B) = 1.66 Å (2.51 kcal/mol above $^3B_2$); and $^3A_2$, R(B–B) = 1.76 Å (3.14 kcal/mol above $^3B_2$). OsB_2^- ($^4A_2$) has R(B–B) of 1.66 Å. Note that these calculations are large-active-space multireference with dynamic electron correlation (see Supporting Information). This tour de force theoretical approach appeared to be required to reproduce experimental spectra for these seemingly simple systems.[16] The close proximity and mixing of many electronic states can be linked to the promiscuity of metal–boron bonding. Table III.B.4 and Figure III.B.17 show the experimental and theoretical photoelectron spectra (OsB_2^- was not done experimentally due to the high toxicity of Os). The good agreement between theory and experiment signifies that theory can adequately describe these clusters and provide an electronic structure insight.

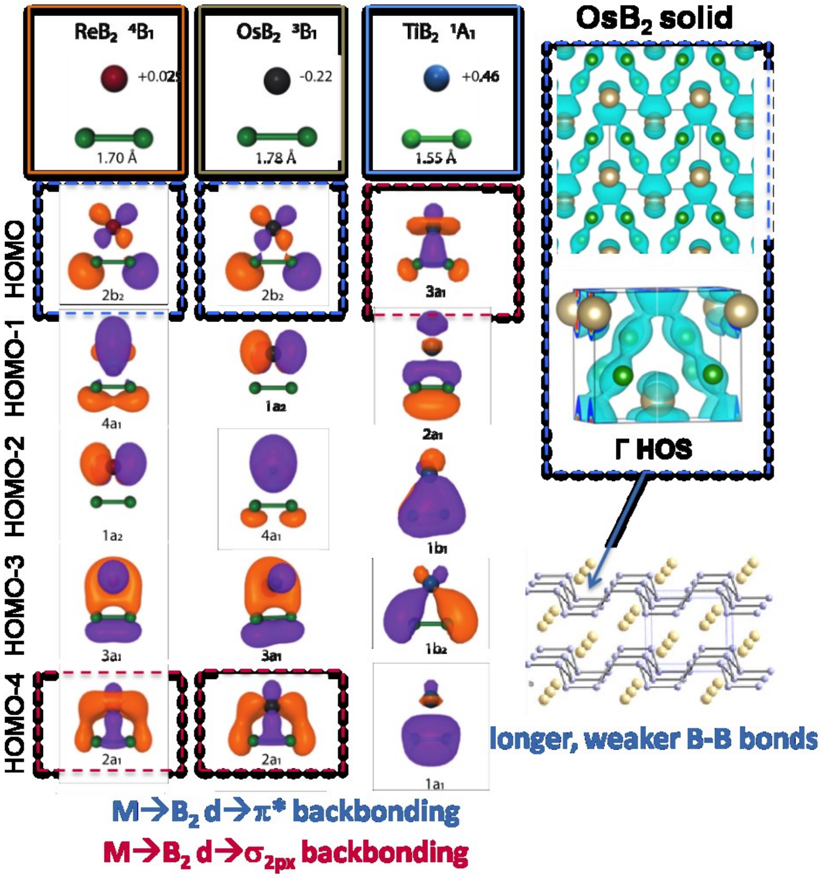

Figure III.B.18. Left: The Kohn-Sham orbitals of ReB_2, OsB_2, and TiB_2, truncated set. NBO charges on atoms are shown. The two types of M→B_2 backbonds are outlined: d→σ_{2px} in red, and d→π^* in blue. Because of the undersaturation of valencies, the HOMOs in ReB_2 and TiB_2 have no analogues among the occupied states in the solids. Right: The d→π^* state occupied in solid OsB_2, corresponding to the donation from Os to the activated B-B bonds.

The chemical bonding in the three neutral clusters (Figure III.B.18) reveals peculiarities of metal–boron interactions and differences between the three clusters. When transition metals interact with B_2, the back-donation first happens to the LUMO of B_2, which is a bonding σ_{2px}-MO. The d-AO → LUMO(B_2) back-donation thus strengthens the B–B bond. The resulting MO falls deep below the HOMO–LUMO gap in ReB_2 and OsB_2, while in TiB_2 it is the HOMO. In addition, Re and Os are capable of back-donation to the LUMO+1 (π^*) of B_2, in the clusters' HOMOs. $d \rightarrow \pi^*$ is bonding between the metal and B_2 and B–B π-antibonding. Due to this MO, R(B–B) in ReB_2 and OsB_2 is elongated. Both back bonds are lower in energy in OsB_2 than in ReB_2, and while this makes little difference for clusters, it will become profoundly important in the corresponding solids. Both types of back bonds are covalent in nature, as seen also from the partial charges on atoms (Figure III.B.18). The ionic M-B_2 bonding component is the strongest in TiB_2. Thus, clusters give us a simple representation of the fundamental M-B_2 interactions possible in the three systems.

In the bulk, the dangling valencies present in clusters are saturated, and so some cluster electronic states become unoccupied. The $d \rightarrow \sigma_{2px}$ HOMO in $TiB_2^{0/-}$ does not have an analogue among the valent states in the bulk TiB_2. The material thus exhibits no covalent Ti–B interactions, and the only bonding present is ionic, as is also clear from the charge of +2 on Ti, corresponding to a typical d^2 configuration (Table III.B.5). Furthermore, the +2 charge persists when Ti is substituted into the boat or chair structures. The TiB_2 structure type is also characteristic of other diborides including those of Mg, V, Cr, Mn, Sc, Zr, Nb, and Mo.[17] The common electronic origin is the presence of a 2+ metal. M^{+2} means that the boron sublattice receives one electron per B. B^{-} is isoelectronic to neutral C, and the flat hexagonal boron sheet is therefore isoelectronic and isostructural to graphene. In fact, it has many attributes of graphene, such as the Dirac points.[18]

Both ReB_2 and OsB_2 retain the d → σ_{2px} states in the bulk, in line with their low energies in the cluster models. These states strengthen both M–B and B–B bonding. However, the d → π* state exists only in OsB_2 and specifically in the longer B–B bonds within the asymmetric "boat" structure (Figure III.B.18). Os has enough electrons to give only half of the B–B bonds a π* character. Thus, the "boat" structure of OsB_2 is dictated by the antibonding M–B_2 interactions, which makes half of the B–B bonds longer and weaker, while in ReB_2 all B–B bonds are strengthened by M–B interactions. The M–B bonds are stronger in OsB_2. Increased covalent character in Re and Os borides reflects in greatly reduced partial charges as compared to those in TiB_2, particularly in the Os systems (Table III.B.5). Hence, we see the chemical bonding origin of the structural differences of the three borides.

TABLE III.B.5. BADER CHARGES OF METALS IN BOTH **NATURAL** AND FOREIGN STRUCTURES (OPTIMIZED TO THE NEAREST STATIONARY POINT).

	Os	Re	Ti
Boat	**+0.04**	+0.44	+2.02
Chair	+0.07	**+0.39**	+1.89
Flat	+0.60	+0.93	**+1.98**

We further quantify the degree of covalency and relative bond strengths in the solids via the quantum theory of atoms in molecules (QTAIM) (Figure III.B.19, Table III.B.6), which analyzes the total rather than per-MO charge density.[19,20] QTAIM detects the presence of critical points (CPs) in the charge density. In the "boat" configuration, there

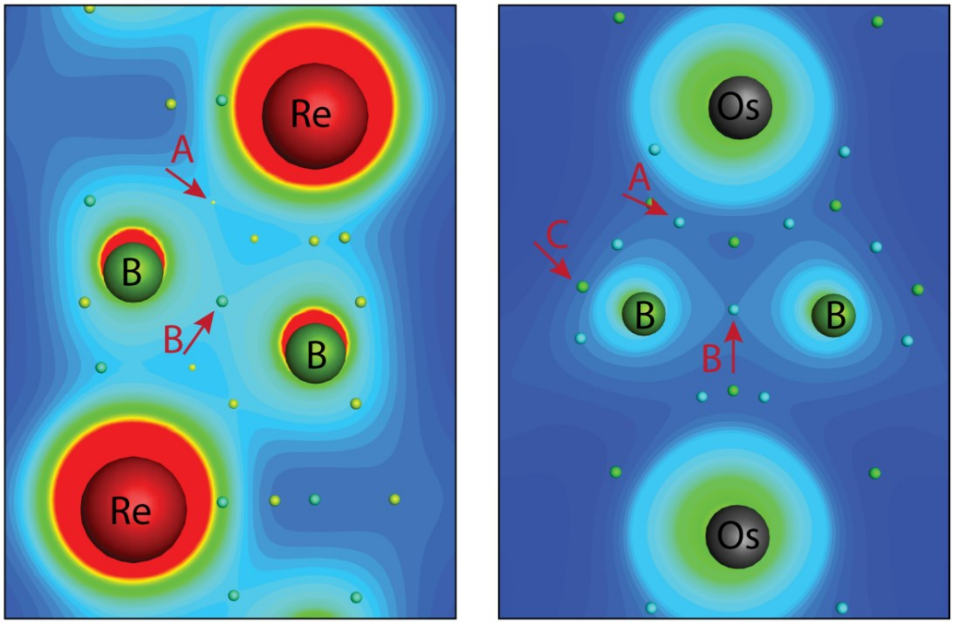

Figure III.B.19. ELECTRON DENSITY PLOTS OF ReB_2 (LEFT) AND OsB_2 (RIGHT). QTAIM CPS ARE INDICATED: BOND CPS - BLUE, RING CPS - GREEN, CAGE CPS - YELLOW. A – M-B CP, B, C – B-B CPS.

are three bond CPs, labeled i (M–B CP), ii (B–B CP), and iii (the second B–B CP). The "chair" structure has two distinct bond CPs, i and ii. The amount of charge at bond CPs correlates with bond strength.[21,22] Both the "boat" and "chair" structures have stronger M–B bonds when containing Os rather than Re. Furthermore, while in general B–B bonds are stronger than M–B bonds, the B–B bonds in the OsB_2 systems are of comparable strength to the Os–B bonds in contrast to the more differentiated ReB_2 systems. Thus, the covalent character of Re/Os–B bonds is confirmed, and it is additionally seen that half of the B–B bonds in OsB_2 are weakened by the interaction with Os, with the charge density flowing from B–B to Os–B bonds.

TABLE III.B.6. THE CHARGE DENSITIES AT THE BOND CPS FOR BOTH RE AND OS IN THE BOAT AND CHAIR STRUCTURES.

	A	**B**	**C**
ReB_2 boat	0.608 e^-	0.740 e^-	0.697 e^-
OsB_2 boat	0.656 e^-	0.732 e^-	0.618 e^-
ReB_2 chair	0.590 e^-	0.713 e^-	X
OsB_2 chair	0.629 e^-	0.668 e^-	X

There transpires a correlation between the relative strengths of the M–B and B–B bonding and the materials' hardness. In order to pin it down, we depart from the static bonding picture constructed at equilibrium. Hardness is a response to external force, and the effect of pressure is comprised of the combination of two types of distortion: compression and shear. High incompressibility and shear modulus are both necessary but not alone sufficient for hardness.[5-10] We examine the materials' response to these two types of stimuli independently, again relying on the cluster models for clarity.

Because the π* back bond is not present in the ReB_2 and TiB_2 solids, at this point, the clusters were charged +1 and +2, respectively, in order to unoccupy the d → π* states. To mimic the effects of compression and shear stress, the B–B compression and M–B_2 shift were applied, and the clusters' responses were monitored (Figure III.B.20).[23] Response to compression should primarily report on the strength of the B–B bonding, whereas that to shear should report on the M–B bonding. The force constants corresponding to the B_2 compression (Figure III.B.20 A) show bond stiffening in order of covalent to ionic character. TiB_2^{2+} has the stiffest B–B bond, because it is compact, and electrons confined to the smaller space resist the deformation, while the stable d^2 Ti^{2+} is not willing to relieve

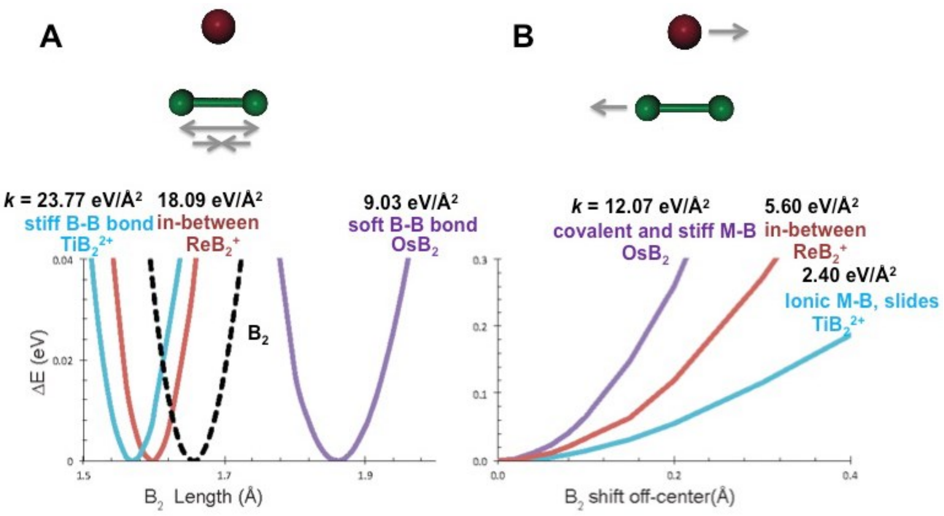

Figure III.B.20. (A) Energies of the clusters as a function of (A) compression along the B-B bond, (B) shear distortion coordinate. Cyan - TiB_2^{2+}, Red - ReB_2^{+}, Purple - OsB_2, dashed black - isolated B_2 for a reference.

the stress by taking electrons back. ReB_2^{+}, with its d → σ_{2px} back bond, has a strengthened B–B bond and some charge flow toward M–B bonds allowing for the flexibility in charge distribution. Thus, B–B bonds are slightly less stiff than in TiB_2^{2+}. Being the most covalent, Os is the other extreme: the B–B bond activation by the d → π* donation leads to charge redistribution toward the covalent Os–B bonds. The system is further capable of relieving the stress by shifting electrons toward Os upon the B–B bond compression as if having a shock absorber both in the cluster and in every unit cell in the solid. This reduces the material's stiffness upon compression.

The clusters' ordering of resistance to shearing is exactly the opposite from that to compressing (Figure III.B.20 B). The M–B_2 bonding is the most covalent in OsB_2, intermediate in ReB_2^{+}, and purely ionic in TiB_2^{2+}. Hence, Ti in TiB_2^{2+} easily slides along B_2, ReB_2^{+} resists the slip more, and OsB_2 is the most resilient because the slip disrupts the strong Os–B bonds. OsB_2 has a force constant 5 times higher than that of TiB_2^{2+} for this mode of deformation. To bridge our understanding to the solids, we examine stiffness tensors (Supporting Information Tables 7–11). Starting with compression of the boron network (C_{11}), we see $ReB_2 \approx TiB_2 > OsB_2$. This shows the same distinction we had in the clusters: Re and Ti stiffen B the same amount, and Os weakens it. Shearing the metal against the B sheet shows ReB_2 (C_{55}) > TiB_2 (C_{44}) > OsB_2 (C_{66}). This is not the same as the cluster model, but we must consider that there are other interactions in real distortions. The cluster model is Os bound to a long B_2, but in the solid there are also shorter, more slippery B_2 bonds. Still, it should be hardest to shear on that long B_2 bond in OsB_2 (C_{66}), and that is the case ($C_{66} > C_{44} \gg C_{55}$). In TiB_2 the shear across the B layer is the easiest ($C_{44} < C_{66}$). Thus, we can explain slip-plane strength in solids.

TABLE III.B.7. THE CALCULATED PROPERTIES OF RE AND OS IN BOTH THE BOAT AND CHAIR STRUCTURES. G IS THE SHEAR MODULUS. X INDICATES THAT THE STRUCTURE ONLY HAS ONE B_2 BOND LENGTH.

	B_2-1 (Å)	B_2-2 (Å)	G (GPa)
OsB_2-Boat	1.80	1.88	166
ReB_2-Boat	1.84	1.81	244
OsB_2-Chair	1.86	X	187
ReB_2-Chair	1.82	X	297

Finally, we computed the geometries and shear moduli of Re and Os in both boat and chair configurations (Table III.B.7). The consequence of more covalent Os–B bonding is a lengthening of the B_2 bonds in the chair structure. This, in turn, lowers the shear modulus. Similarly, Re added to the boat structure causes B_2 bonds to move toward uniformly short, losing the antibonding π* character, and increasing in the shear modulus. Os in the chair structure is significantly harder than its boat counterpart. This results from forcing the B-lattice to be uniform—no B_2 bond becomes overly covalent, but all are weakened. The moduli thus have full support from the cluster bonding models.

In conclusion, a metal that is too covalent with boron will lower the incompressibility, while a metal that is too ionic with boron will lower the shear strength. A “goldilocks metal” would be intermediate, i.e., having only the bonding $d \rightarrow \sigma_{2px}$ and no antibonding $d \rightarrow \pi^*$ B–M bonds. Re within the given family of diborides has just the right electron count to fulfill this requirement; as a result ReB_2 is the only ultrahard boride. This constitutes a new bonding model for ultrahard borides, which is based on promiscuous metal–boron bonding, previously unrecognized as one of the crucial aspects of superhard structures. The model reveals the origin of the structural differences in the TiB_2, ReB_2, and OsB_2 borides and explains their differences in hardness. Beyond the three borides, a chemical bonding based design principle for hard materials is a step toward designing novel materials that rival diamond’s hardness.

Acknowledgements

We thank Garth Billings of Diversified Advanced Technologies, LLC (9310 Prototype Drive, Reno, NV 89521, 775-857-4300, garth.billings@sbcglobal.net) for providing the ReB_2 sample. We thank Professor Richard Kaner, Professor Sarah Tolbert, and Dr. Michael Yeung for a helpful discussion. This work was supported by the Air Force Office of Scientific Research (AFOSR) under Grant FA9550-15-1-0259 (K.H.B.), NSF Career Award CHE1351968 (A.N.A.), the Johns Hopkins University Catalyst Fund (T.M.M.), the NSF’s PARADIM (Platform for the Accelerated Realization, Analysis, and Discovery of Interface Materials) program, a Materials Innovation Platform (T.M.M.), and the donation of Ms. Evers-Manly for the Undergraduate Research Scholars Program in UCLA (P.J.R.). UCLA IDRE cluster Hoffman2 was used for all calculations.

References

1. H. Chung, M. Weinberger, J. Levine, A. Kavner, J. M. Yang, S. H. Tolbert, and R. B. Kaner, *Science* **316**, 436 (2007).
2. R. W. Cumberland, M. B. Weinberger, J. J. Gilman, S. M. Clark, S. H. Tolbert, and R. B. Kaner, *J. Am. Chem. Soc*. **127**, 7264 (2005).
3. R. B. Kaner, J. J. Gilman, and S. H. Tolbert, *Science* **308**, 1268 (2005).
4. A. T. Lech, C. L. Turner, R. Mohammadi, S. H. Tolbert, and R. B. Kaner, *Proc. Natl. Acad. Sci. U. S. A.* **112**, 3223 (2015).
5. J. B. Levine, S. H. Tolbert, and R. B. Kaner, *Adv. Funct. Mater*. **19**, 3519 (2009).
6. J. J. Gilman, R. W. Cumberland, and R. B. Kaner, *Int. J. Refract. Hard Met.* **24**, 1 (2006).
7. V. V. Brazhkin, A. G. Lyapin, and R. J. Hemley, *Philos. Mag. A* **82**, 231 (2002).
8. J. Haines, J. M. Leger, and G. Bocquillon, *Annu. Rev. Mater. Res.* **31**, 1 (2001).
9. J. M. Leger, P. Djemia, F. Ganot, J. Haines, A. S. Pereira, J. A. H. da Jornada, *Appl. Phys. Lett.* **79**, 2169 (2001).
10. W. A. Harrison, "Electronic Structure and the Properties of Solids"; Freeman: San Francisco, 1980.
11. M. T. Yeung, R. Mohammadi, and R. B. Kaner, *Annu. Rev. Mater. Res.* **46**, 465 (2016).
12. Q. Gu, G. Krauss, and W. Steurer, *Adv. Mater.* **20**, 3620 (2008).
13. R. G. Munro, *J. Res. Natl. Inst. Stand. Technol.* **105**, 709 (2000). *Chem. Mater.* **29**, 9892 (2017).

14. R. Hoffmann, “Solids and surfaces: a chemist’s view of bonding in extended structures”; VCH Publishers: 1988.
15. R. Hoffmann, and C. Zheng, *J. Phys. Chem.* **89**, 4175 (1985).
16. P. J. Robinson, X. Zhang, T. McQueen, K. H. Bowen, and A. N. Alexandrova, *J. Phys. Chem. A* **121**, 1849 (2017).
17. G. Akopov, M. T. Yeung, and R. B. Kaner, *Adv. Mater*. **29**, 1604506 (2017).
18. X. Feng, C. Yue, Z. Song, Q. Wu, and B. Wen, arXiv:1705.00511, (2017).
19. A. Morgenstern, T. Wilson, J. Miorelli, T. Jones, and M. E. Eberhart, *Comput. Theor. Chem.* **1053**, 31 (2015).
20. R. F. Bader, “Atoms in Molecules”; John Wiley & Sons: 1990.
21. C. F. Matta, and R. J. Boyd, “The Quantum Theory of Atoms in Molecules: From Solid State to DNA and Drug Design”; John Wiley & Sons: 2007.
22. S. J. Grabowski, *J. Phys. Chem. A* **105**, 10739 (2001).
23. P. J. Robinson and A. N. Alexandrova, *J. Phys. Chem. A* **119**, 12862 (2015).

III.B.6. Tuning the Electronic Properties of Hexanuclear Cobalt Sulfide Superatoms via Ligand Substitution

Gaoxiang Liu, Andrew Pinkard, Sandra M. Ciborowski, Vikas Chauhan, Zhaoguo Zhu, Alexander P. Aydt, Shiv N. Khanna, Xavier Roy, and Kit H. Bowen

Chem. Sci., 2019, 10, 1760 – Published by The Royal Society of Chemistry.

III.B.6.a. Abstract

Molecular clusters are attractive building blocks for creating materials with tailored properties due to their unique combination of atomic precision, tunability and functionality. The ligands passivating these clusters offer an exciting opportunity to control their electronic properties while preserving their closed shells and electron counts. Here we demonstrate this concept by measuring the anion photoelectron spectra of a series of Co6S8 clusters decorated with different ratios of electron-donating and electron-withdrawing ligands, Co6S8(PEt3)6-x(CO)x (x = 0–3). We find that Co6S8(PEt3)6 has a low electron affinity (EA) of 1.1 eV, and that the successive replacement of PEt3 ligands with CO gradually increases its EA to 1.8 eV. Density functional theory calculations reveal that the increase of EA results from a monotonic lowering of the cluster highest occupied and lowest unoccupied molecular orbitals (HOMO and LUMO). Our work provides unique insights into the electronic structure and tunability of superatomic building blocks

III.B.6.b. Introduction

Electron affinity and ionization energy are fundamental properties of the elements. Together they govern the interactions and bonding of close-contacting atoms and control the collective properties of solids. Because they are intrinsic to each element, however, the electron affinity and ionization energy of a given atom cannot be altered. This presents an immense synthetic challenge for the design of tunable materials as substituting atoms often leads to entirely new structures, interactions and collective behaviors.

By analogy to "atomic" building blocks, certain clusters can be used as "superatomic" building blocks for the assembly of novel materials.[1-22] Within this context, the family of metal chalcogenide molecular clusters has recently received renewed attention for the creation of functional solids with tunable properties, including ferromagnetism, electrical conductivity, tunable optical gaps and thermal switching.[1,7, 23-32] One of the key advantages of this approach over traditional atomic solids is that the characteristics of the building blocks can be tuned *pre-assembly* without changing the total electron count of the superatom. Using the molecular cluster $Co_6Te_8L_6$ (L = passivating ligand) as a model system, Khanna *et al.* recently predicted theoretically that changing L from PEt_3 to CO would increase the electron affinity of the Co_6Te_8 core, in effect transforming the cluster from a superatomic alkali metal toward a superatomic halogen.[33,34] Experimentally measuring the electron affinity and/or ionization energy of metal chalcogenide clusters is challenging, however, because it requires bringing the charged clusters into the gas phase without damaging the inorganic core or dissociating the ligands.

In this work, we use anion photoelectron spectroscopy to probe the electron affinity (EA) and electronic structure of a series of cobalt sulfide clusters, whose ligand shells consist of differing combinations of PEt_3 and CO. The clusters $Co_6S_8(PEt_3)_{6-x}(CO)_x$ are synthesized from the parent compound $Co_6S_8(PEt_3)_6$ by ligand substitution with CO. These clusters are then brought into the gas phase, where electrons are attached to form anions, using a unique infrared desorption/photoelectron-emission/supersonic helium expansion source. Mass spectrometry confirms the existence of carbonylated products with x up to 3 (i.e. $Co_6S_8(PEt_3)_5(CO)^-$, $Co_6S_8(PEt_3)_4(CO)_2^-$, and $Co_6S_8(PEt_3)_3(CO)_3^-$). We find that the electron affinity and vertical detachment energy increase with the number of CO ligands, demonstrating the electronic spectral tunability of this family of superatoms. These results are further examples of the superatom concept, and an important step towards designing materials from programmable building blocks.

III.B.6.c. Methods

III.B.6.c.i. Synthesis

Dicobalt octacarbonyl and sulfur were purchased from Strem Chemicals. Triethylphosphine was purchased from Alfa Aesar. All other reagents and solvents were purchased from Sigma Aldrich. Dry and deoxygenated solvents were prepared by elution through a dual-column solvent system. Unless otherwise stated, all reactions and sample preparations were carried out under inert atmosphere using standard Schlenk techniques or in a N_2-filled glovebox. While a multi-step synthesis of $Co_6S_8(PEt_3)_6$ has been previously reported,[35] we have developed an alternative one-pot approach detailed below.

$Co_6S_8(PEt_3)_6$. Sulfur (1.16 g, 36.25 mmol) was suspended in ~30 mL of toluene in a 200 mL Schlenk flask under N_2 atmosphere. In two separate flasks, $Co_2(CO)_8$ (4.12 g, 12.05 mmol) and PEt_3 (4.27 g, 36.14 mmol) were dissolved in ~20 mL of toluene. The $Co_2(CO)_8$ solution was added to the S suspension, followed by quick addition of the PEt_3 solution. The reaction mixture was refluxed under N_2 for 2 days. The reaction mixture was then opened to air, and hot filtered through Celite. The filtrate was cooled to room temperature and left to stand for ~3 h. Black crystals formed during that period; the resulting suspension was filtered through a fine frit and the solid was washed with toluene, and diethyl ether. The dark, black crystals were collected, dried in vacuo, and stored under N_2. Yield: 2.2 g (42%). MS-MALDI m/z+ calculated 1317.92; found, 1317.95.

$Co_6S_8(PEt_3)_{6-x}(CO)_x$. *Safety note: CO is a toxic gas; this reaction can only be performed in a well-ventilated fumehood.* Sulfur (0.15 g, 4.68 mmol) and $Co_6S_8(PEt_3)_6$ (1.00 g, 0.76 mmol) were combined in ~75 mL of toluene in a 200 mL Schlenk flask. An external bubbler was attached to the system, and the mixture was sparged with CO for 30 min. The mixture was heated to 100 °C and stirred under a CO atmosphere for 16 h. The reaction mixture was cooled to room temperature, sparged with N_2, and the solvent was removed in vacuo. The resulting solid was used directly without further purification.

III.B.6.c.ii. Anion Photoelectron Spectroscopy

Anion photoelectron spectroscopy was conducted by crossing a mass-selected negative ion beam with a fixed energy photon beam and analyzing the energies of the resultant photodetached electrons. This technique is governed by the well-known energy-conserving relationship, $h\nu = \text{EBE} + \text{EKE}$, where $h\nu$, EBE, and EKE are the photon energy, electron binding energy (photodetachment transition energy), and the electron kinetic energy, respectively. The details of our apparatus have been described elsewhere.[36] Briefly, the photoelectron spectra were collected on an apparatus consisting of an ion source, a linear time-of-flight mass spectrometer for mass analysis and selection, and a magnetic-bottle photoelectron spectrometer for electron energy analysis (resolution ~35 meV at 1 eV EKE). The third harmonic (355 nm, 3.49 eV/photon) of a Nd:YAG was used to photodetach electrons from the cluster anion of interest. Photoelectron spectra were calibrated against the well-known atomic lines of the copper anion, Cu^-.

To make the parent anions $Co_6S_8(PEt_3)_{6-x}(CO)_x^-$ in the gas phase, a specialized infrared desorption/laser photoemission (IR/PE) supersonic helium expansion source is employed.[37] Briefly, a low power IR pulse (1064 nm) from a Nd:YAG laser hits a translating graphite bar thinly coated with the $Co_6S_8(PEt_3)_{6-x}(CO)_x$ sample. Because the graphite absorbs most of the energy, a localized thermal shock lasting a few nanoseconds propels the clusters into the gas phase. Almost simultaneously, a high power pulse of 532 nm light from a second Nd:YAG laser strikes a close-by photoemitter (Hf wire), creating a shower of electrons that attach to the evaporated neutral clusters. Also, almost simultaneously, a plume of ultrahigh purity helium gas rapidly expands from a pulsed valve located slightly upstream, cooling the nascent anions and directing them into the mass spectrometer, where they are analyzed. Because the $Co_6S_8(PEt_3)_{6-x}(CO)_x$ clusters are slightly sensitive to air and moisture, they are coated onto the graphite bar in a N_2-filled glove box. The graphite bar is then enclosed inside an air-tight "suitcase" container, which is only opened under high vacuum after being transferred to the vacuum chamber.

III.B.6.c.iii. Theoretical Calculations

First-principles electronic structure calculations on the anion and neutral forms of $Co_6S_8(PEt_3)_{6-x}(CO)_x$ ($x = 0$–3) clusters were carried out within density functional theory formalism. The ADF set of codes were used to perform the calculations where a PBE0 hybrid functional comprised of the PBE generalized gradient functional and 25% Hartree-Fock exchange, as proposed by Ernzerhof *et al.*, is used to incorporate exchange and correlation effects.[38-40] The atomic wave functions are expressed in terms of Slater-type orbitals (STO) located at the atomic sites and the cluster wave functions are constructed from a linear combination of these atomic orbitals.[41] A TZ2P basis set and a large frozen electron core was used. The zero-order regular approximation (ZORA) is used to include scalar-relativistic effect.[42,43] The trial structures of the clusters were taken from the previously optimized structure of the $Co_6Te_8(PEt_3)_6$ where the Te sites were replaced by S atoms.[33] The quasi-Newton method without any symmetry restriction is used to determine the lowest energy arrangement for each trial structure of the clusters. The calculations also covered the several possible spin states for all the clusters during optimization.

III.B.6.d. Results and discussions

Figure III.B.21A depicts the structure of $Co_6S_8(PEt_3)_{6-x}(CO)_x$. Our strategy to synthesize these clusters begins by preparing the parent compound $Co_6S_8(PEt_3)_6$ on a multigram scale. To achieve this, we have developed a new approach detailed in the Methods section. Briefly, under a CO atmosphere, $Co_6S_8(PEt_3)_6$ is reacted with six equivalents of S in toluene at ~100 °C to partially substitute CO for PEt_3, which is trapped as $S{=}PEt_3$. Using the mass spectrometry technique described below, we observe a mixture of clusters in which up to three CO ligands have been substituted for PEt_3. It is possible to

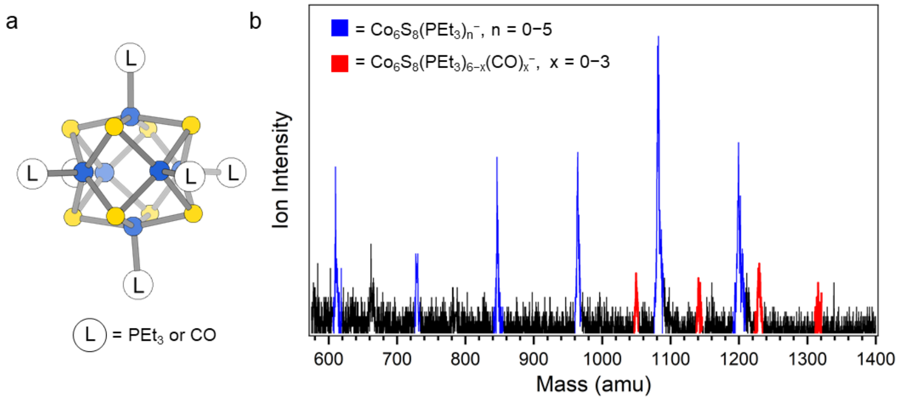

Figure III.B.21. (A) Structure of $Co_6S_8(PEt_3)_{6-x}(CO)_x$. (B) Anion mass spectrum of $Co_6S_8(PEt_3)_{6-x}(CO)_x^-$ generated using IR/PE anion source. This work focuses on the red peaks in the mass spectrum.

separate these different species using column chromatography,[30] but for this study we can use the mixture of clusters without further purification.

Measuring the electron affinity and electronic structure of $Co_6S_8(PEt_3)_{6-x}(CO)_x$ requires a negative ion photoelectron spectroscopic study on their parent anions, $Co_6S_8(PEt_3)_{6-x}(CO)_x^-$, in the gas phase. Common ionization methods (e.g. electrospray ionization and matrix-assisted laser desorption/ionization), however, fail to generate the parent anions $Co_6S_8(PEt_3)_{6-x}(CO)_x^-$ in the gas phase due to the effect of the solvent/matrix on neutral $Co_6S_8(PEt_3)_{6-x}(CO)_x$ clusters: the obtained anions are either dissociated or tagged by the solvent/matrix molecules. To make the parent anions in the gas phase, we instead employ a unique infrared desorption/photoemission (IR/PE) source as described in the Methods section. A typical anion mass spectrum of $Co_6S_8(PEt_3)_{6-x}(CO)_x^-$ obtained with the IR/PE source is shown in Figure III.B.21B. The spectrum contains two major series of anions: $Co_6S_8(PEt_3)_n^-$ (n = 0–5) and $Co_6S_8(PEt_3)_{6-x}(CO)_x^-$ (x = 0–3). The $Co_6S_8(PEt_3)_n^-$ clusters are from the sequential dissociation of PEt_3 from $Co_6S_8(PEt_3)_6$ during infrared desorption, while the $Co_6S_8(PEt_3)_{6-x}(CO)_x^-$ clusters are the anions of interest in this study. Though the $Co_6S_8(PEt_3)_{6-x}(CO)_x^-$ signals are weaker, their high photodetachment cross-sections allow us to collect their anion photoelectron spectra.

Figure III.B.22 presents the anion photoelectron spectra of $Co_6S_8(PEt_3)_{6-x}(CO)_x^-$ (x = 0–3) from which the adiabatic electron affinity (AEA) and vertical detachment energy (VDE) of each cluster are determined. The value of the AEA is taken to be the onset of the lowest electron binding energy (EBE) peak in the photoelectron spectrum. The VDE is the vertical transition energy from the ground state of the anion to the neutral state at the anion

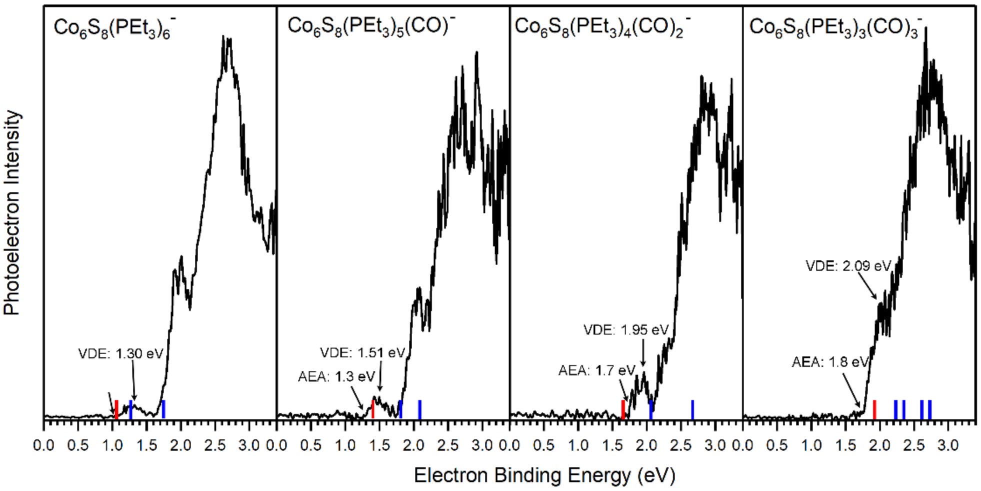

Figure III.B.22. Negative ion photoelectron spectra of $Co_6S_8(PEt_3)_{6-x}(CO)_x^-$ (x = 0–3) anions collected using 355 nm (3.49 eV) photons from a Nd:YAG laser. The arrows point to the experimental values of AEA and VDE; the red lines correspond to theoretical AEA, and the blue lines correspond to vertical transitions from the anion to the singlet and triplet neutral states.

geometry. It is determined as the EBE value at the intensity maximum of the peak of interest, i.e. typically the first EBE peak. Based on the anion photoelectron spectra, the AEA values of $Co_6S_8(PEt_3)_{6-x}(CO)_x$ are 1.1, 1.3, 1.7 and 1.8 eV for x = 0, 1, 2, 3, respectively, while the corresponding anion VDE values are 1.30, 1.51, 1.95 and 2.09 eV, respectively. By sequentially substituting half of the PEt_3 ligands with CO, the AEA of this superatom increases from 1.1 eV to 1.8 eV, all while maintaining the same oxidation state for the Co_6S_8 core. As a reference, the reducing agent SO_2 and oxidizing agent SO_3 have AEA values of 1.11 eV and 1.90 eV,[44,45] respectively, where the increase in AEA is the result of the change in the S atom oxidation state. Thus, the observed changes in AEA values for the ligated superatoms are significant, given that the oxidation state of the Co_6S_8 core does not change across the ligation series: these results underscore the remarkable characteristics of the superatoms. The observed unambiguous trend of increasing AEA and

VDE values with ligand substitution is a direct evidence that the electronic properties of this superatom can be tuned effectively in this way.

The tuning of the electronic properties can be further demonstrated through the spectral features located at higher electron binding energies than that of the first EBE peak. These higher EBE peaks arise from transitions from the anion ground state to various excited electronic states of the neutral cluster. The shape of these features relates to the electronic structure of the neutral clusters. While the photoelectron spectra of $Co_6S_8(PEt_3)_{6-x}(CO)_x^-$ shift to higher electron binding energy as x increases, the overall spectral shapes are remarkably similar, confirming that the sequential exchange of PEt_3 with CO ligand leaves the essential electronic structure of $Co_6S_8(PEt_3)_{6-x}(CO)_x$ superatoms largely unchanged. What is changing with sequential ligation, however, is a monotonic decrease in the energies of the highest occupied and lowest unoccupied molecular orbital (HOMO and LUMO) levels, even though the gap between them remains relatively constant. This is discussed further below.

To support these experimental observations, we modeled the ground state structures of $Co_6S_8(PEt_3)_{6-x}(CO)_x^-$, and calculated their AEA and VDE using density functional theory formalism (Figure III.B.23). In agreement with previous calculations of the $Co_6Te_8(PEt_3)_{6-x}(CO)_x$ system,[33] we find that the anionic clusters $Co_6S_8(PEt_3)_{6-x}(CO)_x^-$ have doublet spin ground states, while the neutral species have singlet spin states. For $Co_6S_8(PEt_3)_4(CO)_2^-$, there are two possible structures: *trans*-$Co_6S_8(PEt_3)_4(CO)_2^-$ and *cis*-$Co_6S_8(PEt_3)_4(CO)_2^-$, with the latter lower in energy by 0.20 eV. The replacement of three PEt_3 ligands with CO leads to *fac*-$Co_6S_8(PEt_3)_3(CO)_3^-$ and *mer*-$Co_6S_8(PEt_3)_3(CO)_3^-$

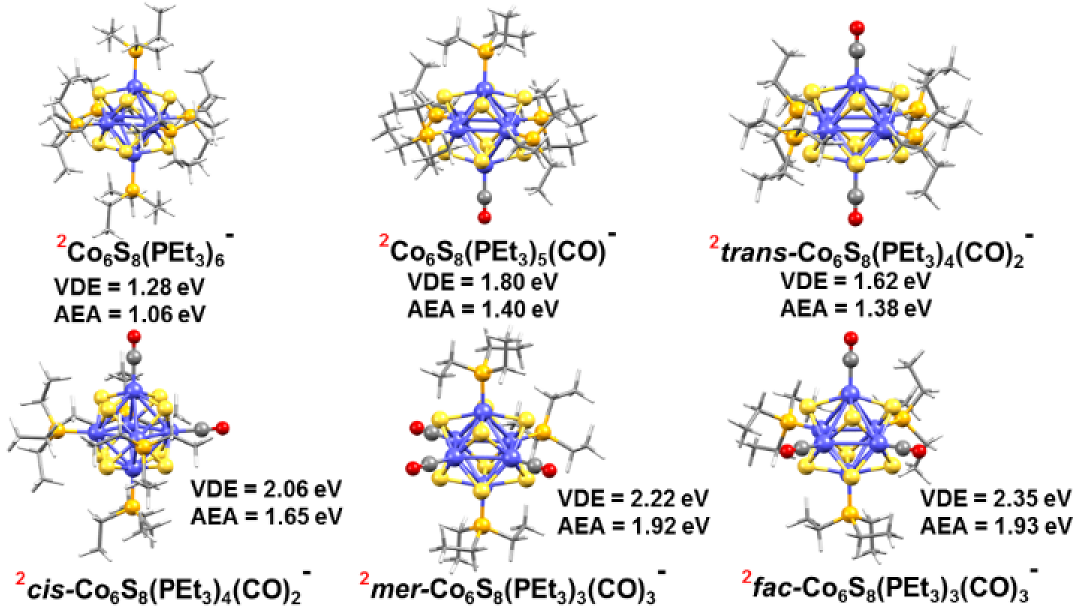

Figure III.B.23. Optimized ground state structure of anionic $Co_6S_8(PEt_3)_{6-x}(CO)_x^-$ (x = 0–3) clusters. The red superscript indicates the spin multiplicity (2S+1) of each cluster.

isomers, with the latter isomer lower in energy by 0.07 eV. The small energy difference between the $Co_6S_8(PEt_3)_3(CO)_3^-$ isomers suggests their co-existence in the experimental beam. Table S1 contains more calculation results on neutral and anionic species.

We modeled the electronic structure of the superatoms using the anion photoelectron spectra as fingerprints of the ground state geometry and electronic states of both the neutral and anionic clusters.[46] Three points of comparison are used to establish the theoretical ground state of the system: AEA, VDE and VDE*. VDE and VDE* are the vertical transitions from the anion ground state to the neutral with singlet and triplet spin multiplicity, respectively. Experimentally, VDE and VDE* correspond to the electron binding energies of the first (lowest EBE) and second (next highest EBE) peaks in the photoelectron spectra.

Table III.B.8 presents both theoretical and experimental values of AEA, VDE and VDE* for all the superatoms considered here. Using AEA, VDE and VDE* as references to validate the computation, we observe close agreement between experimental and calculated values. The agreement between experiments and calculations is further demonstrated by including the computed values in the anion photoelectron spectra in Figure III.B.22. The key result is that the AEA and both VDE values increase as PEt_3 ligands are successively replaced with CO. Starting with $Co_6S_8(PEt_3)_6^-$, the calculated AEA, VDE, and VDE* values of 1.06, 1.28, and 1.74 eV are close to the experimental values of 1.1, 1.30 eV, and 1.91 eV, respectively. Experimentally, the replacement of one PEt_3 with a CO ligand results in a ~0.2 eV increase in the AEA (1.3 eV) and VDE values (1.51 and 2.05 eV), whereas the calculated AEA (1.40 eV) and VDE values (1.80 and 2.08 eV) for $Co_6S_8(PEt_3)_5CO^-$ are only slightly higher. For *cis*-$Co_6S_8(PEt_3)_4(CO)_2^-$ and *trans*-

TABLE III.B.8. THEORETICAL AND EXPERIMENTAL ADIABATIC AND VERTICAL DETACHMENT ENERGIES (1^{ST} AND 2^{ND} PEAK) OF $Co_6S_8(PEt_3)_{6-x}(CO)_x^-$ (X = 0–3) CLUSTERS. THE SUPERSCRIPTS T AND E INDICATE THEORETICAL AND EXPERIMENTAL VALUES, RESPECTIVELY.

Anionic Clusters	**AEA^T (eV)**	**VDE^T (eV)**		**AEA^E (eV)**	**VDE^E (eV)**	
		VDE	**VDE***		**VDE**	**VDE***
$Co_6S_8(PEt_3)_6^-$	1.06	1.28	1.74	1.1	1.30	1.91
$Co_6S_8(PEt_3)_5(CO)^-$	1.40	1.80	2.08	1.3	1.51	2.05
cis-$Co_6S_8(PEt_3)_4(CO)_2^-$	1.65	2.06	2.66	1.7	1.95	2.51
trans-$Co_6S_8(PEt_3)_4(CO)_2^-$	1.38	1.62	2.16			
mer-$Co_6S_8(PEt_3)_3(CO)_3^-$	1.92	2.22	2.71	1.8	2.09	2.67
fac-$Co_6S_8(PEt_3)_3(CO)_3^-$	1.93	2.35	2.60			

$Co_6S_8(PEt_3)_4(CO)_2^-$, the computed ground states have AEA values of 1.65 and 1.38 eV, VDE values of 2.06 and 1.62 eV, and VDE* values of 2.66 and 2.16 eV, respectively. Note that the experimental results for $Co_6S_8(PEt_3)_4(CO)_2^-$ (AEA = 1.7 eV, VDE = 1.95 eV, and VDE* = 2.51 eV) agree best with the *cis*-isomer calculations. For n = 3, both the *mer*-$Co_6S_8(PEt_3)_3(CO)_3^-$ and *fac*-$Co_6S_8(PEt_3)_3(CO)_3^-$ have similar computed AEA and VDE values that are consistent with the experimental data. Because the *mer*- and *fac*-clusters are close in energy in their neutral and anionic forms, it is very likely that they both exist in the ion beam, and that the $Co_6S_8(PEt_3)_3(CO)_3^-$ photoelectron spectrum contains transitions from both isomers.

The replacement of PEt_3 ligands by CO concurrently lowers the energies of the HOMO and LUMO, with the result that the HOMO-LUMO gap is essentially unchanged across the cluster series. Figure III.B.24A illustrates this trend for the neutral species while their absolute energy values are given in Table S1. The lowering of the HOMO and LUMO can be in part understood in terms of the vastly different ligand field effect of the cluster surface passivation: PEt_3 is a strong σ-donor that increases the electron density in the core while CO is a strong π-acceptor that removes electron density from the core, thus lowering the energy of the electronic spectrum.[33] This behavior can be seen in the Figures S1 and S2 which show the one-electron energy levels of $Co_6S_8(PEt_3)_{6-x}(CO)_x$ (x = 0–3). The change in the AEA closely tracks the change in the LUMO as the electron is attached to the LUMO of the neutral. This is illustrated in Figure III.B.24B, which shows the changes in the energy of the LUMO (ΔLUMO), theoretical AEA (ΔAEA^T) and experimental AEA (ΔAEA^E) of $Co_6S_8(PEt_3)_{6-x}(CO)_x$ as x increases from 0 to 3.

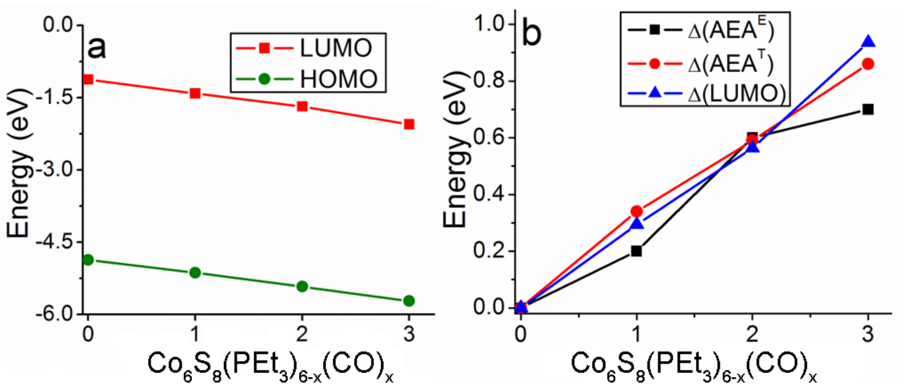

Figure III.B.24. (A) The absolute energy values of the HOMO and LUMO for neutral $Co_6S_8(PEt_3)_{6-x}(CO)_x$ (x = 0–3). (B) Incremental differences in the experimental AEA values, the theoretical AEA values, and the LUMO values of $Co_6S_8(PEt_3)_{6-x}(CO)_x$, each with respect to $Co_6S_8(PEt_3)_6$.

An additional phenomenon combines with the traditional ligand field effect to explain the changes in AEA and VDE: PEt_3 and CO form charge transfer complexes, and the induced dipoles at the cluster surface play a critical role in changing the electronic properties. As a reference, surface dipoles can either increase or decrease the work function of metals.[47,48] In this case, as PEt_3 ligands are replaced by CO, the sign of the dipole changes and hence AEA increases as more CO are bound to the core. Overall, though the ionization energy of $Co_6S_8(PEt_3)_{6-x}(CO)_x$ is not directly measured, the successive rise in AEA and lowering of HOMO are evidence of a trend of increasing ionization energy as PEt_3 is replaced by CO.

III.B.6.e. Conclusion

By combining cluster synthesis, gas-phase anion photoelectron spectroscopy, and electronic structure calculations, we have demonstrated that the electronic properties of metal chalcogenide superatomic clusters can be tuned by varying their capping ligands. While the total electron count of the closed-shell core remains unchanged, substitution of the ligands leads to a simultaneous rise or fall of the HOMO and LUMO levels, resulting in a change of the cluster donor/acceptor behavior. This is exciting at many different levels: for example, we recently showed that these clusters could be used as electron-donating or electron-accepting surface dopants for two-dimensional semiconductors, where the band structures can be controlled by the choice of ligands.[32,49] Such dopants could also be made magnetic because of their finite spin moments.[50] More broadly, our results open the door to the design of tunable functional materials from superatomic building blocks.

Acknowledgements

This material is based on work supported by the Office of Naval Research (ONR), Multidisciplinary University Research Initiative (MURI) under Grant No. N00014-15-1-2681 (KHB), and by the Air Force Office of Scientific Research (AFOSR) under grant number, FA9550-15-1-0259 (KHB). The synthetic work was supported by the NSF MRSEC program through the Center for Precision Assembly of Superstratic and Superatomic Solids (DMR-1420634) (XR) and the US Air Force Office of Scientific Research (AFOSR) Grant No. FA9550-18-1-0020 (XR). Theoretical studies (VC and SNK) were supported by a grant from U.S. Department of Energy (DOE) under the Award No. DE-SC0006420. Part of the theoretical computations used the resources of the National Energy Research Scientific Computing Center, a DOE Office of Science User Facility supported by the Office of Science of the U.S. Department of Energy under Contract No. DE-AC02-05CH11231 (VC and SNK). AP was supported by the NSF Graduate Research Fellowship Program (DGE-16-44869).

References

1. A. Pinkard, A. M. Champsaur, and X. Roy, *Acc. Chem. Res.* **51**, 919 (2018).

2. S. A. Claridge, A. W. Castleman, S. N. Khanna, C. B. Murray, A. Sen, and P. S. Weiss, *ACS Nano*. **3**, 244 (2009).

3. E. G. Tulsky and J. R. Long, *Chem. Mater*. **13**, 1149 (2001).

4. S. A. Baudron, P. Batail, C. Coulon, R. Clerac, E. Canadell, V.´ Laukhin, R. Melzi, P. Wzietek, D. Jerome, P. Auban-Senzier, and S.´ Ravy, *J. Am. Chem. Soc.* **127**, 11785 (2005).

5. B. Yoon, W. D. Luedtke, R. N. Barnett, J. Gao, A. Desireddy, B. E. Conn, T. Bigioni, and U. Landman, *Nat. Mater.* **13**, 807 (2014).

6. J. F. Corrigan, O. Fuhr, and D. Fenske, *Adv. Mater*. **21**, 1867 (2009).

7. X. Roy, C.-H. Lee, A. C. Crowther, C. L. Schenck, T. Besara, R. A. Lalancette, T. Siegrist, P. W. Stephens, L. E. Brus, P. Kim, M. L. Steigerwald, and C. Nuckolls, *Science* **341**, 157 (2013).

8. S. N. Khanna and P. Jena, *Phys. Rev. B*. **51**, 13705 (1995).

9. A. W. Castleman and S. N. Khanna, *J. Phys. Chem. C* **113**, 2664 (2009).

10. A. C. Reber and S. N. Khanna, *Acc. Chem. Res*. **50**, 255 (2017).

11. C.-H. Lee, L. Liu, C. Bejger, A. Turkiewicz, T. Goko, C. J. Arguello, B. A. Frandsen, S. C. Cheung, T. Medina, T. J. S. Munsie, R. D'Ortenzio, G. M. Luke, T. Besara, R. A. Lalancette, T. Siegrist, P. W. Stephens, A. C. Crowther, L. E. Brus, Y. Matsuo, E. Nakamura, Y. J. Uemura, P. Kim, C. Nuckolls, M. L. Steigerwald, and X. Roy, *J. Am. Chem. Soc*. **136**, 16926 (2014).

12. X. Roy, C. L. Schenck, S. Ahn, R. A. Lalancette, L. Venkataraman, C. Nuckolls, and M. L. Steigerwald, *Angew. Chem., Int. Ed*. **51**, 12473 (2012).

13. M. T. Trinh, A. Pinkard, A. B. Pun, S. N. Sanders, E. Kumarasamy, M. Y. Sfeir, L. M. Campos, X. Roy, and X.-Y. Zhu, *Sci. Adv*. **3**, e1700241 (2017).
14. V. Chauhan, S. Sahoo, S. N. Khanna, *J. Am. Chem. Soc*. **138**, 1916 (2016).
15. S. N. Khanna and A. C. Reber, *Nat. Chem*. **9**, 1151 (2017).
16. D. A. Tomalia and S. N. Khanna, *Chem. Rev.* **116**, 2705 (2016).
17. Z. Zheng, J. R. Long, and R. H. Holm, *J. Am. Chem. Soc.* **119**, 2163 (1997).
18. M. Cargnello, A. C. Johnston-Peck, B. T. Diroll, E. Wong, B. Datta, D. Damodhar, V. V. T. Doan-Nguyen, A. A. Herzing, C. R. Kagan, and C. B. Murray, *Nature* **524**, 450 (2015).
19. M. N. O'Brien, M. R. Jones, B. Lee, and C. A. Mirkin, *Nat. Mater.* **14**, 833 (2015).
20. B. Yoon, W. D. Luedtke, R. N. Barnett, J. Gao, A. Desireddy, B. E. Conn, T. Bigioni, and U. Landman, *Nat. Mater.* **13**, 807 (2014).
21. C. L. Poyser, T. Czerniuk, A. Akimov, B. T. Diroll, E. A. Gaudling, A. S. Salasyuk, A. J. Kent, D. R. Yakovlev, M. Bayer, and C. B. Murray, *ACS Nano*. **10**, 1163 (2016).
22. W.-L. Ong, S. M. Rupich, D. V. Talapin, A. J. H. McGaughey, and J. A. Malen, *Nat. Mater*. **12**, 410 (2013).
23. A. Voevodin, L. M. Campos, and X. Roy, *J. Am. Chem*. *Soc*. **140**, 5607 (2018).
24. A. M. Champsaur, J. Yu, X. Roy, D. W. Paley, M. L. Steigerwald, C. Nuckolls, and C. M. Bejger, *ACS Cent. Sci.* **3**, 1050 (2017).
25. A. M. Champsaur, C. Mézière, M. Allain, D. W. Paley, M. L. Steigerwald, C. Nuckolls, and P. Batail, *J. Am. Chem. Soc.* **139**, 11718 (2017).

26. E. S. O’Brien, M. T. Trinh, R. L. Kann, J. Chen, G. A. Elbaz, A. Masurkar, T. L. Atallah, M. V. Paley, N. Patel, D. W. Paley, I. Kymissis, A. C. Crowther, A. J. Millis, D. R. Reichman, X.-Y. Zhu, and X. Roy, *Nat. Chem.* **9**, 1170 (2017).
27. G. Lovat, B. Choi, D. W. Paley, M. L. Steigerwald, L. Venkataraman, and X. Roy, *Nat. Nanotechnol.* **12**, 1050 (2017).
28. W.-L. Ong, E. S. O’Brien, P. S. M. Dougherty, D. W. Paley, C. Fred Higgs Iii, A. J. H. McGaughey, J. A. Malen, and X. Roy, *Nat. Mater.* **16**, 83 (2017).
29. B. Choi, J. Yu, D. W. Paley, M. Tuan Trinh, M. V. Paley, J. M. Karch, A. C. Crowther, C. H. Lee, R. A. Lalancette, X. Zhu, K. Kim, M. L. Steigerwald, C. Nuckolls, and X. Roy, *Nano Lett*. **16**, 1445 (2016).
30. A. M. Champsaur, A. Velian, D. W. Paley, B. Choi, X. Roy, M. L. Steigerwald, and C. Nuckolls, *Nano Lett.* **16**, 5273 (2016).
31. A. Turkiewicz, D. W. Paley, T. Besara, G. Elbaz, A. Pinkard, T. Siegrist, and X. Roy, *J. Am. Chem. Soc.* **136**, 15873 (2014).
32. J. Yu, C. H. Lee, D. Bouilly, M. Han, P. Kim, M. L. Steigerwald, X. Roy, and C. Nuckolls, *Nano Lett.* **16**, 3385 (2016).
33. V. Chauhan, A. C. Reber, and S. N. Khanna, *J. Am. Chem. Soc.* **139**, 1871 (2017).
34. V. Chauhan and S. N. Khanna, *J. Phys. Chem. A* **122** 6014 (2018).
35. F. Cecconi, C. A. Ghilardi, S. Midollini, and A. Orlandini, *Inorg. Chimica Acta* **76**, 183 (1983).
36. X. Zhang, G. Liu, G. Gantefoer, K. H. Bowen, and A. N. Alexandrova, *J. Phys. Chem. Lett.* **5**, 1596 (2014).

37. A. Grubisic, H. Wang, X. Li, Y. J. Ko, S. Kocak, M. R. Pederson, K. H. Bowen, and B. W. Eichhorn, *PNAS* **108**, 14757 (2011).
38. J. P. Perdew and W. Yue, *Phys. Rev. B* **33**, 8800 (1986).
39. M. Ernzerhof and G. E. Scuseria, *J. Chem. Phys.* **110**, 5029 (1999).
40. C. Adamo, *J. Chem. Phys*. **110**, 6158 (1999).
41. E. van Lenthe and E. J. Baerends, *J. Comput. Chem*. **24**, 1142 (2003).
42. E. van Lenthe, R. van Leeuwen, E. J. Baerends, and J. G. Snijders, J. G. *Int. J. Quantum Chem*. **57**, 281 (1996).
43. E. van Lenthe, A. Ehlers, and E. J. Baerends, *J. Chem. Phys*. **110**, 8943 (1999).
44. M. R. Nimlos and G. B. Ellison, *J. Phys. Chem*. **90**, 2574 (1986).
45. E. W. Rothe, S. Y. Tang, and G. P. Reck, *J. Chem. Phys*. **62**, 3829 (1975).
46. P. J. Robinson, G. Liu, S. Ciborowski, C. Martinez-Martinez, J. R. Chamorro, X. Zhang, T. M. McQueen, K. H. Bowen, and A. N. Alexandrova, *Chem. Mater*. **29**, 9892 (2017).
47. P. C. Rusu and G. Brocks, *J. Phys. Chem. B* **110**, 22628 (2006).
48. V. Chauhan, A. C. Reber, and S. N. Khanna, *Nature Comm*. **9**, 2357 (2018).
49. A. C. Reber and S. N. Khanna, *NPJ Computational Material* **4**, 33 (2018).
50. V. Chauhan, A. C. Reber, and S. N. Khanna, *Phys. Chem. Chem. Phys*. **19**, 31940 (2017).

III.B.7. Ligand Effect on the Electronic Structure of Cobalt Sulfide Clusters: A Combined Experimental and Theoretical Study

Gaoxiang Liu, Vikas Chauhan, Alexander P. Aydt, Sandra M. Ciborowski, Andrew Pinkard, Zhaoguo Zhu, Xavier Roy, Shiv N. Khanna, and Kit H. Bowen

Reproduced (adapted) with permission from *J. Phys. Chem. C* **41** 25121 (2019).

III.B.7.a. Abstract

Recent studies have shown that capping ligands offer a new dimension for fine tuning the properties of clusters. Here we investigate this concept by measuring the anion photoelectron spectra of a series of hexanuclear cobalt sulfide clusters, Co_6S_8, passivated by different numbers of triethylphosphine ligands, PEt_3. We find that the addition of PEt_3 gradually shifts the electronic spectrum of the cluster to higher energy, leading to a decrease in its electron affinity. Density functional theory calculations reveal that adding ligands demagnetize the Co_6S_8 core. The decrease in electron affinity results from a monotonic increase in the energy of the cluster lowest unoccupied molecular orbitals (LUMO). This effect is attributed to the electron donation from the ligands to the cluster core, which increases the charge density in the core region.

III.B.7.b. Introduction

Quantum confinement in small symmetric clusters can result in a grouping of electronic states into shells, leading to the formation of stable clusters with a well-defined valence. The resemblance to atomic shells has prompted the description of such entities as superatoms.[1] Utilizing these clusters as the "superatomic" building blocks for the assembly of novel materials represents a frontier in material science.[1-22] Within this context, the family of metal chalcogenide molecular clusters has recently received renewed attention for fabricating functional materials with tunable properties including ferromagnetism, electrical conductivity, optical gaps and thermal conductivity switching.[2,7,23-32] One of the key advantages of such materials over traditional atomic solids is that the properties of the superatomic building blocks can be tailored pre-assembly. While the composition and structure of the cluster are traditionally used to control the behavior of the superatomic building unit, the capping ligands have recently received attention as valuable knobs for fine tuning.[33,34] Capping ligands can modulate the electronic characteristics of the cluster core, and direct the assembly into solid state materials.

Recently, Khanna and coworkers theoretically predicted a variety of properties that can be tuned by modifying the capping ligands of metal chalcogenide clusters. Using $Co_6Te_8L_6$ (L = capping ligand) as a model system, they have shown that changing L from PEt_3 to CO increases the electron affinity of the cluster, in effect transforming it from a superatomic alkali metal to a superatomic halogen.[14] Such an ability to alter the donor/acceptor behavior of the building blocks offers unique opportunity for creating materials with fine-tuned properties.[34] In a related study, it was predicted that the ionization energy of the Co_6Se_8 cluster can be gradually decreased by sequentially coordinating PEt_3 capping ligands to its surface metal atoms.[35] Binding carbon monoxide (CO) ligands to the Co_6Se_8 cluster, on the other hand, results in the gradual demagnetization of the core, thus stabilizing it.[36] Experimentally demonstrating these predictions by measuring the electronic structures of metal chalcogenide clusters is challenging, however, because it requires bringing the charged clusters with a controlled number of ligands into the gas phase without damaging the inorganic core. Common ionization methods (e.g., electrospray ionization and matrix-assisted laser desorption/ionization) fail to generate the desirable anions in the gas phase due to the effect of the solvent/matrix on charged clusters: the obtained anions are either dehydrogenated or tagged by the solvent/matrix molecules.

We recently reported an experimental study supported by theoretical calculations establishing the tunability of the electronic properties of the cluster $Co_6S_8(PEt_3)_{6-n}(CO)_n$ by altering the ligand ratio.[38] The unique infrared desorption/laser photoemission (IR/PE) supersonic expansion source used in that work serves as the ideal tool to bring the cluster into the gas phase with different number of ligands while maintaining the core structure. Here we employ this method to investigate a series of cobalt sulfide clusters passivated with varying numbers of PEt_3 ligands. The cluster $Co_6S_8(PEt_3)_6$ is synthesized and then brought into the gas phase, where ligands are sequentially dissociated and electrons are attached to form anions, using the IR/PE source. Mass spectrometry confirms the existence of $Co_6S_8(PEt_3)_x^-$ with x ranging from 0 to 6. We find that the electron affinity and vertical detachment energy decrease with increasing ligation, demonstrating the electronic spectral tunability of this family of superatoms.

III.B.7.c. Methods

III.B.7.c.i. Synthesis

Dicobalt octacarbonyl and sulfur were purchased from Strem Chemicals. PEt_3 was obtained from Alfa Aesar. All other reagents and solvents were purchased from Sigma Aldrich. Dry and deoxygenated solvents were prepared by elution through a dual-column solvent system (MBraun). Unless otherwise stated, all reactions and sample preparations were carried out under inert atmosphere using standard Schlenk techniques or in a N_2-filled glovebox. While a multi-step synthesis of $Co_6S_8(PEt_3)_6$ has been previously reported,[37] we have developed an alternative one-pot approach detailed below.[38]

$Co_6S_8(PEt_3)_6$. Sulfur (1.16 g, 36.25 mmol) was suspended in 30 mL of toluene in a 200 mL Schlenk flask. In two separate flasks, $Co_2(CO)_8$ (4.12 g, 12.05 mmol) and PEt_3 (4.27 g, 36.14 mmol) were dissolved in 20 mL of toluene. The $Co_2(CO)_8$ solution was added to the S suspension, followed by quick addition of the PEt_3 solution. The reaction mixture was refluxed under N_2 for 2 days. The reaction mixture was then opened to air, and hot filtered through Celite. The filtrate was cooled to room temperature and left to stand for ~3 h. Black crystals formed during that period; the resulting suspension was filtered through a fine frit and the solid was washed with toluene, and diethyl ether. The dark, black crystals were collected, dried *in vacuo*, and stored under N_2. Yield: 2.2 g (42%). The characterization data are as previously published. MS-MALDI m/z^+ calculated 1317.92; found, 1317.95.

III.B.7.c.ii. Anion photoelectron spectroscopy

Anion photoelectron spectroscopy was conducted by crossing a mass-selected negative ion beam with a fixed energy photon beam and analyzing the energies of the resultant photodetached electrons. This technique is governed by the well-known energy-conserving relationship, $h\nu = \mathrm{EBE} + \mathrm{EKE}$, where $h\nu$, EBE, and EKE are the photon energy, electron binding energy (photodetachment transition energy), and the electron kinetic energy, respectively. The details of our apparatus have been described elsewhere.[39,40] Briefly, the photoelectron spectra were collected on an apparatus consisting of an ion source, a linear time-of-flight mass spectrometer for mass analysis and selection, and a magnetic-bottle photoelectron spectrometer for electron energy analysis (resolution

~35 meV at 1 eV EKE). The third harmonic (355 nm, 3.49 eV per photon) of a Nd:YAG was used to photodetach electrons from the cluster anion of interest. Photoelectron spectra were calibrated against the well-known atomic lines of the copper anion, Cu^-.

To make $Co_6S_8(PEt_3)_x^-$ in the gas phase, a specialized infrared desorption/laser photoemission (IR/PE) supersonic helium expansion source was employed.[38,41] Briefly, a low power IR pulse (1064 nm) from a Nd:YAG laser hit a translating graphite bar thinly coated with the $Co_6S_8(PEt_3)_6$ sample. Because the graphite absorbed most of the energy, a localized thermal shock lasting a few nanoseconds propelled the clusters into the gas phase. Almost simultaneously, a high power pulse of 532 nm light from a second Nd:YAG laser struck a close-by photoemitter (Hf wire), creating a shower of electrons that attached to the evaporated neutral clusters. Also, almost simultaneously, a plume of ultrahigh purity helium gas rapidly expanded from a pulsed valve located slightly upstream, cooling the nascent anions and directing them into the mass spectrometer, where they were analyzed. The $Co_6S_8(PEt_3)_6$ cluster was coated onto a graphite bar in a N_2-filled glove box, which was then enclosed inside an air-tight "suitcase" container and opened under high vacuum after being transferred to the vacuum chamber.

III.B.7.c.iii. Theoretical calculations

Electronic structure modeling of the anion and neutral $Co_6S_8(PEt_3)_x$ ($x = 1–5$) were carried out to understand the variation in the adiabatic and vertical detachment energies at the microscopic level. The exchange-correlation effects are included via a generalized gradient functional PBE detailed by Perdew et al.[42] The cluster wave function is formed from a linear combination of atomic orbitals constructed from Slater-type orbitals located on the atomic sites.[43] A TZ2P basis set and a large frozen electron core ($S{:}1s^22s^2p^6$, Co:1s^{2}2s^{2}p^{6}3s^{2}p^6, P:1s^{2}2s^{2}p^6, C:1s^2) are used. The calculations incorporate a zero-order regular approximation (ZORA) to include scalar-relativistic effect.[44,45] The trial structures of the clusters are taken from the previously optimized structure of the $Co_6Se_8(PEt_3)_x$ where the Se sites are replaced by S. A quasi-Newton method without any symmetry restriction allowed a determination of the ground state of the clusters. During optimization, we investigated all possible spin states. Also, none of the clusters in their ground states has the spin-contamination. The adiabatic electron affinity (AEA) is calculated as the difference between the total energy between the anion in its ground state geometry and the neutral cluster in its ground state geometry, while the vertical detachment energy (VDE) is given by the total energy difference between the anion in its ground state and the neutral cluster in the geometry of the anion.

III.B.7.d. Results and discussions

Figure III.B.25 presents a typical mass spectrum of $Co_6S_8(PEt_3)_x^-$ obtained with the IR/PE source. The ultrashort thermal shock induced by IR laser irradiation caused the sequential dissociation of the PEt_3 ligand during the vaporization of the solid $Co_6S_8(PEt_3)_6$ sample into gas phase. $Co_6S_8(PEt_3)_x^-$ with x ranging from 0 to 6 were generated and investigated by anion photoelectron spectroscopy.

Figure III.B.26 presents the anion photoelectron spectra of $Co_6S_8(PEt_3)_x^-$ (x = 2–5) collected with 355 nm (3.49 eV) 3rd harmonic laser. The spectrum of $Co_6S_8(PEt_3)_6^-$ has been published in a previous report.[38] Our attempts to measure the photoelectron spectra of $Co_6S_8^-$ and $Co_6S_8(PEt_3)^-$ (x = 0 and 1) with a 355 nm laser were for the most part unsuccessful: for $Co_6S_8^-$, no photoelectron signal was observed, i.e., its AEA and VDE are above 3.49 eV, while for $Co_6S_8(PEt_3)^-$, only a small portion of its spectrum could be

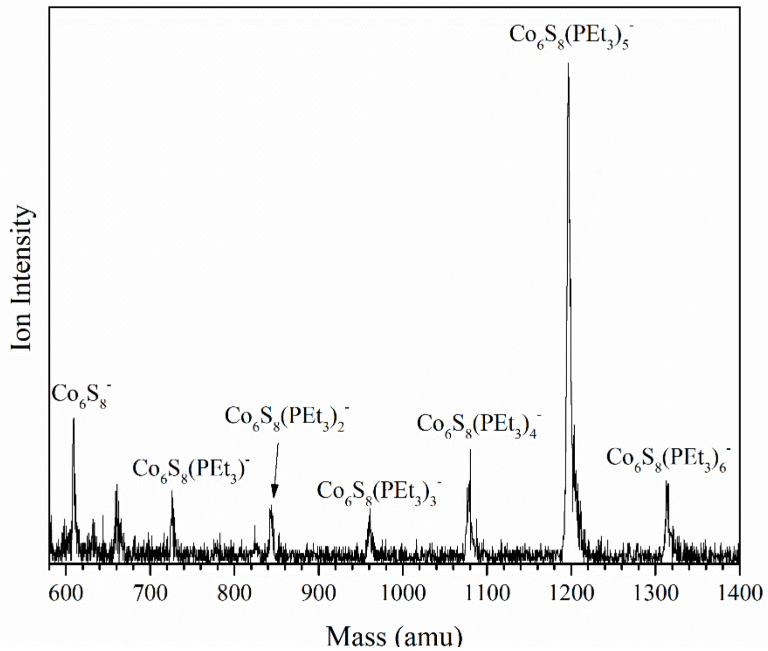

Figure III.B.25. ANION MASS SPECTRUM OF $Co_6S_8(PEt_3)_x^-$ GENERATED USING IR/PE ANION SOURCE.

collected because the majority of its photoelectron spectrum lies beyond the photon energy (Figure S1). The AEA and VDE of each cluster are determined from the photoelectron spectra. The value of the AEA is taken to be the onset of the lowest electron binding energy (EBE) peak in the photoelectron spectrum. The VDE is the vertical transition energy from the ground state of the anion to the neutral ground electronic state at the anion geometry. It is determined as the EBE value at the intensity maximum of the peak of interest. Here, however, due to the large number of electronic states that can be accessed during the photodetachment process, the photoelectron spectra are convoluted. We therefore determine the VDE as the EBE of the first noticeable peak in each spectrum. Based on the anion photoelectron spectra, the AEA values of $Co_6S_8(PEt_3)_x$ are 3.0, 2.6, 2.2, 2.0 and 1.8 eV for $x = 1, 2, 3, 4$, and 5, respectively, while the corresponding anion VDE values are 3.22, 2.71, 2.44, 2.31, and 2.05 eV, respectively. We also report the VDE* values, which

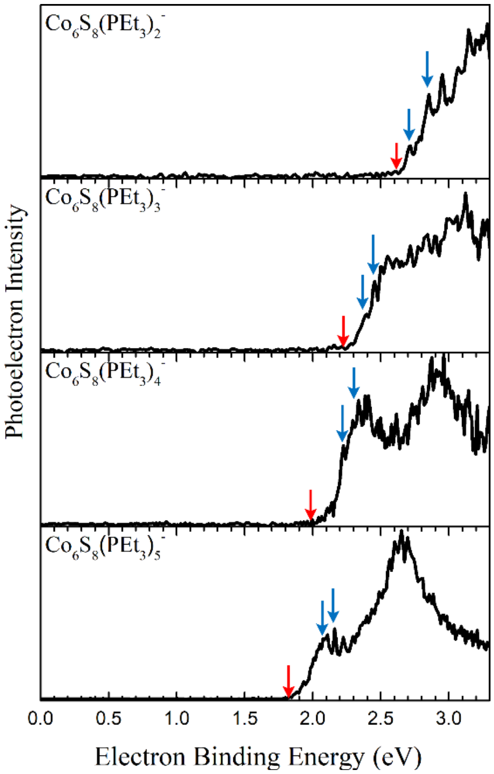

Figure III.B.26. NEGATIVE ION PHOTOELECTRON SPECTRA OF $Co_6S_8(PEt_3)_x^-$ ($x = 2-5$) ANIONS COLLECTED USING 355 NM (3.49 EV) PHOTONS FROM A ND:YAG LASER. THE RED ARROWS INDICATE THE AEA, THE BLUE ARROWS INDICATE THE VDE AND THE VDE*.

correspond to the transition from the anion ground state to the first electronic excited state of the neutral, as the EBE of the second noticeable peak. Their values are 3.35, 2.85, 2.45. 2.29 and 2.16 eV for x = 1, 2, 3, 4, and 5, respectively. By sequentially adding PEt_3 ligands to the Co_6S_8 core, the AEA and VDE of this superatom decrease systematically, which is consistent with the electron-donating nature of the PEt_3 ligands.

Changes in the electronic properties of the cluster are evident in high energy spectral features above the first EBE peak. These higher EBE peaks arise from transitions from the anion ground state to excited electronic states of the neutral cluster and the shape of these features relates to the electronic structure of the neutral clusters. As x increases, the photoelectron spectra of $Co_6S_8(PEt_3)_x^-$ shifts to lower electron binding energy and the overall spectral shapes change significantly. Such observation suggests a change in the electronic structure of $Co_6S_8(PEt_3)_x^-$ as x changes. Note that this is different from the previous study of $Co_6S_8(PEt_3)_{6-n}(CO)_n^-$ where the photoelectron spectra shift to higher electron binding energy as the CO ratio increases, but the overall spectral shapes are maintained, indicating that the essential electronic structure of $Co_6S_8(PEt_3)_{6-n}(CO)_n$ superatoms are largely unchanged.[38]

The structures of the anionic and neutral $Co_6S_8(PEt_3)_x$ clusters were investigated by theoretical calculations. Figure III.B.27 shows the optimized ground state geometries of $Co_6S_8(PEt_3)_x^-$, while those of the neutral species are in Figure S2. For x = 2 and x = 4, the clusters can either be *cis* or *trans* isomers. In both cases, the *trans* isomers are higher in energy, by ~0.14 and ~0.22 eV, respectively. A similar situation arises for the corresponding neutral clusters: the *trans* isomers are ~0.01 and ~0.25 eV higher in energy

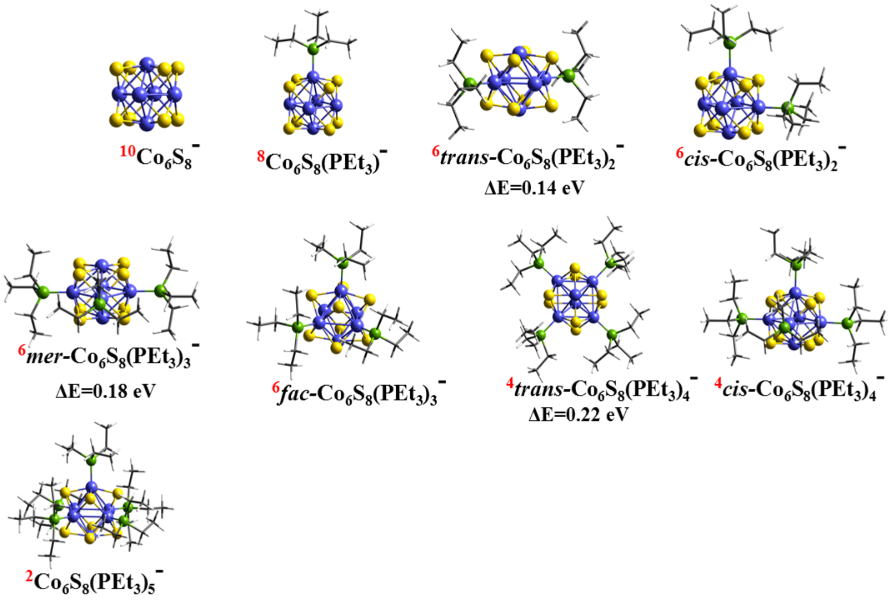

Figure III.B.27. OPTIMIZED GROUND STATE GEOMETRY OF ANIONIC $Co_6S_8(PEt_3)_x$ (X = 0–5) CLUSTERS. SUPERSCRIPTS IN RED TEXT SHOW THE MULTIPLICITY OF THE CLUSTERS.

for x = 2 and x = 4 respectively. For $Co_6S_8(PEt_3)_3$, the cluster can adopt *fac* and *mer* configurations. We find that the *fac* isomer is the ground state for both anionic and neutral clusters, being lower in energy by ~0.18 and ~0.04 eV, respectively. In addition to the ligated clusters, we optimize the anionic and neutral naked Co_6S_8 core in order to complete the analysis although no photoelectron spectrum could be measured as the transitions are outside the range of measurable energies.

The key experimental finding in Figure III.B.26 is that the bonding of PEt_3 to the Co_6S_8 core leads to a change in the peak position and the leading edge of the spectrum. To provide insight into these variations, we calculate the VDE by taking the energy difference between the ground state of the anion and neutral cluster with the same geometry as the anion. The VDE corresponds to the first peak maximum in the photodetachment spectra and provides the most direct comparison with the experiment while an estimation of 2nd VDE is obtained by a vertical transition from the anion ground state to the neutral with next higher spin multiplicity. We also calculated the AEA, which are determined by the

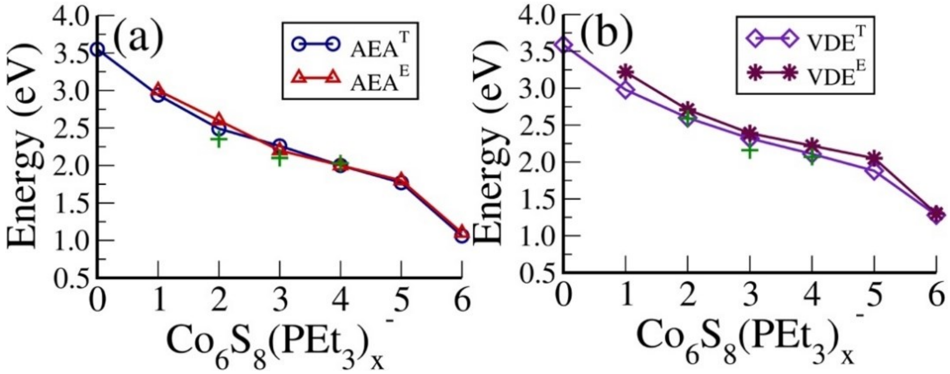

Figure III.B.28. THE EXPERIMENTAL AND THEORETICAL ADIABATIC AND VERTICAL DETACHMENT ENERGY OF $Co_6S_8(PEt_3)_x$ (X = 0 – 6) CLUSTERS. THE PLUS SYMBOL (+) INDICATES THE AEA^T AND VDE^T VALUES OF CLUSTER'S ISOMERS AT X =2, 3, AND 5. THE RESULTS OF $Co_6S_8(PEt_3)_6$ ARE TAKEN FROM REF. 38.

onset of the experimental spectra and corresponds to the energy difference between the ground states of the anion and neutral species. Finally, we examine the excited states of the neutral cluster in the anionic geometry that correspond to the spectral features beyond the first peak. Figure III.B.28 compares the experimental and theoretical AEA and VDE values while Table III.B.9 lists the values of both the theoretical and calculated AEA and VDE. The calculated AEA and VDE of the Co_6S_8 core are 3.55 and 3.59 eV, respectively, which are in accordance with the absence of photoelectron signal when using 355 nm (3.49 eV) photon. The AEA^T for $Co_6S_8(PEt_3)$ is 2.94 eV, agreeing with the AEA^E of 3.0 eV, while VDE^E is 3.22 eV compared to the calculated VDE^T of 2.98 eV. The *cis*-$Co_6S_8(PEt_3)_2$ isomer has an AEA^T of 2.49 eV, which is slightly closer to the AEA^E of 2.6 eV than that of *trans*-

TABLE III.B.9. THEORETICAL AND EXPERIMENTAL ADIABATIC AND 1^{ST} AND 2^{ND} VERTICAL DETACHMENT ENERGIES (VDE AND VDE*) OF $Co_6S_8(PEt_3)_x^-$ (X = 0–5) CLUSTERS.

Cluster	AEA^E (eV)	VDE^E (eV)		Isomers	ΔE (eV)	AEA^T (eV)	VDE^T (eV)	
		VDE	VDE^*				VDE	VDE^*
$Co_6S_8^-$	>3.49	>3.49	>3.49			3.55	3.59	3.96
$Co_6S_8(PEt_3)^-$	3.0	3.22	3.35			2.94	2.98	3.37
$Co_6S_8(PEt_3)_2^-$	2.6	2.71	2.85	*trans*	0.14	2.35	2.59	2.88
				cis		2.49	2.60	2.92
$Co_6S_8(PEt_3)_3^-$	2.2	2.39	2.45	*mer*	0.18	2.10	2.16	2.32
				fac		2.26	2.32	2.33
$Co_6S_8(PEt_3)_4^-$	2.0	2.22	2.29	*trans*	0.22	2.03	2.07	2.15
				cis		2.00	2.11	2.21
$Co_6S_8(PEt_3)_5^-$	1.8	2.05	2.16			1.77	1.88	2.09

$Co_6S_8(PEt_3)_2$ (2.35 eV). Both $Co_6S_8(PEt_3)_2$ isomers have VDE^T around 2.60 eV that are close to the VDE^E of 2.71 eV, suggesting the possible presence of both isomers. The AEA^T and VDE^T of *fac*-$Co_6S_8(PEt_3)_3$ are 2.26 and 2.32 eV, in very good agreement with corresponding experimental values of AEA^E (2.2 eV) and VDE^E (2.39 eV), while the AEA^T and VDE^T for *mer*-$Co_6S_8(PEt_3)_3$ are 2.10 eV and 2.16 eV. Both *trans*- and *cis*-$Co_6S_8(PEt_3)_4$ have AEA^T around 2.0 eV, matching the experimental value of 2.0 eV, while the corresponding VDE^T (2.15 and 2.11 eV) are slightly smaller than the experimental value of 2.31 eV. In order to evaluate the dispersion effect on the calculated AEA^T and VDE^T, we also carried out calculations with Grimme dispersion corrected PBE functional.[46] Similar calculated AEA^T and VDE^T were obtained (Table S1). Overall, the calculated values are in excellent agreement with experimental results, thus validating the calculations. Since the photoelectron spectra are fingerprint of the electronic structures of neutral clusters, the agreement indicates that the calculated atomic structures and the multiplicities match the ones observed experimentally.

The main result is a monotonic decrease in the AEA and VDE as ligands are successively attached to the Co_6S_8 core. Such a decrease is attributed to the fact that PEt_3 ligands are electron donors and thus increase the charge density in the core region. To support this hypothesis, we performed a Hirshfeld charge analysis (Figure S3). The cumulative charge donated from the ligands to the Co_6S_8 core gradually increases, from ~0.32 e in $Co_6S_8(PEt_3)$ to ~0.90 e in $Co_6S_8(PEt_3)_5$. The added charge affects the one-electron levels of the clusters, in particular, the HOMO and LUMO energies, which control the ionization and electron affinity. Figure III.B.29 presents the one-electron levels of the neutral clusters. The values of the HOMO, LUMO and HOMO-LUMO gap for anionic and

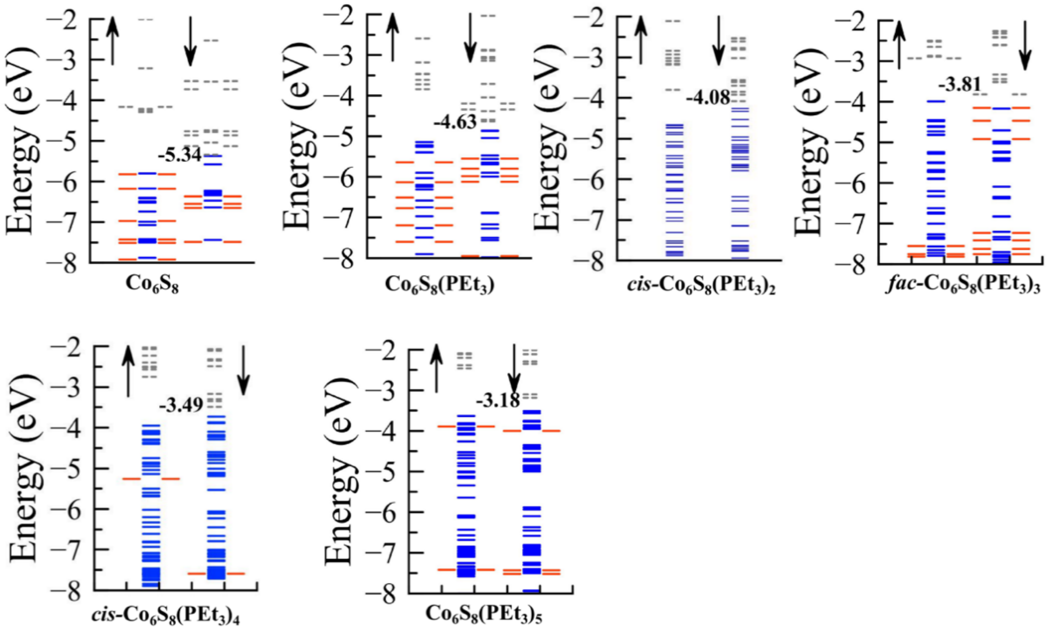

Figure III.B.29. One electron-energy levels of $Co_6S_8(PEt_3)_x$ (x = 0–5) clusters. The solid blue and red bars represent the singly and doubly occupied energy levels, respectively. Unoccupied energy levels are shown by dashed gray lines. The energy of LUMO (in eV) is indicated for each cluster. The *a*-spin and *b*-spin channel are represented by up and down arrows.

neutral clusters are given in Table S2. Note that the addition of successive ligands raises the one-electron levels, as marked by the position of the LUMO. As the position of the LUMO is raised in energy, the electron affinity of the cluster decreases since the extra electron occupies the LUMO of the neutral cluster. The largest increase in the LUMO energy occurs with the attachment of the 1st and 2nd PEt_3. Beyond x = 2, each additional ligand increases the LUMO by around 0.3 eV. Remarkably, we find that the ligands are not bound strongly to the cluster core: the binding energy of the first PEt_3 to Co_6S_8 is 1.53 eV, and decreases to 1.38 eV for the 5th ligand.

Our earlier studies have shown that a complete ligation with either PEt_3 or a mixture of PEt_3 and CO ligands produces the lowest spin state for the $Co_6S_8(PEt_3)_{6-n}(CO)_n$ clusters.

This contrasts drastically with the partially ligated cluster in this study: starting from the bare anionic Co_6S_8 core, with a spin multiplicity of M = 10, the multiplicity is reduced by 2 upon addition of a PEt_3 ligand, leading to $Co_6S_8(PEt_3)^-$ in an octet state. The attachment of the 2nd and 3rd PEt_3 ligands produces a sextet spin state, while the bonding of the 4th and 5th ligands generates a quartet ground state. To support these results, Figure III.B.30A shows the one-electron energy levels of Co_6S_8 in an octahedral symmetry. In the energy range –20 to –18 eV, there are 16 electrons accommodated in A_{1g}, T_{1u}, T_{2g}, and A_{2u} orbitals formed by *s*-states of S and Co sites. The remaining 86 electrons are accommodated in $T_{2g/2u}$, T_{1g}/T_{1u}, $E_{g/u}$, A_{2u}, and $A_{1g/2g}$ states in the energy range from –10 to –2eV. A set of unoccupied T_{1g} (d_{xz}, d_{yz}, $\mathrm{d_{xy}}$), T_{2u} ($d_{xz}, d_{yz}, d_{x^2-y^2}$), T_{1u} (d_{xz}, d_{yz}, d_{z^2}), and E_g (d_{z^2}) states in β-spin channel lead to a spin multiplicity M = 11. In addition, the E_g ($\mathrm{d_{x^2-y^2}}$) in β-spin channel is occupied. As the LUMO is a minority spin state, addition of an electron leads to an anion with a spin multiplicity of 10. The *d*-orbitals in the parentheses with italics text are localized on the Co site along z-axis. Note that two d_{z^2} orbitals form a bonding E_g-type and an anti-bonding T_{1u}-type orbitals with a node along z axis. Figure III.B.30B shows the one-electron energy levels of Co_6S_8 with PEt_3 ligand along the z-axis. Addition of PEt_3 ligand breaks the octahedral symmetry and the *sp*-states of P combine primarily with *d*-states of Co to stabilize the E_g (d_{z^2}) and T_{1g} (d_{xz}, d_{yz}) states while E_g ($\mathrm{d_{x^2-y^2}}$) state is destabilized and becomes a part (MO^β-70) of unoccupied states in the β-spin channel. The E_g (d_{z^2}) states form the occupied bonding (MO^α-49,MO^β-44) states with lone pair of electrons of PEt_3 while corresponding unoccupied anti-bonding (MO^α-78, MO^β-78) states are higher in energy. The remaining T_{2u} ($d_{xz}, d_{yz}, d_{x^2-y^2}$), T_{1u} (d_{xz}, d_{yz}, d_{z^2}) also lose their degeneracy and turn into MO^β-(75,76,72) and MO^β-(73,74,71), respectively. These six states along with

MO^{β}-70 and MO^{β}-77 ($T_{1g}(d_{xy})$) lead to a reduced multiplicity M = 9 in the ground state of $Co_6S_8(PEt_3)$. Further addition of ligands leads to a similar mixing with reduction in multiplicity.

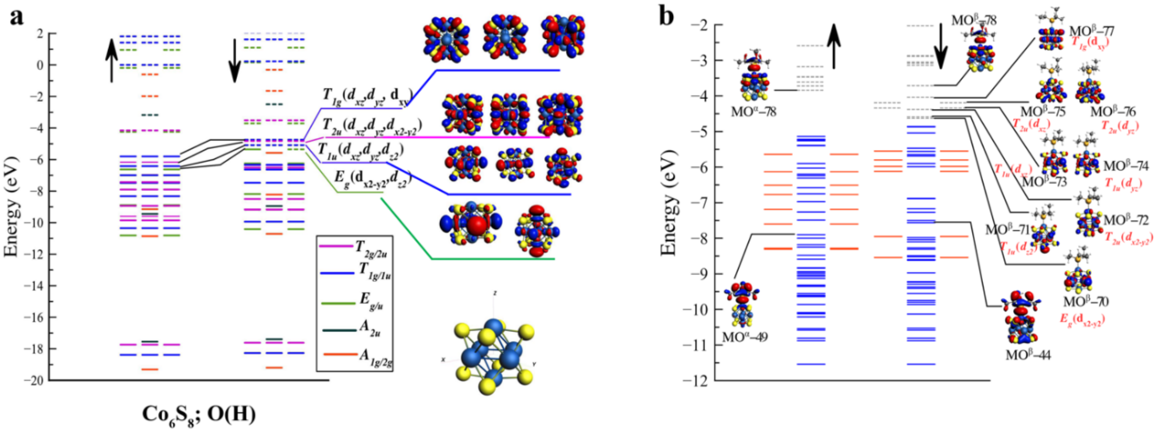

Figure III.B.30. (A) ONE-ELECTRON ENERGY LEVELS WITH THEIR SYMMETRY LABELS FOR Co_6S_8 IN OCTAHEDRON SYMMETRY. THE SOLID AND DASHES LINES REPRESENT OCCUPIED AND UNOCCUPIED ENERGY LEVELS. (B) ONE-ELECTRON ENERGY LEVELS ALONG WITH THEIR ISO-SURFACES FOR $Co_6S_8(PEt_3)$. THE SOLID BLUE AND RED BARS REPRESENT THE SINGLY AND DOUBLY OCCUPIED ENERGY LEVELS, RESPECTIVELY. UNOCCUPIED ENERGY LEVELS ARE SHOWN BY DASHED GRAY LINES. THE *A*-SPIN AND *B*-SPIN CHANNEL REPRESENTED BY UP AND DOWN ARROWS.

III.B.7.e. Summary

By combining inorganic cluster synthesis, gas-phase anion photoelectron spectroscopy, and electronic structure calculations, we have demonstrated that the electronic properties of metal chalcogenide clusters can be tuned by varying the number of phosphine capping ligands. The sequential addition of PEt_3 to the Co_6S_8 core results in a gradual decrease of its electron affinity and a shift of its electronic spectrum to lower energy. Density functional theory calculations reveal that addition of PEt_3 ligands gradually demagnetizes the Co_6S_8 core and increases its charge density. These effects stabilize the core and lift the energy of the LUMO.

Acknowledgements

The gas-phase work is based on work supported by the Office of Naval Research (ONR), Multidisciplinary University Research Initiative (MURI) under Grant No. N00014-15-1-2681 (K. H. B.), and by the Air Force Office of Scientific Research (AFOSR) under grant number FA9550-19-1-0077 (K. H. B.). Theoretical studies (V. C. and S. N. K.) were supported by a grant from from the Department of Energy under Award Number DE-SC0006420. Synthetic work was supported by the Center for Precision Assembly of Superstratic and Superatomic Solids at Columbia University, an NSF MRSEC (DMR-1420634) (X.R.), and by the Air Force Office of Scientific Research (AFOSR) under grant number FA9550-18-1-0020 (X.R.).

Supplementary Materials

Figure S1-S3, Table S1-S5, and Cartesian coordinates of optimized anionic $Co_6S_8(PEt_3)_x$ (x= 0-5) clusters.

References

1. A. C. Reber and S. N. Khanna, *Acc. Chem. Res*. **50**, 255 (2017).
2. A. Pinkard, A. M. Champsaur, and X. Roy, *Acc. Chem. Res.* **51**, 919 (2018).
3. S. A. Claridge, A. W. Castleman, S. N. Khanna, C. B. Murray, A. Sen, and P. S. Weiss, *ACS Nano.* **3**, 244 (2009).
4. E. G. Tulsky and J. R. Long, *Chem. Mater*. **13**, 1149 (2001).

5. S. A. Baudron, P. Batail, C. Coulon, R. Clerac, E. Canadell, V. Laukhin, R. Melzi, P. Wzietek, D. Jerome, P. Auban-Senzier, and S. Ravy, *J. Am. Chem. Soc.* **127**, 11785 (2005).

6. B. Yoon, W. D. Luedtke, R. N. Barnett, J. Gao, A. Desireddy, B. E. Conn, T. Bigioni, and U. Landman, U. *Nat. Mater.* **13**, 807 (2014).

7. J. F. Corrigan, O. Fuhr, and D. Fenske, *Adv. Mater*. **21**, 1867 (2009).

8. X. Roy, C. H. Lee, A. C. Crowther, C. L. Schenck, T. Besara, R. A. Lalancette, T. Siegrist, P. W. Stephens, L. E. Brus, P. Kim, M. L. Steigerwald, and C. Nuckolls, *Science* **341**, 157 (2013).

9. S. N. Khanna and P. Jena, *Phys. Rev. B* **51**, 13705 (1995).

10. A. W. Castleman and S. N. Khanna, *J. Phys. Chem. C* **113**, 2664 (2009).

11. C. H. Lee, L. Liu, C. Bejger, A. Turkiewicz, T. Goko, C. J. Arguello, B. A. Frandsen, S. C. Cheung, T. Medina, T. J. S. Munsie, R. D'Ortenzio, G. M. Luke, T. Besara, R. A. Lalancette, T. Siegrist, P. W. Stephens, A. C. Crowther, L. E. Brus, Y. Matsuo, E. Nakamura, Y. L. Uemura, P. Kim, C. Nuckolls, M. L. Steigerwald, and X. Roy, *J. Am. Chem. Soc*. **136**, 16926 (2014).

12. X. Roy, C. L. Schenck, S. Ahn, R. A. Lalancette, L. Venkataraman, C. Nuckolls, and M. L. Steigerwald, *Angew. Chem., Int. Ed*. **51**, 12473 (2012).

13. M. T. Trinh, A. Pinkard, A. B. Pun, S. N. Sanders, E. Kumarasamy, M. Y. Sfeir, L. M. Campos, X. Roy, and X. Y. Zhu, *Sci. Adv*. **3**, e1700241 (2017).

14. V. Chauhan, S. Sahoo, and S. N. Khanna, *J. Am. Chem. Soc*. **138**, 1916 (2016).

15. S. N. Khanna and A. C. Reber, *Nat. Chem*. **9**, 1151 (2017).

16. D. A. Tomalia and S. N. Khanna, *Chem. Rev.* **116**, 2705 (2016).

17. Z. Zheng, J. R. Long, and R. H. Holm, *J. Am. Chem. Soc.* **119**, 2163 (1997).

18. M. Cargnello, A. C. Johnston-Peck, B. T. Diroll, E. Wong, B. Datta, D. Damodhar, V. V. T. Doan-Nguyen, A. A. Herzing, C. R. Kagan, and C. B. Murray, *Nature* **524**, 450 (2015).

19. M. N. O'Brien, M. R. Jones, B. Lee, and C. A. Mirkin, *Nat. Mater.* **14**, 833 (2015).

20. M. A. Boles and D. V. Talapin, *J. Am. Chem. Soc*. **137**, 4494 (2015).

21. C. L. Poyser, T. Czerniuk, A. Akimov, B. T. Diroll, E. A. Gaudling, A. S. Salasyuk, A. J. Kent, D. R. Yakovlev, M. Bayer, and C. B. Murray, *ACS Nano*. **10**, 1163 (2016).

22. W. L. Ong, S. M. Rupich, D. V. Talapin, A. J. H. McGaughey, and J. A. Malen, *Nat. Mater*. **12**, 410 (2013).

23. A. Voevodin, L. M. Campos, and X. Roy, *J. Am. Chem*. *Soc*. **140***,* 5607 (2018).

24. A. M. Champsaur, J. Yu, X. Roy, D. M. Paley, M. L. Steigerwald, C. Nuckolls, and C. M. Bejger, *ACS Cent. Sci.* **3**, 1050 (2017).

25. A. M. Champsaur, C. Mézière, M. Allain, D. W. Paley, M. L. Steigerwald, C. Nuckolls, and P. Batail, *J. Am. Chem. Soc.* **139**, 11718 (2017).

26. E. S. O'Brien, M. T. Trinh, R. L. Kann, J. Chen, G. A. Elbaz, A. Masurkar, T. L. Atallah, M. V. Paley, N. Patel, D. W. Paley, I. Kymissis, A. C. Crowther, A. J. Millis, D. R. Reichman, X. Y. Zhu, and X. Roy, *Nat. Chem.* **9**, 1170 (2017).

27. G. Lovat, B. Choi, D. W. Paley, M. L. Steigerwald, L. Venkataraman, and X. Roy, *Nat. Nanotechnol.* **12**, 1050 (2017).

28. W. L. Ong, E. S. O'Brien, P. S. M. Dougherty, D. W. Paley, C. Fred Higgs Iii, A. J. H. McGaughey, J. A. Malen, and X. Roy, *Nat. Mater.* **16**, 83 (2017).

29. B. Choi, J. Yu, D. W. Paley, M. Tuan Trinh, M. V. Paley, J. M. Karch, A. C. Crowther, C. H. Lee, R. A. Lalancette, X. Zhu, K. Kim, M. L. Steigerwald, C. Nuckolls, and X. Roy, *Nano Lett*. **16**, 1445 (2016).

30. A. M. Champsaur, A. Velian, D. W. Paley, B. Choi, X. Roy, M. L. Steigerwald, and C. Nuckolls, *Nano Lett.* **16**, 5273 (2016).

31. A. Turkiewicz, D. W. Paley, T. Besara, G. Elbaz, A. Pinkard, T. Siegrist, and X. Roy, *J. Am. Chem. Soc.* **136**, 15873 (2014).

32. J. Yu, C. H. Lee, D. Bouilly, M. Han, P. Kim, M. L. Steigerwald, X. Roy, and C. Nuckolls, *Nano Lett.* **16**, 3385 (2016).

33. M. Walter, J. Akola, O. Lopez-Acevedo, P. D. Jadzinsky, G. Calero, C. J. Ackerson, R. L. Whetten, H. Grönbeck, and H. Häkkinen, *Proc. Natl. Acad. Sci. U. S. A.* **105***,* 9157 (2008).

34. C. M. Aikens, *Acc. Chem. Res.* **51**, 3065 (2018).

35. A. C. Reber and S. N. Khanna, *NPJ Comput. Mater.* **4**, 33 (2018).

36. V. Chauhan and S. N. Khanna, *J.* P*hys. Chem. A* **122**, 6014 (2018).

37. F. Cecconi, C. A. Ghilardi, S. Midollini, and A. Orlandini, *Inorg. Chimica Acta* **76**, 183 (1983).

38. G. Liu, A. Pinkard, S. M. Ciborowski, V. Chauhan, Z. Zhu, A. P. Aydt, S. N. Khanna, X. Roy, and K. H. Bowen, *Chem. Sci.* **10**, 1760 (2019).

39. X. Zhang, G. Liu, G. Gantefoer, K. H. Bowen, and A. N. Alexandrova, *J. Phys. Chem. Lett.* **5**, 1596 (2014).

40. G. Liu, S. M. Ciborowski, and K. Bowen, *J. Phys. Chem. A* **121**, 5817 (2017).

41. A. Grubisic, H. Wang, X. Li, Y. J. Ko, S. Kocak, M. R. Pederson, K. H. Bowen, and B. W. Eichhorn, *Proc. Nat. Acad. Sci*. **108**, 14757 (2011).

42. J. P. Perdew and W. Yue, *Phys. Rev. B* **33**, 8800 (1986).

43. E. van Lenthe and E. J. Baerends, *J. Comput. Chem.* **24**, 1142 (2003).

44. E. van Lenthe, R. van Leeuwen, E. J. Baerends, and J. G. Snijders, *Int. J. Quantum Chem.* **57**, 281 (1986).

45. E. van Lenthe, A. Ehlers, and E. J. Baerends, *J. Chem. Phys.* **110**, 8943 (1999).

46. S. Grimme, S. Ehrlich, and L. Goerigk, L. *J. Comp. Chem.* **32**, 1456 (2011).

IV. Appendices

IV.A. Designs for Glove Box & Diffusion Pump Control Box

IV.A.1. Glove Box Control Box

Over the course of a few years, the glove box began to act abnormally. More specifically, there was a situation in which the box was over-pressurized to the point of exploding the gloves; another time the solenoid valve to the mechanical pump failed open, allowing the pump to pull vacuum on the box and imploding the gloves. Both situations compromised the materials inside of the box and posed safety hazards.

The glove box had a control box that included a Dwyer A3000 Photohelic Differential Pressure Switch/Gauge and two ASCO Redhat solenoid valves, connected by metal tubing. The two solenoid valves dictate whether the tank of nitrogen gas is open to or the vacuum pump is interacting with the glove box. If either of these is to be opened is controlled by the set points on the photohelic gauge, as well as the foot pedal.

The photohelic pressure gauge along with the two solenoid valves were in question from both situations, so all were replaced. A redundant pressure gauge, ProSense EPS25-14-1001 (AutomationDirect), was installed as a back up to the photohelic gauge, as well as two ice cube control relays (AutomationDirect, 781-1C-24D) that are controlled by both pressure gauges. The ProSense pressure gauge required a 24 VDC power supply (AutomationDirect, RHINO switching power supply) that is also used to power the coils of the relays, while the A3000 photohelic gauge and solenoid valves run off of 120 VAC.

In Figure A.1, the electrical circuit diagram is presented for this upgrade. The settings for the ProSense gauge are given in the table: the unit is inH_2O, the transistor setting in PnP, and color scheme is G-12. The LO Relay is set at 0.5 (inH_2O) to trigger before the box goes to vacuum, and the HI Relay is set at 4.5 (inH_2O) to prevent over-pressurizing of the glove box. The other two settings for the LO and HI Relays are kept at values beyond the other, so that the LO Relay is focused on when the box needs to be refilled, like the right pointer on the photohelic gauge, and the HI Relay dictates when the pump needs to act on the box, similar to the left pointer on the photohelic gauge.

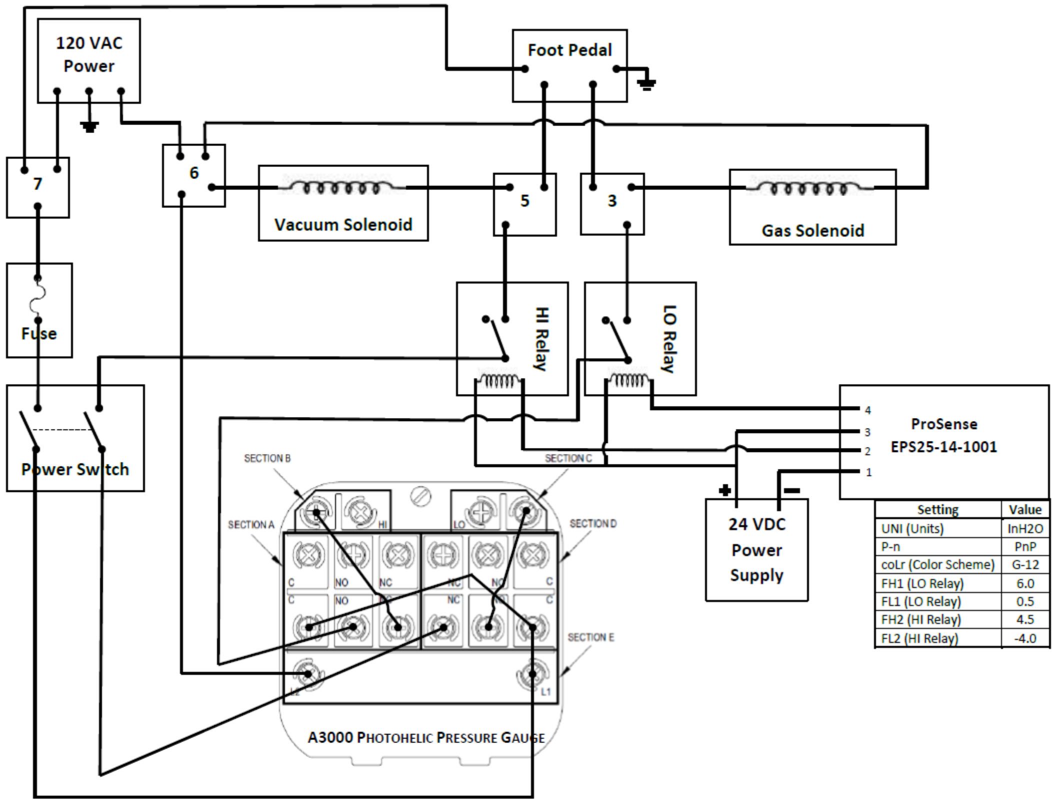

Setting	Value
UNI (Units)	InH2O
P-n	PnP
coLr (Color Scheme)	G-12
FH1 (LO Relay)	6.0
FL1 (LO Relay)	0.5
FH2 (HI Relay)	4.5
FL2 (HI Relay)	-4.0

Figure A.1. Electronic Circuit Diagram for the Glove Box as of 2018.

IV.A.2. Diffusion Pump Control Box on PSA-RET

Originally, breakers were used to control the power to the diffusion pump heaters on the PSA-RET instrument. This proved ineffective and problematic as time went on and multiple breakers, plugs, and/or outlets had to be replaced. In general, a circuit breaker works similarly to a switch, where once the breaker is engaged it stays there and will often not open if something goes wrong. A contactor has an external power supply for its coil, which helps prevent this issue and allows the contactor to open should something happen to the system.

In our box, as shown in Figure A.2, a 24-volt power supply (Automation Direct, RHINO switching power supply, P/N: PSB24-060-P) was added which supplies voltage to three switches (Automation Direct, selector switch, 22-mm, two-position, maintained, LED illuminated, (1) N.O. contact(s), plastic base, plastic bezel, 24 VAC/VDC, full voltage, P/N: GCX3252-24L, GCX3253-24L and GCX3254-24L) and three contactors. Chamber 0's 10" diffusion pump has its own switch and contactor (Automation Direct, WEG Electric CWC series IEC miniature contactor, 12A, three N.O. power poles, 24 VDC coil voltage, low consumption, P/N: CWC012-10-30L03), mainly due to the voltage

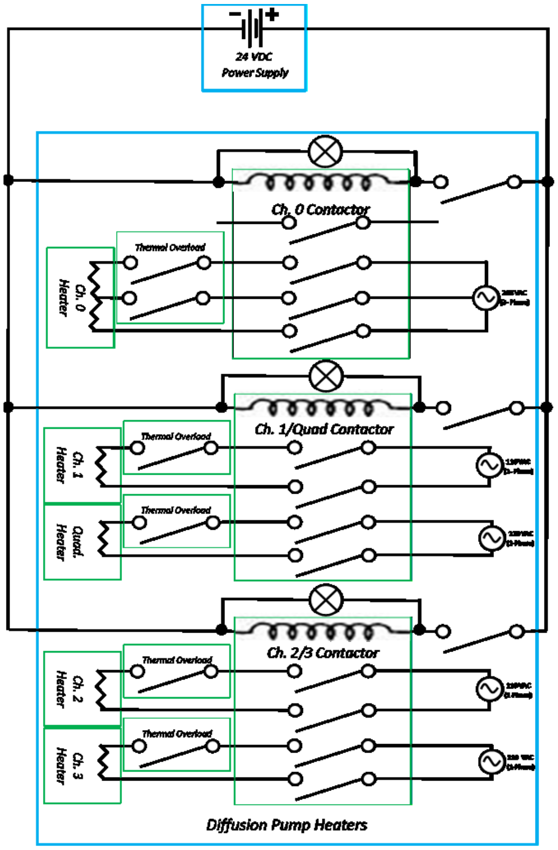

Figure A.2. Electronic Circuit Diagram for Contactor Box on PSA-RET Instrument.

needed for the heater is three-phase and higher than the 6” diffusion pumps on the remainder of the instrument. There is one contactor (Automation Direct, WEG Electric CWC series IEC miniature contactor, 16A, four N.O. power poles, 24 VDC coil voltage, low consumption, P/N: CWC016-00-40L03)/switch combination that works for the Ch. 1 and Quad. diffusion pumps, and the last is for Ch. 2 and Ch. 3 diffusion pumps. Each switch is lit when the associated contactor is engaged, so there is a visual indication when the heaters are connected to the wall voltage.

IV.A.3. Diffusion Pump Control with Interlocks: Plan Only

Adding to the electrical diagram above, an interlock system that involves water flow meters, thermocouple gauge controls, air flow meters, pneumatic gate valves, relays, lights, and more switches has been designed for a time when ordering and implementing such parts would be possible.

Briefly, each diffusion pump would need its own pneumatic gate valve and water flow meter; each foreline requires a pneumatic gate valve. While they are not part of Figure A.3, air flow meters for the pneumatic devices may be good to include in a final design, so that if air pressure is lost and the gate valves shut there would be some indication. There is a switch that allows the interlocked system to be bypassed and a momentary switch for testing purposes. There is a light to indicate if the interlock is enabled, another to signify if the bypass is in use, and another with an alarm to show the interlock has activated. The portion involving the diffusion pump heaters has only been adjusted to be dependent upon these other components but is otherwise unchanged from Figure A.2. Two relays are connected so that power is interrupted should the foreline pressure violate the set points, the water pressure violate those set points, or the power supply fail.

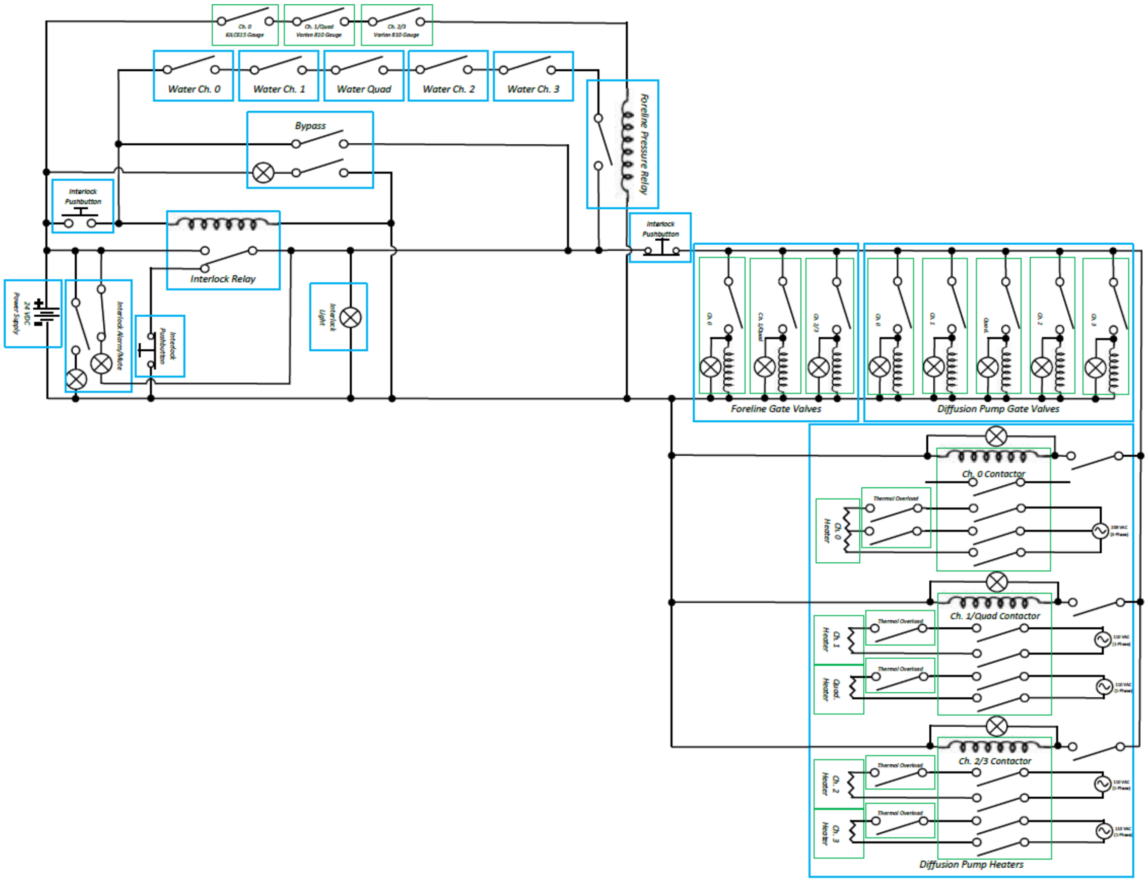

Figure A.3. Electronic Circuit Diagram Plan for Contactor Box on PSA-RET Instrument with Interlocking Capabilities.

IV.B. LVS Motor Setup

IV.B.1. Gear Designs

Since there is limited room within the source chamber, the design for the motor driving the rod for laser vaporization incorporated some space-saving measures. One of these was having two gears side by side so that the motor can be parallel to the rod but separated by some distance. The first set of gears was a simplistic design (as seen in Figure A.4) found online but adjusted to the spacing needed between the motor and the threaded rod to drive the sample rod.

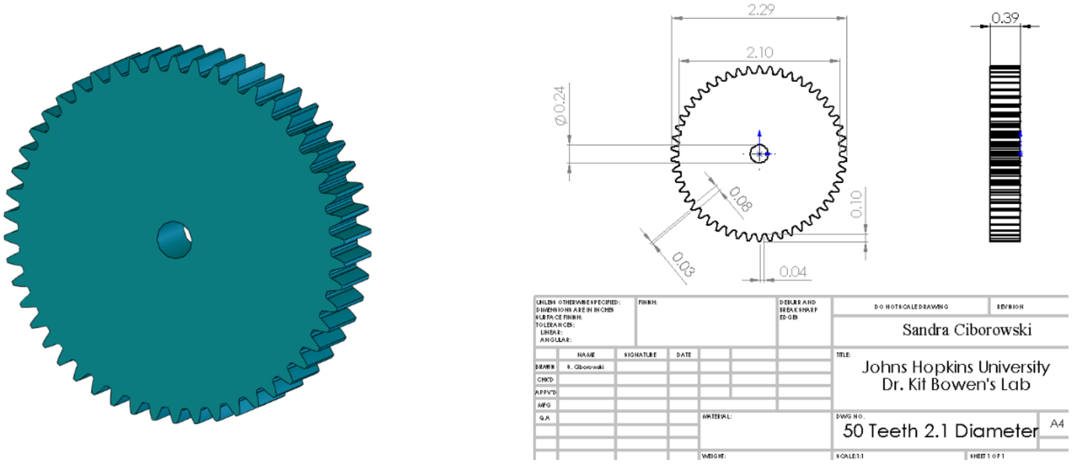

Figure A.4. Simplest Gear Design, Utilizing 40 Straight Teeth.

After having a number of issues with the teeth slipping, Moritz suggested that we use helical gears. The teeth are chiral when it comes to helical gears, so there were two designs made: one with right-handed and another with left-handed teeth. The two complementary designs can be seen in Figure A.5.

However, the stepper motors that we use, after taking them off of surplus instruments from the NIH warehouse, turn quicker than the other motors that we've typically used in our lab, even at their lowest setting. Two helical gears were designed that

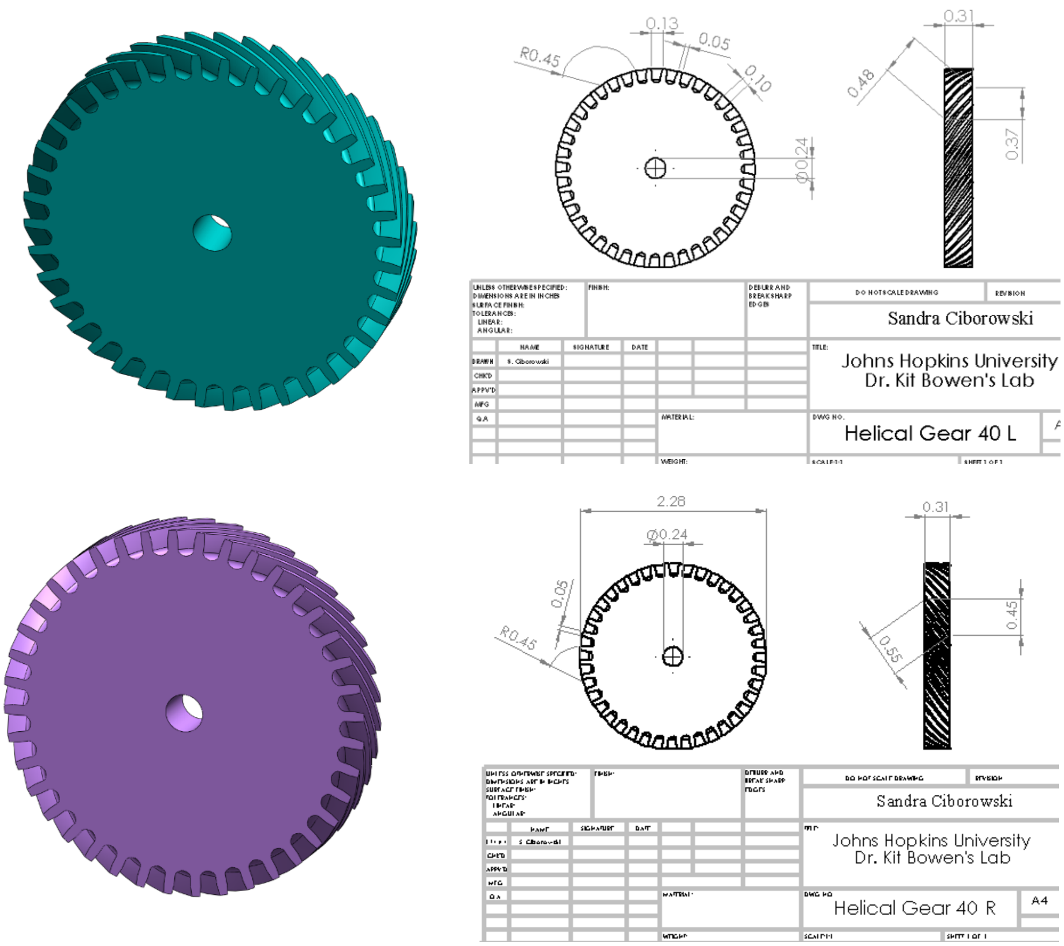

Figure A.5. Helical Gear Designs with 40 (A) Left-Handed Teeth and (B) Right-Handed Teeth.

used a suggested ratio of 8:40 teeth, as in Figure A.6. These gears have yet to be printed and/or implemented due to the 3-D printer not functioning properly. The thought is that the smaller gear would go on the motor side of the setup and the larger would go on the rod side, turning the rod a fraction of what it used to while the laser still ablates a new spot with each shot.

The center hole was intentionally made slightly smaller than 0.25" so that a short piece of tubing would need to be pressed without the fear of it falling out while running. However, when putting the short pieces of tubing or 0.25" stainless steel rod in the gears, I suggest using the press to keep the rod perpendicular to the faces of the gears. A few times the rod was put in at an angle when a hammer alone pressed it into place.

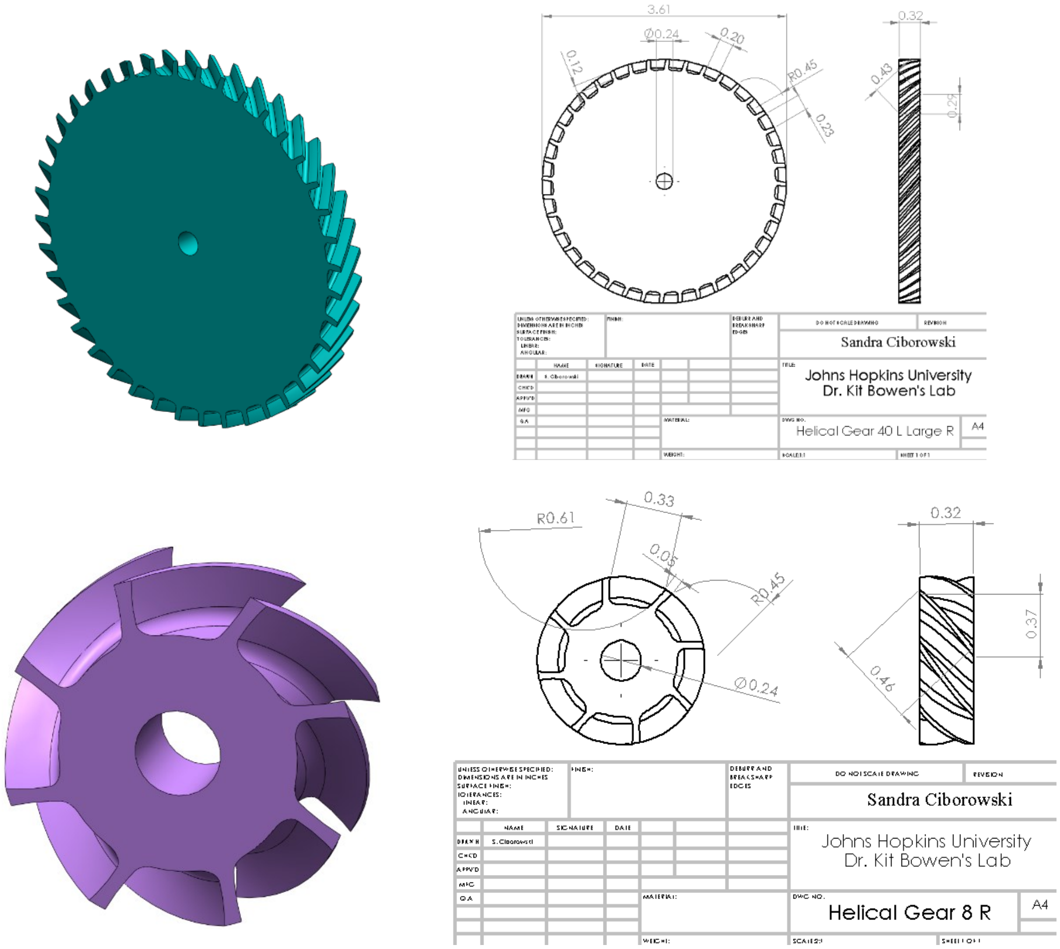

Figure A.6. Helical Gear Designs with (A) 40 Left-Handed Teeth and (B) 8 Right-Handed Teeth.

IV.B.2. Motor Support Designs

As stated above, the motor was set 180° to the rod, which means that there must be sufficient space between the motor and the rotating/translating portion associated with the rod’s movement. We were able to find small bearings (Barden SFR4) on an unused setup that we could reuse for the motor. These were placed in reamed holes in the Gear Mount plate (Figure A.7). The rod/tube used in the gears fits snugly in the bearings. To make sure that the gears do not wander from the plate, two retaining rings with set screws are utilized.

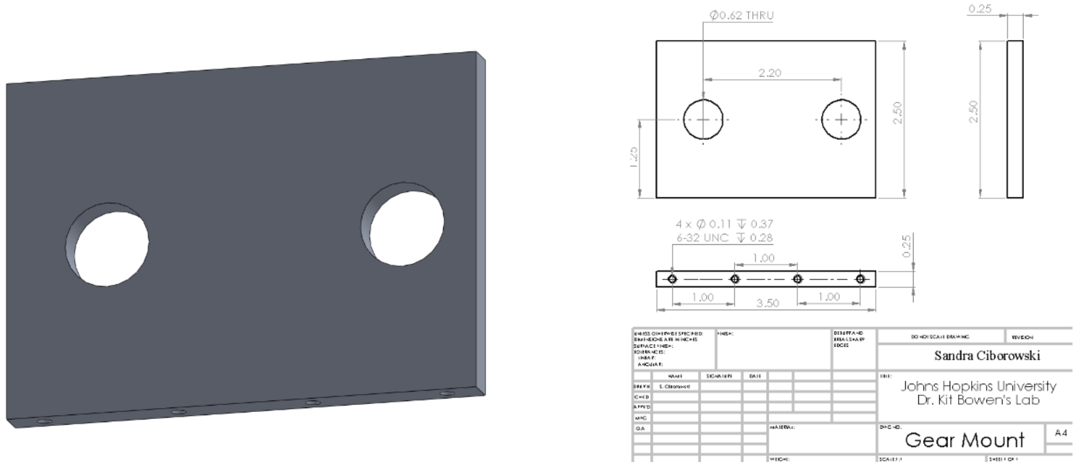

Figure A.7. Gear Mount Plate, into which Small Bearings are Press Fit.

One of the rods is a simple 1" length of stainless-steel tubing, while the other has two small holes where cotter pins are inserted so that the square brass pieces have an anchor point. The square pieces fit within one another yet are sized so that the smaller one causes the larger to turn, giving the ability to translate and rotate. The stainless steel and brass pieces are shown in Figure A.8. The most important part of these is that there is good alignment between the holes for the cotter pins in both the stainless steel and brass tubes.

The other brass piece has cotter pin holes that align with a rigid coupling that marries the brass pieces to the threaded rod, which when rotated within the Threaded Mount (both shown in Figure A.9) also causes the rod to translate in or out of the housing. At the other end of the threaded rod, as well as between the motor and the closest gear, are flexible couplings that allow for small misalignments in the setup.

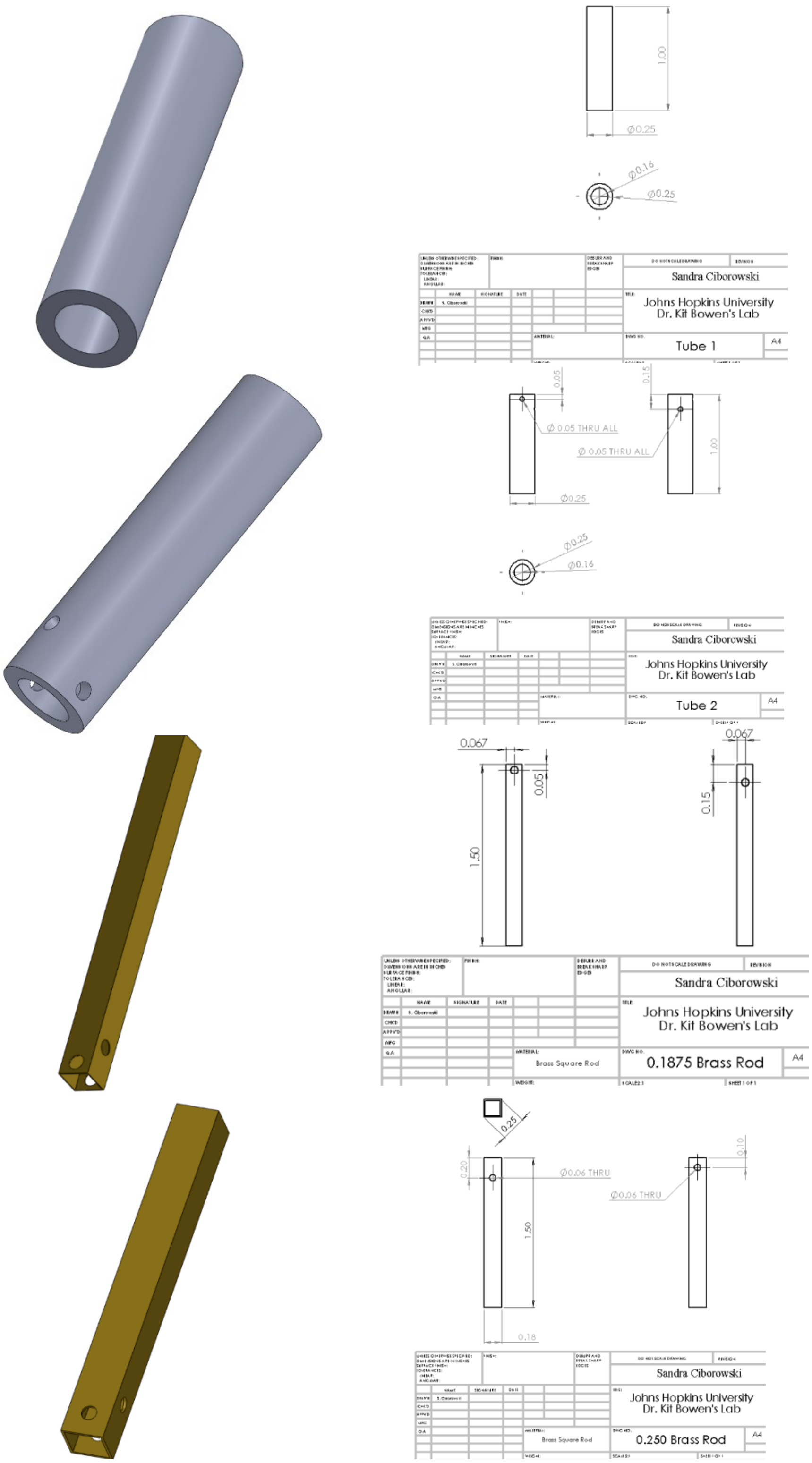

Figure A.8. (A) Tube which Connects the Motor to its Gear; (B) Tube which Connects the Rigid Coupling to the Gear; (C) Smaller Brass Rod; (D) Larger Brass

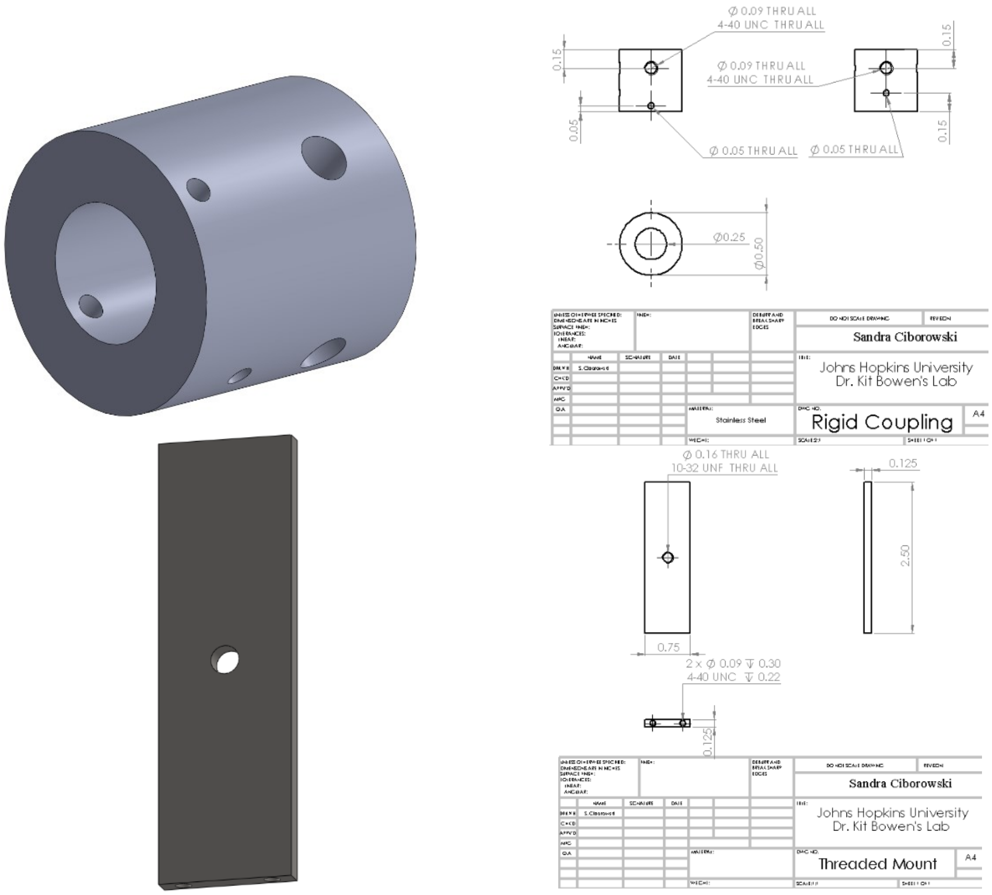

Figure A.9. (A) Rigid Coupling that Connects the Threaded Rod to the Brass Rod; (B) Threaded Mount Plate.

The motor itself mounts onto a particular plate, as shown in Figure A.10. This plate along with the Gear Mount plate and Threaded Mount plate is affixed to a base plate (Figure

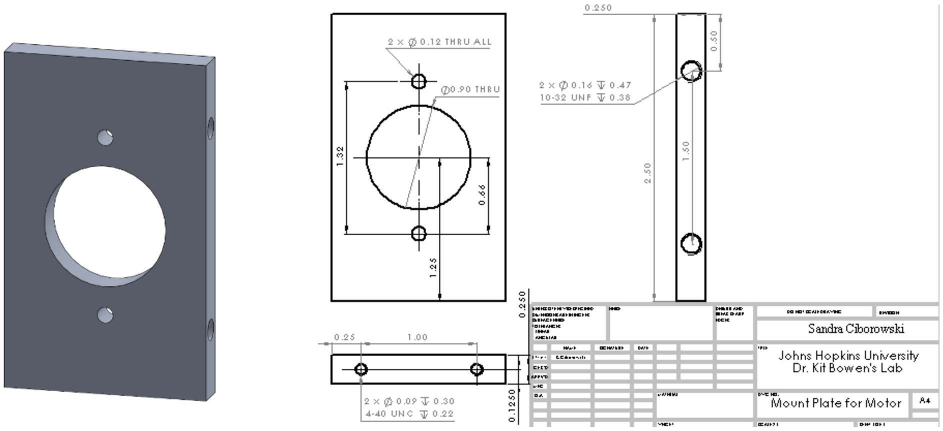

Figure A.10. Motor Mount Plate.

A.11A). The base plate includes slots where ¼-20 bolts fit through and are responsible for attaching the entire setup to a stand in the chamber via mount plates (Figure A.11B).

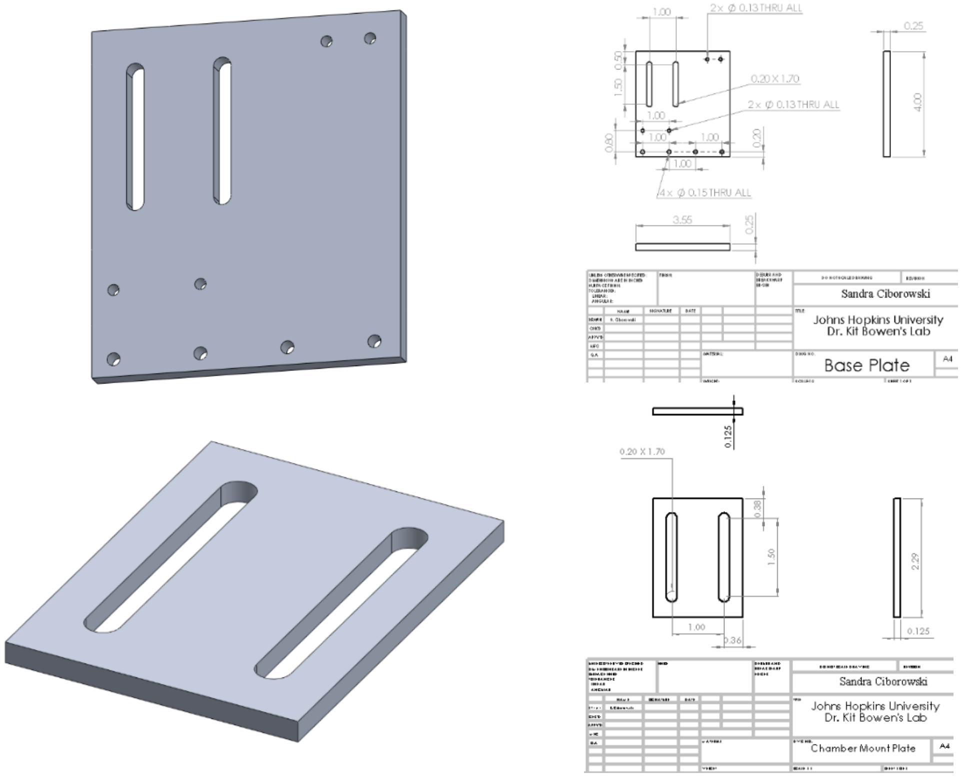

Figure A.11. (A) Base Plate for LVS Motor Setup and (B) Stand Clamp, used to Hold the Setup to the Source Stand.

Just to mention, we have one appropriate adapter so that the manufactured cable can be used from the chamber to the motor driver. Rachel Harris has designed, manufactured, and implemented this on Ch. 0 of the PSA-RET instrument.

IV.B.3. Program for Movement

There is a software package available on the website, www.arunmicro.com/products/stepper-motor-controller/, under the Downloads tab. The SMD210 software is very rudimentary and requires some certain inputs. In the SMD2 Demo Program window, an Initialise (I) line needs to be first added (Line 1), then the appropriate motor needs to be activated, so lines 2 and 3 should be Activate (A) with choice

1 and Motor (B) with the appropriate choice (Motor 1 or Motor 2), depending on where the cable is plugged into the driver box. The acceleration profile, i.e., Acc Profile (X), comes next, and we've typically used the lowest allowed values of 10, 10, and 30 for the start rate, slew rate, and ramp, respectively. The loop should then be started by choosing Loop (L) and Loop start. We determine whether to use Move CW (+) or Move CCW (-) based on the movement of the motor itself. Note that this may change if the phases are hooked up differently the next time they are changed in the chamber. The number of steps is dependent on how far you want the rod to move in either direction. We have found that the Verify (V) function is helpful to put every so often to keep track of what point the rod is at, since this program does not offer an on-screen position counter otherwise. Once the whole loop is complete, Loop (L) should be chosen again with the Loop end option and up to 255 loops total.

This program is very limited in that you must fully save the program before it will run correctly; there is no easy way to tell where the motor believes it is in its run without periodic "verifies" of the position counter along the way; and the speed is limited to the allowed values (10, 10 and 20 are the lowest available) which are not as low as the driver allows in manual mode. A major improvement to this setup would be a program that allows someone to see the position at all times, as well as more flexibility in the speed of the motor. Nic Blando and Lucas Hansen have started this process and are making some headway toward a more modifiable program, which allows for slower motor movement.

IV.C. Source & Skimmer Designs for Gas-Phase Instruments

IV.C.1. Rod-Style Laser Vaporization Source

Over the course of a few years, the necessity for variations in our laser vaporization housing for ablating ¼” diameter rods became clear. Other researchers have inspired some of our new designs and iterations. One researcher is Lai-Sheng Wang, whose group inspired the housing that was used to create the $Au_n(py)^-$ clusters, presented in Section III.B.1. Another was Michael Duncan, who frequently uses an assortment of housings to tag different atoms and clusters with noble gas atoms.

IV.C.1.a. Lai-Sheng Wang-Style Housing

At Brown University, Dr. Lai-Sheng Wang’s group uses a laser vaporization housing that allows the laser to enter through the same orifice as the ion beam exits and consists of two pulse valves angled almost backwards in comparison with the ion axis.[REF] The housing, presented in Figure A.12, was made with that in mind. The laser enters through the orifice on the front face, in which a nozzle can be threaded, and encounters a rotating and translating rod in the rear. Since our conventional housings require the pulse valve to be positioned directly behind the housing and over the rod where the plasma is formed, the position of the pulse valve on the housing was adjusted to an angle that would allow the gas to enter the housing close to where the plasma is formed from the laser striking the rod. As evidenced by Figure A.12, this angle positioned the gas entrance just in front of the rod but behind the end of the threads for the nozzle. Four 8-32 threaded bolt holes allow the pulse valve to be attached and four 4-40 threaded holes on the front face append a reaction cell, as needed.

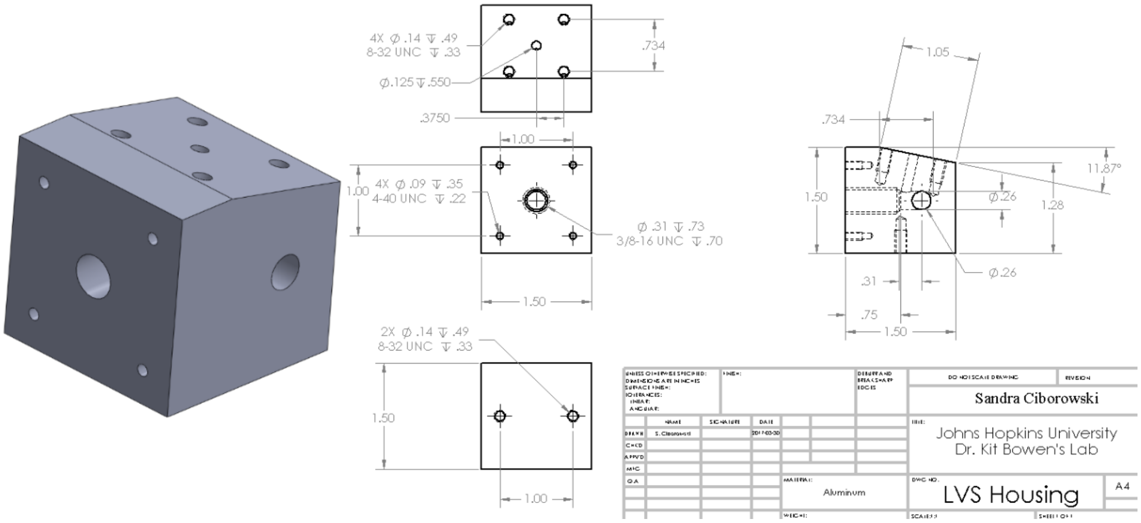

Figure A.12. Part and Schematic Drawing of the Lai-Sheng Wang-Inspired Housing.

Such a reaction cell was designed so that a second gas could be added to the ion beam farther downstream. Simply, four 6-32 thru holes align the front face of the housing with the back of the reaction cell, which also aligns the nozzle with the entrance into the 4-mm channel; see Figure A.13 for more details. Adding a reactant gas downstream from the initial plasma created by the ablation of a metal rod allows the observation of the ions generated by the ablation alone and then how those ions interact with other gaseous

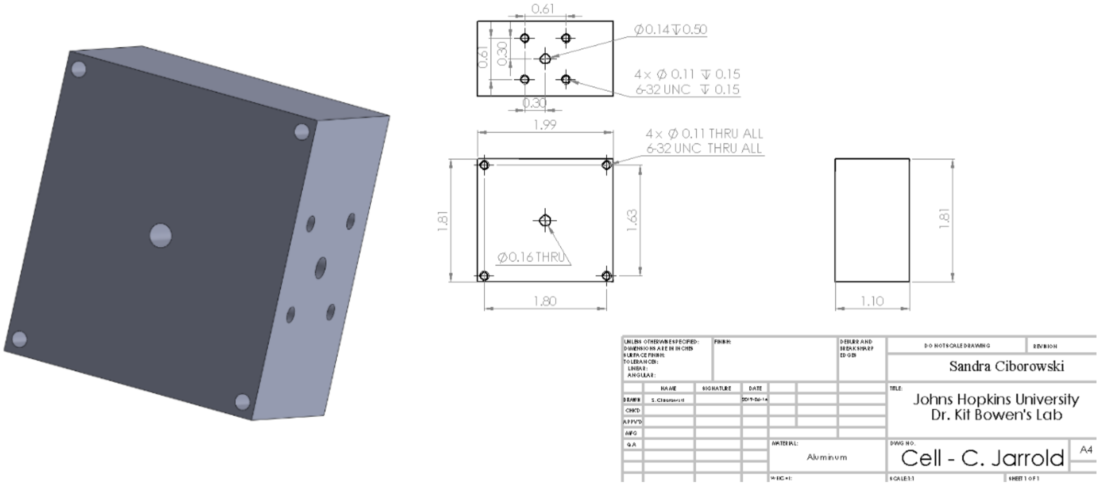

Figure A.13. Part and Schematic Drawing of the Reaction Cell that pairs with the Lai-Sheng Wang-Inspired Housing.

substances. This separation of the interactions is more credible when claiming that the product was formed purely from the ion mingling with the gas and had no effect from the plasma, e.g., electrons, formed during the initial interaction of the laser.

IV.C.1.b. Smaller Housing/Duncan

Dr. Michael Duncan's lab at University of Georgia uses a "cutaway" laser vaporization cluster source to create large clusters of argon.^{REF} Based off of designs given to Dr. Bowen at a meeting, the Duncan LVS Housing was brought to fruition, using a 1.5"x1.5"x0.25" stock piece of 316 stainless steel from McMaster-Carr and a few hours in the shop with Rachel Harris. The drawing and a picture of the design are presented in Figure A.14. Briefly, a pulse valve is attached using four 6-32 bolts to the rear of the housing; a rod slides into the larger, horizontal groove on the front of the housing; the laser enters through the smaller groove on the front, striking the rod just below the opening for the pulse valve. The laser can be aligned so that it strikes the directly on or slightly off the top of the rod, while the rod is held by external optics posts and/or the motor setup.

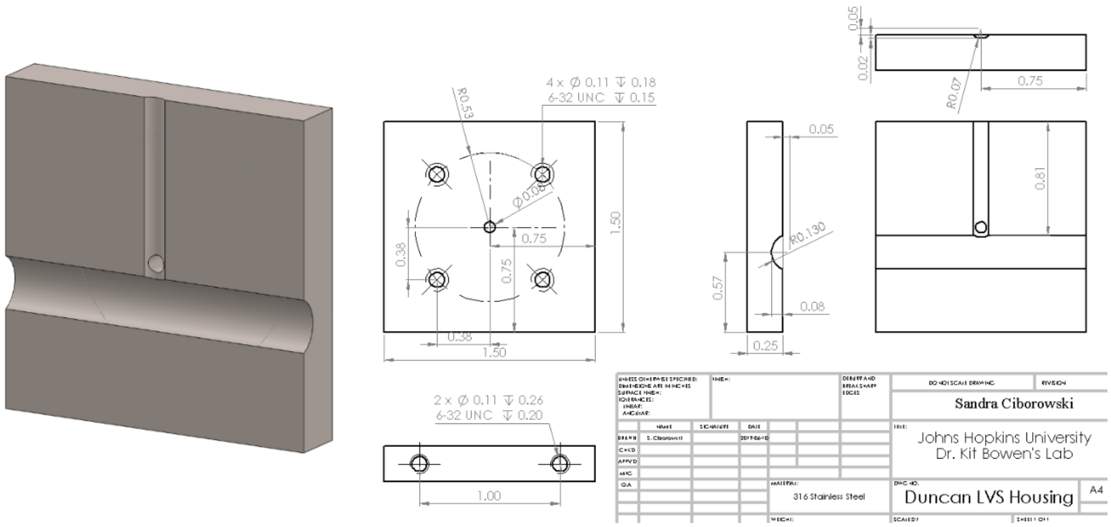

Figure A.14. Part and Schematic Drawing of the "Cutaway" Housing.

This source has been successfully used to tag argon atoms to a variety of metal rods. Initially, it was tested using gold but was deemed unsuccessful because we were getting a lot of carbon, aluminum, and unidentifiable contamination, which we postulated were from the glue holding the foil to the aluminum rod. We, then, used a purely silver rod and found small numbers of argon atoms tagged the cations of silver. Finally, we were able to make argon tagged (up to 5 Ar atoms) uranium and uranium oxide anions, which were made from a pure uranium rod.

IV.C.1.c. Two PV with Detachable Rod

To have a modular design for a housing that could be used with a rod and take the laser either through a nozzle in the front or from the top of the housing, a section that would hold a ¼” rod was designed; see Figure A.15. The rod would sit in the 0.26” hole on the side of the housing. The laser can come either through the 4-mm orifice in the top of the part or through the 0.26” hole in the front face of the piece.

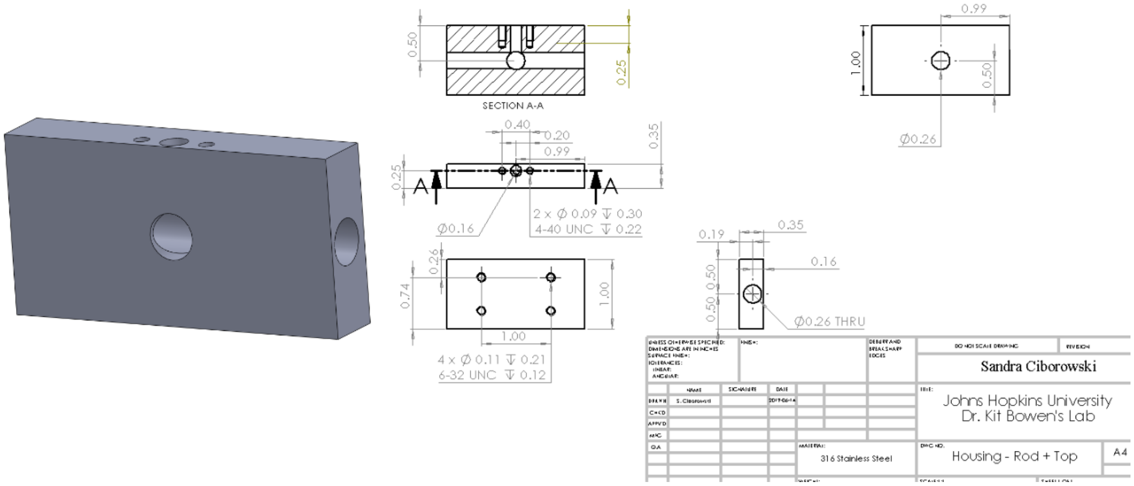

Figure A.15. Part and Schematic Drawing of the Rod Adapter Housing.

If the latter option is chosen, i.e., to bring the laser through the front of the housing, then the hole on the top of the housing could present an issue. The plug in Figure A.16 fits

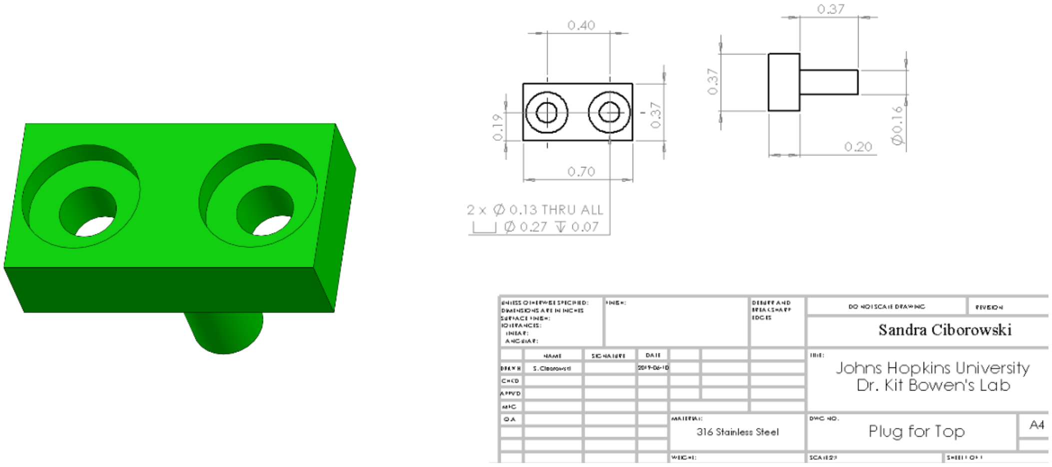

Figure A.16. Plug for Rod Adapter Housing.

snuggly in the 4 mm hole and attaches to the rod adapter housing using two 4-40 bolts to prevent gas flow through the 4 mm opening.

The rod adapter housing connects to a housing that can hold two pulse valves, see Figure A.17. All of the bolt holes are size 4-40. This includes those holes that hold on the rod housing, a nozzle, and the two pulse valves. Two holes on the top and bottom of the housing allows the rod housing to be held, using two adapters, and to attach both to an already-existing stand. The two holes on the front are meant to hold in a nozzle, whose

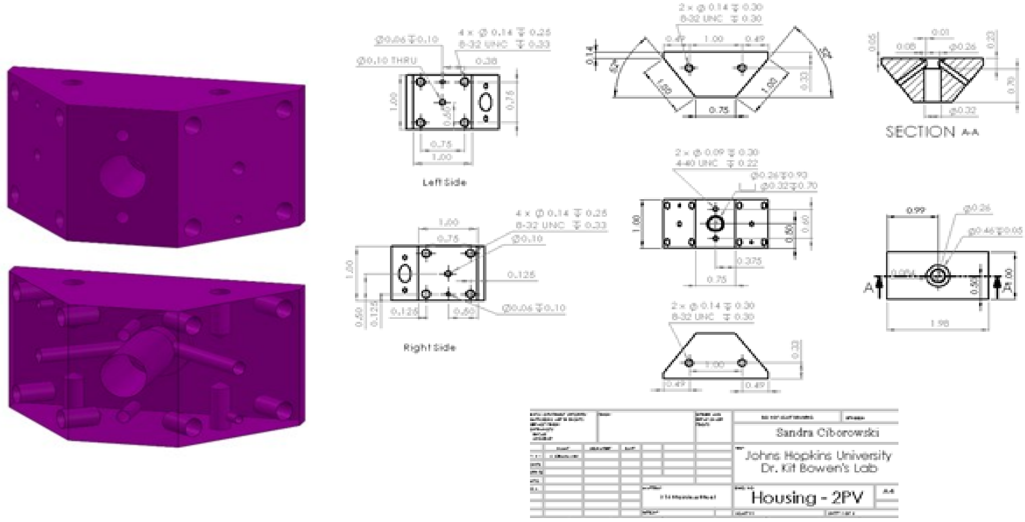

Figure A.17. Part and Schematic Drawing of Housing for Two Pulse Valves.

design could be adjusted depending on need except that the OD needs to fit within the 0.32” opening and should match with the 0.26” opening that lies in the housing’s interior. There are four holes on each face where a pulse valve could be attached; on each of these faces there is also a pin hole (0.06” diameter) that will be explained in more detail later.

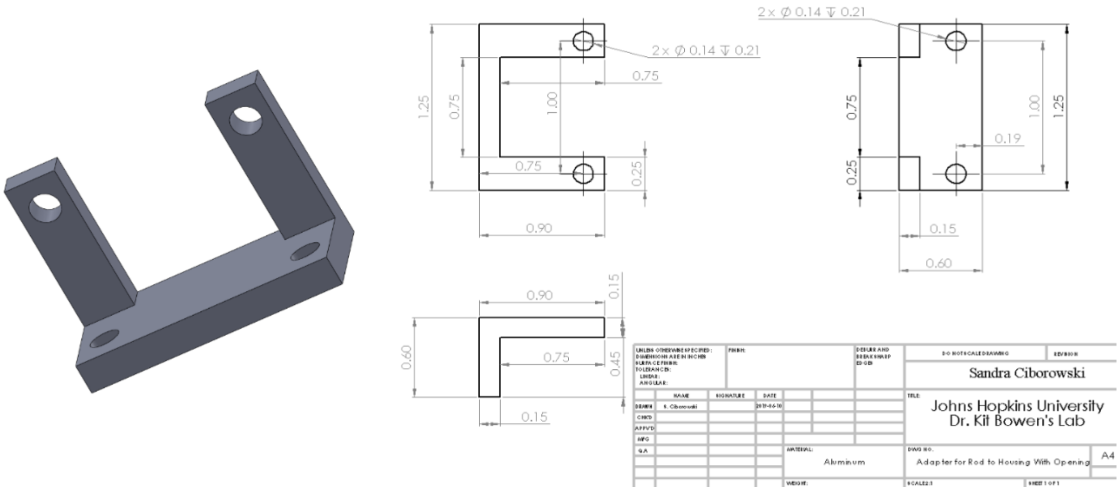

Figure A.18. Top Adapter to Affix Rod Adapter to 2-Pulse Valve Housing.

There are two adapters to hold the rod portion to this two-pulse valve housing. One major difference between the two parts is the ability for the plug to be in place and bolted onto the rod adapter housing or the source laser to be brought in to strike the rod from above the housing. This opening is clearly seen in Figure A.18. The other adapter, i.e.,

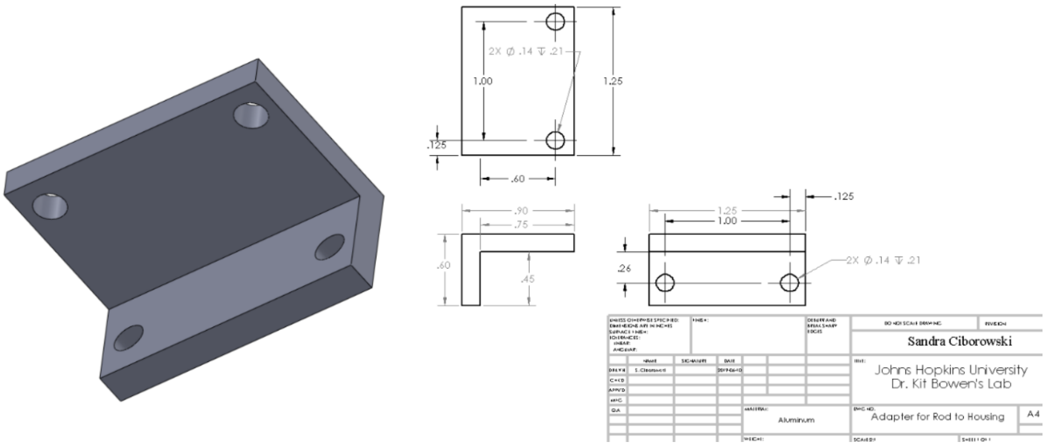

Figure A.19. Bottom Adapter to Affix Rod Adapter Housing to 2-Pulse Valve Housing.

Figure A.19, is a similar design but without the cutout portion of the one shown in Figure A.18. These both bolt to the housing and the rod adapter housing. The bolts holding on the bottom adapter may need to go through a pre-existing stand for mounting purposes, and this can be easily done with long enough bolts.

Since we typically run with only one pulse valve, it was necessary to consider the loss of gas when one channel is open to vacuum. Similar to the plug for the rod adapter housing, a plug has been designed for the pulse valve opening on the two-pulse valve housing. See Figure A.20, which shows the same bolt pattern as a pulse valve but includes a solid cylindrical portion that plunges into the opening where gas would otherwise be pulsed. A dowel pin has been inserted in the 0.06" hole on the plug to insure alignment within the housing; if this plug were inserted incorrectly, the cylindrical portion would block the flow of gas from the pulse valve and/or ablated rod.

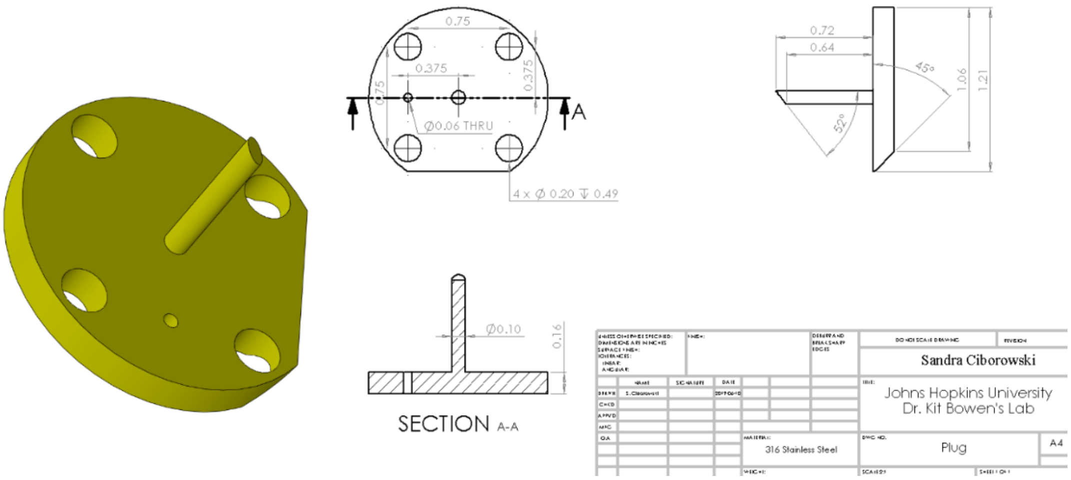

Figure A.20. Plug for Pulse Valve Opening on 2-Pulse Valve Housing.

An example of the conical nozzle for this housing is presented in Figure A.21. The features can easily be changed but may involve EDM.

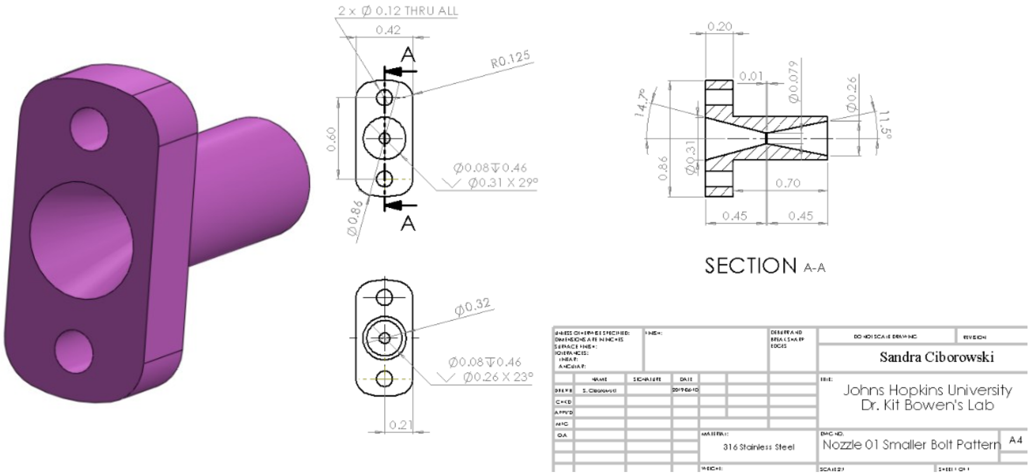

Figure A.21. Conical Nozzle for 2-Pulse Valve Housing.

IV.C.2. Disk-Style Laser Vaporization Source

The magnetron source, as well as a newly designed and manufactured disk laser vaporization source, used by our surface (upstairs) lab uses 2" disk targets to create ions of interest. Zachary Hicks designed the disk LVS for that lab; refer to his thesis for more details. Using that design as a model, a disk laser vaporization source has been made for our gas-phase (downstairs) lab, which can be used on PSA-RET or PIPES.

From the previous section, the two-pulse valve housing, plug for the pulse valve opening, and nozzle were also designed to adapt to this new disk laser vaporization source. Additional pieces in this disk source are three plates, a target holder and peg, a 3-D printed set of gears, two adapters, two stands, two stand clamps, and a number of bolts, spacers, and nuts.

The front plate, which is made from stainless steel, has a cone that begins at 4 mm and opens to 0.25" at 0.5" from the center of the plate, as seen in Figure A.22A. When Zach designed his source, he chose a set of gears that when offset by this distance creates a 91-petal pattern across the entire surface of the disk. There are two series of two threaded holes where the adapters hold the housing to the plate. Four more holes are made for ¼-20 bolts, which with spacers will hold the three plates together. These four holes are identical for all three plates. The center, a.k.a. the gear, plate is made out of aluminum and

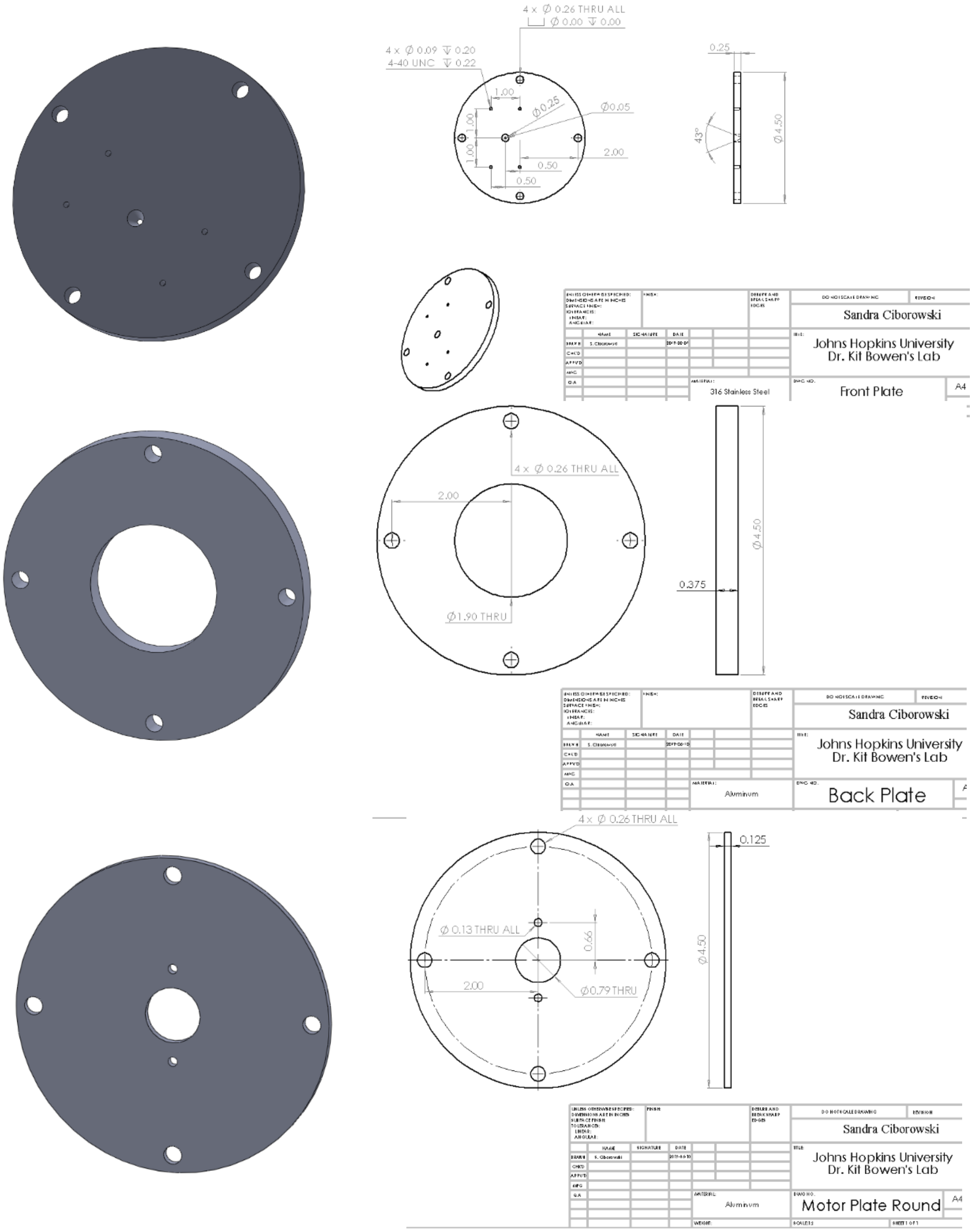

Figure A.22. (A) Front Plate, (B) Gear (Center) Plate, and (C) Motor (Back) Plate of the Target LVS.

in which the center hole is the same size as the sun (outer) gear (Figure A.22B). The back, i.e., motor, plate holds the stepper motor in place and is also made from aluminum (Figure A.22C).

There are two designs for a target holder: (A) Zach's original design, made from aluminum, and (B) a solid, stainless steel cup, meant for directly pressing powders. Both are presented in Figure A.23 and have an o-ring that seals in the gas, as well as allows the target to glide along the back side of the front plate. While the advantage of the first design was to have small bolt holes where the target could be pushed out, the holes pose a potential

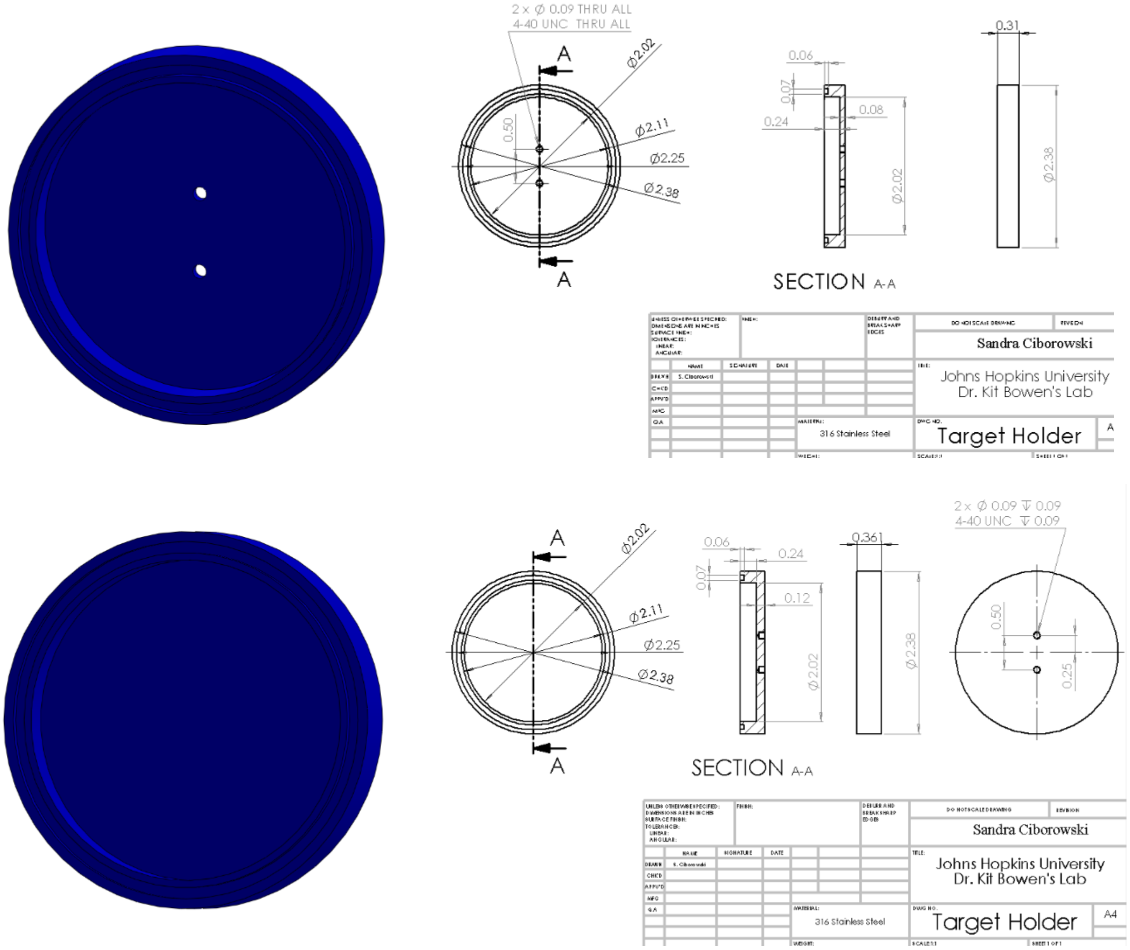

Figure A.23. Target Holder for LVS in (A) Aluminum, with threaded holes through the back, or (B) Stainless Steel, with a solid back.

issue when metal powders would be pressed in the machine shop or in the PARADIM facilities' Spark Plasma Sintering (SPS) instrument. To press powders directly into a stainless-steel target holder, two dye pieces, i.e., Figure A.24, were designed and manufactured with Nicolas Blando's assistance out of 304 stainless steel. The stainless-steel target holder fits snugly in the bottom piece, where loose powder would be added through the large hole. The top piece fits closely into the same opening and can be used to press the loose powder into a solid disk, using the simpler press in the chemistry machine shop.

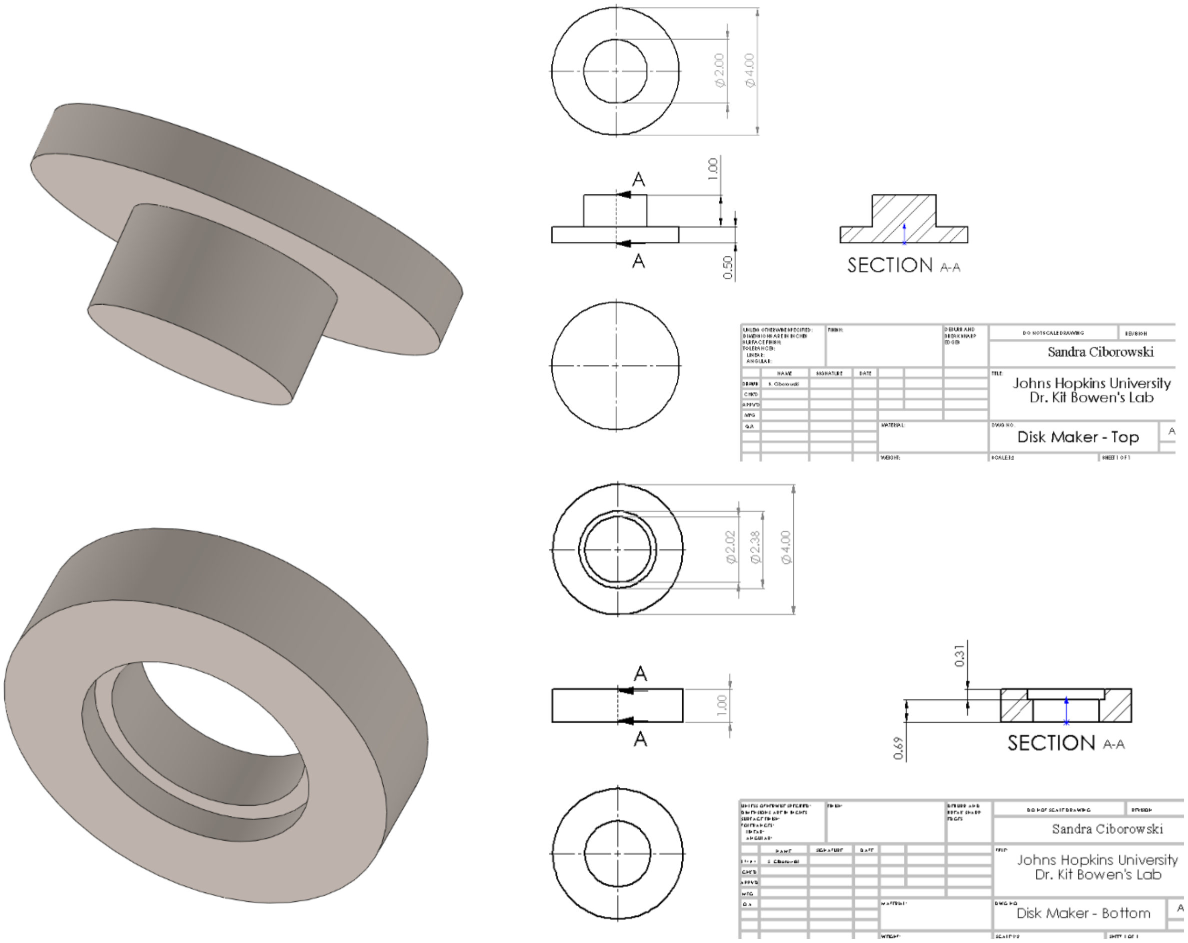

Figure A.24. (A) Top and (B) Bottom Press Pieces to Use in Chemistry Shop with a Solid-Backed Target Holder.

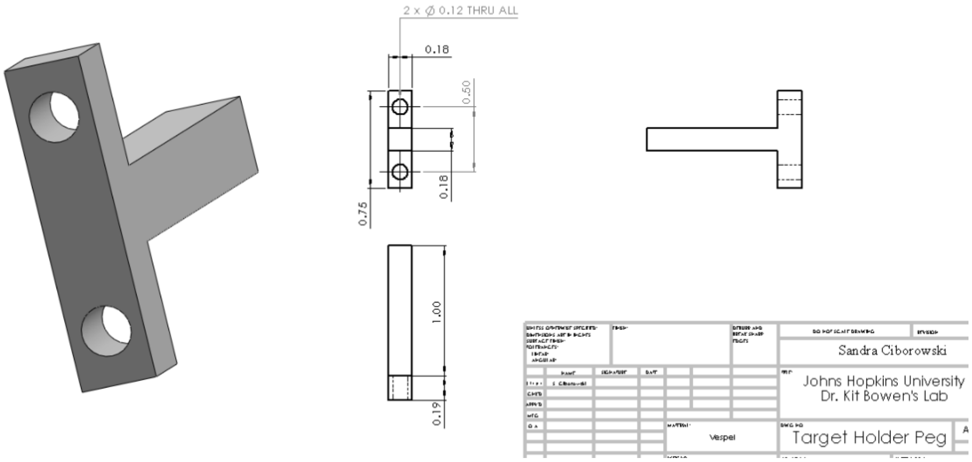

Figure A.25. Square Peg for Target Holders.

The target holder is held in place with a square peg (see Figure A.25) and a spring. The spring also ensures that the smaller gear stays in place, since it pushes against the back

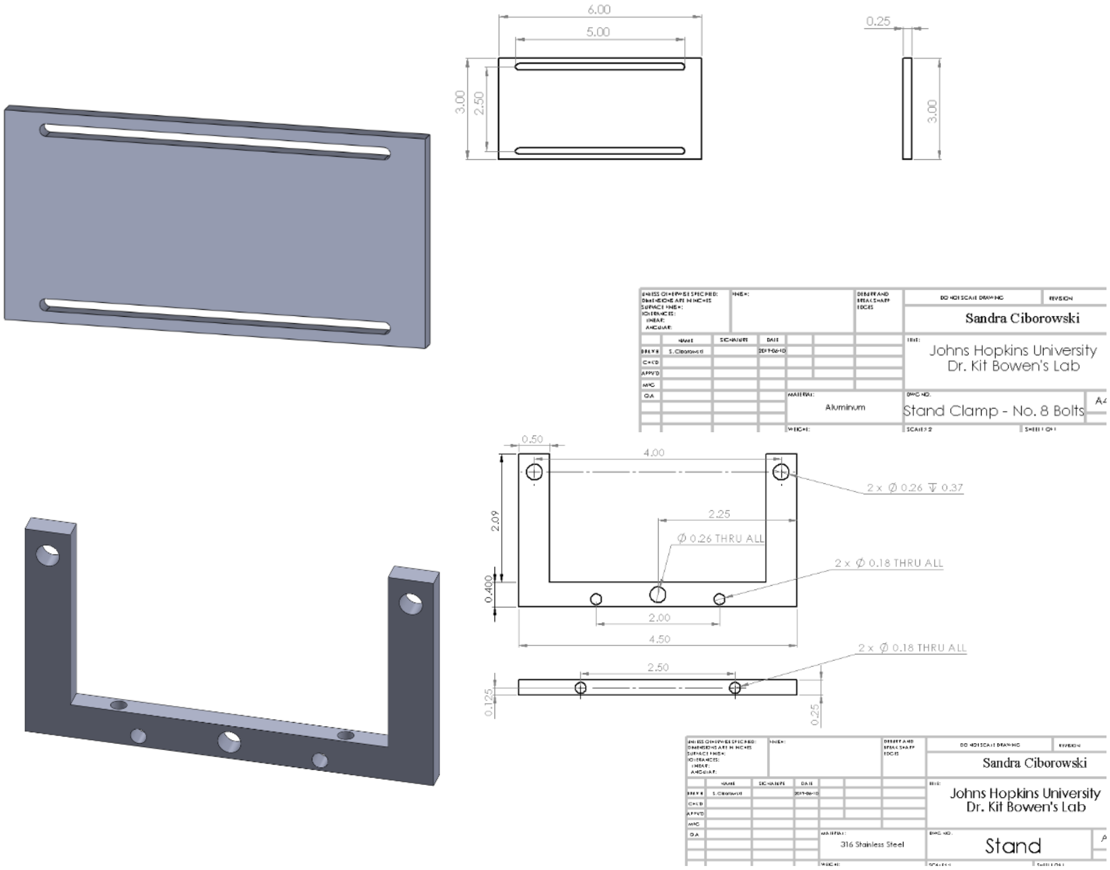

Figure A.26. Aluminum (A) Stand and (B) Stand Clamp to Hold LVS Setup Vertically or Horizontally in the Source Chamber.

of both the target holder end of the peg and the top of the gear into which the peg slides. The center gear is held in place by the coupling to the motor.

The two aluminum stands line up with three of the four ¼-20 bolts that hold all three plates in place. They have two sets of 8-32 through holes which align with the slots in the two stand clamps. Depending on whether the intention is to use the LVS setup vertically or horizontally, the appropriate set of 8-32 holes must be chosen. These parts and drawings can be found in Figure A.26. Due to the necessary spacing between the plates, aluminum spacers have been purchased from McMaster-Carr, which also take into

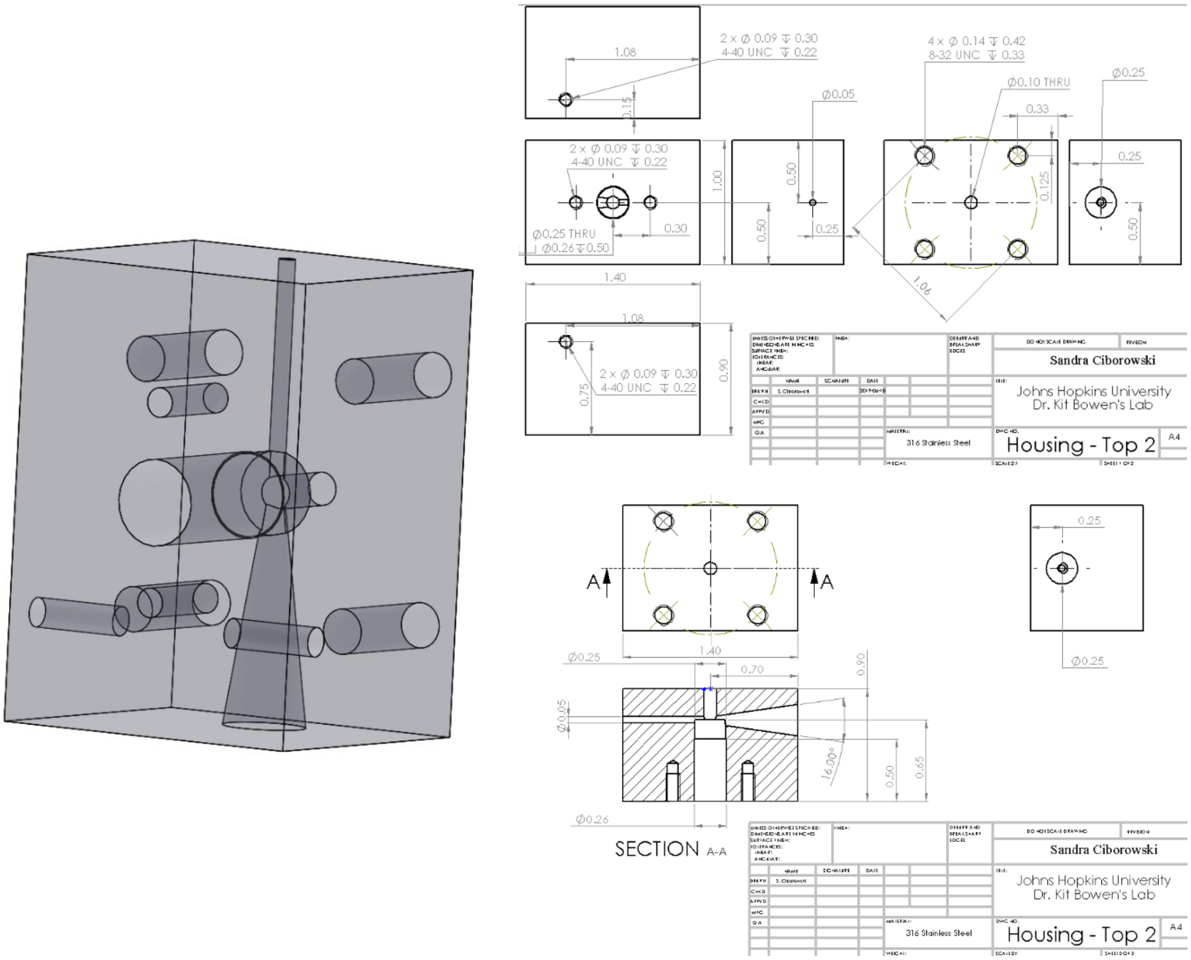

Figure A.27. Housing for Target LVS with Laser Perpendicular to Ion Axis.

account that three of the four bolts will also have 0.25” aluminum stands both between the front and gear plates and between the gear and back plates.

On the subject of being able to clamp or hold the entire setup vertically or horizontally, another housing was necessary so that the ion beam was not traveling perpendicularly to the skimmer (Figure A.27). This housing allows the laser light to entire only through the top, where it will strike the target and the resulting plasma will be confined within a conical feature that meets the pulse from the pulse valve. The same nozzle design is used for this housing.

A figure that shows the Target LVS setup with the two-pulse valve, laser down the same axis as the ions housing, inclusive of the stands and clamps is presented in Figure

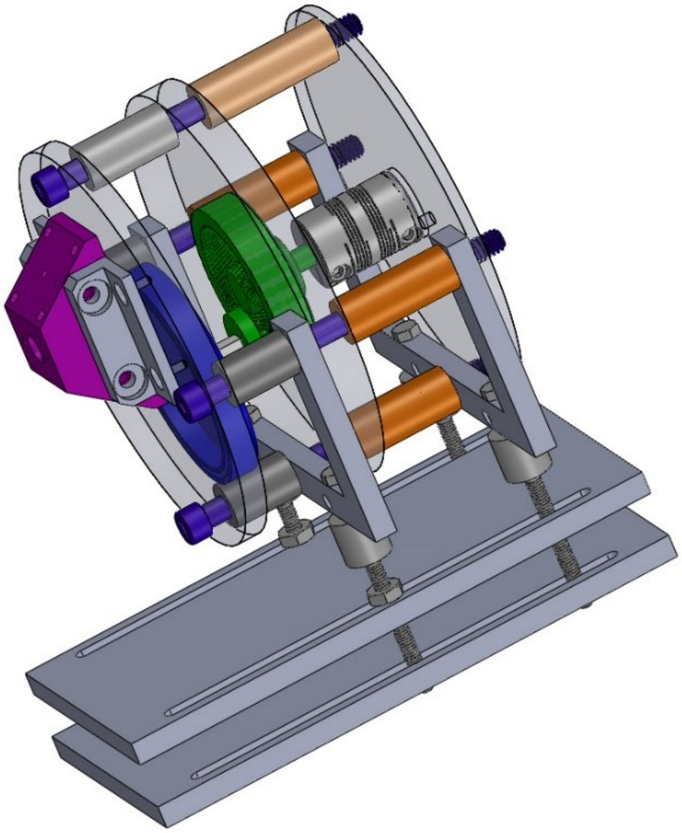

Figure A.28. Full Target LVS Setup with Laser Colinear to Ion Axis, Omitting the Motor, Spring, Washers, and Nuts.

A.28. The motor, spring, washers, and nuts have been omitted from the figure but are necessary for functionality and stability of the source.

IV.C.3. Implemented Skimmer Design for PSA-RET Instrument

The skimmer that was being used when I began studying on the PSA-RET instrument was originally set up to be used with a heater ring around the area that mounted to the chamber wall. Since this is not routinely required for this machine and the orifice was slightly damaged, a new skimmer that allowed some flexibility and had a well-defined orifice was designed and manufactured (by Michael Kratfel). The design has a base flange, shown in Figure A.29, that is mounted on the chamber wall and can have a skimmer with an appropriate orifice size slid into it, where it is held by four 4-40 set screws. On the suggestion of Mike Kratfel, the set screws are brass so that they will deform under pressure before the skimmer.

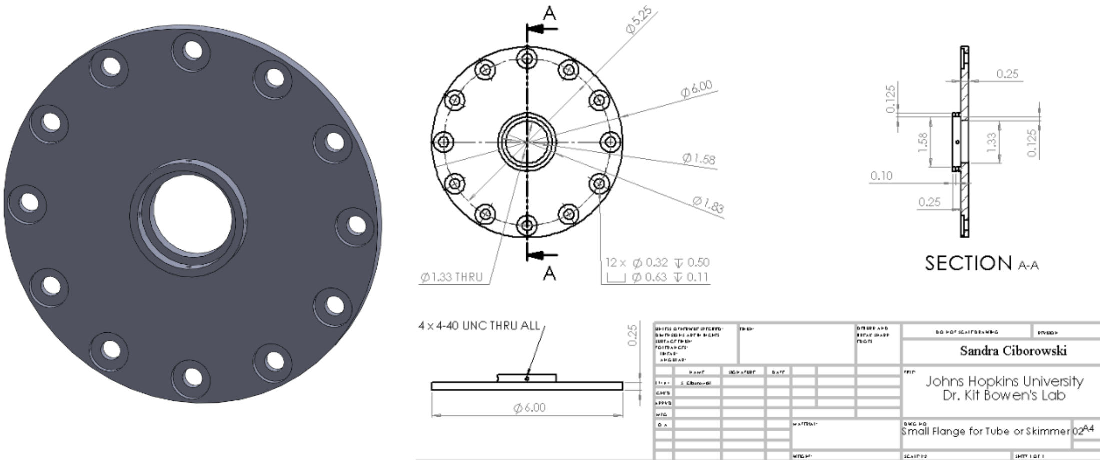

Figure A.29. Base Flange for Skimmer design on PSA-RET Instrument.

The two skimmers that have been manufactured feature 2-mm and 6-mm (nearly 0.25”) orifices (see Figure A.30), as well as a conical feature that matches the opening in the base flange. In addition to the inner cone, the outer edge of the base of the skimmers fits snugly into the protrusion on the base flange, where it is also held in place by the four 4-40 set screws.

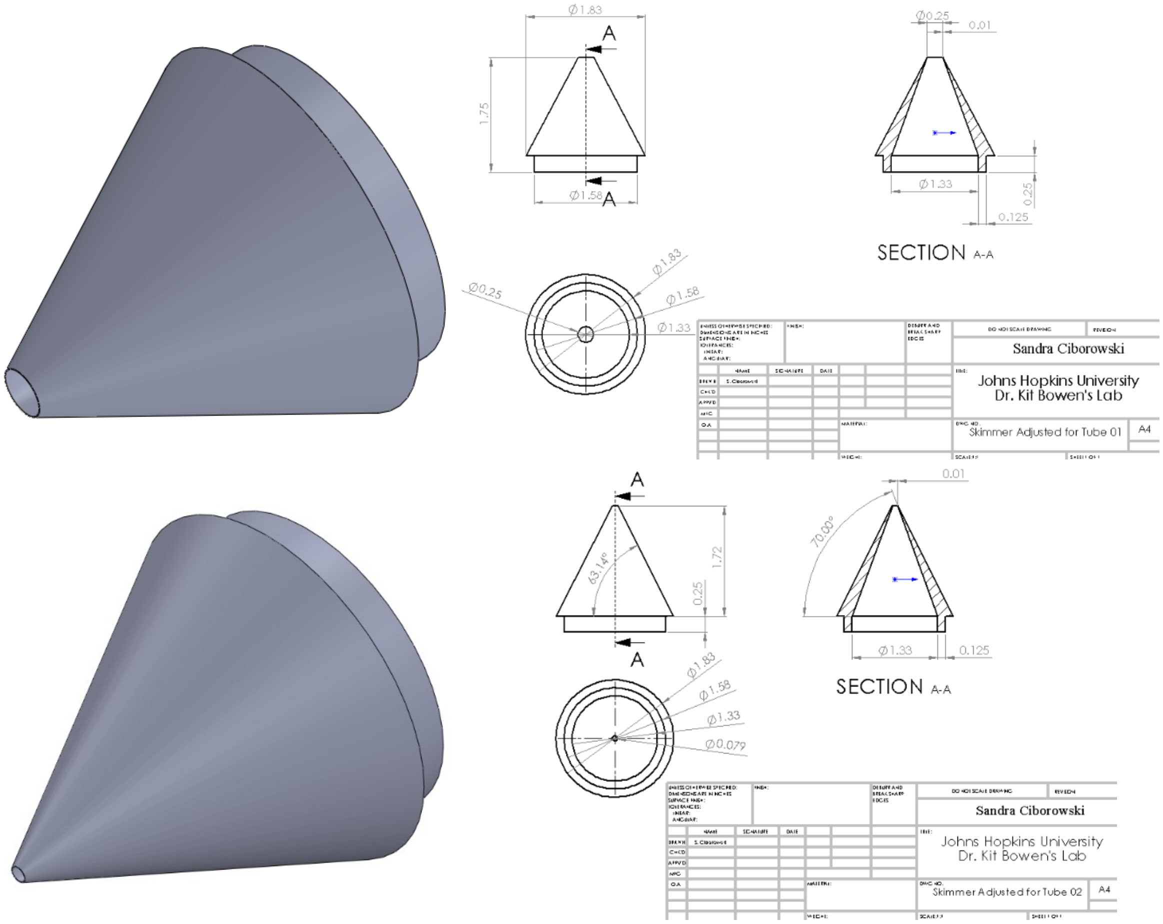

Figure A.30. Skimmers with (A) 2-mm and (B) 6-mm (0.25”) Orifices.

In some LVS studies, the source is pulled back from the extraction region of the TOF-MS and the skimmer is also extended into the source chamber. So that this is an option on the source chamber, a tube has been manufactured, which extends the skimmer about 2.5” into Chamber 0 from the base flange. The tube has one end that fits snugly into the base flange, like the skimmers, and another end in which the skimmers fit tightly. See Figure A.31 for more details.

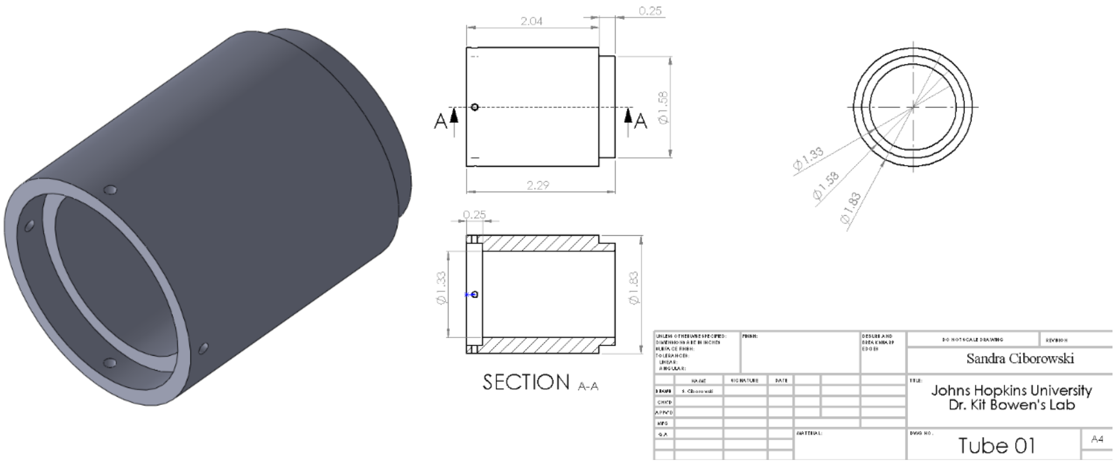

Figure A.31. Tube to Extend Skimmer into the Source Chamber.

IV.C.4. Skimmer Adaptation for Beam Dynamics Skimmer

The Beam Dynamics (BD) Skimmer was previously purchased, I believe by Allyson Buytendyk. It is a very small and precise skimmer that is quite delicate and permanently housed on one of the top shelves above my previous desk within a plastic box. To make sure that these skimmer designs would allow us to also use this BD Skimmer, two pieces are necessary. Since the flange of the BD Skimmer is relatively small and the cone is obviously smaller than either of the new skimmers, an adapter to the base flange is necessary; likewise, we didn't want to physically change anything about the BD Skimmer, so a top flange that sandwiches the BD Skimmer to the adapter is essential. Both of these parts are presented in Figure A.32.

IV.C.5. Skimmer Design for SNIPES Instrument

With the addition and successful implementation of the new skimmer on the PSA-RET instrument, the interest in a similar design for SNIPES grew. It was also brought to my attention that the skimmer currently being used on SNIPES has a damaged knife edge, to the point that two orifices seem to exist and the edge is blunt. The skimmer design uses

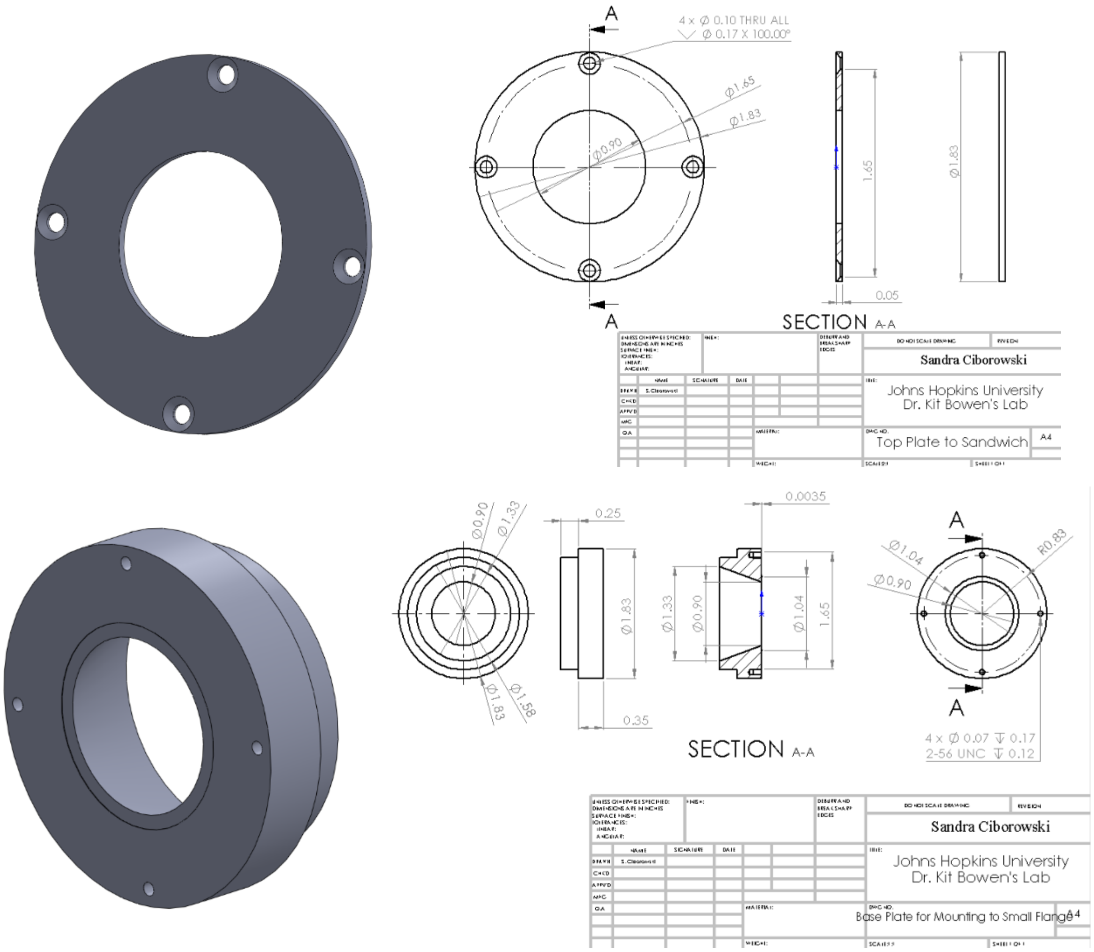

Figure A.32. Beam Dynamics Skimmer Adapter and Sandwich Flange.

the same 2-mm and 6-mm skimmers and extension tube but, due to alignment restraints, requires a couple of extra holes in the base plate. The bolts, even when used in conjunction with isolating washers, alone tend to give some flexibility to the alignment of the base plate. The thru holes are meant to be used as more specific alignment of the skimmer using dowel pins that are removed before running an experiment. The current skimmer is aligned using this same system so the new one would not require extra training or procedures. The skimmer design for SNIPES, which has yet to be manufactured and/or implemented is presented in Figure A.33.

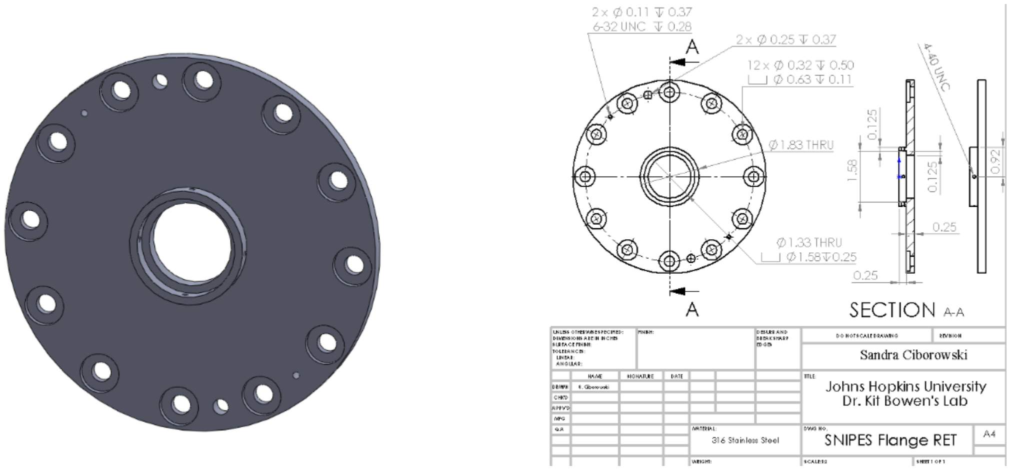

Figure A.33. Skimmer for the SNIPES Apparatus.

After this design was presented to Kit and Sarah Stokes, it was brought to my attention that SNIPES uses a wire mesh behind the skimmer to better direct the ions by

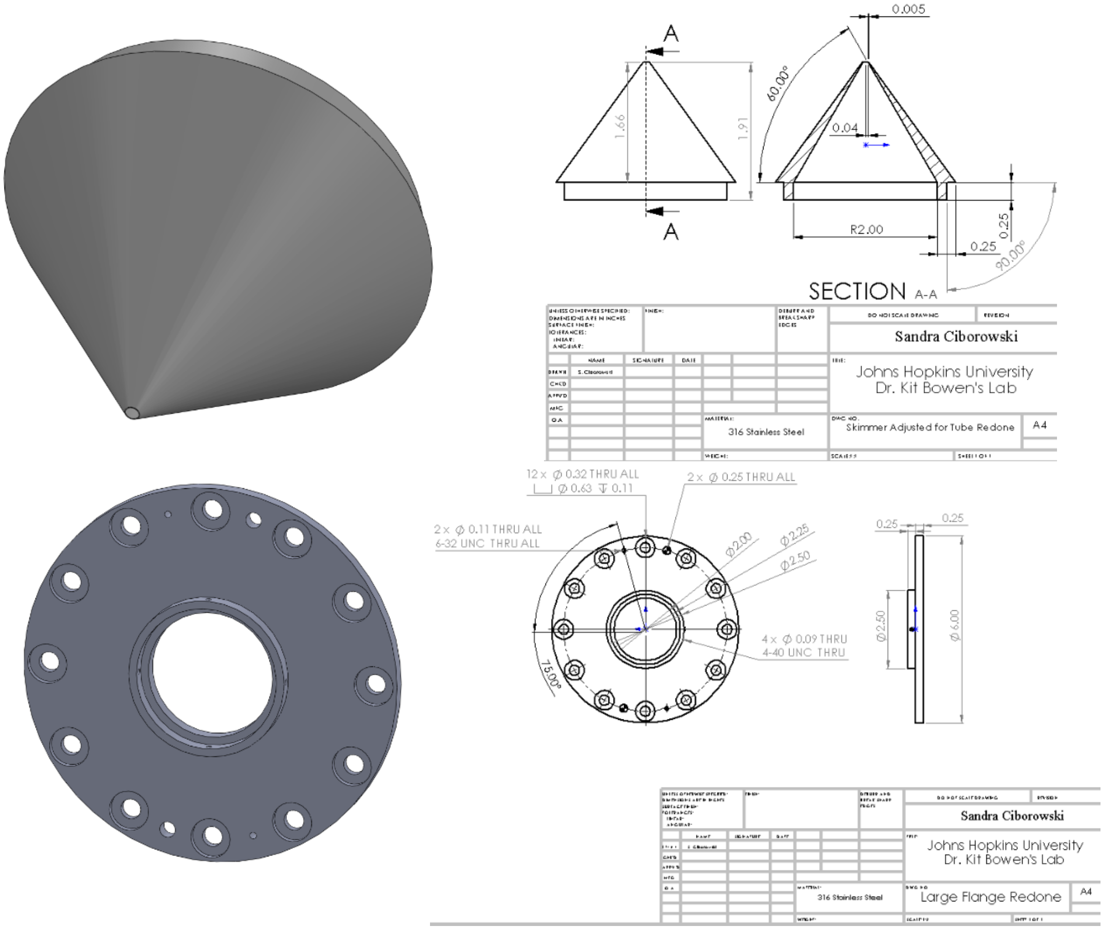

Figure A.34. Skimmer/Base Plate with Wider Opening to Adapt to the Wire Mesh on SNIPES.

allowing less space interrupting the electric field from the ion guides. This does create a likely need for a wide skimmer, which would mean a different, less universal design for the skimmers and which is obviously less ideal. These other designs, for the skimmer and the base plate are in Figure A.34, below. However, I would suggest redesigning the wire mesh and using the same overall design as PSA-RET so that one skimmer may be used on both machines. Additionally, the smaller skimmer, i.e., PSA-RET design, saves some space that is difficult to get back with such a wide opening required for the wire mesh.

IV.D. Heated Pulse Valve

Rainer Weinkauf at Uni. Düsseldorf completed a few studies where the pulse valve was heated to higher temperatures than the solenoid can typically handle. He accomplished these by designing and manufacturing a spacer, made from Vespel, that would separate the pulse valve face and the solenoid. This design was adapted to our machines by Evan Collins and is shown in Figure A.35.

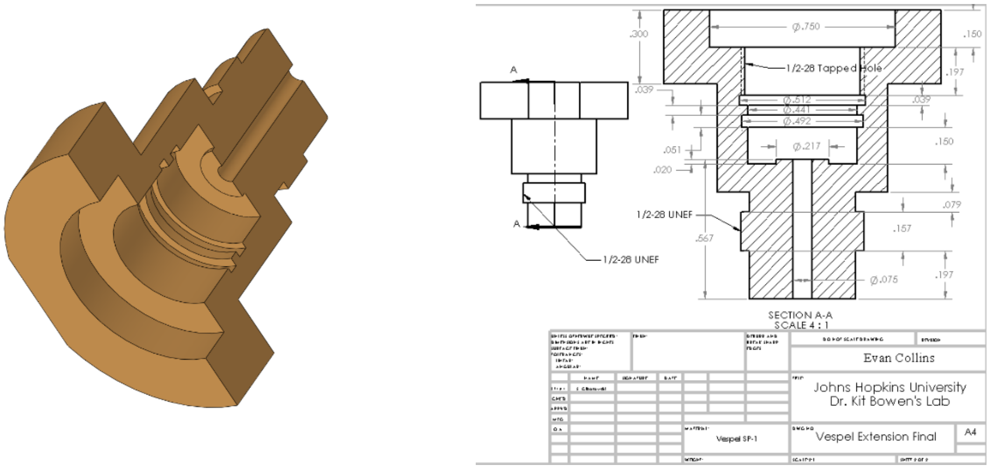

Figure A.35. Vespel Spacer for Heating the Pulse Valve.

The elongation of the distance from the solenoid to the face made it necessary to design and make longer poppets. So far, we have only had Mike Kratfel make and used Vespel SP-1 poppets with this setup. However, to save on Vespel material, Paul, one of

Dr. Weinkauf's graduate students, suggested two things. First, they started making poppets that were half Vespel and half aluminum. The end of the Vespel portion slides in, snugly,

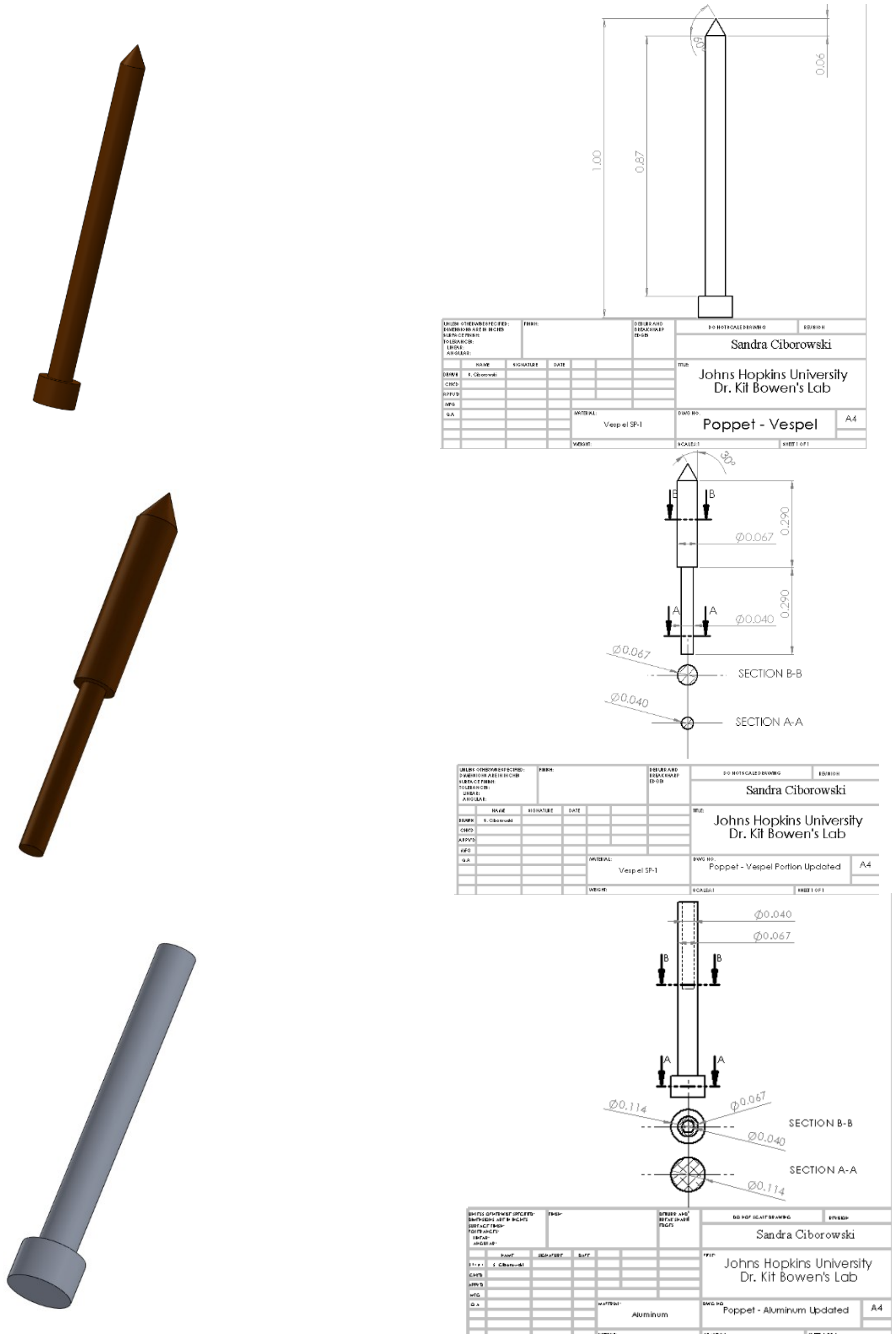

Figure A.36. Poppet Designs for the Heated Set up Made from (A) Vespel, (B) Vespel (Half), and (C) Aluminum (Half).

to the aluminum piece, without the OD of the poppet changing. Second, using various sandpaper grits and a Dremel, they resurface the poppets themselves. Paul had a rough alignment of the appropriate angle, where he held the poppet against the sandpaper until it smoothed and had a fresh, clean finish. This is more difficult for us to implement currently since our Vespel, all-in-one poppets have a heal at the end that would be held by the Dremel tool. I have gotten quotes from Mike for this setup, i.e., half Vespel-half aluminum poppets, but it has seemed too expensive for that time. The design we've used for the entirely Vespel poppets and preliminary designs for a partial Vespel/aluminum poppet are displayed in Figure A.36.

A note on the Vespel material: we have typically used Vespel SP-1 due to its properties for isolating electrically and thermally. The SP-1 also tends to be easier to machine than some of the other varieties. More recently, Vespel SCP-5000 has come to my attention. While we haven't used this, the SCP-5000 is supposed to have more enhanced properties of the SP-1 and be even easier to machine. I was given some stock material gratis from Dupont sales representatives.

A few heaters were purchased from Prof. Dr. Weinkauf. The heaters were designed for the modified faces that the Weinkauf group uses at Uni. Düsseldorf, so an adapter ring is necessary to use these with our normal pulse valve faces. While I did not make a specific part or design, the idea is that the aluminum ring has the same OD as the ID of the heater ring and the ID is the same as the OD of the back of the pulse valve face, i.e., the smaller diameter of the pulse valve. We wound up having to countersink one side because the pulse valve is curved and we want the whole face to be heated as consistently as possible.

IV.E. Lineberger-Style Source

Carl Lineberger *et al* detailed a source that was able to make ions from plasma entrainment in a supersonic expansion in their *J. Chem. Phys.* paper (**142** (2015) 044201/1-7), and see its supplemental information for more specific information on the designs. This source makes cool ions since the main expansion is perpendicular to the axis that the ions ultimately travel into the time-of-flight extraction region. Using their designs, Ryan Wood, a former undergraduate, attempted to make multiple pieces that could be used toward a discharge source that would be perpendicular to the ion axis. There are five main parts of this source: (1) a modified pulse valve face, (2,3) two stainless steel electrodes, and (4,5) Macor insulators; all of which are displayed in Figures A.37-39. The "S" numerical values correspond to the design in the supplementary material for the paper mentioned previously. Just to mention, it is important that the electrodes come very close to each other, so the small protrusion of the one toward the other becomes a crucial distance.

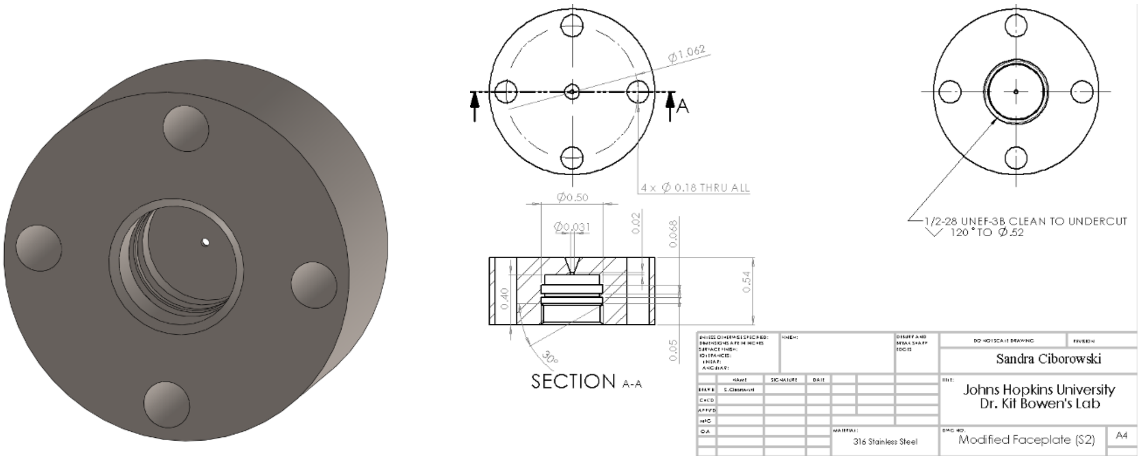

Figure A.37. Modified Pulse Valve Face, Designed and Manufactured.

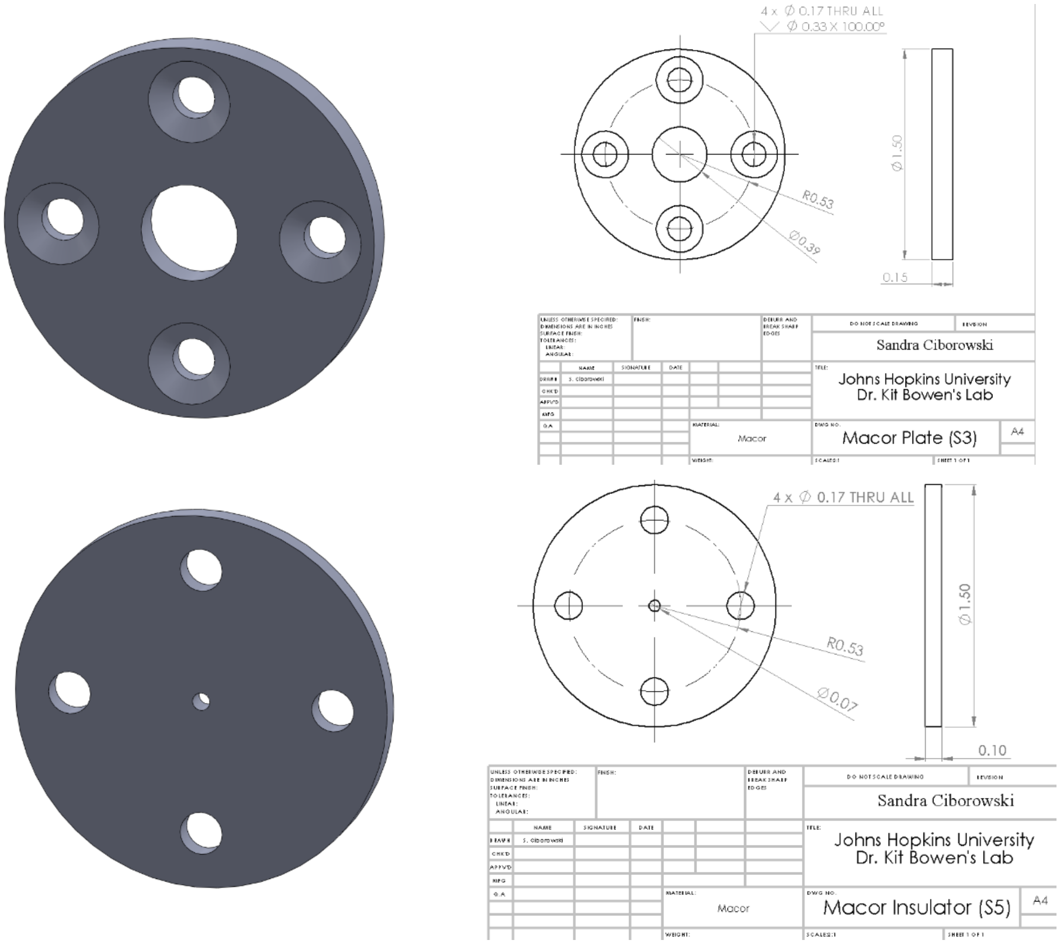

Figure A.38. (A) Macor Front Plate and (B) Macor Insulating Plate.

Since this time, I have updated designs; see Figure A.40. The improvements that I have made include minimizing the amount of difficult-to-machine materials, i.e., Macor, while maintaining the crucial distances between the electrodes. The Vespel spacer would have a smaller outer diameter compared to the stainless-steel pieces and thus requires an inset on both of the electrodes for alignment purposes. Another reason that the Vespel pieces have smaller outer diameters was to use what Vespel material we already have in stock, including the Vespel SCP-5000. Just to mention, no changes were made to the modified face for the pulse valve, except to have thru holes to be able to mount to our existing housings.

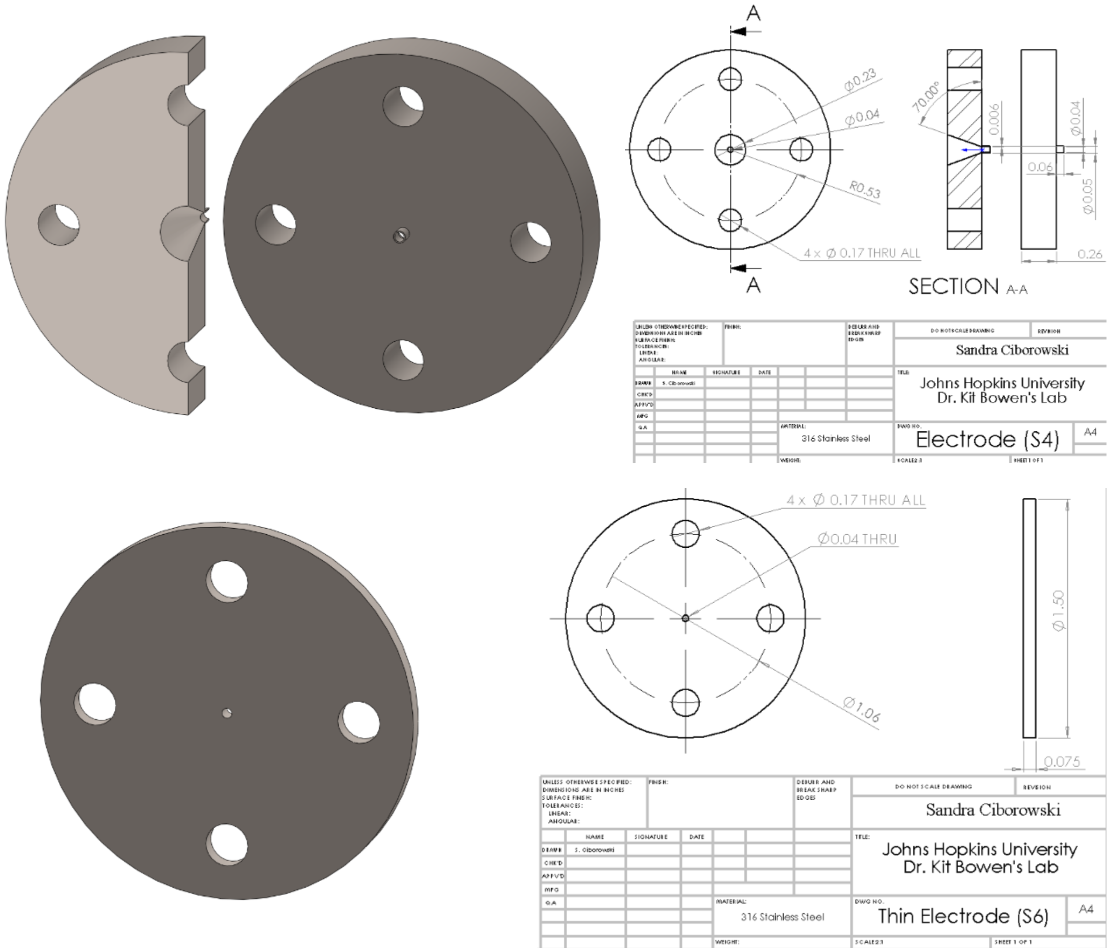

Figure A.39. (A) Front Electrode Plate and (B) Thin Electrode.

A variation of the Lineberger source was used to create uranium dimer anions; see Section XI.B of the Appendices for more specific experimental results. The experimental setup married the "open-housing" laser vaporization source with the Wang-Inspired Housing in Figure A.12. A stand to hold the housing perpendicular to the ion axis was designed, as seen in Figure A.41, and manufactured. This allows the laser to be brought in directly through the nozzle on the Wang-Inspired Housing, but the light would still enter from the top of the chamber instead of through the skimmer. The nozzle of this housing can be placed just below the opening of the pulse valve in the "open-housing" source, with

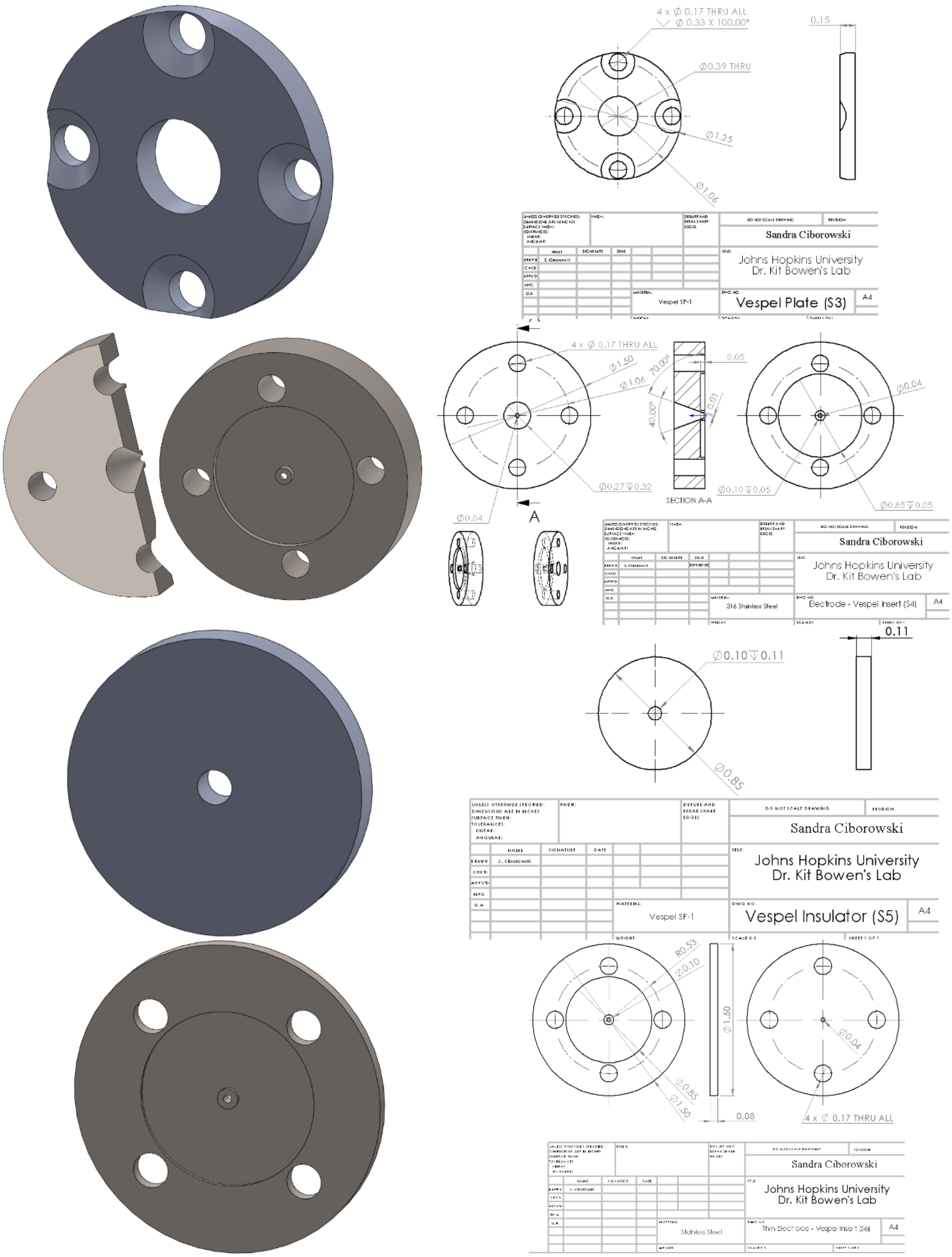

Figure A.40. Modified Lineberger Source Parts with Vespel Instead of Macor.

the rod rotating and translating beneath it. Using argon gas behind the pulse valve on the Wang-Inspired Housing and helium gas in the main pulse valve, a.k.a. that of the "open-housing" setup, a different variety of anionic clusters was seen in the mass spectrum when compared to the traditional LVS with pure helium. One note about this setup would be to pay attention to the length and positioning of the rod with respect to the skimmer; the longer copper rods that are available will easily hit the skimmer or chamber wall if the motor is positioned too close to the housing.

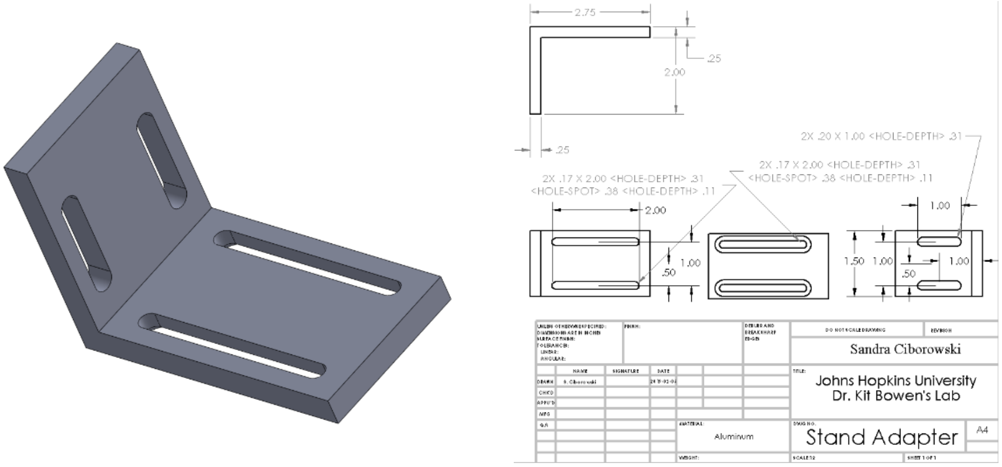

Figure A.41. Stand to Adapt the Wang-Inspired Housing Perpendicular to the Axis of Ion Travel and Below the Main Pulse Valve.

IV.F. Ion Trap Setup for Ch. 0 on PSA-RET

James Damewood, under the supervision of Evan Collins, completed designs for implementing an ion trap in the source chamber of the PSA-RET apparatus. The main idea behind having this capability was to further separate when we introduce a reactant gas. Using the reaction cell, the reactant gas is still introduced within the same chamber as and has the possibility of reacting directly with the plasma created by the ablation of a metal rod.

The ion trap itself came out of an instrument originally from the NIH warehouse. James put together a few power supplies so that the trap can function. He also married the trap to our setup by making a few brackets that would hold the trap within an isolation chamber that was already present in the lab; this chamber has the same bolt pattern as the skimmer, so the skimmer is extended further into Ch. 0 when the ion trap is in place.

IV.G. Electron Bombardment Ionization (Kondow) Source

IV.G.1. General Information and Design

The electron bombardment ionizer that resides on the PSA-RET machine was designed by Jacob D. Graham while he was a graduate student in the Bowen Lab. The designs did not make it in his thesis, and since I helped manufacture and maintain the source, I wanted to include them. He used the designs of Kondow *et al* from *J. Phys. Chem.* **90,** 1552 (1986).

First, the source has a front plate that is oriented toward the source chamber of PSA-RET. The designs and drawing of the front plate is presented in Figure A.42. This front plate encases and protects the majority of the EBI source. There is also an outer tube and a back plate that hold the source together.

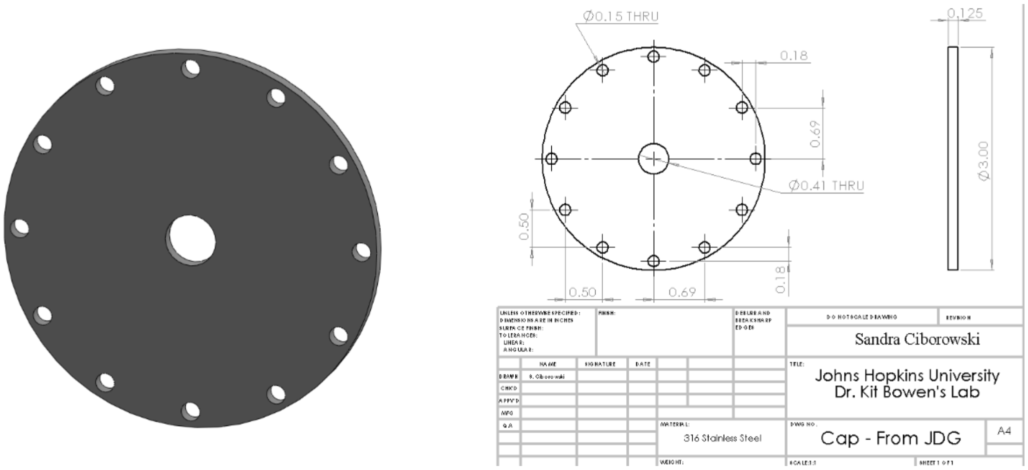

Figure A.42. Front Plate of the EBI Source.

The tube has two feedthrough holes on the sides, in addition to an NPT thread to insert an adapter (NPT to Swagelok) so that gas can be easily introduced. This tube is shown in Figure A.43. The feedthroughs allow a copper wire to enter into the center, so that the voltage for the filaments can connect to the power supply. What is not shown well in these images is that there are three grooves in the bottom of the tube, i.e., the edge further from the feedthrough holes, so that the wires which connect each of the grids can individually feed through the side of the source.

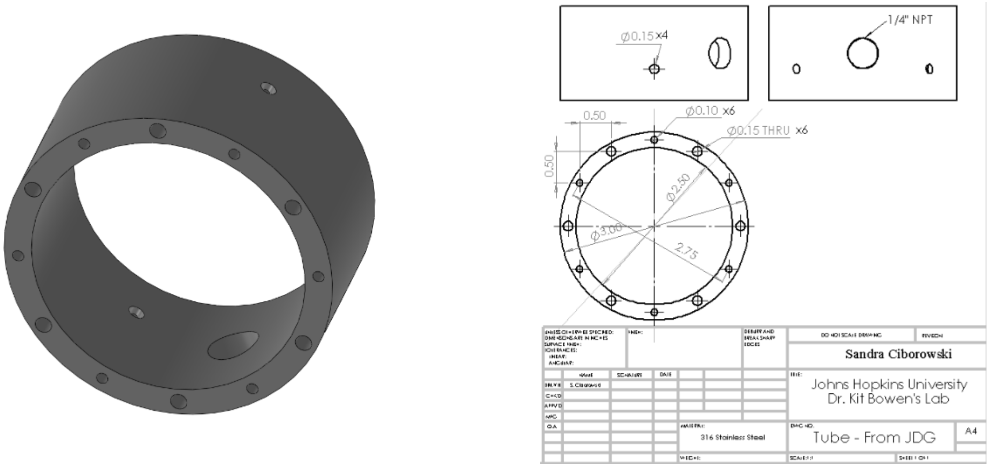

Figure A.43. Outer Tube of the EBI Source.

The back plate is arguably the most complex piece of this source. It not only has holes to adapt to the tube but also for holding the grids, standoffs, ruby balls, and adapter to the chamber. All of these holes can be seen in Figure A.44. Six of the outer 12 holes are meant to adapt the entire source to the chamber and the other six are threaded so that the front plate, tube and back plate can be held together, mainly for easy removal of the source from the chamber. The four 0.15” holes are for the attachment of standoffs which hold the filaments, which is why they are counterbored. The four 1/8” holes are threaded so that the Kimball parts plates which hold the three grids (made from stainless steel wire mesh (P/N: 080X080T0012W48T from TWP, Inc.) can be secured. The remaining small holes are meant to align/hold small ruby balls in place; these are for isolating the grids from the rest of the source. Ruby balls are also placed in between each of the Kimball parts plates to isolate them from one another.

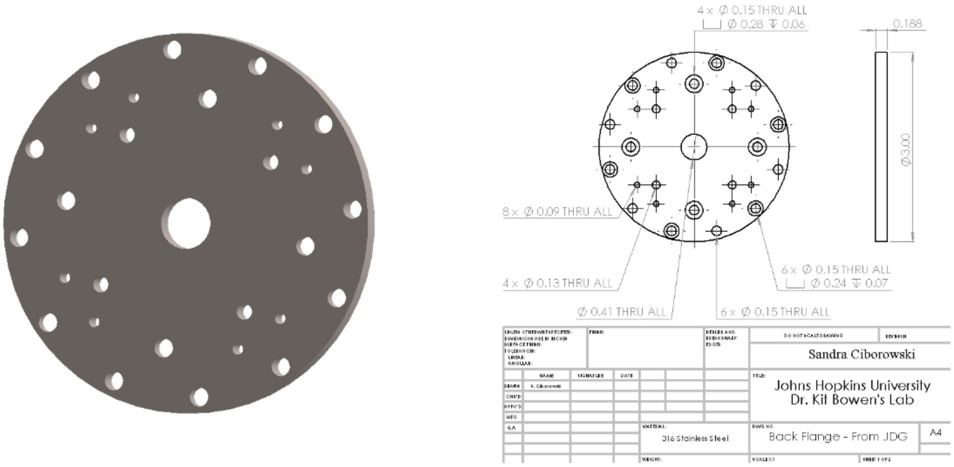

Figure A.44. Back Plate of the EBI Source.

The ceramic stand-offs that are held to the back plate also connect to stainless steel stand-offs which attach to the filaments and the copper feedthroughs, which were previously discussed. Two of the four stainless steel stand-offs have two holes 120° to one another, which are held in place by short 6-32 bolts; note that the bolts need to be short enough to not interact with the top plate of the source. The other two stand-offs have three holes so that they can hold two filaments in addition to the copper feedthroughs, which are isolated from the tube by small ceramic spacers. One of each of these stand-offs is shown in Figure A.45.

To create the filaments, a small length, e.g., a little longer than one inch, of thoriated tungsten wire (P/N: W-W99TH1-006-10 from the Electron Tube Store, dimensions: 0.15mm (0.006") by 3m (10')) is wound around a small Allen wrench to create a coil before being secured in the stand-offs. In theory, this allows for more surface area for the current, and thus more electrons to be released. This part is most easily done using tweezers and

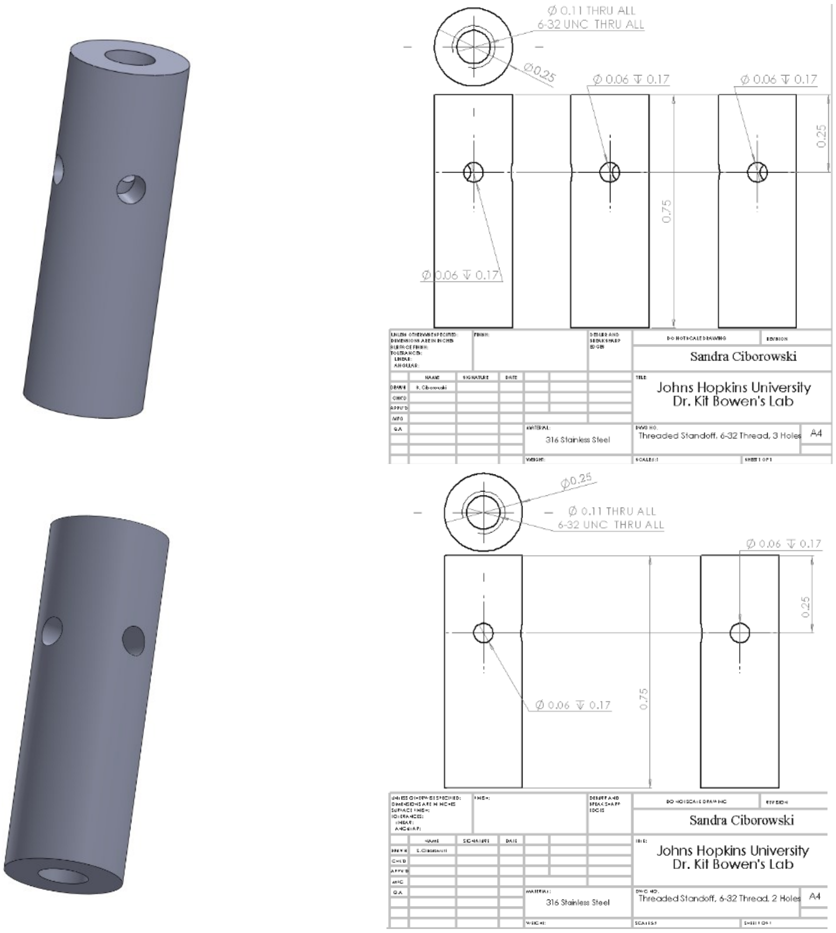

Figure A.45. Two Stand-Offs used in the EBI Source to hold the filaments and feedthroughs.

potentially two people, so that one may hold the wires and the other would tighten the bolt. The stainless-steel grids are spot-welded to the Kimball parts plates with the corresponding opening by the use of multiple small tabs of stainless-steel shim. The same shim is used as a structure for the grid material to be wrapped around to create the cylindrical grids. There are Teflon pieces in the Kondow source box above what was my desk that serve as molds or casts for the grids. The corners of the Kimball parts plates are removed so that there is no chance of them touching or interfering with the stand-offs for the filament.

Outside of the source, there is an adapter plate to mount the entire source to Chamber 2 in PSA-RET. This plate remains in Chamber 1, on the outer surface of Ch. 2, at all times. When installing or removing the source, the other portion is unthreaded from this adapter plate. For more information, see Figure A.46.

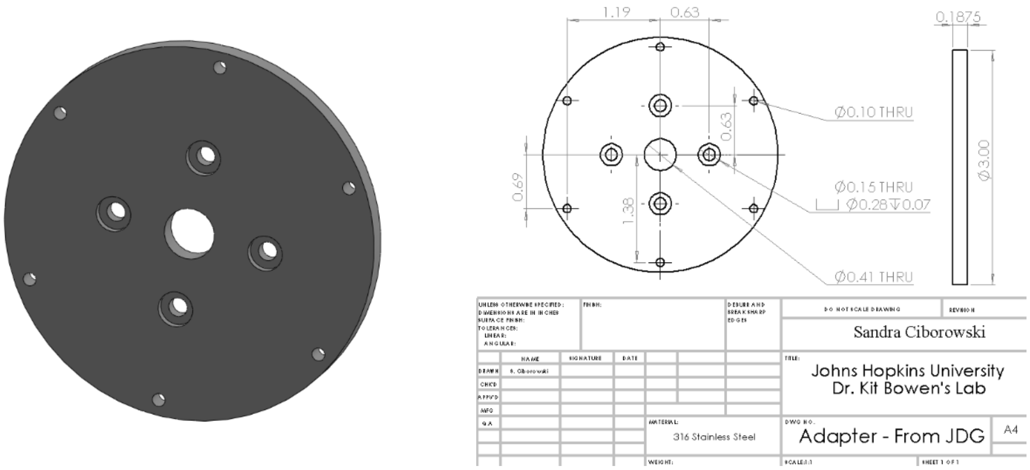

Figure A.46. Adapter Plate for the EBI Source which Remains on the Outer Wall of Ch. 2 of PSA-RET.

To give an overall look at the outside of the EBI source, Figure A.47 was made with a semi-transparent top plate and tube. The orientation shown would be similar to what one sees when looking at the source through the skimmer in Chamber 0 of PSA-RET, where the NPT threading is to the lower right and the main copper feedthroughs are on either side.

IV.G.2. Operating Procedure

1. Set up source as if running RET with the alkali oven. Xenon gas (or appropriate Rydberg atom source) may need to be leak checked.
2. The (3) grids should have individual power supplies, and the filament should be connected to the power supply that is able to be floated. Typical running voltages: -20,

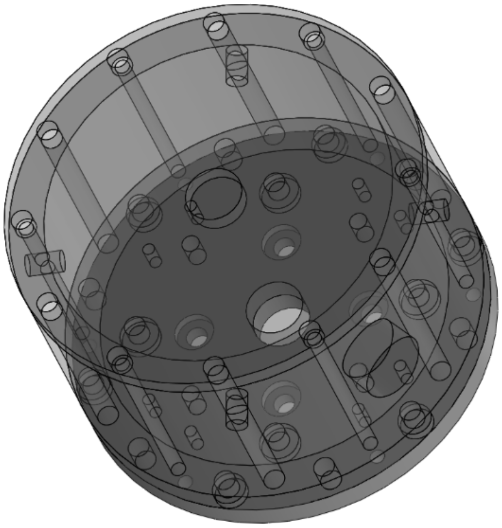

Figure A.47. Outer Portion of Electron Bombardment Source with Semi-Transparent Top Plate and Tube.

-100, -5, and -180 V on the outer, middle, and inner grids and filament bias, respectively.

Note: while running the experiment, most often the voltage on the inner grid needs to be tuned.

IV.G.3. Cleaning/Repairing Procedure

1. Vent chambers 0, 1, and 2. Remove the optics on the top of Ch. 1; lift and secure the top of Ch. 1.

   Note: lifting the top flange will take two people: one will use the rope (on the laser table side) to lift and one will help lift (from Ch. 0 side) and secure the pin. Ch. 1 should be wiped with water before removing the source.
2. Remove the source and skimmer from Ch. 0. Open the inline gate valve between chambers 0 and 1, and begin loosening the (6 hex head) bolts that hold the Kondow source to the side of Ch. 2.

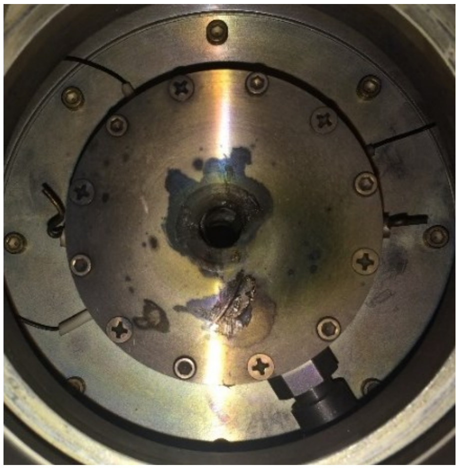

Figure A.48. Picture of EBI Source from Ch. 0 on PSA-RET.

3. Loosen the Ultra-Torr and take out the copper tubing. Disconnect the (3) leads for the grids and the (2) leads for the filaments.

   Note: this may require the use of tweezers or tongs.

4. Hold the Kondow source through Ch. 1 (requires someone with small hands) while the bolts are removed from Ch. 0. To remove the source from Ch. 1, the source needs to be lowered below Ch. 2 – it does not fit between the top edges of Ch. 1 and 2; this will require a second person to reach beneath Ch. 2 as the person (with small hands) lowers the source.

5. Once out of the chamber, the (6 Phillips) screws holding the top flange to the outer cylinder.

6. Remove the (4) stainless steel standoffs, the (4) bolts for the standoffs, the (2) copper feedthroughs, and the (4) filaments.

   Note: these need to be replaced: the new standoffs need to have holes drilled for the filaments that are 0.25” from one end of the standoffs; two standoffs will have two holes approximately 90° to one another and the other two will have an additional hole that is about halfway between those two holes (~120° separation).

7. To remove the grids, remove the (6) bolts holding the outer cylinder to the back plate and remove the cylinder. Going forward, work in a tray. Loosen the (4) bolts holding the Kimball parts plates. Carefully remove the plates and the ruby balls that separate them.

   Note: tweezers are useful during this step.

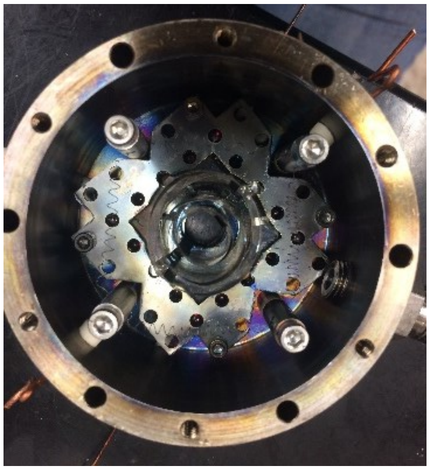

Figure A.49. EBI Source without the front cover, outside of the chambers.

8. To remake the grids, use the plastic "molds" that are in the "Kondow Source Materials" box to spot-weld an outline of stainless-steel shim. Then spot-weld the stainless-steel mesh to the shim. Tabs made from the shim will be used to hold the grids to their Kimball parts plates. If the Kapton-coated wires need to be replaced, cut the appropriate length, wrap an easily-spot-welded wire around the end, and spot-weld to a corner of the plate. Note: if the spot-welding is too high or wire is too thick, the plates will come in contact and ground the grid(s).
9. Rebuild the source.
   a. Using tweezers, place the ruby balls and grids, carefully. While bolting these in place, do not tighten to the point of bending the Kimball parts plates. Use a

voltmeter to check that the grids are independent of one another and the back plate of the source.

b. Replace the standoffs, trying to line up the holes with the appropriate angles. Overtightening the standoffs will likely break the ceramic spacers. Replace the outer cylinder of the source.

c. Remake the (4) filament wires by twisting the wire around a small Allen wrench until there is approximately 1" of coiled wire. Tighten the bolt into the standoff as two of the filaments (and possibly copper feedthrough) are inserted in the standoff.

   Note: after each bolt is tightened, verify that the filaments are being held in place.

d. Using a voltmeter, verify that the filaments and grids are connected correctly. Replace the top flange.

10. Place the source back in the chamber using the opposite order of steps 1-4.

    Note: once the leads are connected, each should be checked for connectivity and grounding.

IV.H. RET Modifications/Information

IV.H.1. Retaining Ring for Internal Oven

Figure A.50. Close up of RET Internal Oven, Showing Previously Used Stainless-Steel Clips for Alignment.

Allyson Buytendyk and Jacob Graham used three clips made of stainless steel to hold the internal oven centered within the ceramic, heating tube. This can be seen in Figure A.50. Gaoxiang Liu and I ran into a number of issues with these clips, especially after a few months of heating and cooling cycles. For example, a few of them broke into pieces

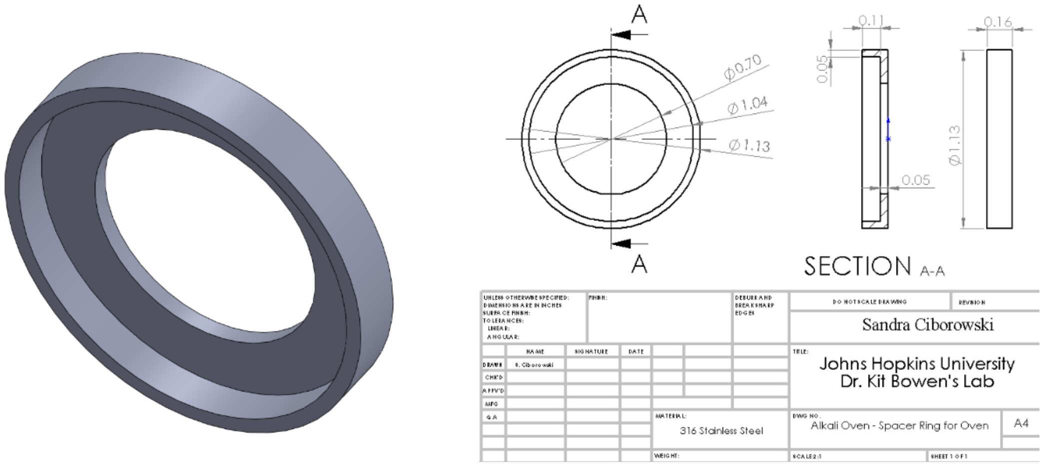

Figure A.51. New and Implemented Retaining Ring for Internal RET Oven.

in the middle where they were originally bent. Obviously, with the clips breaking at random times, the alignment of the oven was compromised.

A solid retaining ring made out of stainless steel now replaces these clips. The ring's ID is slightly wider than the internal oven and its OD is slightly thinner than the ceramic tube's ID, so that it may expand upon heating. The designs of the part in use are presented in Figure A.51.

IV.H.2. PSA-RET Instrument-Specific Information/Manual

IV.H.2.a. Turning on Machine

1. Close (3) vent valves and turn on (3) mechanical pumps.
2. Turn on (5 sets) water valves for diffusion pumps (DP).
3. If necessary (for RET), turn on alkali oven (1 A for ~30 min, then increase to 18 V).
4. Open (3) foreline valves (mechanical to DP) and verify DP's feel cold.
5. Turn on (5) DP circuit breakers.
6. After about 45 minutes, slowly open (5) gate valves (between chambers and DP), making sure that the foreline pressures do not reach 500 mTorr or above while opening.
7. Once the pressures reach reasonable levels, power supplies can be turned on and experiments run. (Ch. 0: Mid 10^{-6}, Ch. 1: Low 10^{-6}, Ch. 3: Below $5x10^{-7}$)

IV.H.2.b. Turning off Machine

1. Close (3) inline gate valves. Turn down and off all power supplies (including alkali oven heater, if on) and Stanford boxes.
2. Close (5) gate valves that isolate DP's; turn off (3) switches for DP's.
3. Plug in (2) fans. Close valve(s) to any gas tank(s), pump out lines and cart.

4. After at least 30 minutes, close (3) foreline valves, shut off (5 sets) water valves for DP's, shut off and vent (3) mechanical pumps.

IV.H.2.c. Setting Up Source

1. Vent and remove flange for Ch. 0.
2. If using solid/liquid in face of pulse valve, remove face from pulse valve.

   Note: make sure gas is pumped out of line before removal; valve from the chamber to the gas cart is closed.
3. Replace front of pulse valve, use approximately 60 psig of backing pressure, and verify alligator clips are attached and secure to top feedthroughs and pulse valve leads.
4. Test pulse valve by turning on "Box 1" (Stanford) and changing to "Int" (Internal), with 300 μs gas duration (driver box).
5. If doing laser vaporization or photoemission, check alignment of "source" laser ("Box 2", C – power and D – timing).
6. Replace flange, close bleed valve, and close foreline valve.
7. Open mechanical pump/roughing valve to Ch. 0.

   Note: watch foreline pressure while opening to verify that foreline valve is sealed.
8. After pumping to 450 mTorr or below, open foreline valve slowly, making sure foreline pressure stays below 200 mTorr.
9. If DP is warmed up, close mechanical pump valve and open gate valve to Ch. 0, while making sure that the foreline pressure does not reach 500 mTorr or above.

IV.H.2.d. Changing Polarity

1. Turn down and shut off Lens, Ion MCP, both Extraction Plates, and DH3 power supplies.

2. Change polarity switch on the back of the Ion MCP and both Extraction Plates power supplies using a flathead screwdriver.
3. Change the BNC cable position on the external MCP box (directly attached to machine near the interaction region) with the cap.
4. Switch the Behlke switches, back of machine (silver = cation, blue = anion).
5. Switch polarity on the front of the Lens power supply.
6. Change sign of deflectors (anions = +).
7. Turn all power supplies on and change the output setting on “Box 1”, Channel D: High Z (anions) or 50 ohms (cations).

IV.H.2.e. Computer Program Settings

Linear TOF, RET, MBS

Mode (File Menu): Mass

Sections of ScopeSetup

Select Rate:	200 MHz (for checking K^+, this may change depending on system studied)		
Select CH:	A (linear TOF, RET);	Scan Cycle:	20
	B (MBS)	Data Points:	10000
Time Offset:	0 µs		
Trigger Slope:	Negative	Trigger Level:	10%
Trigger Range:	5 V	Depth:	64 kV
Input Range:	200 mV (tune K^+ to 2 V)	Coupling:	DC
Input Offset:	0 mV	Impedance:	50 ohms

*Channels A and B should be the same.

IV.H.2.f. Stanford Box Settings

TABLE A.1. BOX 1 (GAS/EXTRACTION PLATES)

Setting\Line	A	B	AB	C	D	CD
Timing	T+	A+	--	T+	T+	--
Impedance	High Z	High Z	High Z	High Z	High Z/50 Ω	High Z
TTL	TTL	TTL	TTL	TTL	TTL	TTL
Inverted/Normal	Normal	Normal	--	Normal	Normal	--
Typical Delay	0	50 ms	--	3.400 μs	4015 μs	--
Part of Machine	--	--	--	Gas Time	Ext. Plates	--

TABLE A.2. BOX 2 (RED/SOURCE LASERS)

Setting\Line	A	B	AB	C	D	CD
Timing	B-	T+	--	D-	T+	--
Impedance	High Z	High Z	High Z	High Z	High Z	High Z
TTL	TTL	TTL	TTL	TTL	TTL	TTL
Inverted/Normal	Inverted	Inverted	--	Inverted	Inverted	--
Typical Delay	190 μs	4000 μs*	--	240 μs	4000 μs	--
Part of Machine	Red Laser	Red Laser	--	Source Laser	Source Laser	--

TABLE A.3. BOX 3 (BLUE LASER/MG)

Setting\Line	A	B	AB	C	D	CD
Timing	T+	A+	--	D-	T+	--
Impedance	High Z	High Z	High Z	High Z	High Z	High Z
TTL	TTL	TTL	TTL	TTL	TTL	TTL
Inverted/Normal	Inverted	Inverted	--	Inverted	Inverted	--
Typical Delay	4045.02 μs	600 ns	--	250 μs	3999.85 μs	--
Part of Machine	--	--	MG	Blue Laser	Blue Laser	--

TABLE A.4. BOX 4 (VMI LASER AND MCP)

Setting\Line	A	B	AB	C	D	CD
Timing	D-	D+	--	D-	T+	--
Impedance	High Z	High Z	High Z	High Z	High Z	High Z
TTL	TTL	TTL	TTL	TTL	TTL	TTL
Inverted/Normal	Normal	Normal	--	Inverted	Inverted	--
Typical Delay	3 μs	2 μs	--	240 μs	4051.09 μs	--
Part of Machine	--	PC	PMCP TTL	PES Laser	PES Laser	--

Table A.5. Box 5 (MD/Excimer/PES Laser)

Setting\Line	A	B	AB	C	D	CD
Timing	T+	A+	--	D-	T+	--
Impedance	High Z	High Z	High Z	High Z	50 Ω	High Z
TTL	TTL	TTL	TTL	TTL	TTL	TTL
Inverted/Normal	Normal	Normal	--	Inverted	Normal	--
Typical Delay	4053.6 μs	500 ns	--	220 μs	4053.91 μs	--
Part of Machine	Reref. Tube	--	MD	--	Excimer	--

* This is a time that will not change with source/setup.

IV.H.2.g. Power Supply Settings (Anion Mode)

IV.H.2.g.i. Linear TOF

1st Extraction Plate	-1500 V	
2nd/3rd Extraction Plates	-1400 V	*System specific, resolution
Front MCP (Ion)	0 V	
Back MCP (Ion)	+2000 V	
DH3 (Deflector Horizontal #3)	500 V	*Reads 450 V on display
Lens	-1500 V	

IV.H.2.g.ii. Reflectron TOF

Note: Black gate valve can be closed. MCP cord change.

1st Extraction Plate	-1500 V		
2nd/3rd Extraction Plates	-1400 V	*System specific	
Front MCP (Ion)	0 V	Back MCP (Ion)	+2000 V
DH3 (Deflector Horizontal #3)	500 V		
Lens	-1500 V		
Reflectron Front	-817 V	Back	-2100 V

IV.H.2.g.iii. Magnetic Bottle (MB) PES

1^{st} Extraction Plate	-1500 V		
$2^{nd}/3^{rd}$ Extraction Plates	-1400 V	*System specific	
Front MCP (Ion)	0 V		
Back MCP (Ion)	+2000 V		
DH3 (Deflector Horizontal #3)	500 V		
Lens	-1500 V		
V_{ion}	1450 V	V_{MD}	+1600 V
V_{MG}	-1700 V	V_{eMCP}	+4000 V
I_{coil}	15 V		
$I_{coil\ (aux)}$	3.25 A		
h_{MAG} (YAG/EXC)	Unchanged		

TABLE A.6. BOX 5 SETTINGS (ELIMINATES BOX 4)

Setting\Line	A	B	AB	C	D	CD
Timing	T+	A+	--	D-	B+	--
Impedance	High Z	High Z	High Z	High Z	High Z	High Z
TTL	TTL	TTL	TTL	TTL	TTL	TTL
Inverted/Normal	Normal	Normal	--	Inverted	Inverted	--
Typical Delay	4053.6 μs	500 ns	--	220 μs	400 ns	--
Part of Machine	Reref. Tube	--	MD	PES Laser	PES Laser	--

IV.H.2.g.iv. VMI Stack (λ Dependent)

Note: V_{RT} and V_{REP} are always equal; V_{REP}: V_{EXT1} and V_{REP}:V_{EXT2} are kept same by divider circuit.

1st Extraction Plate	-1500 V		
2nd/3rd Extraction Plates	-1400 V	*System specific	
Front MCP (Ion)	0 V		
Back MCP (Ion)	+2000 V		
DH3 (Deflector Horizontal #3)	500 V		
Lens	-1500 V		
V_{ion}	1450 V		
V_{MG}	-1700 V		
V_{REP}	-2000 V		
V_{RT}	-2000 V		
V_{PC}	-6000 V		
$V_{P\text{-MCP (F)}}$	+36 V	$V_{P\text{-MCP (B) – LV}}$	+1.6 kV
$V_{P\text{-MCP (B) – HV}}$	+2.12 kV	$V_{P\text{-MCP (P. Scr.)}}$	+4.0 kV

IV.H.2.h. Running Instructions

IV.H.2.h.i. Magnetic Bottle (MB) PES

1. Find ion of interest using mass mode. Mass gate the ion of interest.
2. Set Box 5, Channel A to the same value as the mass gate and increase until the signal dies and then returns to full strength.
3. For Channel B, increase until the signal dies.

   Note: for low masses, 500 ns may be too large.

4. Computer settings: PES mode, Ch. B, Time Offset: 2 μs, Scan Cycle: 20 (may change), Data Points: 2000, Base Line: -2 mV. Make sure the Channel B settings are the same as Channel A. Flip switch (above Box 3) to B.

   Note: for the excimer laser, the Stanford box should be B- rather than B+ like the Nd:YAG photoelectron laser.
5. Just before collecting, Cut Baseline: ~~V~~.

IV.H.2.h.ii. Velocity-Map Imaging (VMI) PES

1. Find ion of interest using mass mode. Mass gate the ion of interest.
2. Input values for the mass gate and extraction time into "Imaging Timing" spreadsheet, and set rereferencing tube and PES laser to suggested timing. Turn on all VMI power supplies, i.e., MCP voltages, phosphor screen, VMI stack, rereferencing tube, and pulsed collar.
3. Open the BLANK Program on the second computer and push the arrow button in the top left to start the run.
4. Lower the DH3 voltage to 50 V. Adjust the timing of the rereferencing tube and PES laser until the maximum signal is achieved.
5. Periodically save the spectrum. Include the molecule of study along with the wavelength of the PES laser, number of counts, and any other identifying information for the run, when naming the file.
6. To symmetrize the spectrum, run the Symmetrize program. Run the BASEX program, using 0.25 step size and a speed distribution, to get a photoelectron spectrum. Run the calibration program, making sure the calibration file is in the same folder as the original file and the wavelength matches the PES wavelength.

IV.H.2.i. Laser Alignment

IV.H.2.i.i. Magnetic Bottle Spectrometer

Note: For 3rd harmonic, “THG” crystal and for 4th harmonic, “FHG” crystal need to be installed after 2nd harmonic crystal (sticks straight up). Both sit with adjuster 90° to the 2nd harmonic crystal, away from wall with water system.

1. Adjust laser crystals for mostly blue light (4th harmonic). [266 nm (4th) or 355 nm (3rd) filter.]
2. Adjust “filter” if beam doesn’t follow optics well. Proceed to adjust the optics that follow.
3. Using the lower optic on the stand, optimize the blue light through the first aperture. Use the upper one to optimize the beam through the last aperture before the chamber.
4. With the aperture after the chamber mostly open and the two optics from #3, align through the chamber.

   Note: if too difficult, the minimizing pinholes can be removed momentarily. Once aligned, pinholes should be replaced at angles (to minimize light back to laser as reflections).

IV.H.2.i.ii. Velocity-Map Imaging

1. Adjust laser crystals for mostly green light (2nd harmonic). [532 nm (2nd) filter.]
2. Adjust “filter” if beam doesn’t follow optics well. Proceed to adjust the optics that follow.
3. An optic should take the beam toward the wall (with water system), then two stacked optics should take it up to the iris level, and a final optic should take it through the irises and chamber.

4. Using the lower optic on the stand, optimize the beam through the first aperture. Use the upper one to optimize the beam through the last aperture before the chamber.

   Note: the last optic can hopefully be left stationary and just the two stacked optics adjusted.

5. With the aperture after the chamber mostly open and the two optics from #3, align through the chamber.

   Note: if too difficult, the minimizing pinholes can be removed momentarily. Once aligned, apertures/pinholes should be replaced at angles (to minimize light back to laser as reflections).

   Note: if using 1st harmonic, the UV card and goggles must be worn while aligning. For 1st, 3rd, and 4th harmonics, the last optic described is unnecessary given the polarity of the beam.

IV.H.2.j. Alkali Oven Cleaning Procedure

IV.H.2.j.i. Routine Cleaning

1. Turn off the turbo pump (power button on box in front of Quad), making sure that the interlock is enabled. Chambers 1 and 2 should also be vented for alignment purposes.

   Note: if chambers 1 and 2 venting results in a pressure increase in the alkali chamber, the gate valve is probably leaking.

2. Fill the antechamber of the glovebox with air or nitrogen so that the door can be opened.
3. Turn off and remove the water lines from the bottom of the oven.

   Note: this step usually requires a solvent bucket to catch water that is still in the water jacket. The remainder of the procedure should be done with gloves and goggles.

4. Loosen the nuts and bolts at the base of the alkali oven.

5. While someone holds the base of the oven, open the black vent valve on the turbo pump.

   Note: the oven is relatively heavy and can be difficult to maneuver out of the small space. Also, one of the wooden boxes can be used to hold the oven without damaging the water lines.

6. Move the beam flag out of the way, remove the copper plate and metal spacers and place in a ceramic-like tray. Often, there is a buildup of alkali on the beam flag; remove it and place it in the same ceramic-like dish for cleaning. Use an 8-32 screw to pull out the oven. The oven should be placed in the antechamber of the glove box and stored under vacuum until cleaning is finished.

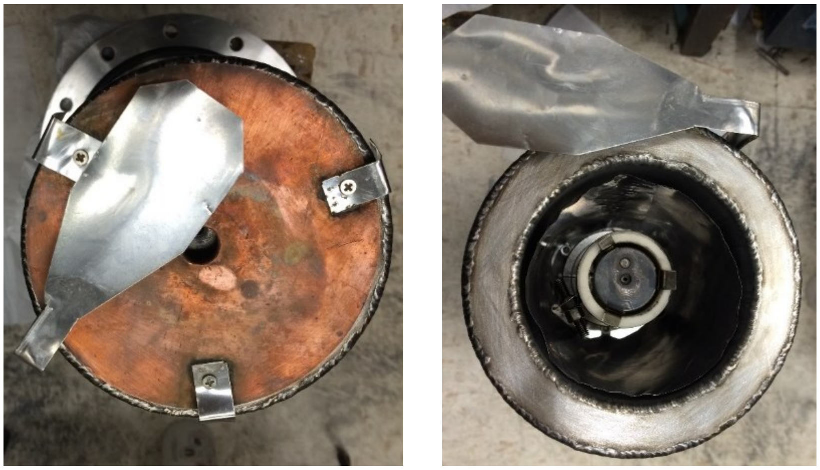

Figure A.52. Alkali Oven with and without the copper plate in place; original photographs from Allyson Buytendyk.

7. After slightly loosening the ultra-torr connections, remove the water jacket and place it in a ceramic-like dish. The ceramic-like trays should be placed in the back hood for cleaning.

8. Lower the hood and use a squirt bottle with water to clean the alkali off of the pieces in the ceramic dish.

Note: CAUTION should be taken during this step to use as little water as possible, as alkali has a violent reaction with water; use small, short sprays until all of the alkali has reacted.

9. Wipe down the remainder of the oven with plenty of water on a Kim wipe, making sure to get the feedthroughs and other supports.

Figure A.53. Alkali Oven without the copper plate and water jacket in place; original photograph from Allyson Buytendyk.

10. Clean the alkali chamber by wiping with plenty of water on a Kim wipe, using forceps may make this process a bit easier for the top of the chamber. Chamber 1 should also be wiped down in this way, especially the top of the gate valve, bottom of the internal box, and window at the top of the chamber.
11. Using a flashlight, verify that the gate valve has been cleaned; it may need to be removed for further cleaning. If this is necessary, place in ceramic-like dish for cleaning in the hood.

Note: a build-up of alkali can prevent the gate valve from completely sealing. Apiezon grease (501) can be used on the o-rings of the gate valve to aid in sealing.

12. Once all pieces have been cleaned with water and rinsed with acetone, reassemble the water jacket.
13. Clean the ceramic-like dishes, making sure to dry with acetone and Kim wipes, and line the smaller one with aluminum foil. Gather a flathead screwdriver for opening the oven; get a new razor blade and a few extra Kim wipes. Open the antechamber, remove and open the oven, and assess whether more alkali is needed.
14. If alkali is needed, remove a small section from the bottle, clean off and mop up excess mineral oil with a Kim wipe, and then use the razor blade to remove the outer, oxidized layer. The remaining alkali may need to be cut in order to fit in the oven. Close the oven firmly and, using the same 8-32 screw as before, replace it in the assembly.
15. The spacers will help to hold the oven away from the walls. The copper plate will need to be rotated until the oven's top hole is visible and relatively centered. Place the beam flag over the copper plate, so that it won't hinder replacing the oven in the chamber.
16. Carefully replace the flange with the alkali oven back in the chamber, using a bolt on either side to hold it up. Using a flashlight and mirror, check that the hole on the oven is visible through the top of Chamber 1.

    Note: it may be easier to see if the lights in the lab are turned off momentarily. If this is necessary, be sure to talk with the other people working in the lab first.
17. When the source looks well-aligned, replace all of the bolts on the bottom of the oven, close the gate valve, and close the vent valve on the turbo pump.

18. Change the interlock box to hold the foreline open, so that the alkali chamber will be pumped down by mechanical pump.
19. Once the pressure has fallen below 500 mTorr (generally, closer to 200 mTorr), turn on the turbo pump and enable the interlock.
20. Clean up the excess alkali in the ceramic dish by using the same procedure as the water jacket (Step 8). Try to move all of the alkali off of the aluminum foil first because the foil will catch fire from the alkali-water reaction. Dispose of the razor in the sharps container after rinsing with water.

IV.H.2.j.ii. Wire Replacement

The wire, 99.95% tungsten with dimensions of 0.015” diameter and 25’ length, for the heating of the alkali oven was originally purchased by Allyson Buytendyk from Thermo Shield (www.thermoshld.com), and then I ordered a slightly thicker (0.02”) wire of 85’ length. Approximately 22 feet are needed to fully wrap the ceramic heating element. This wire has only needed to be replaced once so far but becomes brittle upon numerous heating and cooling cycles. We began having a number of issues keeping the connectivity of the heating wires as we installed the oven in the chamber, which led us to investigate the wire and found multiple weak points. Due to the wire being very thin, it is easy to kink, which obviously can cause its own problems. During the replacement of the wire, it is prudent to keep the wire straight as well as keeping a few extra inches at each end to connect to the feedthroughs on the chamber flange. I suggest securing one end of the wire, e.g., at the top of the ceramic tube, and carefully lining the ceramic, making sure the wire rests tightly within the groove. Take your time.

IV.I. Glove Box Procedures

IV.I.1. General Description of Glove Box

The VAC Glove Box is a controlled atmosphere apparatus, providing an inert environment for handling highly reactive materials. Though ours only has the first two, most glove boxes have 4 accessories to create and monitor its atmosphere:

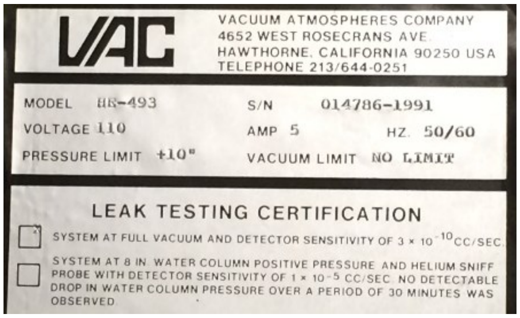

VAC

VACUUM ATMOSPHERES COMPANY
4652 WEST ROSECRANS AVE.
HAWTHORNE, CALIFORNIA 90250 USA
TELEPHONE 213/644-0251

MODEL HE-493
S/N 014786-1991
VOLTAGE 110
AMP 5
HZ. 50/60
PRESSURE LIMIT +10"
VACUUM LIMIT NO LIMIT

LEAK TESTING CERTIFICATION

☐ SYSTEM AT FULL VACUUM AND DETECTOR SENSITIVITY OF 3×10^{-10} CC/SEC.

☐ SYSTEM AT 8 IN. WATER COLUMN POSITIVE PRESSURE AND HELIUM SNIFF PROBE WITH DETECTOR SENSITIVITY OF 1×10^{-5} CC/SEC. NO DETECTABLE DROP IN WATER COLUMN PRESSURE OVER A PERIOD OF 30 MINUTES WAS OBSERVED.

Figure A.54. Information Specific to the Glove Box.

1. Pedatrol (PC-1): Provides manual and automatic control of the pressure in the glove box.
2. Dri-Train (HE-493): Removes excess oxygen and moisture from the glove box atmosphere.
3. Oxygen Analyzer (AO-316-C): Monitors trace oxygen in the inert atmosphere.
4. Moisture Analyzer (AM-2): Monitors moisture content in the inert atmosphere.

IV.I.2. Precautions

- Do not use sharps in the glove box. If you must, be careful not to puncture the gloves.
- Open any container sealed in air before pumping down the antechamber; it could burst or introduce air into the glove box.
- Kimwipes should be pumped overnight due to water content.

IV.I.3. General Operating Procedures

Note that most of these sections are taken from the manual written for the Glove Box. Some of them are tips from Bryan Eichhorn (collaborator at University of Maryland, College Park, who gave us the glove box) or his students.

IV.I.3.a. Creating an Inert Atmosphere

1. Set the left red pointer of the photohelic to 5-inch positive, and the right red pointer to 4-inch positive.
2. Turn the photohelic on.
3. Open the refill valve to the antechamber halfway. Open the antechamber hatch; this causes the pedatrol to continually push the inert gas in and push out the existing gas.
4. The pressure of the inert gas can be raised from 20 psi to 40-50 psi to speed the process.

   Note: Never let the pressure in the glove box drop below 2-inch positive.
5. Approximately 8 glove box volumes of gas should be used for a good purge.
6. Close the antechamber hatch and the refill valve.
7. Set the Pedatrol to normal operation pressure; return the inert gas regulator to 20 psi.

   Note: After purging, oxygen content should be ~200 ppm.

IV.I.3.b. Pedatrol (Manual) Operation

1. Turn the Photohelic off.
2. Using the foot pedal:
   a. Raise the pressure by pressing the right side ("R") of the pedal.
   b. Lower the pressure by pressing the left side ("L") of the pedal.

      Note: The pressure is still shown on the Photohelic.

IV.I.3.c. Automatic Operation

1. Turn the Photohelic on.
2. Set the desired pressure of the glove box:
    a. Set the maximum (high) pressure with the left red pointer.
    b. Set the minimum (low) pressure with the right red pointer.

   Note: The pressure should remain as desired as long as the Photohelic is on and there is enough inert gas pressure, usually about 5 psi on the regulator gauge. See Updates to Solenoid Valves/Photohelic Setup below.

IV.I.3.d. Sample Handling

1. Take off jewelry (watches, rings, etc.), put on gloves and lab coat.
2. Make sure the refill valve and the chamber hatch on the inside of the glove box are closed.
3. Open the chamber hatch on the outside of the glove box and load specimens/instruments.
4. Make sure that all bottles are open or contain argon/nitrogen.

   Note: Any bags, containers, etc. that are sealed with air inside could contaminate the atmosphere in the glove box.
5. Close the outer hatch.
6. Open the evacuate valve and wait for the pressure to reach full vacuum (~30 min.).
7. Open the refill valve partially; do not allow the glove box to go to zero on the Photohelic.
8. Once the pressure is about halfway to zero, close the refill valve and repeat steps 6-8 three times to ensure that there is no residual air.

9. Leave the refill valve partially open until the pressure is the same as the glove box, usually about zero.
10. Open the internal glove box hatch.

IV.I.3.e. Dry Box Indicator (Oxygen Content)

1. Dissolve 1 gram of titanocene dichloride (Cp_2TiCl_2) in 50 mL dry toluene.
2. Add 2.5 equivalents of zinc dust.
3. Stir at least 12 hours.

   Note: Solution should be green or blue; if red of yellow, add 1 equivalent of zinc dust and stir until green or blue.
4. Use 1-3 drops on a well plate or other nonreactive material and let solvent completely evaporate.
5. Check the color: green or blue is good; yellow is bad; orange or red is terrible.

IV.I.3.f. Dry Box Regeneration

1. Make sure the regeneration gas (95% N_2/5% H_2) tank contains adequate gas.
2. Turn switch from circulate to center/off position.
3. Close the dri-train inlet and outlet valves.
4. Turn regeneration timer to start.
5. Turn switch from center position to regenerate. The column will heat to approximately 200°C; this takes about 3 hours.
6. Run tubing from the metal vent tube to a water trap and then into a hood. (Not necessary to have the water trap for our purposes.)
7. Run tubing from the regeneration gas take to the regeneration gas inlet tube. (This may already be in place.)

8. Before the timer reaches the purge position, make sure that the regeneration gas is turned on (approx. 5 psi) and the manual valve (by the solenoid marked “VENT”) is opened. When the timer goes to purge, make sure the purge valve is adjusted to 20CFH; this takes about 1 hour.
9. Before the timer reaches the vacuum position, run tubing from the metal vacuum tube to a liquid nitrogen trap and then to the vacuum pump. (We don’t use a nitrogen trap; we change the mechanical pump oil after regenerations.)
10. Make sure that when the purge cycle is completed, the timer actually goes to the vacuum position. The manual valve (near the solenoid valve marked “VACUUM”) must be opened and the “VENT” manual valve closed. Shut off the regeneration gas. It should be under vacuum for at least 6 hours, overnight is okay.
11. After 8 or more hours of vacuum, turn operation switch to center/off position. Open dri-train inlet and outlet valves, and turn operation switch to circulate position.
12. Disconnect and close off vent and vacuum tubes. Note: vacuum pump oil should be changed after regeneration.

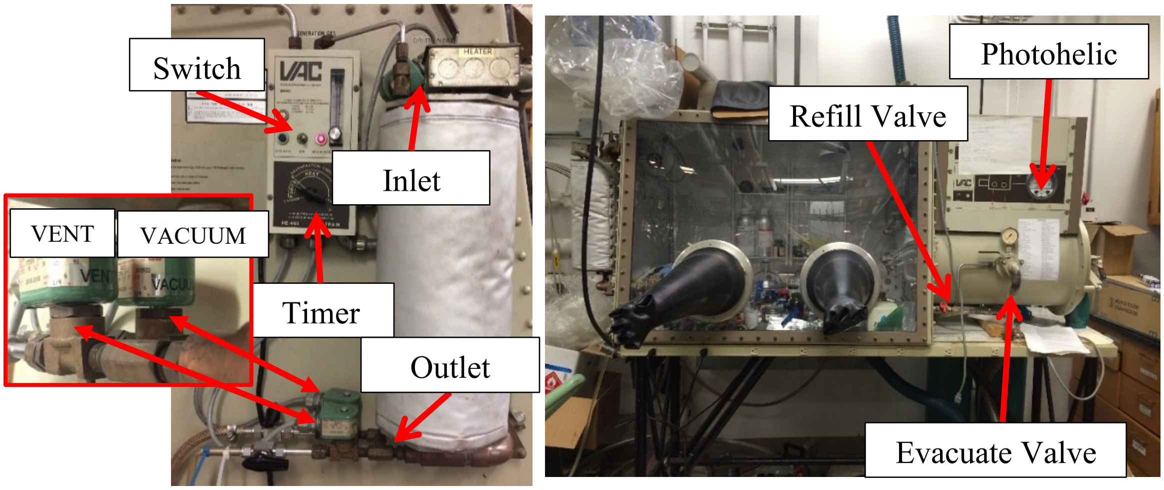

Figure A.55. Descriptive Photos of the Glove Box.

IV.I.3.g. Updates to Solenoid Valves/Photohelic Setup – Jan. 2018

1. An A3310 Photohelic Gage replaced the old photohelic gage on 01/17/18. The tubing in the control box was also redone.
2. See wiring diagram below.
    a. Prosense Digital Pressure Sensor (EPS25-14-1001, Automation Direct) was added to the pressure sensing line in the control box, along with two relays:
        i. One for HI – interrupts the HI side of photohelic gage in the case of too low of pressure.
        ii. One for LO – interrupts the LO side of photohelic gage in the case of overpressure.
    b. Prosense and relays required a DC power supply, which was added with its own power cable.

IV.I.3.h. Changing the Purifier (Catalyst) Charge

Note: Respirators are highly suggested, especially when working with the Q-5 reactant, and may need to be purchased to ensure one's safety. Gloves and goggles/glasses are required.

1. Set the glove box pressure to +4 or +5 and close the circulation valves.
2. Disconnect the stainless-steel tubing from the valve on top of the purifier.
3. Loosen the 4 nuts for the flange on the bottom of the purifier.

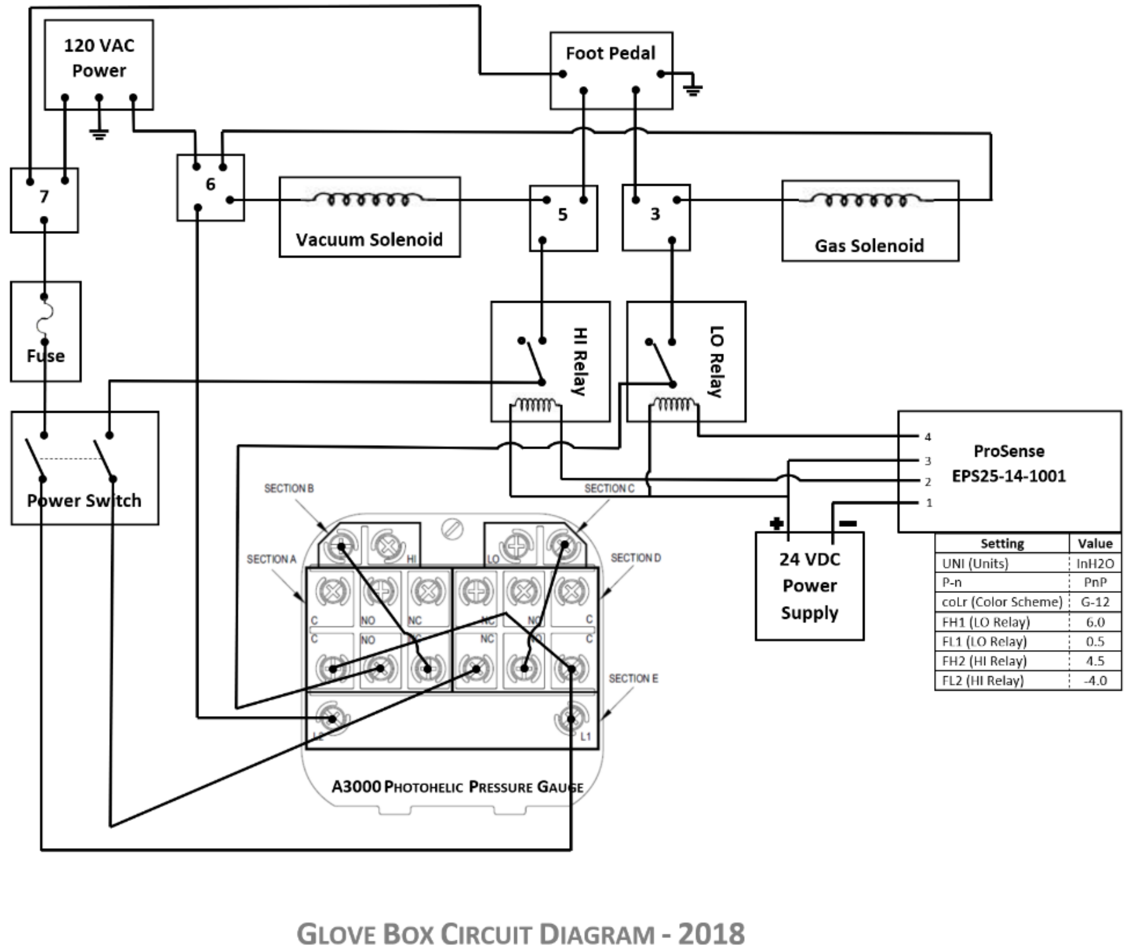

Setting	Value
UNI (Units)	InH2O
P-n	PnP
coLr (Color Scheme)	G-12
FH1 (LO Relay)	6.0
FL1 (LO Relay)	0.5
FH2 (HI Relay)	4.5
FL2 (HI Relay)	-4.0

Figure A.56. Wiring Diagram for the Glove Box with the Backup Pressure Gauge, i.e., ProSense Gauge.

4. Remove the 3 nuts from the triangular flange at the upper circulation valve.
5. Remove the 4 nuts holding the elbow plumbing to the top of the purifier and remove the elbow (the purifier will need to be tilted). Be careful to hold the valve against the box. Use tape to hold the valve against the box after the elbow is removed.
6. Use a shop-vac or powerful hose-type vacuum cleaner to vacuum out the old purifier charge.

Note: You will probably need to obtain a piece of tubing that will fit through the hole on the top of the purifier and affix it to the shop-vac hose. If a shop-vac or comparable system is not available, see #7.

7. If #6 cannot be completed as described, remove the 4 nuts at the bottom of the purifier. Open the electrical box on top of the purifier and disconnect the heater wires. Loosen the tubing from the valve on the top of the purifier. Remove the purifier from the system and dump out the old purifier charge. After dumping out the purifier, replace it on the bottom flange.
8. Using a large funnel, pour in the new purifier charge through the top port:
    a. Large (4 lbs) bag of molecular sieve (white balls)
    b. Large (5 lbs) bag of Q-5 reactant (brown particles)
    c. Small (1.75 lbs) bag of molecular sieve.
9. Replace the elbow on the purifier, making sure that the o-ring is in place.
10. Remove the tape and tilt the purifier back into position; make sure the o-rings are in place.
11. Tighten the nuts on all of the flanges and replace the tubing on the valve on the top of the purifier.

Any questions: VAC Service Department (310) 644 – 0255

IV.J. Using the Burleigh Wavemeter

During the alignment of the wavemeter, it is possible to get two readings for the same wavelength. While it’s confusing, we’ve mapped out some of the values we’ve gotten using the Coumarin 480 dye in the Spectra Physics PDL dye laser (old laser, pre-Cobra).

> Note: The highlighted values are ones we are confident are for the 15d level of potassium. This was confirmed when the Cobra dye laser was set to 466.31 nm and the wavemeter read 466.16 nm. We believe this is due to the age of the wavemeter and the likely need for recalibration of such.

TABLE A.7. POTASSIUM LEVELS FROM QUANTUM DEFECT CALCULATIONS, THE NIST LEVEL DATABASE, AND THE BURLEIGH WAVEMETER.

Principle No.		From Quantum Defect			From NIST Level Database			Burleigh Wavemeter	
nd	n*	eV (Level)	eV (after D2)	nm (after D2)	eV (Level)	eV (after D2)	nm (after D2)	Lower	Higher
40	39.75	4.33209	2.71498	456.66722	4.33002	2.71291	457.01531	--	--
39	38.75	4.33164	2.71453	456.74295	4.32957	2.71246	457.09127	--	--
38	37.75	4.33115	2.71404	456.82481	4.32908	2.71197	457.17339	--	--
37	36.75	4.33063	2.71352	456.91347	4.32856	2.71145	457.26233	--	--
36	35.75	4.33005	2.71294	457.00972	4.32798	2.71087	457.35889	--	--
35	34.75	4.32943	2.71232	457.11444	4.32736	2.71025	457.46394	--	--
34	33.75	4.32876	2.71165	457.22866	4.32668	2.70957	457.57854	--	--
33	32.75	4.32801	2.71090	457.35357	4.32594	2.70883	457.70387	--	--
32	31.75	4.32720	2.71009	457.49054	4.32513	2.70802	457.84131	--	--
31	30.75	4.32631	2.70920	457.64119	4.32423	2.70712	457.99249	--	--
30	29.75	4.32533	2.70822	457.80740	4.32325	2.70614	458.15929	--	--
29	28.75	4.32424	2.70713	457.99139	4.32216	2.70505	458.34395	--	--
28	27.75	4.32303	2.70592	458.19581	4.32095	2.70384	458.54913	--	--
27	26.75	4.32169	2.70458	458.42378	4.31960	2.70249	458.77798	--	--
26	25.75	4.32018	2.70307	458.67911	4.31809	2.70098	459.03429	--	--
25	24.75	4.31849	2.70138	458.96634	4.31639	2.69928	459.32266	--	--
24	23.75	4.31658	2.69947	459.29104	4.31448	2.69737	459.64870	--	--
23	22.75	4.31441	2.69730	459.66005	4.31231	2.69520	460.01926	--	--
22	21.75	4.31194	2.69483	460.08185	4.30983	2.69272	460.44286	460.62	--
21	20.75	4.30910	2.69199	460.56705	4.30698	2.68987	460.93020	461.13	--
20	19.75	4.30582	2.68871	461.12907	4.30369	2.68658	461.49476	461.73	461.07
19	18.75	4.30200	2.68489	461.78513	4.29986	2.68275	462.15385	462.44	461.77
18	17.75	4.29752	2.68041	462.55755	4.29536	2.67825	462.92995	463.27	462.6
17	16.75	4.29221	2.67510	463.47575	4.29003	2.67292	463.85262	463.19	463.55
16	15.75	4.28585	2.66874	464.57915	4.28366	2.66655	464.96152	464.36	464.75
15	14.75	4.27816	2.66105	465.92155	4.27594	2.65883	466.31074	465.79	466.16
14	13.75	4.26874	2.65163	467.57800	4.26648	2.64937	467.97572	467.56	467.92
13	12.75	4.25700	2.63989	469.65582	4.25471	2.63760	470.06429	469.70	470.16
12	11.75	4.24215	2.62504	472.31308	4.23981	2.62270	472.73517	472.61	472.98
11	10.75	4.22297	2.60586	475.79076	4.22056	2.60345	476.23001	476.32	476.68
10	9.75	4.19758	2.58047	480.47206	4.19511	2.57800	480.93241	481.33	--
9	8.75	4.16299	2.54588	486.99880	4.16046	2.54335	487.48298	--	--
8	7.75	4.11417	2.49706	496.51982	4.11165	2.49454	497.02296	--	--
7	6.75	4.04208	2.42497	511.28053	4.03979	2.42268	511.76498	--	--
6	5.75	3.92919	2.31208	536.24628	3.92796	2.31085	536.53098	--	--
5	4.75	3.73768	2.12057	584.67458	3.74075	2.12364	583.82909	--	--
4	3.75	3.37318	1.75607	706.03056	3.39522	1.77811	697.28039	--	--
3	2.75	2.54160	0.92449	1341.10889	2.66872	1.05161	1178.99930	--	--

IV.K. Unpublished Results

A few studies have been completed in the lab with sufficient amounts of data to be published at some point but are not yet fully ready for publication. At this time, that includes the following three drafts: The Reaction of Metal Tetraphenylporphyrins with O_2 and CO_2, The Photoelectron Spectrum of the Uranium Dimer, and The Photoelectron Spectra of $Ru_1Sb_{7,9,11}^-$. In each case, theoretical calculations would help solidify the geometric structures based on what is observed in the photoelectron spectra.

Much of the work for the first of these three was completed in part by Zhaoguo Zhu and Mary Marshall on the ESI-PIPES instrument. Using a traditional closed-housing laser vaporization source, different species were mass-analyzed when O_2 or CO_2 were mixed in the helium backing gas of the pulse valve. Complexes involving oxygen from both mixtures were studied by anion photoelectron spectroscopy.

The uranium dimer took a number of renditions but was successfully accomplished with a Lineberger Source-like setup using the Lai-Sheng Wang-Style housing and the pulse valve stand of the open-housing LVS. When the Wang-Style housing's pulse valve was backed with argon gas and the other pulse valve had helium, the uranium dimer anion was able to be selected and analyzed by photoelectron spectroscopy.

The $RuSb_n$-containing sample was acquired from Yi Wang in Bryan Eichhorn's group at the University of Maryland, College Park, and was finished using the Biosource, since the sample is air sensitive and, as such, needed to be loaded within the glove box's nitrogen atmosphere. Peaks corresponding to $Ru_1Sb_{7,9,11}^-$ anions were most clearly seen in the mass spectrum and, thus, analyzed by photoelectron spectroscopy.

IV.K.1. The Reaction of Metal Tetraphenylporphyrins with O_2 and CO_2

Sandra M. Ciborowski, Zhaoguo Zhu, Mary A. Marshall, Gaoxiang Liu, Maria C. Dipalo, and Kit H. Bowen

Unpublished Results.

IV.K.1.a. Experimental Methods

Anion photoelectron spectroscopy is conducted by crossing a mass-selected beam of negative ions with a fixed frequency laser beam. This process is governed by the energy-conserving relationship, hν = EBE + EKE, where hν is the photon energy, EBE is the electron binding energy, and EKE is the electron kinetic energy. EKE values are determined by magnetic bottle spectroscopy, using the third (355 nm, 3.49 eV) or fourth (266 nm, 4.66 eV) harmonic of a Nd:YAG laser, which has a resolution of ~35 meV at an EKE of 1 eV. Photoelectron spectra were calibrated against the well-known atomic transitions of Cu^-.[1]

The anions were generated using a laser vaporization source, consisting of a rotating and translating metal rod coated with the porphyrin of interest and the second harmonic (532 nm, 2.33 eV) of a Nd:YAG laser. The apparatus has been described previously.[2] Briefly, once generated, the anions drifted into the extraction region of the time-of-flight mass spectrometer, where they were mass-analyzed. After deceleration, the ions interacted with the photodetachment laser and the electrons were energy-analyzed with the magnetic bottle spectrometer.

IV.K.1.b. Results and Discussion

Backing gases of various compositions, i.e., pure helium, 5% CO_2 in helium, or 5% O_2 in helium, were introduced to the tetraphenylmetalloporphyrins, $M(TPP)^-$, where M was Ni, Mg, or Fe. While there was no evidence of Ni or Mg reacting with CO_2 or O_2, the mass spectra of these gases with $Fe(TPP)^-$ exhibited new peaks belonging to complexes: $Fe(TPP)O_{1,2,3}^-$, as displayed in Figure A.57.

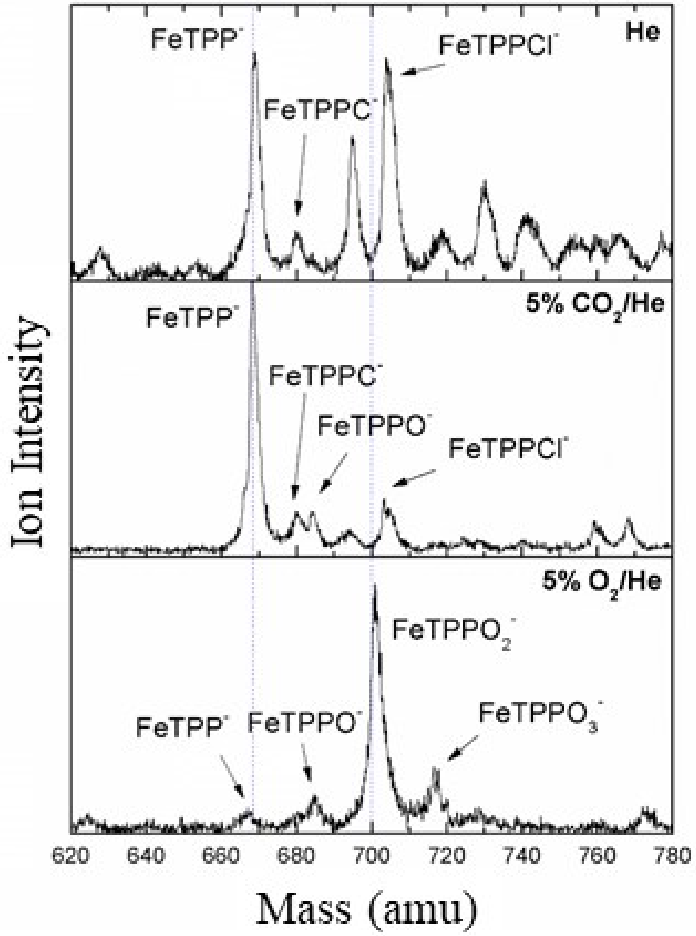

Figure A.57. Mass Spectra in the 620 – 780 amu Region to Highlight the Different Species Observed with Varied Composures Backing Gases: (A) Helium, (B) 5% CO_2 in Helium, and (C) 5% O_2 in Helium.

The photoelectron spectra of Fe(TPP)O$^-$ anions taken with the 3rd and 4th harmonics of a Nd:YAG laser are presented in Figure A.58. The electron affinity is defined as the energy difference between the anion and the ground state of the neutral and is considered the onset of an anion's photoelectron spectrum. The maximum of each peak in a spectrum are vertical detachment energies, i.e., the difference between the anion and higher electronic states of the neutral. A discernable peak, labeled as X in the spectra, has an EA value equal to 1.5 eV and a VDE value of 2.0 eV. There is a second, large, broad peak that convolutes the higher side of the aforementioned peak; although a higher photon energy

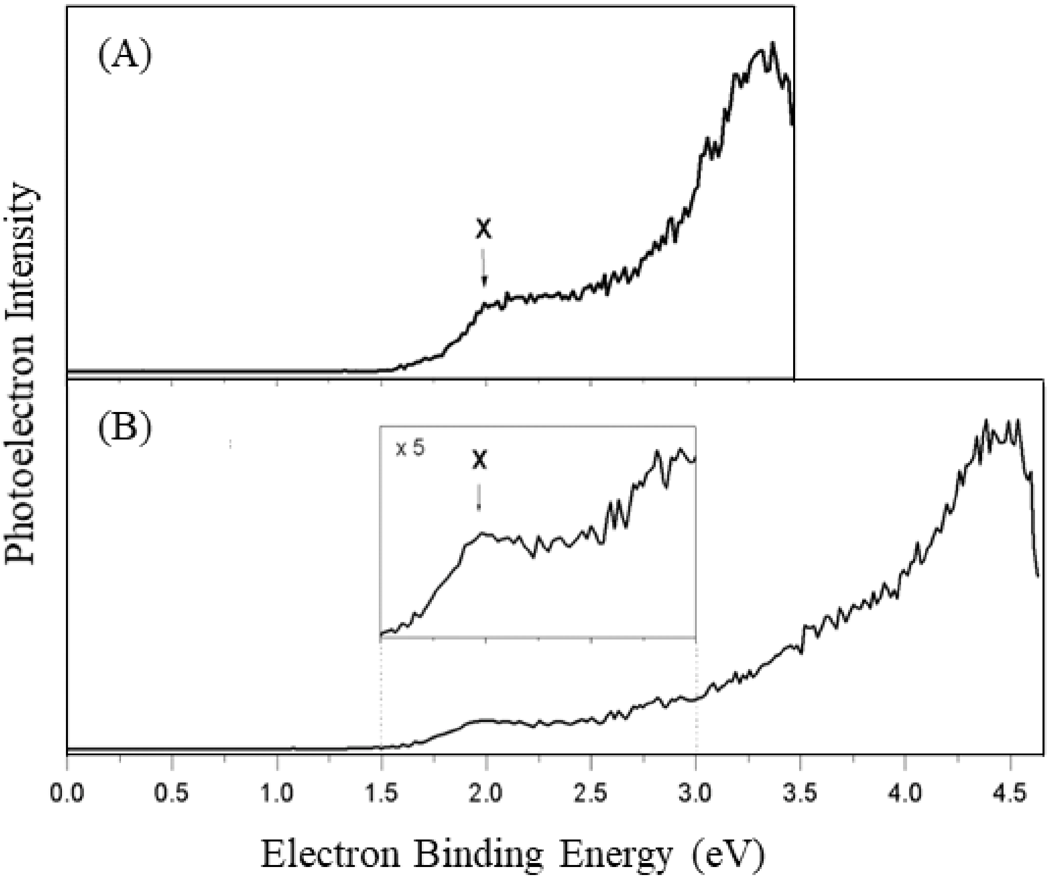

Figure A.58. Photoelectron Spectra of Fe(TPP)O$^-$ Taken with the (A) 3rd Harmonic (355 nm, 3.49 eV) and (B) 4th Harmonic (266 nm, 4.66 eV) of a Nd:YAG Laser.

was used, the maximum of this second peak is not able to be observed. When compared with the photoelectron spectrum of Fe(TPP)$^-$, previously taken,[3] the spectra have a different shape and the premier peak does not seem to significantly shift, suggesting more than simply physisorption is occurring.

Similarly, the photoelectron spectrum of Fe(TPP)O_2^- taken with the 4th harmonic of a Nd:YAG laser is displayed in Figure A.59. Its multiple, broad peaks also indicate that O_2 does not just interact with the Fe(TPP)$^-$ but may become activated or otherwise deformed. In addition to a VDE value at 2.0 eV, the Fe(TPP)O_2^- complex has more distinct peaks centered at 2.8, 3.6, 3.8, and 4.3 eV. These values may signify transitions to excited states of the neutral complex.

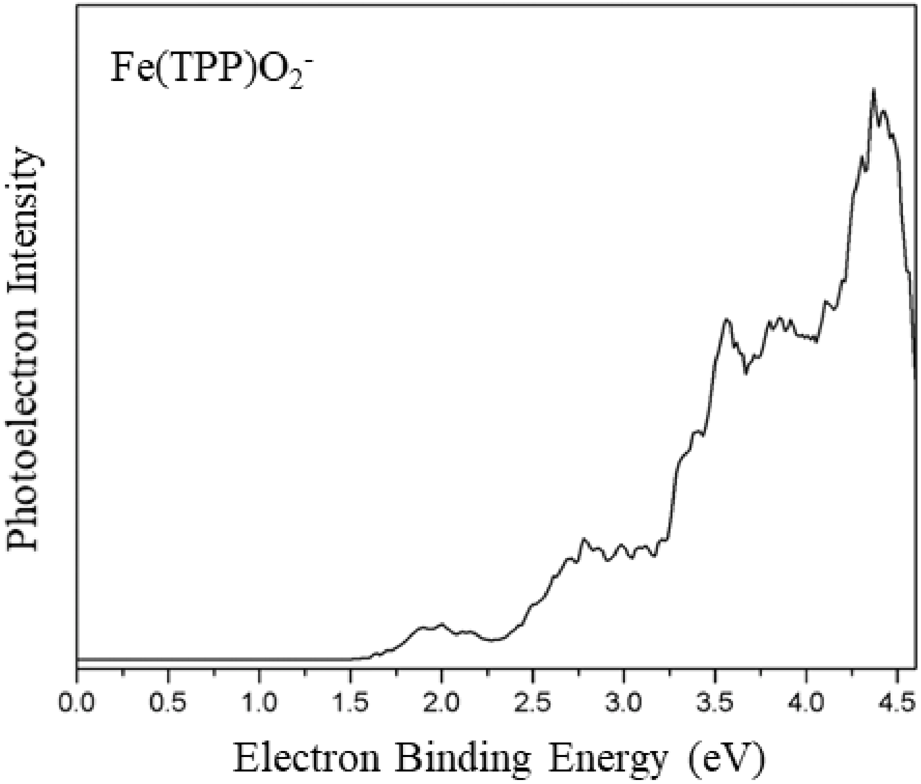

Figure A.59. Photoelectron Spectrum of Fe(TPP)O_2^- Taken with the 4th Harmonic (266 nm, 4.66 eV) of a Nd:YAG Laser.

Acknowledgements

This work is supported by the U. S. National Science Foundation (NSF) under grant number, CHE-1952511.

References

1. J. Ho, K. M. Ervin, and W. C. Lineberger, *J. Chem. Phys.* **93**, 6987 (1990).
2. O. C. Thomas, W. Zheng, and K. H. Bowen, *J. Phys. Chem.* **114**, 5514 (2001).
3. A. M. Buytendyk, J. D. Graham, J. Gould, and K. H. Bowen, *J. Phys. Chem. A* **119**, 8643 (2015).

IV.K.2. The Photoelectron Spectrum of the Uranium Dimer

Sandra M. Ciborowski, Rachel M. Harris, (Moritz Blankenhorn), Gaoxiang Liu, and Kit H. Bowen

Unpublished Results.

IV.K.2.a. Experimental Methods

Anion photoelectron spectroscopy is conducted by crossing a beam of mass-selected negative ions with a fixed-frequency photon beam and energy-analyzing the resultant photodetached electrons. The photodetachment process is governed by the energy-conserving relationship: hν = EBE + EKE, where hν is the photon energy, EBE is the electron binding energy, and EKE is the electron kinetic energy. Our apparatus consists of a laser vaporization cluster anion source perpendicular to a pulse valve, a time-of-flight mass spectrometer, a Nd:YAG photodetachment laser, and a magnetic bottle electron energy analyzer.[1] The photoelectron spectrometer resolution is ~35 meV at 1 eV EKE. The third (355 nm) harmonic output of a Nd:YAG laser was used to photodetach electrons from the mass-selected U_2^- dimer. Photoelectron spectra were calibrated against the well-known atomic transitions of atomic Cu^-.[2]

A schematic of our LVS-coupled pulse valve source is shown in Figure A.60 and was inspired an electric discharge source designed by Lineberger *et al.*[3] Uranium dimer anions were generated by the laser vaporization of a pure uranium rod. The resultant plasma was cooled with argon gas delivered by a pulsed valve (PV1) having a backing pressure of a 60 psig. The resulting uranium cluster anions then were further cooled with a pulsed valve (PV2) set perpendicularly to the laser axis and linear to the ion axis. The resulting U_2^-

anionic dimer was mass-analyzed by the time-of-flight mass spectrometer and its photoelectron spectrum was recorded.

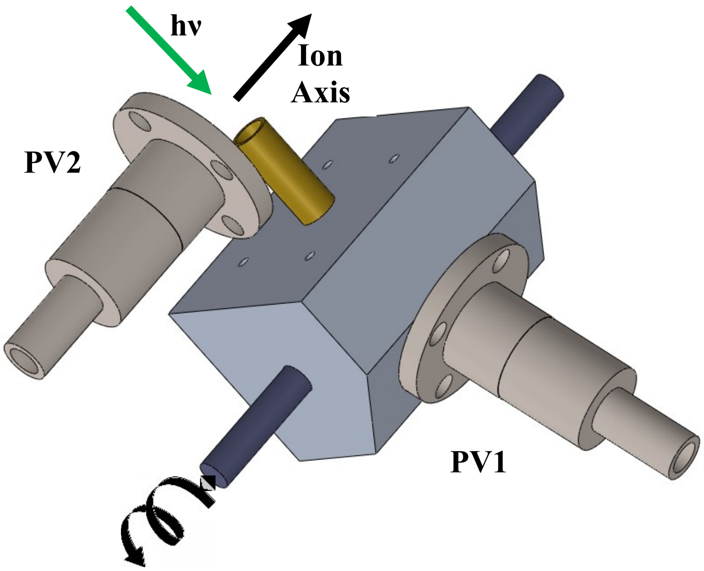

Figure A.60. Schematic of the LVS-Coupled Pulse Valve Source, Showing the Rotating, Translating Uranium Rod, Pulse Valves backed with Either Argon (PV1) or Helium (PV2), the Ablation Laser (hν), and the Axis of Ion Travel.

IV.K.2.b. Results and Discussion

The U_2^- dimer anions were clearly seen in the mass spectrum and their photoelectron spectrum was taken with the third harmonic (355 nm, 3.49 eV) of a Nd:YAG laser (see Figure A.61). The spectrum is rich in electronic transitions. The first of which has an EA value of 1.0 eV and first VDE value equal to 1.12 eV. Three subsequent peaks of approximately the same magnitude are observed at 1.16, 1.20, and 1.28 eV. Various other peaks saturate the remainder of the spectrum and may belong to transitions from the anion state to diverse excited states of the neutral U_2 dimer.

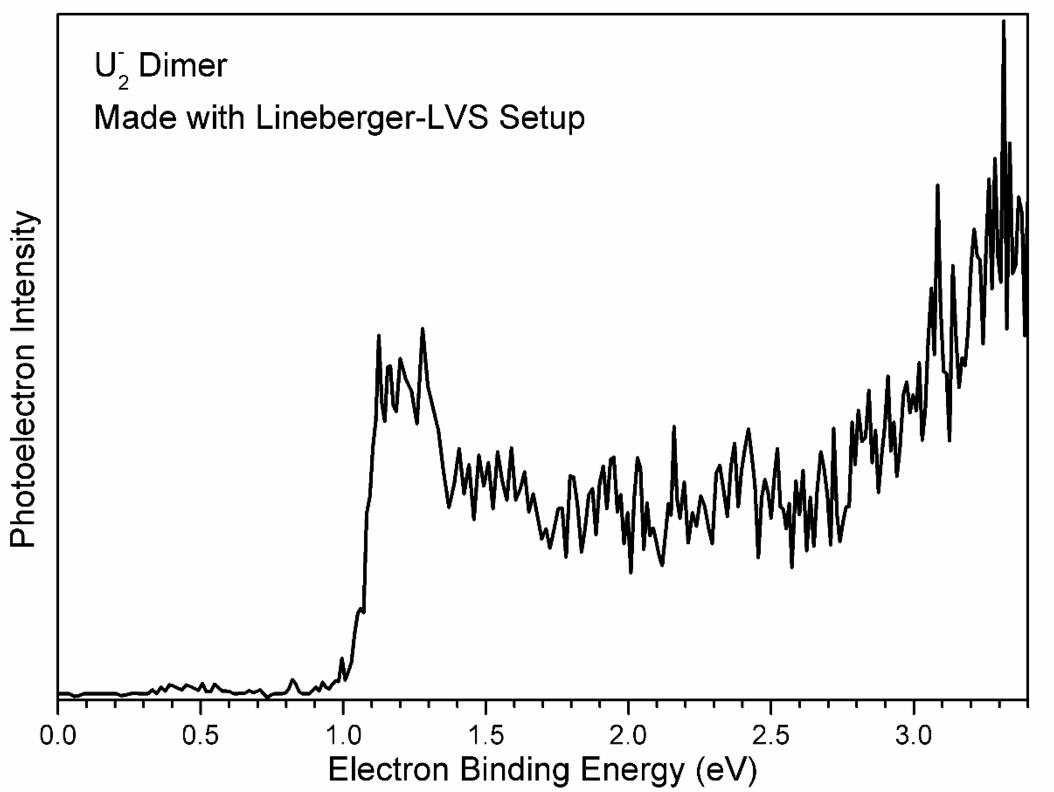

Figure A.61. Photoelectron Spectrum of the U_2^- Dimer Anion Taken with the 3rd Harmonic (355 nm, 3.49 eV) of a Nd:YAG Laser.

There has been much debate on the electronic structure of the uranium dimer.[4,5] With this new, unique experimental evidence, examination of the different theoretical methods, as well as the geometric structure of the U_2 dimer, both as a negative ion and neutral molecule, will be able to be remedied and completed.

Acknowledgements

This work supported by a grant from from the U. S. Department of Energy (DOE) under Award Number ##.

References

1. O. C. Thomas, W. Zheng, and K. H. Bowen, *J. Phys. Chem.* **114**, 5514 (2001).
2. J. Ho, K. M. Ervin, and W. C. Lineberger, *J. Chem. Phys.* **93**, 6987 (1990).

3. Y.-J. Lu, J. H. Lehman, and W. C. Lineberger, *J. Chem. Phys.* **142**, 044201 (2015).
4. L. Gagliardi and B. O. Roos, *Nature* **433**, 848 (2005).
5. S. Knecht, H. J. A. Jensen, and T. Saue, *Nature Chem.* **11**, 40 (2019).

IV.K.3. Eichhorn Sample: $Ru_1Sb_{7,9,11}^-$

Sandra M. Ciborowski,[1] Yi Wang,[2] Gaoxiang Liu,[1] Chalynette J. Martinez-Martinez,[1] Lauren Stevens,[2] Rachel M. Harris,[1] Bryan Eichhorn,[2] and Kit H. Bowen[1]

[1] Department of Chemistry, Johns Hopkins University, Baltimore, MD 21218

[2] Department of Chemistry & Biochemistry, University of Maryland, College Park, MD 20742

Unpublished Results.

IV.K.3.a. Experimental Methods

Anion photoelectron spectroscopy is conducted by crossing a mass-selected beam of negative ions with a fixed-frequency photon beam. It is governed by the energy-conserving relationship: hν = EKE + EBE, where hν is the photon energy, EKE is the electron kinetic energy, and EBE is the electron binding energy. Our spectrometer has been described previously.[1] Briefly, once the ions of interest are mass-selected, they are decelerated until they enter the interaction region, where the pulse from a Nd:YAG laser photodetaches the electrons from the anions. The resultant electrons are then energy analyzed by the magnetic bottle spectrometer, which has a resolution of about 35 meV at an EKE of 1 eV. The photoelectron spectra were calibrated against the well-known atomic transitions of Cu^-.[2]

The anions of interest were created using a laser desorption – laser photoemission technique. Under a nitrogen atmosphere, the sample was coated onto a graphite bar that was placed within an air-tight suitcase. The first harmonic (1064 nm, 1.07 eV) of a Surelite Minilite Nd:YAG laser was slightly focused onto the translating graphite bar in order to transmit the sample into the gas phase. Concurrently, the second harmonic (532 nm, 2.33 eV) of a Nd:YAG laser was focused onto a hafnium wire as a source of electrons. A pulse valve was used to transfer the resultant ions into the extraction region of the time-of-flight mass spectrometer, where they were mass analyzed and, eventually, whose electrons were photodetached.

IV.K.3.b. Results and Discussion

The $[K(2,2,2\text{-crypt})]_2[Ru_2(Cp^*)Sb_6]\bullet2(C_7H_8)$ sample was made by Yi Wang, a post-doctoral researcher with Bryan Eichhorn at the University of Maryland, College Park.

The peaks of particular anionic clusters of the compositions $RuSb_n^-$, n = 7, 9, 11 were clearly observed in the mass spectrum; see Figure A.62. The isotope patterns of each cluster are also discernable.

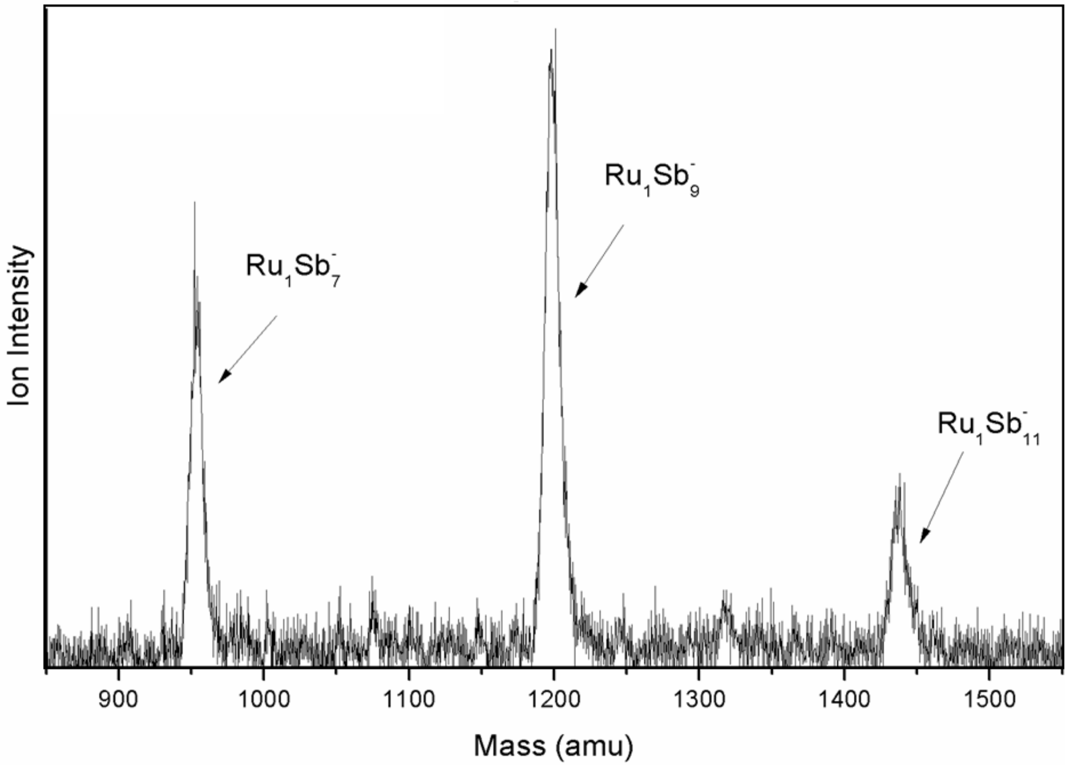

Figure A.62. Mass Spectrum of the $[K(2,2,2\text{-crypt})]_2[Ru_2(Cp^*)Sb_6]\bullet2(C_7H_8)$ Sample Taken with the Laser Desorption – Laser Photoemission Source.

Photoelectron spectra of the three prominent peaks were obtained; see Figure A.63(A-C). The electron affinity (EA) is the onset of the photoelectron spectrum and represents the transition energy from the anion to the corresponding neutral cluster's ground state. While all three, $RuSb_n^-$ clusters present multiple, broad peaks, the $RuSb_{11}^-$ anion exhibits a significantly higher EA, i.e., the first peak originates at 2.2 eV. The anionic

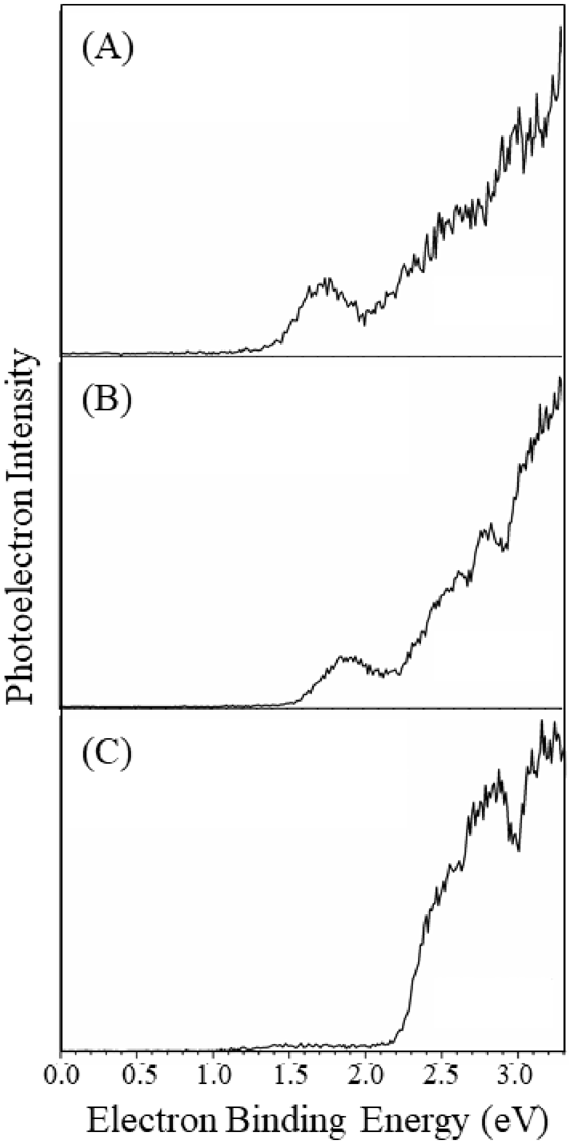

Figure A.63. Photoelectron Spectra of the (A) $RuSb_7^-$ Anion, (B) $RuSb_9^-$ Anion, and (C) $RuSb_{11}^-$ Anion Taken with the 3rd Harmonic (355 nm, 3.49 eV) of a Nd:YAG laser.

clusters, $RuSb_7^-$ and $RuSb_9^-$ spectra display one small peak, beginning at 1.4 eV and 1.6 eV, respectively. Vertical detachment energies are considered the transitions from the anion to other states of the analogous neutral; the most intense of which would have the greatest Franck-Condon overlap. Each spectrum has multiple VDE peaks. The maximum, i.e., VDE, of the first peak lies at 1.75 eV for $RuSb_7^-$, 1.88 eV for $RuSb_9^-$, and 2.58 eV for $RuSb_{11}^-$.

Acknowledgements

The gas-phase work is based on work supported by the Office of Naval Research (ONR), Multidisciplinary University Research Initiative (MURI) under Grant No. N00014-15-1-2681.

References

1. O. C. Thomas, W. Zheng, and K. H. Bowen, *J. Phys. Chem.* **114**, 5514 (2001).
2. J. Ho, K. M. Ervin, and W. C. Lineberger, *J. Chem. Phys.* **93**, 6987 (1990).

Curriculum Vitae/Resumé

SANDRA M. CIBOROWSKI

✿ sciboro1@jhu.edu ✿ www.linkedin.com/in/sandra-ciborowski-72001786 ✿

PROFESSIONAL SUMMARY

Spectroscopic and synthetic experimental and computational chemist with expertise in scientific communication, teamwork, and collaboration.

- Practiced in leadership and teamwork, e.g., headed multiple small groups in laboratories, oversaw multiple tutors at different times throughout graduate career, and worked within teams of 2-5 students to complete various published projects.
- Exceptional oral and written communicator, i.e., invited to talk at a small college and during a research-abroad experience, given numerous lectures and poster presentations, published manuscripts (two first-authored out of seventeen published/submitted), and acted as a teaching assistant and/or tutor for twelve years.

EDUCATION

Johns Hopkins University, Baltimore, MD

Doctor of Philosophy in Chemistry Expected Graduation Dec. 2019
Masters of Arts in Chemistry, GPA: 3.63 July 2017
Thesis: "The Creation of Anions by Laser Vaporization and Rydberg Electron Transfer and Studied by Anion Photoelectron Spectroscopy", *Advisor*: Dr. Kit H. Bowen

- Conducted experiments on and maintained a pulsed source apparatus, which included multiple ion sources, a linear time-of-flight mass spectrometer, a magnetic bottle photoelectron spectrometer, and a velocity-map imaging photoelectron spectrometer
- Requested quotes and fielded offers from multiple companies for chemicals and parts
- Designed various sources, skimmers, etc. in SolidWorks for fabrication by graduate students and/or professional machinists
- Acted as the group's safety officer
  - Maintained an accurate, up-to-date inventory of chemicals in Microsoft Excel
  - Completed training in chemical waste management, use of fire extinguishers, and respiratory protection
  - Monitored cleanliness of the lab
  - Communicated any issues with Dr. Bowen and the HSE office

University of Massachusetts Dartmouth, North Dartmouth, MA

Masters of Science in Chemistry, GPA: 3.68 May 2014
Thesis: "A Computational Study of the Effects of Substituents on the Energy of the Porphyrin Molecule", *Advisor*: Dr. Emmanuel Ojadi

- Conducted synthetic steps toward a nitrated porphyrin molecule
- Determined and validated structures of intermediate steps using NMR spectroscopy, in addition to LCMS and GCMS methods
- Completed computational studies on the effects of substituents on a porphyrin macrocycle

Catawba College, Salisbury, NC

Bachelors of Arts in Chemistry, GPA: 2.94 May 2010
Minors: Secondary Education and Math
Thesis: "The Effects of pH Changes and Metals on the Binding of the Natural Dye, Brazilwood, to Silk", *Advisors*: Dr. Carol Ann Miderski and Dr. James Beard

- Prepared solutions of Brazilwood with assorted metals and at varying pH values for treatment of silk samples
- Studied samples by UV-Vis, IR, and NMR spectroscopies
- Made stock solutions for various chemistry courses

AWARDS/HONORS

Langmuir-Cresap Research Award, Johns Hopkins Univ. Chemistry Dept. May 2018
Graduate Teaching Assistant Award, UMass Dartmouth Chemistry Dept. April 2012
Gamma Sigma Epsilon, Chemistry Honor Soc., Catawba College Apr. 2008 – May 2010

INVITED TALKS

Heinrich-Heine-Universität Düsseldorf (Germany), Research Presentation 2016
Messiah College (Mechanicsburg, PA), Invited Talk 2017

POSTER PRESENTATIONS

International Symposium on Clusters and Nanomaterials: Energy and Medicine, Richmond, VA, USA, Nov. 3-7, 2019, P29 (Nov. 6).
American Chemical Society 47th Middle Atlantic Regional Meeting 2019, Baltimore, MD, USA, May 30 – June 1, 2019.
Women in STEM Symposium, Baltimore, MD, USA April 2019
International Bunsen Discussion Meeting: Gas Phase Model Systems for Catalysis, Ulm, Germany, June 18 – 20, 2018, P1.
Delocalized Electrons in Atomic and Molecular Nanoclusters, Erice, Italy July 2016
Symposium on Size-Selected Clusters, Davos, Switzerland March 2016
Sigma Xi, North Dartmouth, MA April 2012
ACS National Meeting, San Francisco, CA March 2010

PROFESSIONAL MEMBERSHIPS

American Chemical Society, Student Member
OSA The Optical Society, Student Member

COURSE LECTURES

Johns Hopkins University (Baltimore, MD) 2016 [2], 2017 [4], 2018 [2]
Chemical Kinetics (AS.030.610)
University of Mass. Dartmouth (N. Dartmouth, MA) Spring 2014
Introductory Chemistry II (CHM 152)

TEACHING EXPERIENCE

Head Teaching Assistant
Chemistry Dept., Johns Hopkins Univ. Jan. 2016 – May 2016

- Coordinated teaching assistants' schedules for general chemistry help sessions
- Oversaw and aided in grading exams
- Ran a problem-solving course

    - Made packets (3-5 questions) related to lecture material in Microsoft Word
    - Solved problems in person and in collaboration with the students
    - Constructed answer keys to be uploaded to Blackboard
    - Worked with individual students and small groups

Graduate Instructor

Chemistry Dept., Univ. of Mass. Dartmouth Jan. 2014 – May 2014

- Instructed Introductory Chemistry II (CHM 152, ≤105 students)
- Developed and graded three one-hour exams and a final exam in Microsoft Word
- Created Microsoft PowerPoint presentations to display material
- Used the online homework system, Mastering Chemistry
- Utilized Microsoft Excel to store and calculate grades

Graduate Teaching Assistant

Chemistry Dept., Univ. of Mass. Dartmouth Aug. 2011 – Dec. 2013

- Instructed two sections (≤128 students) of general chemistry labs each semester
- Taught a directed study, general chemistry (CHM 151) course during the summer
    - Used Microsoft Word to create periodic quizzes and two exams
    - Worked through problems with students
- Planned pre-lab lectures in PowerPoint before each week’s chemistry lab
- Graded formal reports and lab exams and guided certain aspects of grading
- Attended weekly meetings and trainings with lab supervisor

Instructor

Johns Hopkins Centers for Talented Youth June 2012 – Aug. 2014

- Instructed three-week courses on crystals and polymers
- Coordinated lectures and lab experiments for 10- to 13-year-old students
- Modified course materials based on pre-assessment and students’ backgrounds
- Worked closely with a teaching assistant

Teaching Assistant

Chemistry Dept., Johns Hopkins Univ. Aug. 2014 – Dec. 2015
Chemistry Dept., Univ. of Mass. Dartmouth Aug. 2010 – Aug. 2011

- Graded pre- and post-laboratory assignments
- Guided students on and graded lab notebooks
- Recorded grades in Microsoft Excel and submitted to instructor

Tutor

Science & Engineering Center, Univ. of Mass. Dartmouth Jan. 2011 – June 2013

- Tutored students in chemistry, physics and mathematics courses
- Created and ran multiple, weekly, large-scale chemistry tutoring groups
    - Constructed packets (≤10 questions) related to lecture material in Word
    - Wrote answer keys and uploaded them to Blackboard website
    - Kept weekly attendance and points in Microsoft Excel
    - Met with professors periodically
- Coordinated general and organic chemistry group tutors
- Assisted in the development of a bridge program for incoming chemistry majors
- Launched TutorTrac (online appointment system)
    - Introduced and presented to director, office staff and tutors
    - Facilitated generating reports of center usage

  - Operated online tutorials for general chemistry courses using a Wacom Bamboo tablet

Private Tutor, Glenelg High School Sept. 2005 – May 2006
Tutoring Center, Catawba College Jan. 2007 – May 2009

- Assisted individual students and small groups of students
- Guided students on assignments in chemistry, physics, calculus, and French
- Recorded and submitted hours worked

PUBLICATIONS

G. Liu, V. Chauhan, A. Aydt, **S. Ciborowski**, A. Pinkard, Z. Zhu, X. Roy, S. Khanna, K. Bowen, "Ligand Effect on the Electronic Structure of Cobalt Sulfide Clusters: A Combined Experimental and Theoretical Study", *J. Phys. Chem. C* **123** (2019) 25121-25127.

G. Liu, **S. M. Ciborowski**, J. D. Graham, A. M. Buytendyk, K. H. Bowen, "The Ground State, Quadrupole-Bound Anion of Succinonitrile Revisited", *J. Chem. Phys.* **151** (2019) 101101/1-5.

G. Liu, **S. M. Ciborowski**, C. R. Pitts, J. D. Graham, A. M. Buytendyk, T. Lectka, and K. H. Bowen,"Observation of the Dipole- and Quadrupole-Bound Anions of 1,4-Dicyanocyclohexane", *Phys. Chem. Chem. Phys.* **21** (2019) 18310-18315.

G. Liu, N. Fedik, C. Martinez-Martinez, **S. M. Ciborowski**, X. Zhang, A. I. Boldyrev, K. H. Bowen, "Realization of Lewis Basic Na Anion in the $NaBH_3^-$ Cluster", *Angew. Chem. Int. Ed.* **58** (2019) 13789-13793.

X. Zhang, G. Liu, **S. Ciborowski**, W. Wang, C. Gong, Y. Yao, K. H. Bowen, "Spectroscopic Measurement of a Halogen Bond Energy", *Angew. Chem. Int. Ed.* **58** (2019) 11400-11403.

G. Liu, **S. M. Ciborowski**, Z. Zhu, Y. Chen, X. Zhang, and K. H. Bowen, "The Metallo–Formate Anions, $M(CO_2)^-$, M = Ni, Pd, Pt, formed by Electron–Induced CO_2 Activation", *Phys. Chem. Chem. Phys.* **21**, (2019) 10955-10960. (Selected as 2019 PCCP Hot Paper.)

G. Liu, V. Chauhan, A. Aydt, **S. Ciborowski**, A. Pinkard, Z. Zhu, X. Roy, S. Khanna, K. H. Bowen, "Ligand Effect on the Electronic Structure of Metal Chalcogenide Clusters: A Combined Experimental and Theoretical Study", *J. Phys. Chem. C* **123** (2019) 25121-25127.

S. M. Ciborowski, R. M. Harris, G. Liu, C. J. Martinez-Martinez, P. Skurski, and K. H. Bowen, "The correlation-bound anion of p-chloroaniline", *J. Chem. Phys.* **150** (2019) 161103/1-4.

G. Liu, Z. Zhu, **S. M. Ciborowski**, I. R. Ariyarathna, E. Miliordos, K. H. Bowen, "Selective Activation of the C-H Bond in Methane by Single Platinum Atomic Anions", *Angew. Chem. Int. Ed.* **58** (2019) 7773-7777.

G. Liu, A. Pinkard, **S. M. Ciborowski**, V. Chauhan, Z. Zhu, A. P. Aydt, S. N. Khanna, X. Roy, and K. H. Bowen, "Tuning the Electronic Properties of Hexanuclear Cobalt Sulfide Superatoms via Ligand Substitution", *Chem. Sci.* **10** (2019) 1760-1766.

G. Liu, **S. M. Ciborowski**, Z. Zhou, and K. H. Bowen, "Activation of Hydroxylamine by A Single Anionic Gold Atom", *Int. J. Mass Spectrom.* **435** (2019) 114-117.

G. Liu, E. Miliordos, **S. M. Ciborowski**, M. Tschurl, U. Boesl, U. Heiz, X. Zhang, S. Xantheas, and K. Bowen, "Water Activation and Splitting by Single Metal-Atom Anions", *J. Chem. Phys.* **149** (2018) 221101.

S. M. Ciborowski, G. Liu, J. D. Graham, A. M. Buytendyk, and K. H. Bowen, "Dipole-Bound Anions Formed by Rydberg Electron Transfer (RET) and Studied by Velocity Map Imaging-Anion Photoelectron Spectroscopy (VMI-aPES)", *Eur. Phys. J. D* **72** (2018) 139-143.

E. F. Belogolova, G. Liu, E. P. Doronina, **S. M. Ciborowski**, V. F. Sidorkin, K. H. Bowen, "Dipole-Bound Anions of Intra-Molecular Complexes", *J. Phys. Chem. Lett.* **9** (2018) 1284-1289.

P. J. Robinson, G. Liu, **S. Ciborowski**, C. Martinez-Martinez, J. R. Chamorro, X. Zhang, T. M. McQueen, K. H. Bowen, and A. N. Alexandrova, "Mystery of Three Borides: Differential Metal Boron Bonding Governing Superhard Structures", *Chem. Mater.* **29** (2017) 9892-9896.

G. Liu, **S. M. Ciborowski**, K. Bowen, "Photoelectron Spectroscopic and Computational Study of Pyridine-Ligated Gold Cluster Anions", *J. Phys. Chem. A* **121** (2017) 5817-5822.

X. Zhang, G. Liu, **S. Ciborowski**, K. Bowen, "Stabilizing Otherwise Unstable Anions with Halogen Bonding", *Angew. Chem. Int. Ed.* **56** (2017) 9897-9900.

S. Ciborowski, "A Computational Study of the Effects of Substituents on the Energy of the Porphyrin Molecule: A Thesis in Chemistry", University of Massachusetts Dartmouth, Department of Chemistry & Biochemistry, degree granting institution (2014).